Making, probing and understanding ultracold Fermi gases

Wolfgang Ketterle and Martin W. Zwierlein

Department of Physics, MIT-Harvard Center for Ultracold Atoms, and Research Laboratory of Electronics,
Massachusetts Institute of Technology, Cambridge, Massachusetts, 02139, USA

Table of contents

3

1. – Introduction

1˙1. *State of the field*. – This paper summarizes the experimental frontier of ultracold fermionic gases. It is based on three lectures which one of the authors gave at the Varenna summer school describing the experimental techniques used to study ultracold fermionic gases, and some of the results obtained so far. In many ways, the area of ultracold fermionic gases has grown out of the study of Bose-Einstein condensates. After their first experimental realizations in 1995 [1, 2], the field of BEC has grown explosively. Most of the explored physics was governed by mean-field interactions, conveniently described by the Gross-Pitaevskii equation. One novel feature of trapped inhomogeneous gases was the spatially varying density, that allowed for the direct observation of the condensate, but also led to new concepts of surface effects and collective excitations which depended on the shape of the cloud. The experimental and theoretical explorations of these and other features have been a frontier area for a whole decade!

A major goal had been to go beyond mean field physics, which is in essence single particle physics, and to find manifestations of strong interactions and correlations. Three avenues have been identified: lower dimensions that enhance the role of fluctuations and correlations, optical lattices that can suppress the kinetic energy in the form of tunnelling [3, 4], and Feshbach resonances [5, 6, 7, 8] that enhance interactions by resonantly increasing the interparticle scattering length. In bosonic systems, the tuning of interactions near Feshbach resonances was of limited applicability due to rapid losses. Feshbach resonances were used mainly to access molecular states of dimers and trimers. In contrast, for fermions, losses are heavily suppressed (see below), and so most of this review focuses on strongly interacting fermions near Feshbach resonances.

By addressing the physics of strongly correlated matter, the field of ultracold atoms is entering a new stage where we expect major conceptional advances in, and challenges to many-body theory. We regard it as fortunate that BEC turned out to be a less complex target (both experimentally and theoretically), and over a decade, important techniques and methods have been developed and validated, including experimental techniques to confine and cool nanokelvin atoms, the use of Feshbach resonances to modify their properties, and many theoretical concepts and methods to describe trapped ultracold gases and their interactions. What we are currently experiencing is the application of these powerful methods to strongly correlated systems, and due to the maturity of the field, the developments have been breath-taking, in particular with bosons in optical lattices and fermions interacting via Feshbach resonances. It is possible that the most important conceptional advances triggered by the advent of Bose-Einstein condensation are yet to be discovered.

It is amusing to note that in certain limits, strongly correlated fermion pairs are again described by a mean-field theory. Their wave function is a product of identical pair wave functions (albeit correctly anti-symmetrized), that for strong binding of the pairs turns into the state described by the Gross-Pitaevskii equation. This is the simplest description of the BEC-BCS crossover. Still, the fact that pairing has now become a many-body affair stands for the advent of a new era in ultracold atom physics.

1˙2. *Strongly correlated fermions - a gift of nature?.* – It shows the dynamics of the field of ultracold atoms that the area of strongly interacting fermions has not been expected or predicted. This may remind us of the pre-BEC era, when many people considered BEC to be an elusive goal, made inaccessible by inelastic interactions at the densities required [9]. When Feshbach resonances were explored in bosonic systems, strong interactions were always accompanied by strong losses, preventing the study of strongly interacting condensates [7, 10, 11]. The reason is that a Feshbach resonance couples the atomic Hilbert space to a resonant molecular state which is vibrationally highly excited. Collisions can couple this state to lower lying states (vibrational relaxation).

What occurred in Fermi gases, however, seemed too good to be true: all relaxation mechanisms were dramatically suppressed by the interplay of the Pauli exclusion principle and the large size of the Feshbach molecules. So what we have got is a Hilbert space which consists of atomic levels plus one single molecular level resonantly coupled to two colliding atoms. All other molecular states couple only weakly. As a result, pair condensation and fermionic superfluidity could be realized by simply ramping down the laser power in an optical trap containing ^{6}Li in two hyperfine states at a specific magnetic field, thereby evaporatively cooling the system to the superfluid state. Even in our boldest moments we would not have dared to ask Nature for such an ideal system.

Before the discovery of Feshbach resonances, suggestions to realize fermionic superfluidity focused on lithium because of the unusually large and negative triplet scattering length [12, 13, 14]. However, a major concern was whether the gas would be stable against inelastic collisions. The stability of the strongly interacting Fermi gas was discovered in Paris in the spring of 2003, when long-lived Li_2 molecules were observed despite their high vibrational excitation [15][1]. This and subsequent observations [17, 18] were soon explained as a consequence of Pauli suppression [19]. Within the same year, this unexpected stability was exploited to achieve condensation of fermion pairs. This unique surprise has changed the field completely. Currently, more than half of the research program of our group is dedicated to fermions interacting near Feshbach resonances.

There is another aspect of Fermi gases, which turned out to be more favorable than expected. Early work on the BCS state in ultracold gases suggested a competition between superfluidity and collapse (for negative scattering length) or coexistence and phase separation (for positive scattering length) when the density or the absolute value of the scattering length a exceeded a certain value, given by $k_F|a| = \pi/2$, where k_F is the Fermi wave vector [13, 20, 21]. This would have implied that the highest transition temperatures to the superfluid state would be achieved close to the limit of mechanical stability, and that the BCS-BEC crossover would be interrupted by a window around the Feshbach resonance, where phase separation occurs. Fortunately, unitarity limits the maximum attractive energy to a fraction of the Fermi energy (βE_F with $\beta \approx -0.58$), completely eliminating the predicted mechanical instability.

---

[1] The observation of long lifetimes of molecules outside a narrow Feshbach resonance [16] is not yet understood and has not been used to realize a strongly interacting gas.

Finally, a third aspect received a lot of attention, namely how to detect the superfluid state. Since no major change in the spatial profile of the cloud was expected [21], suggested detection schemes included a change in the decay rate of the gas [21], optical light scattering of Cooper pairs [22, 23], optical breakup of Cooper pairs [24], modification of collective excitations [25, 26], or small changes in the spatial shape [27]. All these signatures are weak or complicated to detect. Fortunately, much clearer and more easily detectable signatures were discovered. One is the onset of pair condensation, observed through a bimodal density distribution in expanding clouds, observed either well below the Feshbach resonance or after rapid sweeps of the magnetic field. Another striking signature was the sudden change in the cloud shape when fermion mixtures with population imbalance became superfluid, and finally, the smoking gun for superfluidity was obtained by observing superfluid flow in the form of quantized vortices.

Our ultimate goal is to control Nature and create and explore new forms of matter. But in the end, it is Nature who sets the rules, and in the case of ultracold fermions, she has been very kind to us.

1˙3. *Some remarks on the history of fermionic superfluidity.* –

1˙3.1. BCS superfluidity. Many cold fermion clouds are cooled by sympathetic cooling with a bosonic atom. Popular combinations are ^{6}Li and ^{23}Na, and ^{40}K and ^{87}Rb. It is remarkable that the first fermionic superfluids were also cooled by a Bose-Einstein condensate. Kamerlingh Onnes liquefied ^{4}He in 1908, and lowered its temperature below the superfluid transition point (the λ-point) at $T_\lambda = 2.2$ K. In his Nobel lecture in 1913, he notes "that the density of the helium, which at first quickly drops with the temperature, reaches a maximum at 2.2 K approximately, and if one goes down further even drops again. Such an extreme could possibly be connected with the quantum theory" [28]. But instead of studying, what we know now was the first indication of superfluidity of bosons, he first focused on the behavior of metals at low temperatures. In 1911, Onnes used ^{4}He to cool down mercury, finding that the resistivity of the metal suddenly dropped to non-measurable values at $T_C = 4.2$ K, it became "superconducting". Tin (at $T_C = 3.8$ K) and lead (at $T_C = 6$ K) showed the same remarkable phenomenon. This was the discovery of superfluidity in an electron gas.

The fact that bosonic superfluidity and fermionic superfluidity were first observed at very similar temperatures, is due to purely technical reasons (because of the available cryogenic methods) and rather obscures the very different physics behind these two phenomena.

Bosonic superfluidity occurs at the degeneracy temperature, i.e. the temperature T at which the spacing between particles $n^{-1/3}$ at density n becomes comparable to the thermal de Broglie wavelength $\lambda = \sqrt{\frac{2\pi\hbar^2}{mk_BT}}$, where m is the particle mass. The predicted transition temperature of $T_{\text{BEC}} \sim \frac{2\pi\hbar^2}{m}n^{2/3} \approx 3$ K for liquid helium at a typical density of $n = 10^{22}$ cm^{-3} coincides with the observed lambda point.

In contrast, the degeneracy temperature (equal to the Fermi temperature $T_F \equiv E_F/k_B$) for conduction electrons is higher by the mass ratio $m(^4\text{He})/m_e$, bringing it

up to several ten-thousand degrees. It was only in 1957 when it became clear why in fermionic systems, superfluidity occurs only at temperatures much smaller than the degeneracy temperature.

Of course, the main difference to Bose gases is that electrons, being fermions, cannot be in one and the same quantum state but instead must arrange themselves in *different* states. An obvious scenario for superfluidity might be the formation of tightly bound pairs of electrons that can act as bosons and could form a condensate. But apart from the problem that the condensation temperature would still be on the order of E_F/k_B, there is no known interaction which could be sufficient to overcome the strong Coulomb repulsion and form tightly bound electron pairs (Schafroth pairs [29]). The idea itself of electrons forming pairs was indeed correct, but the conceptual difficulties were so profound that it took several decades from the discovery of superconductivity to the correct physical theory.

In 1950, it became clear that there was indeed an effective attractive interaction between electrons, mediated by the crystal lattice vibrations (phonons), that was responsible for superconductivity. The lattice vibrations left their mark in the characteristic variation $T_C \propto 1/\sqrt{M}$ of the critical temperature T_C with the isotope mass M of the crystal ions, the isotope effect [30, 31] predicted by H. Fröhlich [32]. Vibrational energies in the lattice are a factor $\sqrt{m_e/M}$ smaller than the typical electronic energy[2] E_F, on the order of $k_B\times$ several 100 K (the Debye temperature T_D of the metal). While the isotope effect strongly argues for T_C being proportional to T_D, the Debye temperature is still one or two orders of magnitude higher than the observed critical temperature.

A breakthrough came in 1956, when L. Cooper realized that fermions interacting via an arbitrarily weak attractive interaction on top of a filled Fermi sea can form a bound pair [33]. In other words, the Fermi sea is unstable towards pair formation. However, unlike the tightly bound pairs considered before, the "Cooper" pair is very large, much larger than the interparticle spacing. That is, a collection of these pairs necessarily needs to overlap very strongly in space. In this situation, it was far from obvious whether interactions between different pairs could simply be neglected. But it was this simplifying idea that led to the final goal: Bardeen, Cooper and Schrieffer (BCS) developed a full theory of superconductivity starting from a new, stable ground state in which pair formation was included in a self-consistent way [34]. Using the effective phonon-mediated electron-electron interaction V, attractive for energies smaller than $k_B T_D$ and assumed constant in this regime, the pair binding energy was found to be $\Delta = 2k_B T_D\, e^{-1/\rho_F|V|}$, with $\rho_F = m_e k_F/2\pi^2\hbar^2$ the density of states at the Fermi energy and $\rho_F|V|$ assumed small compared to 1. The bound state energy or the pairing gap depended in the non-analytic fashion $e^{-1/\rho_F|V|}$ on the effective electron-electron

---

[2] The average distance between electrons r_0 is on the order of atomic distances (several Bohr radii a_0), the Fermi energy $E_F \sim \hbar^2/m_e r_0^2$ is thus on the scale of typical Coulomb energies in an atom. Vibrational energies of the lattice ions are then on the order $\hbar\omega_D \approx \hbar\sqrt{\frac{\partial^2 U_{\text{Coulomb}}}{\partial r^2}/M} \sim \hbar\sqrt{E_F/Mr_0^2} \sim \sqrt{m_e/M}\, E_F$.

| BEC of Molecules | Crossover Superfluid | BCS state |
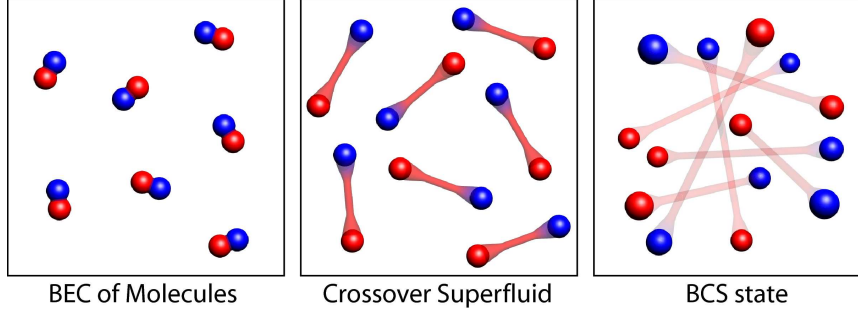
Fig. 1. – The BEC-BCS crossover. By tuning the interaction strength between the two fermionic spin states, one can smoothly cross over from a regime of tightly bound molecules to a regime of long-range Cooper pairs, whose characteristic size is much larger than the interparticle spacing. In between these two extremes, one encounters an intermediate regime where the pair size is comparable to the interparticle spacing.

interaction V, explaining why earlier attempts using perturbation theory had to fail. Also, this exponential factor can now account for the small critical temperatures $T_C \simeq$ 5 K: Indeed, it is a result of BCS theory that $k_B T_C$ is simply proportional to Δ_0, the pair binding energy at zero temperature: $k_B T_C \approx 0.57 \, \Delta_0$. Hence, the critical temperature $T_C \sim T_D \, e^{-1/\rho_F |V|}$ is proportional to the Debye temperature T_D, in accord with the isotope effect, but the exponential factor suppresses T_C by a factor that can easily be 100.

1˙3.2. The BEC-BCS crossover. Early work on BCS theory emphasized the different nature of BEC and BCS type superfluidity. Already in 1950 Fritz London had suspected that fermionic superfluidity can be understood as a pair condensate in momentum space, in contrast to a BEC of tightly bound pairs in real space [35]. The former will occur for the slightest attraction between fermions, while the latter appears to require a true two-body bound state to be available to a fermion pair. Schrieffer points out that BCS superfluidity is not Bose-Einstein condensation of fermion pairs, as these pairs do not obey Bose-Einstein statistics [36]. However, it has become clear that BEC and BCS superfluidity are intimately connected. A BEC is a special limit of the BCS state.

It was Popov [37], Keldysh and collaborators [38] and Eagles [39] who realized in different contexts that the BCS formalism and its ansatz for the ground state wave function provides not only a good description for a condensate of Cooper pairs, but also for a Bose-Einstein condensate of a dilute gas of tightly bound pairs. For superconductors, Eagles [39] showed in 1969 that, in the limit of very high density, the BCS state evolves into a condensate of pairs that can become even smaller than the interparticle distance and should be described by Bose-Einstein statistics. In the language of Fermi gases, the scattering length was held fixed, at positive and negative values, and the interparticle spacing was varied. He also noted that pairing without superconductivity can occur above the superfluid transition temperature. Using a generic two-body potential, Leggett

9

showed in 1980 that the limits of tightly bound molecules and long-range Cooper pairs are connected in a smooth crossover [40]. Here it was the interparticle distance that was fixed, while the scattering length was varied. The size of the fermion pairs changes smoothly from being much larger than the interparticle spacing in the BCS-limit to the small size of a molecular bound state in the BEC limit (see Fig. 1). Accordingly, the pair binding energy varies smoothly from its small BCS value (weak, fragile pairing) to the large binding energy of a molecule in the BEC limit (stable molecular pairing).

The presence of a paired state is in sharp contrast to the case of two particles interacting in free (3D) space. Only at a critical interaction strength does a molecular state become available and a bound pair can form. Leggett's result shows that in the many-body system the physics changes smoothly with interaction strength also at the point where the two-body bound state disappears. Nozières and Schmitt-Rink extended Leggett's model to finite temperatures and verified that the critical temperature for superfluidity varies smoothly from the BCS limit, where it is exponentially small, to the BEC-limit where one recovers the value for Bose-Einstein condensation of tightly bound molecules [41].

The interest in strongly interacting fermions and the BCS-BEC crossover increased with the discovery of novel superconducting materials. Up to 1986, BCS theory and its extensions and variations were largely successful in explaining the properties of superconductors. The record critical temperature increased only slightly from 6 K in 1911 to 24 K in 1973 [42]. In 1986, however, Bednorz and Müller [43] discovered superconductivity at 35 K in the compound $La_{2-x}Ba_xCuO_4$, triggering a focused search for even higher critical temperatures. Soon after, materials with transition temperatures above 100 K were found. Due to the strong interactions and quasi-2D structure, the exact mechanisms leading to High-T_C superconductivity are still not fully understood.

The physics of the BEC-BCS crossover in a gas of interacting fermions does not directly relate to the complicated phenomena observed in High-T_C materials. However, the two problems share several features: In the crossover regime, the pair size is comparable to the interparticle distance. This relates to High-T_C materials where the correlation length ("pair size") is also not large compared to the average distance between electrons. Therefore, we are dealing here with a strongly correlated "soup" of particles, where interactions between different pairs of fermions can no longer be neglected. In both systems the normal state above the phase transition temperature is far from being an ordinary Fermi gas. Correlations are still strong enough to form uncondensed pairs at finite momentum. In High-T_C materials, this region in the phase diagram is referred to as the "Nernst regime", part of a larger region called the "Pseudo-gap" [44].

One point in the BEC-BCS crossover is of special interest: When the interparticle potential is just about strong enough to bind two particles in free space, the bond length of this molecule tends to infinity (unitarity regime). In the medium, this bond length will not play any role anymore in the description of the many-body state. The only length scale of importance is then the interparticle distance $n^{-1/3}$, the corresponding energy scale is the Fermi energy E_F. In this case, physics is said to be universal [45]. The average energy content of the gas, the binding energy of a pair, and (k_B times)

the critical temperature must be related to the Fermi energy by universal numerical constants. The size of a fermion pair must be given by a universal constant times the interparticle distance.

It is at the unitarity point that fermionic interactions are at their strongest. Further increase of attractive interactions will lead to the appearance of a bound state and turn fermion pairs into bosons. As a result, the highest transition temperatures for fermionic superfluidity are obtained around unitarity and are on the order of the degeneracy temperature. Finally, almost 100 years after Kamerlingh Onnes, it is not just an accidental coincidence anymore that bosonic and fermionic superfluidity occur at similar temperatures!

1˙3.3. *Experiments on fermionic gases.* After the accomplishment of quantum degeneracy in bosons, one important goal was the study of quantum degenerate fermions. Actually, already in 1993, one of us (W.K.) started to set up dye lasers to cool fermionic lithium as a complement to the existing experiment on bosons (sodium). However, in 1994 this experiment was shut down to concentrate all resources on the pursuit of Bose-Einstein condensation, and it was only in early 2000 that a new effort was launched at MIT to pursue research on fermions. Already around 1997, new fermion experiments were being built in Boulder (using ^{40}K, by Debbie Jin) and in Paris (using ^{6}Li, by Christophe Salomon, together with Marc-Oliver Mewes, a former MIT graduate student who had worked on the sodium BEC project).

All techniques relevant to the study of fermionic gases had already been developed in the context of BEC, including magnetic trapping, evaporative cooling, sympathetic cooling [46, 47], optical trapping [48] and Feshbach resonances [7, 8]. The first degenerate Fermi gas of atoms was created in 1999 by B. DeMarco and D. Jin at JILA using fermionic ^{40}K [49]. They exploited the rather unusual hyperfine structure in potassium that allows magnetic trapping of two hyperfine states without spin relaxation, thus providing an experimental "shortcut" to sympathetic cooling. All other schemes for sympathetic cooling required laser cooling of two species or *optical* trapping of two hyperfine states of the fermionic atom. Until the end of 2003, six more groups had succeeded in producing ultracold degenerate Fermi gases, one more using ^{40}K (M. Inguscio's group in Florence, 2002 [50]) and five using fermionic ^{6}Li (R. Hulet's group at Rice [51], C. Salomon's group at the ENS in Paris [52], J. Thomas' group at Duke [53], our group at MIT [54] in 2001 and R. Grimm's group in Innsbruck in 2003 [55]).

Between 1999 and 2001, the ideal Fermi gas and some collisional properties were studied. 2002 (and late 2001) was the year of Feshbach resonances when several groups managed to optically confine a two-component mixture and tune an external magnetic field to a Feshbach resonance [56, 57, 58, 58, 59]. Feshbach resonances were observed by enhanced elastic collisions [57], via an increase in loss rates [56], and by hydrodynamic expansion, the signature of a strongly interacting gas [60]. The following year, 2003, became the year of Feshbach molecules. By sweeping the magnetic field across the Feshbach resonance, the energy of the Feshbach molecular state was tuned below that of two free atoms ("molecular" or "BEC" side of the Feshbach resonance) and molecules

could be produced [61]. These sweep experiments were very soon implemented in Bose gases and resulted in the observation of Cs_2 [62], Na_2 [63] and Rb_2 [64] molecules. Pure molecular gases made of bosonic atoms were created close to [62] or clearly in [63] the quantum-degenerate regime. Although quantum degenerate molecules were first generated with bosonic atoms, they were not called Bose-Einstein condensates, because their lifetime was too short to reach full thermal equilibrium.

Molecules consisting of fermionic atoms were much more long-lived [15, 17, 16, 18] and were soon cooled into a Bose-Einstein condensate. In November 2003, three groups reported the realization of Bose-Einstein condensation of molecules [65, 66, 55]. All three experiments had some shortcomings, which were soon remedied in subsequent publications. In the ^{40}K experiment the effective lifetime of 5 to 10 ms was sufficient to reach equilibrium in only two dimensions and to form a quasi- or nonequilibrium condensate [65]. In the original Innsbruck experiment [55], evidence for a long-lived condensate of lithium molecules was obtained indirectly, from the number of particles in a shallow trap and the magnetic field dependence of the loss rate consistent with mean-field effects. A direct observation followed soon after [67]. The condensate observed at MIT was distorted by an anharmonic trapping potential.

To be precise, these experiments realized already crossover condensates (see section **6**) consisting of large, extended molecules or fermion pairs. They all operated in the strongly interacting regime with $k_F a > 1$, where the size of the pairs is not small compared to the interparticle spacing. When the interparticle spacing $\sim 1/k_F$ becomes smaller than the scattering length $\sim a$, the two-body molecular state is not relevant anymore and pairing is a many-body affair. In fact, due to the increase of collisional losses on the "BEC" side, experiments have so far explored pair condensates only down to $k_F a \approx 0.2$ [68]. Soon after these first experiments on fermion pair condensates, their observation was extended throughout the whole BEC-BCS crossover region by employing a rapid ramp to the "BEC"-side of the Feshbach resonance [69, 70].

During the following years, properties of this new crossover superfluid were studied in thermodynamic measurements [71, 72], experiments on collective excitations [73, 74], RF spectroscopy revealing the formation of pairs [75], and an analysis of the two-body part of the pair wave function was carried out [76]. Although all these studies were consistent with superfluid behavior, they did not address properties unique to superfluids, i.e. hydrodynamic excitations can reflect superfluid or classical hydrodynamics, and the RF spectrum shows no difference between the superfluid and normal state [77]. Finally, in April 2005, fermionic superfluidity and phase coherence was directly demonstrated at MIT through the observation of vortices [68]. More recent highlights (in 2006 and 2007) include the study of fermionic mixtures with population imbalance [78, 79, 80, 81, 82], the (indirect) observation of superfluidity of fermions in an optical lattice [83], the measurement of the speed of sound [84] and the measurement of critical velocities [85]. Other experiments focused on two-body physics including the formation of p-wave molecules [86] and the observation of fermion antibunching [87].

System	T_C	T_F	T_C/T_F
Metallic lithium at ambient pressure [88]	0.4 mK	55 000 K	10^{-8}
Metallic superconductors (typical)	1–10 K	50 000 – 150 000 K	$10^{-4\cdots-5}$
^{3}He	2.6 mK	5 K	$5 \cdot 10^{-4}$
MgB$_2$	39 K	6 000 K	10^{-2}
High-T_C superconductors	35–140 K	2000 – 5000 K	$1\ldots5 \cdot 10^{-2}$
Neutron stars	10^{10} K	10^{11} K	10^{-1}
Strongly interacting atomic Fermi gases	200 nK	1 μK	0.2

TABLE I. – *Transition temperatures, Fermi temperatures and their ratio T_C/T_F for a variety of fermionic superfluids or superconductors.*

1˙3.4. High-temperature superfluidity. The crossover condensates realized in the experiments on ultracold Fermi gases are a new type of fermionic superfluid. This superfluid differs from ^{3}He, conventional and even High-T_C superconductors in its high critical temperature T_C when compared to the Fermi temperature T_F. Indeed, while T_C/T_F is about $10^{-5}\ldots10^{-4}$ for conventional superconductors, $5\,10^{-4}$ for ^{3}He and 10^{-2} for High-T_C superconductors, the strong interactions induced by the Feshbach resonance allow atomic Fermi gases to enter the superfluid state already at $T_C/T_F \approx 0.2$, as summarized in table I. It is this large value which allows us to call this phenomenon *"high-temperature superfluidity"*. Scaled to the density of electrons in a metal, this form of superfluidity would already occur far above room temperature (actually, even above the melting temperature).

1˙4. Realizing model systems with ultracold atoms. – Systems of ultracold atoms are ideal model systems for a host of phenomena. Their diluteness implies the absence of complicated or not well understood interactions. It also implies that they can be controlled, manipulated and probed with the precision of atomic physics.

Fermions with strong, unitarity limited interactions are such a model system. One encounters strongly interacting fermions in a large variety of physical systems: inside a neutron star, in the quark-gluon plasma of the early Universe, in atomic nuclei, in strongly correlated electron systems. Some of the phenomena in such systems are captured by assuming point-like fermions with very strong short range interactions. The unitarity limit in the interaction strength is realized when the scattering length characterizing these interactions becomes longer than the interparticle spacing. For instance, in a neutron star, the neutron-neutron scattering length of about -18.8 fm is large compared to the few fm distance between neutrons at densities of $10^{38}\,\mathrm{cm}^{-3}$. Thus, there are analogies between results obtained in an ultracold gas at unitarity, at densities of $10^{12}\,\mathrm{cm}^{-3}$, and the physics inside a neutron star. Several communities are interested in the equation of state, in the value of the total energy and of the superfluid transition temperature of simple models of strongly interacting fermions [89].

Strongly interacting fermions can realize flow deep in the hydrodynamic regime, i.e. with vanishing viscosity. As discussed in chapter **6**, the viscosity can be so small that no

change in the flow behavior is observed when the superfluid phase transition is crossed. This kind of dissipationless hydrodynamic flow allows to establish connections with other areas. For instance, the anisotropic expansion of an elongated Fermi gas shares features with the elliptical (also called radial) flow of particles observed in heavy ion collisions, which create strongly interacting quark matter [90].

The very low viscosity observed in strongly interacting Fermi gases [73, 91, 74] has attracted interest from the high energy physics community. Using methods from string theory, it has been predicted that the ratio of the shear viscosity to the entropy density can not be smaller than $\frac{1}{4\pi}$ [92]. The two liquids that come closest to this lower bound are strongly interacting ultracold fermions and the quark gluon plasma [93].

Another idealization is the pairing of fermions with different chemical potentials. This problem emerged from superconductivity in external fields, but also from superfluidity of quarks, where the heavy mass of the strange quark leads to "stressed pairing" due to a shift of the strange quark Fermi energy [94, 95]. One of the authors (W.K.) still remembers vividly how an MIT particle physics colleague, Krishna Rajagopal, asked him about the possibility of realizing pairing between fermions with different Fermi energies (see [96]), even before condensation and superfluidity in balanced mixtures had become possible. At this point, any realization seemed far away. With some satisfaction, we have included in these Varenna notes our recently observed phase diagram for population imbalanced ultracold fermions [82].

This overlap with other areas illustrates a special role of cold atom experiments: They can perform "quantum simulations" of simple models, the results of which may then influence research in other areas. Of course, those simulations cannot replace experiments with real quarks, nuclei and condensed matter systems.

1˙5. *Overview over the chapters.* – With these notes we want to give a comprehensive introduction into experimental studies of ultracold fermions. The first focus of this review is on the description of the experimental techniques to prepare and manipulate fermionic gases (chapter **2**), and the methods to diagnose the system including image analysis (chapter **3**). For those techniques which are identical to the ones used for bosons we refer to our review paper on bosons in the 1998 Varenna proceedings. The second focus is on the comprehensive description of the physics of the BEC-BCS crossover (chapter **4**) and of Feshbach resonances (chapter **5**), and a summary of the experimental studies performed so far (chapters **6** and **7**). Concerning the presentation of the material we took a bimodal approach, sometimes presenting an in-depth discussion, when we felt that a similar description could not be found elsewhere, sometimes giving only a short summary with references to relevant literature. Of course, the selection of topics which are covered in more detail reflects also the contributions of the MIT group over the last six years. The theory chapter on the BCS-BEC crossover emphasizes physical concepts over formal rigor and is presented in a style that should be suitable for teaching an advanced graduate course in AMO physics. We resisted the temptation to include recent experimental work on optical lattices and a detailed discussion of population imbalanced Fermi mixtures, because these areas are still in rapid development, and the value of a

review chapter would be rather short lived.

These notes include a lot of new material not presented elsewhere. Chapter **3** on various regimes for trapped and expanding clouds summarizes many results that have not been presented together and can serve as a reference for how to fit density profiles of fermions in all relevant limits. Chapter **4** on BCS pairing emphasizes the density of states and the relation of Cooper pairs in three dimensions to a two-particle bound state in two dimensions. Many results of BCS theory are derived in a rigorous way without relying on complicated theoretical tools. In chapter **5**, many non-trivial aspects of Feshbach resonances are obtained from a simple model. Chapter **6** presents density profiles, not published elsewhere, of a resonantly interacting Fermi gas after expansion, showing a direct signature of condensation. In chapter **6**, we have included several unpublished figures related to the observation of vortices.

2. – Experimental techniques

The "window" in density and temperature for achieving fermionic degeneracy is similar to the BEC window. At densities below 10^{11} cm^{-3}, thermalization is extremely slow, and evaporative cooling can no longer compete with (technical) sources of heating and loss. At densities above 10^{15} cm^{-3}, three body losses usually become dominant. In this density window, degeneracy is achieved at temperatures between 100 nK and 50 μK.

The cooling and trapping techniques to reach such low temperatures are the same as those that have been developed for Bose-Einstein condensates. We refer to our Varenna paper on BEC [9] for a description of these techniques. Table II summarizes the different cooling stages used at MIT to reach fermionic superfluidity in dilute gases, starting with a hot atomic beam at 450 °C and ending with a superfluid cloud of 10 million fermion pairs at 50 nK.

Although no major new technique has been developed for fermionic atoms, the nature of fermionic gases emphasizes various aspects of the experimental methods:

- Different atomic species. The most popular atoms for BEC, Rb and Na, do not have any stable fermionic isotopes. The workhorses in the field of ultracold fermions are ^{40}K and ^{6}Li.

- Sympathetic cooling with a different species (Na, Rb, ^{7}Li). This requires techniques to load and laser cool two different kinds of atoms simultaneously, and raises the question of collisional stability.

- All optical cooling. When cooling ^{6}Li, the need for a different species can be avoided by all optical cooling using two different hyperfine states. This required further development of optical traps with large trap depth.

- Two-component fermionic systems. Pairing and superfluidity is observed in a two-component fermionic system equivalent to spin up and spin down. This raises issues of preparation using radiofrequency (RF) techniques, collisional stability, and detection of different species. All these challenges were already encountered in spinor BECs, but their solutions have now been further developed.

- Extensive use of Feshbach resonances. Feshbach resonances were first observed and used in BECs. For Fermi gases, resonantly enhanced interactions were crucial to achieve superfluidity. This triggered developments in rapid switching and sweeping of magnetic fields across Feshbach resonances, and in generating homogeneous fields for ballistic expansion at high magnetic fields.

- Lower temperatures. On the BCS side of the phase diagram, the critical temperature decreases exponentially with the interaction strength between the particles. This provides additional motivation to cool far below the degeneracy temperature.

In this chapter, we discuss most of these points in detail.

Stage	Temperature	Density	T/T_F
Two-species oven	720 K	$10^{14}\,\mathrm{cm}^{-3}$	10^8
Laser cooling (*Zeeman slower & MOT*)	1 mK	$10^{10}\,\mathrm{cm}^{-3}$	10^4
Sympathetic cooling (*Magnetic trap*)	1 μK	$10^{13}\,\mathrm{cm}^{-3}$	0.3
Evaporative cooling (*Optical trap*)	50 nK	$5\cdot10^{12}\,\mathrm{cm}^{-3}$	0.05

TABLE II. – *The various preparatory stages towards a superfluid Fermi gas in the MIT experiment. Through a combination of laser cooling, sympathetic cooling with sodium atoms, and evaporative cooling, the temperature is reduced by 10 orders of magnitude. The first steps involve a spin-polarized gas. In the last step, strong attractive interactions are induced in a two-state Fermi mixture via a Feshbach resonance. This brings the critical temperature for superfluidity up to about $0.3\,T_F$ - the ultracold Fermi gas becomes superfluid.*

2˙1. *The atoms.* – At very low temperatures, all elements turn into solids, with the exception of helium which remains a liquid even at zero temperature. For this reason, ^{3}He had been the only known neutral fermionic superfluid before the advent of laser cooling. Laser cooling and evaporative cooling prepare atomic clouds at very low densities, which are in a metastable gaseous phase for a time long enough to allow the formation of superfluids.

Neutral fermionic atoms have an odd number of neutrons. Since nuclei with an even number of neutrons are more stable, they are more abundant. With the exception of beryllium each element has at least one isotope, which as a neutral atom is a boson. However, there are still many choices for fermionic atoms throughout the periodic table. Because alkali atoms have a simple electronic structure and low lying excited states, they are ideal systems for laser cooling. Among the alkali metals, there are two stable fermionic isotopes, ^{6}Li and ^{40}K, and they have become the main workhorses in the field. Recently, degenerate Fermi gases have been produced in metastable ^{3}He* [97] and Ytterbium [98], and experiments are underway in Innsbruck to reach degeneracy in strontium.

2˙1.1. Hyperfine structure. Pairing in fermions involves two hyperfine states, and the choice of states determines the collisional stability of the gas, e.g. whether there is a possible pathway for inelastic decay to lower-lying hyperfine states. Therefore, we briefly introduce the hyperfine structure of ^{6}Li and ^{40}K.

The electronic ground state of atoms is split by the hyperfine interaction. The electrons create a magnetic field that interacts with the nuclear spin $\mathbf{I}$. As a result, the total electron angular momentum, sum of angular momentum and spin, $\mathbf{J} = \mathbf{L} + \mathbf{S}$, is coupled to the nuclear spin to form the total angular momentum of the entire atom, $\mathbf{F} = \mathbf{J} + \mathbf{I}$. Alkali atoms have a single valence electron, so $S = 1/2$, and in the electron's orbital ground state, $\mathbf{L} = 0$. Hence the ground state splits into two hyperfine manifolds with
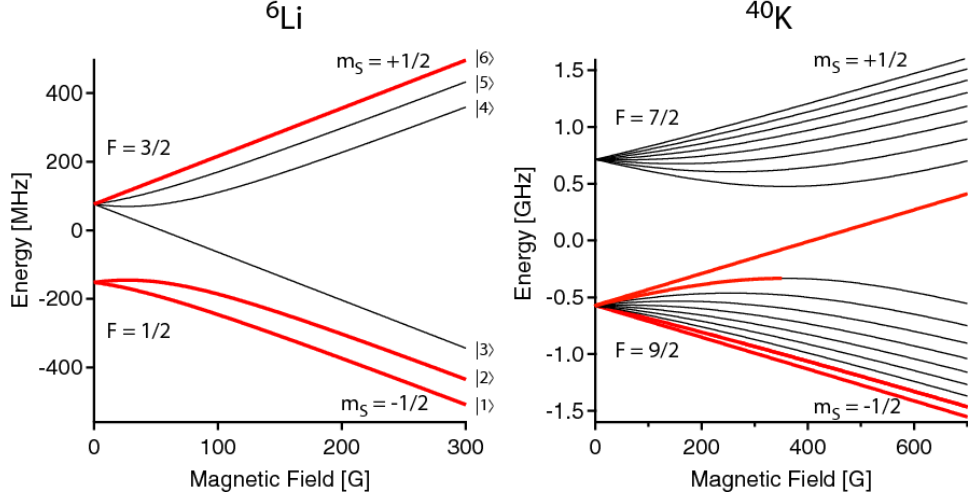
Fig. 2. – Hyperfine states of ^{6}Li and ^{40}K. Energies are relative to the atomic ground state without hyperfine interaction. ^{6}Li has nuclear spin $I = 1$, for ^{40}K it is $I = 4$. The ^{6}Li hyperfine splitting is $\Delta\nu_{\mathrm{hf}}^{^6\mathrm{Li}} = 228$ MHz, for ^{40}K it is $\Delta\nu_{\mathrm{hf}}^{^{40}\mathrm{K}} = -1.286$ GHz. The minus sign indicates that the hyperfine structure is reversed for ^{40}K, with $F = 9/2$ being lower in energy than $F = 7/2$. Thick lines mark hyperfine states used during cooling to degeneracy.

total angular momentum quantum numbers $F = I + 1/2$ and $F = I - 1/2$. In a magnetic field $\mathbf{B}$, these hyperfine states split again into a total of $(2S + 1)(2I + 1) = 4I + 2$ states. The hamiltonian describing the various hyperfine states is

$$(1) \qquad H_{\mathrm{hf}} = a_{\mathrm{hf}}\mathbf{I} \cdot \mathbf{S} + g_s\mu_B\mathbf{B} \cdot \mathbf{S} - g_i\mu_N\mathbf{B} \cdot \mathbf{I}$$

Here, a_{hf} is the hyperfine constant of the alkali atom, $g_s \approx 2$ and g_i are the electron and nuclear g-factors, $\mu_B \approx 1.4$ MHz/G is the Bohr magneton and μ_N the nuclear magneton.

The hyperfine states of ^{6}Li and ^{40}K are shown in Fig. 2. Good quantum numbers at low field are the total spin F and its z-projection, m_F. At high fields $B \gg a_{\mathrm{hf}}/\mu_B$, they are the electronic and nuclear spin projections m_S and m_I.

2˙1.2. *Collisional Properties.* The Pauli exclusion principle strongly suppresses collisions between two fermions in the same hyperfine state at low temperatures. Because of the antisymmetry of the total wave function for the two fermions, s-wave collisions are forbidden. Atoms in the same hyperfine state can collide only in odd partial waves with p-wave as the lowest angular momentum channel.

For p-wave collisions, with the relative angular momentum of $\hbar$, atomic mass m and a thermal velocity of v_T, the impact parameter of a collision is $\hbar/mv_T$, which is equal to the thermal de Broglie wavelength $\lambda_T = \sqrt{\frac{2\pi\hbar^2}{mk_BT}}$. When the range of the interaction

potential r_0 is smaller than λ_T, the atoms "fly by" each other without interaction. For a van-der-Waals potential, the range is $r_0 \approx (mC_6/\hbar^2)^{1/4}$. Below the temperature $k_B T_p = \hbar^2/mr_0^2$, p-wave scattering freezes out, and the Fermi gas becomes cohesionless, a truly ideal gas! For ^{6}Li, $T_p \approx 6\,\mathrm{mK}$, much larger than the temperature in the magneto-optical trap (MOT). For ^{40}K, $T_p = 300\,\mu\mathrm{K}$. Since these values for T_p are much higher than the window for quantum degeneracy, a second species or second hyperfine state is needed for thermalization and evaporative cooling. We now discuss some general rules for inelastic two-body collisions.

- Energy. Inelastic collisions require the internal energy of the final states to be lower than that of the initial states. Therefore, a gas (of bosons or fermions) in the lowest hyperfine state is always stable with respect to two-body collisions. Since the lowest hyperfine state is a strong magnetic field seeking state, optical traps, or generally traps using ac magnetic or electric fields are required for confinement.

- Angular momentum. The z-component M of the total angular momentum of the two colliding atoms (1 and 2) is conserved. Here, $M = M_{int} + M_{rot}$, where the internal angular momentum $M_{int} = m_{F,1} + m_{F,2}$ at low fields and $M_{int} = m_{I,1} + m_{I,2} + m_{S,1} + m_{S,2}$ at high fields, and M_{rot} is the z-component of the angular momentum of the atom's relative motion.

- Spin relaxation. Spin relaxation occurs when an inelastic collision is possible by exchanging angular momentum between electrons and nuclei, without affecting the motional angular momentum. Usually, the rate constant for this process is on the order of $10^{-11}\,\mathrm{cm^3 s^{-1}}$ which implies rapid decay on a ms scale for typical densities. As a general rule, mixtures of hyperfine states with allowed spin relaxation have to be avoided. An important exception is ^{87}Rb where spin relaxation is suppressed by about three orders of magnitude by quantum interference [46]). Spin relaxation is suppressed if there is no pair of states with lower internal energy with the same total M_{int}. Therefore, degenerate gases in a state with maximum M_{int} cannot undergo spin relaxation.

- Dipolar relaxation. In dipolar relaxation, angular momentum is transferred from the electrons and/or nuclei to the atoms' relative motion. Usually, the rate constant for this process is on the order of $10^{-15}\,\mathrm{cm^3 s^{-1}}$ and is sufficiently slow (seconds) to allow the study of systems undergoing dipolar relaxation. For instance, all magnetically trapped Bose-Einstein condensates can decay by dipolar relaxation, when the spin flips to a lower lying state.

- Feshbach resonances. Near Feshbach resonances, all inelastic processes are usually strongly enhanced. A Feshbach resonance enhances the wave function of the two colliding atoms at short distances, where inelastic processes occur (see **5**). In addition, the coupling to the Feshbach molecule may induce losses that are entirely due to the closed channel. It is possible that the two enhanced amplitudes for the same loss process interfere destructively.

- (Anti-)Symmetry. At low temperature, we usually have to consider only atoms colliding in the s-wave incoming channel. Colliding fermions then have to be in two different hyperfine states, to form an antisymmetric total wave function. Spin relaxation is not changing the relative motion. Therefore, for fermions, spin relaxation into a pair of identical states is not possible, as this would lead to a symmetric wave function. Two identical final states are also forbidden for ultracold fermions undergoing dipolar relaxation, since dipolar relaxation obeys the selection rule $\Delta L = 0, 2$ for the motional angular momentum and can therefore only connect even to even and odd to odd partial waves.

We can now apply these rules to the hyperfine states of alkalis. For magnetic trapping, we search for a stable pair of magnetically trappable states (weak field seekers, i.e. states with a positive slope in Fig. 2). For atoms with $J = 1/2$ and nuclear spin $I = 1/2$, 1 or $3/2$ that have a normal hyperfine structure (i.e. the upper manifold has the larger F), there is only one such state available in the lower hyperfine manifold. The partner state thus has to be in the upper manifold. However, a two-state mixture is not stable against spin relaxation when it involves a state in the upper hyperfine manifold, and there is a state leading to the same M_{int} in the lower manifold. Therefore, ^{6}Li (see Fig. 2) and also ^{23}Na and ^{87}Rb do not have a stable pair of magnetically trappable states. However, ^{40}K has an inverted hyperfine structure and also a nuclear spin of 4. It thus offers several combinations of weak-field seeking states that are stable against spin relaxation. Therefore, ^{40}K has the unique property that evaporative cooling of a two-state mixture is possible in a magnetic trap, which historically was the fastest route to achieve fermionic quantum degeneracy [49].

An optical trap can confine both weak and strong field seekers. Mixtures of the two lowest states are always stable against spin relaxation, and in the case of fermions, also against dipolar relaxation since the only allowed output channel has both atoms in the same state. Very recently, the MIT group has realized superfluidity in ^{6}Li using mixtures of the first and third or the second and third state [99]. For the combination of the first and third state, spin relaxation into the second state is Pauli suppressed. These two combinations can decay only by dipolar relaxation, and surprisingly, even near Feshbach resonances, the relaxation rate remained small. This might be caused by the small hyperfine energy, the small mass and the small van der Waals coefficient C_6 of ^{6}Li, which lead to a small release energy and a large centrifugal barrier in the d-wave exit channel.

For Bose-Einstein condensates at typical densities of 10^{14} cm^{-3} or larger, the dominant decay is three-body recombination. Fortunately, this process is Pauli suppressed for any two-component mixture of fermions, since the probability to encounter three fermions in a small volume, of the size of the molecular state formed by recombination, is very small. In contrast, three-body relaxation is not suppressed if the molecular state has a size comparable to the Fermi wavelength. This has been used to produce molecular clouds (see section **2**˙4.2).

After those general considerations, we turn back to the experimentally most relevant hyperfine states, which are marked with thick (red) lines in Fig. 2. In the MIT

experiment, sympathetic cooling of lithium with sodium atoms in the magnetic trap is performed in the upper, stretched state $|6\rangle \equiv |F = 3/2, m_F = 3/2\rangle$. In the final stage of the experiment, the gas is transferred into an optical trap and prepared in the two lowest hyperfine states of ^{6}Li, labelled $|1\rangle$ and $|2\rangle$, to form a strongly interacting Fermi mixture around the Feshbach resonance at 834 G. The same two states have been used in all ^{6}Li experiments except for the very recent MIT experiments on mixtures between atoms in $|1\rangle$ and $|3\rangle$, as well as in $|2\rangle$ and $|3\rangle$ states. In experiments on ^{40}K at JILA, mutual sympathetic cooling of the $|F = 9/2, m_F = 9/2\rangle$ and $|F = 9/2, m_F = 7/2\rangle$ states is performed in the magnetic trap. The strongly interacting Fermi mixture is formed using the lowest two hyperfine states $|F = 9/2, m_F = -9/2\rangle$ and $|F = 9/2, m_F = -7/2\rangle$ close to a Feshbach resonance at 202 G.

As we discussed above, evaporative cooling requires collisions with an atom in a different hyperfine state or with a different species. For the latter approach, favorable properties for interspecies collisions are required. Here we briefly summarize the approaches realized thus far.

The stability of mixtures of two hyperfine states has been discussed above. Evaporation in such a system was done for ^{40}K in a magnetic trap [49] using RF-induced, simultaneous evaporation of both spin states. In the case of ^{6}Li, laser cooled atoms were directly loaded into optical traps at Duke [53] and Innsbruck [17] in which a mixture of the lowest two hyperfine states was evaporatively cooled by lowering the laser intensity. Other experiments used two species. At the ENS [52] and at Rice [51], spin-polarized ^{6}Li is sympathetically cooled with the bosonic isotope of lithium, ^{7}Li, in a magnetic trap. At MIT, a different element is used as a coolant, ^{23}Na. This approach is more complex, requiring a special double-species oven and two laser systems operating in two different spectral regions (yellow and red). However, the ^{6}Li-^{23}Na interspecies collisional properties have turned out to be so favorable that this experiment has led to the largest degenerate Fermi mixtures to date with up to 50 million degenerate fermions [100]. Forced evaporation is selectively done on ^{23}Na alone, by using a hyperfine state changing transition around the ^{23}Na hyperfine splitting of 1.77 GHz. The number of ^{6}Li atoms is practically constant during sympathetic cooling with sodium. Other experiments on sympathetic cooling employ ^{87}Rb as a coolant for ^{40}K [101, 102, 103, 87] or for ^{6}Li [104, 105].

Another crucial aspect of collisions is the possibility to enhance elastic interactions via Feshbach resonances. Fortunately, for all atomic gases studied so far, Feshbach resonances of a reasonable width have been found at magnetic fields around or below one kilogauss, rather straightforward to produce in experiments. Since Feshbach resonances are of central importance for fermionic superfluidity, we discuss them in a separate chapter (**5**).

2˙2. *Cooling and trapping techniques*. – The techniques of laser cooling and magnetic trapping are identical to those used for bosonic atoms. We refer to the comprehensive discussion and references in our earlier Varenna notes [9] and comment only on recent advances.

One development are experiments with two atomic species in order to perform sym-

pathetic cooling in a magnetic trap. An important technical innovation are two-species ovens which create atomic beams of two different species. The flux of each species can be separately controlled using a two-chamber oven design [106]. When magneto-optical traps (MOTs) are operated simultaneously with two species, some attention has to be given to light-induced interspecies collisions leading to trap loss. Usually, the number of trapped atoms for each species after full loading is smaller than if the MOT is operated with only one species. These losses can be mitigated by using sequential loading processes, quickly loading the second species, or by deliberately applying an intensity imbalance between counter-propagating beams in order to displace the two trapped clouds [100].

Another development is the so-called all-optical cooling, where laser cooled atoms are directly transferred into an optical trap for further evaporative cooling. This is done by ramping down the laser intensity in one or several of the beams forming the optical trap. All-optical cooling was introduced for bosonic atoms (rubidium [107], cesium [108], sodium [109], ytterbium [110]) and is especially popular for fermionic lithium, where evaporative cooling in a magnetic trap is possible only by sympathetic cooling with a second species.

In the following two sections, we address in more detail issues of sympathetic cooling and new variants of optical traps, both of relevance for cooling and confining fermions.

2.2.1. Sympathetic cooling. *Overlap between the two clouds.* One limit to sympathetic cooling is the loss of overlap of the coolant with the cloud of fermions. Due to different masses, the sag due to gravity is different for the two species. This is most severe in experiments that employ ^{87}Rb to cool ^{6}Li [104, 105]. For harmonic traps, the sag is given by $\Delta x_{1,2} = g/\omega_{1,2}^2$ for species 1 and 2, with g the earth's gravitational acceleration, and ω the trapping frequency along the vertical direction. The spring constant $k = m\omega^2 \approx \mu_B B''$ is essentially the same for all alkali atoms, when spin-polarized in their stretched state and confined in magnetic traps with magnetic field curvature B''. It is of the same order for alkalis confined in optical traps, $k = \alpha I''$, where the polarizability α is similar for the alkalis and lasers far detuned from atomic resonances, and I'' is the curvature of the electric field's intensity. The thermal cloud size, given by $\sqrt{k_B T/k}$, is thus species-independent, while the sag $\Delta x_{1,2} \approx g m_{1,2}/k$ is proportional to the mass. The coolant separates from the cloud of fermions once $g(m_2 - m_1)/k \approx \sqrt{k_B T/k}$, or $k_B T \approx g^2(m_2 - m_1)^2/k$. For trapping frequencies of 100 Hz for ^{6}Li, and for ^{87}Rb as the coolant, this would make sympathetic cooling inefficient at temperatures below 30 μK, more than an order of magnitude higher than the Fermi temperature for 10 million fermions. For ^{23}Na as the coolant, the degenerate regime is within reach for this confinement. Using the bosonic isotope ^{7}Li as the coolant, gravitational sag evidently does not play a role. To avoid the problem of sag, one should provide strong confinement along the axis of gravity. A tight overall confinement is not desirable since it would enhance trap loss due to three-body collisions.

Role of Fermi statistics. When fermions become degenerate, the collision rate slows down. The reason is that scattering into a low-lying momentum state requires this state to be empty, which has a probability $1 - f$, with f the Fermi-Dirac occupation number.

22

As the occupation of states below the Fermi energy gets close to unity at temperatures $T \ll T_F$, the collision rate is reduced. Initially, this effect was assumed to severely limit cooling well below the Fermi temperature [49]. However, it was soon realized that although the onset of Fermi degeneracy changes the kinetics of evaporative cooling, it does not impede cooling well below the Fermi temperature [111, 112]. The lowest temperature in evaporative cooling is always determined by heating and losses. For degenerate Fermi systems, particle losses (e.g. by background gas collisions) are more detrimental than for Bose gases, since they can create hole excitations deep in the Fermi sea [113, 114, 115].

Role of Bose statistics. If the coolant is a boson, the onset of Bose-Einstein condensation changes the kinetics of evaporation. It has been proposed that sympathetic cooling becomes highly inefficient when the specific heat of the coolant becomes equal or smaller than that of the Fermi system [51, 116]. However, although an almost pure Bose-Einstein condensate has almost zero specific heat, its capacity to remove energy by evaporating out of a trap with a given depth is even larger than that of a Boltzmann gas, since the initial energy of the Bose gas is lower. On the other hand, the rate of evaporation is lower for the Bose condensed gas, since the number of thermal particles is greatly reduced. In the presence of heating, a minimum rate of evaporation is required [116]. This might call for additional flexibility to independently control the confinement for bosons and fermions, which is possible via the use of a two-color trap [117]. In particular, on can then expand the bosonic coolant and suppress the onset of Bose-Einstein condensation.

Other work discussed phenomena related to the interacting condensate. When the Fermi velocity becomes smaller than the critical velocity of a superfluid Bose-Einstein condensate, then the collisional transfer of energy between the fermions and bosons becomes inefficient [118]. Another phenomenon for sufficiently high boson density is mean-field attraction or repulsion of the fermions, depending on the relative sign of the intraspecies scattering length [119]. Attractive interactions can even lead to a collapse of the condensate as too many fermions rush into the Bose cloud and cause three-body collisions, leading to losses and heating [120, 121].

Given all these considerations, it is remarkable that the simplest scheme of evaporating bosons in a magnetic trap in the presence of fermions has worked very well. In the MIT experiment, we are currently limited by the number of bosons used to cool the Fermi gas. Without payload (the fermions), we can create a sodium Bose-Einstein condensate of 10 million atoms. When the fermions outnumber the bosons, the cooling becomes less efficient, and we observe a trade-off between final number of fermions and their temperature. We can achieve a deeply degenerate Fermi gas of $T/T_F = 0.05$ with up to 30 million fermions [100], or aim for even larger atom numbers at the cost of degeneracy. On a day-to-day basis, we achieve 50 million fermions at $T/T_F = 0.3$. This degenerate, spin-polarized Fermi gas can subsequently be loaded into an optical trap for further evaporative cooling as a two-component Fermi mixture.

The preparation of a two-component mixture by an RF pulse and decoherence (see section **2**˙3.5) lowers the maximum occupation number to $1/2$ and increases the effective T/T_F to about 0.6. Therefore, there is no benefit of cooling the spin polarized Fermi cloud to higher degeneracy.

2˙2.2. Optical trapping. Optical traps provide the confinement for almost all experiments on ultracold fermions. The reason is that most of the current interest is on interacting two-component systems. Optical traps confine both strong- and weak-field seeking states. Trapping atoms in the lowest lying hyperfine states (which are always strong-field seeking) suppresses or avoids inelastic collisions, as discussed in section **2**˙1.2.

Most importantly, using electric fields for trapping frees the magnetic field to be tuned to Feshbach resonances and thereby to enhance elastic interactions. There is only one experiment on ultracold atoms that studied Feshbach resonances in a magnetic trap (in ^{85}Rb [11]), all others have been performed in optical traps.

The important case of ^{6}Li has led to advances in optical traps with large volume and trap depth. All-optical cooling to BEC has been convenient in some experiments with rubidium and sodium Bose-Einstein condensates eliminating the need for magnetic traps [107, 109]. However, standard magnetic traps are not considerably increasing the complexity of the experiment. One could take the position that a magnetic trap is easier to operate and to maintain than a high power laser or an enhancement cavity. However, bypassing the magnetic trap for ^{6}Li also bypasses the need for another species (^{7}Li, Rb, Na) and therefore an additional laser system(^{3}).

In the following section, we discuss some optical trapping geometries used in ultracold Fermi experiments. For a more detailed discussion on optical trapping, we refer the reader to [9] and [122].

So far, all optical traps for fermions have used red detuned laser beams where the atoms are confined in the intensity maximum of the laser beam(s). The trapping potential is given by the AC Stark shift

$$(2) \qquad U(\mathbf{r}) = -\frac{\hbar\omega_R^2(\mathbf{r})}{4}\left(\frac{1}{\omega_0 - \omega_L} + \frac{1}{\omega_0 + \omega_L}\right) \simeq \frac{\hbar\omega_R^2(\mathbf{r})}{4\Delta}$$

where ω_0 is the atomic resonance frequency, ω_L is the frequency of the laser light, and $\Delta = \omega_L - \omega_0$ the laser's detuning from resonance. The approximation on the right hand side holds for $|\Delta| \ll \omega_0$. ω_R is the position-dependent Rabi frequency describing the strength of the atom-field coupling. In terms of the intensity $I(\mathbf{r})$ of the laser light and atomic parameters, it is defined by $2\omega_R^2(\mathbf{r})/\Gamma^2 = I(\mathbf{r})/I_{\text{SAT}}$, where Γ is the natural decay rate of the atom's excited state, and $I_{\text{SAT}} = \hbar\omega_0^3\Gamma/12\pi c^2$ is the saturation intensity. For ^{6}Li, $\Gamma = 2\pi \cdot 6\,\text{MHz}$ and $I_{\text{SAT}} = 3\,\text{mW/cm}^2$, for ^{40}K, $\Gamma = 2\pi \cdot 6\,\text{MHz}$ and $I_{\text{SAT}} = 2\,\text{mW/cm}^2$.

(^{3}) In other cases magnetic trapping has not been an option due to inelastic collisions [108] or vanishing magnetic moment [110].

Single-beam optical trap. The simplest trap consists of a single, red-detuned, focused gaussian laser beam, with intensity profile

$$(3) \qquad I(\rho, z) = \frac{2P}{\pi \text{w}^2 \left(1 + z^2/z_R^2\right)} \exp\left(-\frac{2\,\rho^2}{\text{w}^2 \left(1 + z^2/z_R^2\right)}\right).$$

The beam parameters are the laser power P, the $1/e^2$ beam waist radius w, and the Rayleigh range z_R. ρ and z are the distances from the beam focus along the radial and axial directions, respectively. The Rayleigh range is related to the beam waist and the wavelength of the laser via $z_R = \pi \text{w}^2/\lambda$. The bottom of the potential well formed by the laser beam can be approximated as a harmonic oscillator with trapping frequencies $\omega_\rho/2\pi = \sqrt{2P/\pi^3 m \text{w}^4}$ and $\omega_z/2\pi = \sqrt{P/\pi^3 m \text{w}^2 z_R^2}$. For ^{6}Li, a laser beam operating at a wavelength $\lambda = 1064$ nm with 100 mW of power, focused down to a waist of w $= 25\,\mu$m, provides a trap depth $U \simeq 6\,\mu$K, a radial frequency $\omega_\rho/2\pi = 1.2$ kHz and an aspect ratio $\omega_\rho/\omega_z = \sqrt{2}\pi \text{w}/\lambda \simeq 100$. This is sufficient for loading atoms that were evaporatively or sympathetically pre-cooled in a magnetic trap.

Loading atoms directly from a millimeter-sized MOT, at temperatures of several $100\,\mu$K, into a single beam optical trap requires larger trap depths, a larger waist and ideally a smaller aspect ratio to enhance the overlap with the rather spherical MOT region. One solution is the use of Quasi-Electrostatic Traps (QUEST) [123] formed by a focused CO_2 laser at $\lambda = 10.6\,\mu$m. Due to the large detuning from atomic resonance the trap operates in the quasi-electrostatic regime where $\omega_L/\omega_0 \to 0$ and the dipole potential $U = \frac{\hbar \Gamma^2}{4\omega_0} \frac{I}{I_{\text{SAT}}}$ no longer depends on the frequency of the laser light. The longer wavelength allows for a larger waist at still moderate aspect ratios. In the group at Duke University [53], 65 W of power was focused to a waist of 47 μm (Rayleigh range 660 μm), providing a trap depth for ^{6}Li atoms of 690 μK. The resulting radial and axial frequencies were 6.6 kHz and 340 Hz, respectively. This deep trap allowed to capture 1.5×10^6 atoms from the MOT at Doppler-limited temperatures of $150\,\mu$K. The tight confinement ensured good starting conditions for evaporative cooling.

Hybrid trap. A large beam waist is preferable for several purposes, e.g. for creating a large trap volume or for controlling any aberrations which would cause a deviation from cylindrical symmetry — this was crucial for the creation of vortices [68]. To avoid the large aspect ratio of the optical trap, a confining magnetic curvature can be added along the axial direction by using two coils with a separation larger (smaller) than the Helmholtz configuration (distance equals radius) for low field (high field) seekers. Maxwell's equations then require an anti-confining curvature along the radial direction, which, however, is negligible compared to the tight optical confinement. As a result, this hybrid trap features optical radial confinement and axial magnetic confinement. In addition, high bias fields are needed to tune across the Feshbach resonance. Such a setup has been used in many experiments in Innsbruck, at Rice, and at MIT. Details of the MIT magnetic field configuration are discussed in section **2**·4.1. In our experiments, the axial confinement is almost purely magnetic ($\omega_z/2\pi \simeq 23$ Hz). The optical trap provides radial confinement
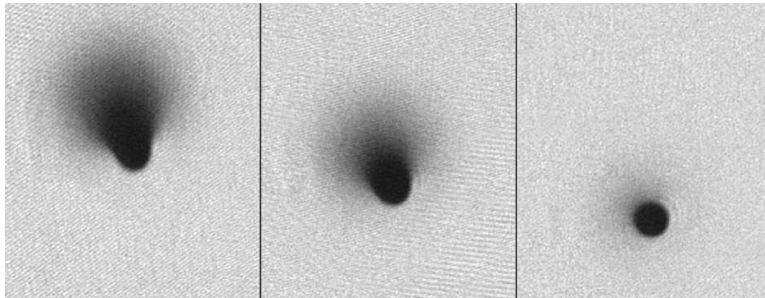
Fig. 3. – Alignment of the optical trap to achieve a radially symmetric potential. In the left image, the trap is still far from the "sweet spot". In the right image, stray gradients are almost completely cancelled. The absorption images are of a lithium pair condensate after 10 ms of expansion. The field of view for each image is 1.1×1.3 mm.

with $\omega_r/2\pi$ in the range of 50 to 300 Hz, which varies the aspect ratio of the cloud between about 2 and 12.

We will now discuss two other important aspects of optical traps. One is the compensation of gravity that is crucial for creating traps with cylindrical symmetry, the other one is the issue of the trap depth that controls evaporative cooling.

In the MIT experiment [68], the hybrid trap has a typical aspect ratio of $\omega_r/\omega_z = 6$. The optical trapping beam and the magnetic field coils are horizontally aligned. Compensation for gravity is ensured by "sitting on one side of the saddle".

Along the vertical (x-)axis, the combined potential of gravity+magnetic fields is $-\frac{1}{4}m\omega_z^2 x^2 - mgx$, where we used $i\omega_z/\sqrt{2}$ as the anti-confining curvature. Thus, gravity shifts the saddle potential by an amount $2g/\omega_z^2 \approx 1$ mm. The "sweet spot" in the radial plane to which the optical trap needs to be aligned is thus not the center of the magnetic field coils, but about 1 mm above it. In this position no gradients act on the atoms. If the optical trap is round in the radial plane, the combined potential experienced by the atoms is round as well. Round traps are crucial for the observation of vortices, and also for the study of collective excitations with radial symmetry.

The alignment procedure of the optical trap is shown in Fig. 3. At the end of evaporation of the lithium condensate, the trap depth is reduced in about 30 ms to a very shallow depth which is not sufficient to hold the atoms if they are not in the "sweet spot". After 10 ms of expansion from the optical trap one clearly observes in which direction the atoms spill out, and one can counteract by moving the optical trap.

A low intensity tightly focused beam and a larger intensity beam with a softer focus provide the same radial confinement. However, the trap depth is very different. This is important if the cloud needs to be cooled by evaporation, e.g. during the nucleation of a vortex lattice after stirring up the cloud. Cooling of the cloud will be efficient if the trap depth U is not much higher than the Fermi energy E_F. This condition sets a stringent constraint for the beam waist.

We illustrate this by discussing the situation in the MIT vortex experiment, where we wanted to have a rather small aspect ratio $a = \omega_r/\omega_z$. The axial trapping frequency ω_z was fixed by the magnetic field curvature. The relation between U and the waist w is

$$(4) \qquad U = \frac{1}{4}m\omega_r^2 \text{w}^2 = \frac{1}{4}m\omega_z^2 a^2 \text{w}^2$$

The Fermi energy per spin state for a total number of atoms N is given by (using the harmonic approximation for the radially gaussian potential):

$$(5) \qquad E_F = \hbar(\omega_r^2 \omega_z)^{1/3}(3N)^{1/3} = \hbar\omega_z a^{2/3}(3N)^{1/3}$$

Requiring $U \gtrsim E_F$ results in

$$(6) \qquad \text{w} \gtrsim 2\sqrt{\frac{\hbar}{m\omega_z}}a^{-2/3}(3N)^{1/6}$$

If we want to trap $N = 1 \times 10^7$ atoms with an aspect ratio $a = 5$ and an axial trapping frequency $\omega_z/2\pi = 20\,\text{Hz}$ (typical values), we need the waist to be larger than 100 μm. Note that this requirement is quite stringent. Changing ω_z is limited: Increasing the current in the curvature coils by a factor of two (which increases power dissipation in the curvature coils by four) only reduces the required waist by 20%. Allowing for an aspect ratio of 10 would give another reduction by only 35%. A longer aspect ratio would have had adverse effects for the alignment of the stirring beam and the observation of vortex cores after expansion.

For our choice of w $= 120\,\mu$m, the Rayleigh range is $z_0 = \pi\text{w}^2/\lambda > 4\,\text{cm}$ while a typical axial cloud size is 1 mm. The maximum power in the laser beam is 4 W, which limits the trap depth to about 10 μK. This is still deep enough to load about 3×10^7 degenerate fermions from the magnetic trap after the sympathetic cooling stage with sodium (The Fermi temperature in the combined magnetic and optical trap during this loading is 5 μK, and the degenerate cloud at $T/T_F \approx 0.3$ is not much larger than a zero-temperature Fermi sea). These numbers illustrate that optical traps for fermions need much more power than for a Bose-Einstein condensate because of the combined need for a deeper and larger trap.

Crossed dipole trap. Another option for loading atoms from a MOT into an optical potential is the use of crossed laser beams. This geometry provides a roughly spherical trapping volume, and offers a good trade-off between trap depth and volume. This configuration allowed the first demonstration of Bose-Einstein condensation of atoms by all-optical means [107]. Fermionic atoms were loaded into a crossed dipole trap by the Paris group [124] after pre-cooling in a magnetic trap. When magnetic fields are applied, e.g. for tuning near a Feshbach resonance, the tight optical confinement in all three dimensions makes the trap more robust against potential magnetic field gradients which could drag atoms out of the trap. Crossed dipole traps have also been used to prepare

fermionic clouds for loading into optical lattices [83, 87].

Resonator-enhanced standing wave trap. The Innsbruck group enhanced the laser intensity and thus the trap depth by forming a standing-wave optical resonator [125]. The power of a 2 W Nd:YAG laser at $\lambda = 1064$ nm was resonantly enhanced by a factor of ~ 120, resulting in a trap depth of ~ 1 mK in the focus with $115\,\mu$m waist. This was deep enough to capture atoms directly from the MOT. The standing wave presented a 1D lattice potential to the atoms, that were thus tightly confined in several pockets along the direction of the standing wave. The high density in each pocket provided good starting conditions for evaporative cooling. After some initial cooling, the atoms were transferred into a single-beam optical trap [55].

2˙3. *RF spectroscopy.* – A single-component ultracold Fermi gas, with all atoms occupying the same spin states, is an almost perfect realization of an ideal non-interacting gas. s-wave collisions are forbidden due to the Pauli principle, and p-wave collisions are frozen out. In the absence of p-wave or higher partial wave scattering resonances, no phase transition occurs down to exponentially small temperatures (^{4}).

Physics becomes interesting only in the presence of interactions, and the obvious way to introduce interactions into a Fermi gas is by forming a two-component system, such as a mixture of the two lowest hyperfine states of ^{6}Li. s-wave scattering is then allowed between fermions of opposite spin. More accurately speaking, as the spin-part of the two-particle wave function can now be antisymmetric, symmetric s-wave scattering is now allowed. Such a two-state mixture can be created via optical pumping after the MOT phase, or via RF spectroscopy, starting from a pure single-component gas. Since RF spectroscopy is an invaluable tool to prepare, manipulate and probe ultracold gases, we review it here in more detail. First, we summarize basic aspects of RF spectroscopy, and then focus on clock shifts and mean field energies.

2˙3.1. Basics. Let us note some important properties of RF spectroscopy: a) The RF field has a very long wavelength (≈ 3m), so there is negligible momentum transfer. The coupling takes place only between internal states of each individual atom. b) The RF field (typically from a $\sim$ cm-large antenna) is essentially constant over the size of the sample ($\sim 100\,\mu$m). Thus, the entire cloud is simultaneously addressed by the same coupling. c) The RF pulse generally creates a superposition of the two coupled states. Such coherences can be long-lived in the absence of decay mechanisms.

In many cases, one can approximate a system of two coupled states $|1\rangle$ and $|2\rangle$ with energies E_1 and E_2 as an isolated two level system driven by a field $V = V(t)\left(|2\rangle\langle 1| + e^{i\phi}|1\rangle\langle 2|\right)$ oscillating close to the resonant frequency $\omega_0 = (E_2 - E_1)/\hbar$. Such a two-level system is conveniently described as a pseudo spin-1/2, for which $|\uparrow\rangle \equiv |1\rangle$ and $|\downarrow\rangle \equiv |2\rangle$. Keeping only the part of the interaction that resonantly drives the transition ("rotating wave

---

(^{4}) For attractive p-wave interactions with scattering length a, the critical temperature is $T_C \sim (E_F/k_B)\exp[-\pi/2(k_F|a|)^3]$ [21].

approximation"), the Hamiltonian is written as

(7) $\qquad H = H_0 + V; \quad H_0 \equiv -\frac{\hbar\omega_0}{2}\sigma_z; \quad V \equiv -\frac{\hbar\omega_R}{2}\left(\sigma_x \cos\omega t + \sigma_y \sin\omega t\right)$

where σ_i are the Pauli spin matrices and ω_R is the Rabi frequency, giving the strength of the coupling. ω_R depends on the drive field (in our experiments a magnetic field generated by an antenna) and the coupling matrix element between the two hyperfine states. A typical value for $\omega_R/2\pi$ is several kHz. The free Hamiltonian H_0 has its natural interpretation as a constant magnetic field in the z-direction of pseudospin-space. In the same way, the interaction V represents a (real or fictitious) rotating magnetic field in the transverse (x-y) plane. Transforming into the frame rotating at frequency ω, the direction of the transverse field is constant, while the z-field (and thus the energy splitting between the two states in the rotating frame) is reduced to $-\hbar\delta = \hbar(\omega_0 - \omega)$. For a resonant drive with $\delta = 0$, only the constant transverse field is left, and - borrowing from the classical picture - the spin (or pseudospin) precesses around it at frequency ω_R. A complete inversion of the spin-direction - and thus a complete transfer from state $|1\rangle$ into state $|2\rangle$ - is achieved for a RF pulse length $t = \pi/\omega_R$ (so-called π-pulse). An equal superposition $\frac{1}{\sqrt{2}}\left(|1\rangle + |2\rangle\right)$ is achieved for $t = \pi/2\omega_R$ ($\pi/2$-pulse).

2˙3.2. Adiabatic rapid passage. For general detuning δ, the (fictitious) magnetic field in the rotating frame is $\mathbf{B}_{\rm rot} = \frac{\hbar\delta}{2}\hat{\mathbf{z}} - \frac{\hbar\omega_R}{2}\hat{\mathbf{x}}$. At large positive detuning $\delta \gg \omega_R$, it is predominantly pointing in the $+z$-direction, and the pseudospin precesses around it. If the initial state is either state $|1\rangle$ or state $|2\rangle$, then the pseudospin is pointing up or down, and the angle between it and the fictitious magnetic field is small. If the detuning is now *slowly* swept from $\delta \gg \omega_R$ through resonance ($\delta = 0$) and towards large and negative values, the pseudospin will adiabatically follow the direction of the changing magnetic field and thus end up, for $\delta \ll -\omega_R$, aligned opposite to its original direction. One has thus adiabatically transferred the atom from state $|1\rangle$ to state $|2\rangle$ (or vice versa). The condition of adiabaticity requires that the pseudospin's precession frequency is always fast compared to the change of the magnetic field's direction, given by the azimuthal angle $\theta = \arctan\frac{\delta}{\omega_R}$. This condition is most stringent on resonance, where it reads $\omega_R \gg \dot{\theta} = \frac{\dot{\delta}}{\omega_R}$ or $\dot{\delta} \ll \omega_R^2$. For a non-adiabatic transfer, the probability for a successful transfer is given by the formula due to Landau and Zener:

(8) $$P_{|1\rangle \to |2\rangle} = 1 - \exp\left(-2\pi\frac{\omega_R^2}{\dot{\delta}}\right)$$

It is important to realize that both a short RF-pulse as well as a non-adiabatic Landau-Zener transfer will leave the atom in a superposition state $\cos\alpha\,|1\rangle + \sin\alpha\,e^{i\phi}\,|2\rangle$. If these processes are applied to a Fermi gas initially polarized in a single spin state $|1\rangle$, it will still be a fully polarized Fermi gas after the RF-pulse, with the only difference that now all the atoms are in one and the same superposition state of $|1\rangle$ and $|2\rangle$.

It is only by decoherence discussed below (section **2˙3.5**) that the superposition state

transforms into an incoherent mixture of atoms in states $|1\rangle$ and $|2\rangle$.

2˙3.3. Clock shifts. Clock shifts are density dependent shifts of transition frequencies due to interactions between the atoms. The name derives from their presence in atomic clocks. Indeed, they are one of the dominant sources of systematic error in current cold atom fountain clocks [126]. The absence of clock shifts in two-state Fermi mixtures facilitates the use of RF transitions to create spin mixtures and allows to accurately calibrate magnetic fields. The emergence of clock shifts in three component Fermi systems provides an important tool to probe the many-body physics underlying such shifts.

Absence of clock shifts in a fully polarized Fermi gas. It is tempting - but incorrect - to calculate clock shifts by considering the energy shift due to interactions of the two atomic states involved and then associating the resulting energy difference with a shifted transition frequency. Let us take for example a Fermi gas fully polarized in state $|1\rangle$, and let a_{12} be the scattering length for collisions between $|1\rangle$ and $|2\rangle$. An atom in state $|2\rangle$ would experience a mean-field energy shift $\delta E_2 = \frac{4\pi\hbar^2}{m}a_{12}n_1$ due to interactions with the cloud of $|1\rangle$-atoms at density n_1. As an RF pulse transfers $|1\rangle$ atoms into state $|2\rangle$, one might incorrectly conclude that the RF resonance is shifted by an amount δE_2. However, the RF pulse does not incoherently transfer some atoms into state $|2\rangle$, where they would experience the shift δE_2. Such a process would increase entropy, while RF radiation is a unitary transformation which conserves entropy. Rather, the RF pulse transfers all atoms simultaneously into a new superposition state $|\alpha\rangle \equiv \cos\alpha\,|1\rangle + \sin\alpha\,e^{i\phi}\,|2\rangle$. The fermions are still fully spin-polarized, they all occupy the same (rotated) quantum state. Therefore, each pair of fermions has to be in an antisymmetric motional state which excludes s-wave collisions. As a consequence, there is no interaction energy in the final state and the clock shift is zero. *Clock shifts are absent in an ultracold spin-polarized Fermi gas.* This was directly demonstrated in the MIT experiment [127].

A similar argument shows that in the case of thermal bosons (with intrastate scattering lengths $a_{11} = a_{22} = 0$), there *is* a clock shift, but it is twice the energy shift δE_2 for an infinitesimal RF transfer [128]. The factor of two results from correlations in a spin-polarized thermal Bose gas, which are preserved during the RF pulse: In a coherent collision, two indistinguishable thermal bosons either preserve their momenta or exchange them. If, in contrast, RF spectroscopy is performed on a pure Bose-Einstein condensate, the colliding bosons have the same momenta, hence exchange collisions are absent and the mean-field shift is indeed δE_2 [129, 130].

Absence of clock shifts in a two-state mixture of fermions. Switching back to fermions, one may ask whether there is a clock shift if the initial state is *not* spin-polarized, but a decohered mixture of populations in state $|1\rangle$ and $|2\rangle$. Interactions are now clearly present, the energy levels of atoms in states $|1\rangle$ and $|2\rangle$ are now truly shifted by $\delta E_1 = \frac{4\pi\hbar^2}{m}a_{12}n_2$ and δE_2, and one might (incorrectly) expect a clock shift $\delta E_2 - \delta E_1$ for transitions from state $|1\rangle$ to $|2\rangle$. However, similar to the case of the spin-polarized sample, one has to distinguish between the state which can be accessed by the transition, and some

30
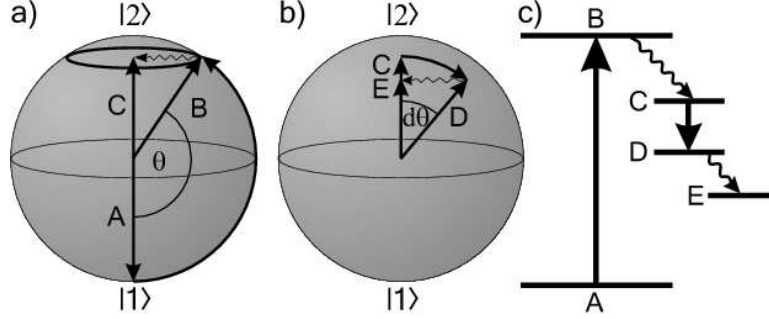
Fig. 4. – Bloch sphere representation of RF transitions. a) An RF pulse rotates a pure state A into B. The superposition state decoheres into a "ring" distribution which has "lost" its definite phase and is represented by the vertical vector C. b) A second RF pulse transforms the fully decohered state C into a partially coherent state D. The final state E is reached only after further decoherence. c) Transfers A→B and C→D are coherent and reversible. B→C and D→E are irreversible. From [128].

other incoherent state which can be reached only by an entropy increasing decoherence process (see Fig. 4). Even though the initial mixture had no coherence (i.e. the off-diagonal elements of the density matrix were zero), the RF pulse reintroduces coherence into the system. The final state after the RF pulse is not an incoherent mixture with different particle numbers, but a state in which each $|1\rangle$ atom has been transferred into the superposition state $|\alpha\rangle$, and each $|2\rangle$ atom into the orthogonal superposition state. One can show that for fermions, interaction energies are invariant under such a coherent transfer. The outcome is that in spite of possibly strong interactions between atoms in state $|1\rangle$ and $|2\rangle$, *there is no interstate clock-shift in a two-state mixture of fermionic atoms* [128].

Clock shifts in transitions to a third state. While RF transitions between two populated fermionic states do not reveal energy shifts, transitions from e.g. state $|2\rangle$ into a third, empty state reveal the presence of interactions. A priori, such transitions require knowledge of three scattering lengths, a_{12}, a_{13} and a_{23}. However, the preceding discussion shows that the coherent transfer from $|2\rangle$ to state $|3\rangle$ is not affected by interactions between these two states. To first approximation, the clock shift will be given by the differential mean-field shift experienced by an atom in state $|3\rangle$ compared to that experienced by an atom in state $|2\rangle$. The clock shift should thus read $\Delta\omega = \frac{4\pi\hbar}{m}(a_{13} - a_{12})\, n_1$. This dependence was used to observe the change of the scattering length near a Feshbach resonance [131, 127]. However, this expression is valid only for small scattering lengths, much smaller than the range of the potential r_0 and $1/k_F$. Its extension will be discussed in the next section.

Sum rule expression for the average clock shift. It is possible to derive a general expression for the average clock shift of an RF transition, valid for any many-body state of bosons and fermions [132]. Of course, knowledge of the average shift may be of limited use in cases where the RF spectrum has a complex line shape, e.g. is asymmetric, has high-energy tails or shows several peaks, but it still provides an important consistency check. The starting point is an initial many-body state $|12\rangle$ with energy E_{12} that contains atoms in state $|1\rangle$ and $|2\rangle$. The RF pulse resonantly drives transitions between state $|2\rangle$ and $|3\rangle$. As before in the discussion of RF transitions in a two-state mixture, it is incorrect to calculate the clock shift via the energy difference between two fully decohered states with different particle numbers in state $|2\rangle$ and $|3\rangle$. The expression for the differential mean-field shift $\Delta\omega = \frac{4\pi\hbar}{m}(a_{13} - a_{12})n_1$ thus cannot be generally true. Rather, to obtain the average clock shift, one must calculate the average energy cost per atom for rotating all atoms in state $|2\rangle$ into a coherent superposition of $|2\rangle$ and $|3\rangle$, a state $|\vartheta\rangle = \cos\vartheta\,|2\rangle + \sin\vartheta\,|3\rangle$. The many-body state is then changed into $|1\vartheta\rangle$, which has the same spatial many-body wave function as the original state. The total number of transferred atoms is $N_2\vartheta^2$ for small ϑ, with N_2 the number of atoms originally in $|2\rangle$. The average energy cost per atom for this rotation is thus

$$(9) \qquad \hbar\bar{\omega} = \hbar\omega_{23} + \hbar\Delta\omega = \lim_{\vartheta\to 0} \frac{\langle 1\vartheta|\,H\,|1\vartheta\rangle - \langle 12|\,H\,|12\rangle}{N_2\vartheta^2}$$

where $\hbar\omega_{23}$ is the hyperfine+Zeeman energy difference between $|2\rangle$ and $|3\rangle$, and H is the total Hamiltonian of the interacting mixture in three hyperfine states. The latter can be split into the internal hyperfine+Zeeman Hamiltonian and the external Hamiltonian H_{ext} describing the kinetic and interaction energy. The rotated state $|1\vartheta\rangle$ is generated by the many-body analogue of the transverse (fictitious) magnetic field above, $S_x = \frac{1}{2}\int \mathrm{d}^3 r(\Psi_3^\dagger \Psi_2 + \Psi_2^\dagger \Psi_3)$. So we have $|1\vartheta\rangle = e^{-i\vartheta S_x}\,|12\rangle \approx (1 - i\vartheta S_x)\,|12\rangle$, and Eq. 9 gives

$$(10) \qquad \hbar\Delta\omega = \frac{1}{2N_2}\,\langle 12|\,[S_x, [H_{\text{ext}}, S_x]]\,|12\rangle$$

An identical expression for the clock shift can be calculated using Fermi's Golden Rule [132]. This general sum rule for the spectral response can be applied to strongly interacting fermions [132, 133]. For weak interactions with the scattering lengths small compared to the characteristic size r_0 of the interatomic potential, one indeed obtains the mean field expression of the previous section. For scattering lengths larger than r_0 (but still smaller than $1/k_F$) this expression is modified to

$$(11) \qquad \Delta\omega = \frac{4\pi\hbar}{m}\frac{a_{12}}{a_{13}}(a_{13} - a_{12})n_1.$$

The general result, valid for all scattering lengths large than r_0, is

$$(12) \qquad \Delta\omega = \frac{1}{\hbar}\left(\frac{1}{k_F a_{13}} - \frac{1}{k_F a_{12}}\right)\frac{\partial(E_{12}/N_2)}{\partial\left(\frac{1}{k_F a_{12}}\right)}$$

where $\partial(E_{12}/N_2)/\partial\left(\frac{1}{k_F a_{12}}\right)$ is the change in the energy of the original state $|12\rangle$ under a change of the interaction strength $1/k_F a_{12}$. This change is varying smoothly as a function of $1/k_F a_{12}$ and is well-behaved even for resonant interactions, $1/k_F a_{12} = 0$. This expression shows that for strong interactions, the clock shift is expected to approach zero. This explains, at least qualitatively, the observation of vanishing clock shifts in a strongly interacting, unpaired Fermi gas [127].

2˙3.4. The special case of ^{6}Li. The usefulness of RF spectroscopy strongly depends on the spectral resolution one can achieve in the laboratory. The characterization of interaction effects on the order of a tenth of the Fermi energy requires a resolution on the kilohertz level. At high magnetic fields around the Feshbach resonance in ^{6}Li, typical magnetic field stabilities are about 10 mG, day-to-day fluctuations can be ten times larger. It is one of the many fortuitous facts about the ^{6}Li atom that due to its small hyperfine interactions, magnetic fields of several hundred Gauss completely decouple the electron from the nuclear spin. Therefore there are several RF transitions which flip only the nuclear spin and thus have only a very weak field sensitivity. For example, the $|1\rangle$-$|2\rangle$ atomic resonance has a field dependence smaller than 2.7 kHz/G above 600 G, which makes it easy to have sub-kHz resolution without any special field stabilization.

This unique property of ^{6}Li has allowed numerous RF experiments on unitarity limited interactions [127], on strong interaction effects in resonantly interacting gases [75, 134], precision spectroscopy of atoms and molecules [135] and on imbalanced Fermi gases [77]. In contrast, ^{40}K has a field dependence of 170 kHz/G for transitions between states $|2\rangle$ and $|3\rangle$ near the Feshbach resonance at 202 G. This was still sufficient for RF-dissociation of molecules [61] and the characterization of a Feshbach resonance [131].

2˙3.5. Preparation of a two-component system. Here we discuss how we use RF pulses and magnetic fields to transform a single-component Fermi cloud at low magnetic fields into a strongly interacting two-component mixture near a high-field Feshbach resonance.

Experimental Procedure. In the MIT experiment, a spin-polarized Fermi gas is produced by sympathetic cooling in a magnetic trap (see section **2**˙4.1 and Fig. 6 for details). Loading into the optical trap is performed in several steps. First, the radial confinement of the magnetic trap is removed by reducing the current in the cloverleaf coils to zero. This is a delicate process, as the center of the magnetic trap needs to remain aligned with the optical trap at all times during the current ramp-down. The atoms are still polarized in the stretched state $|F, m_F\rangle = |3/2, 3/2\rangle$. They experience the radial confinement of the optical trap plus the axial magnetic curvature. After the transfer into state
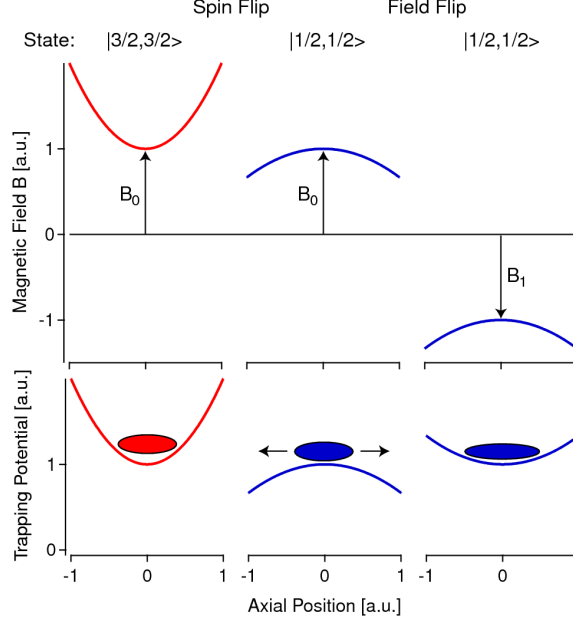
Fig. 5. – Hyperfine transfer of the cloud in a magnetic field curvature. The atoms are initially trapped in state $|3/2, 3/2\rangle$. After the spin transfer into state $|1/2, 1/2\rangle$, atoms are no longer trapped. A quick adiabatic reversal of the sign of the magnetic field retraps the atoms.

$|1\rangle \equiv |F = 1/2, m_F = 1/2\rangle$ (an adiabatic Landau-Zener RF-transfer close to the zero-field hyperfine splitting of 228 MHz), the atoms are in a high-field seeking state and thus experience an *anti-trapping* axial curvature. By quickly reversing the sign of the axial magnetic bias field the atoms are trapped again (see Fig. 5). At this stage, the magnetic field is increased to values near the Feshbach resonance between state $|1\rangle$ and $|2\rangle$, located at $B = 834\,\text{G}$ (see chapter **5**). Starting with the fully polarized gas in state $|1\rangle$, a non-adiabatic Landau-Zener RF sweep (around the hyperfine splitting of $\sim 76\,\text{MHz}$ on resonance) transfers atoms into a superposition of states $|1\rangle$ and $|2\rangle$. The admixture of state $|2\rangle$ can be freely controlled via the Landau-Zener sweep rate.

Decoherence. RF spectroscopy will not produce a decohered two-state mixture, but a coherent superposition state, by applying a suitable RF pulse or via a non-adiabatic Landau-Zener sweep. A decoherence mechanism is required for the gas to develop into a mixture of two states, i.e. to incoherently populate two distinct quantum states described by a diagonal density matrix. Only such a mixture will interact via s-wave collisions and possibly show pairing and superfluidity at achievable temperatures.

We found experimentally that an efficient decoherence mechanism for the trapped gas is provided by the magnetic field curvature of the optical/magnetic hybrid trap. Atoms that follow different trajectories in the inhomogeneous field will acquire different

phases. After some time, the relative phases of atoms are scrambled and one is left with an incoherent mixture. Being no longer in identical states, s-wave interactions between atoms are allowed. To demonstrate that decoherence has occurred, the emergence of clock shifts in transitions to a third, empty state has been recorded in [127]. The timescale for decoherence was found to be tens of milliseconds.

We can estimate the decoherence time from the spread of magnetic fields across the sample. Since the axial potential is mainly magnetic, the atoms experience a spread of Zeeman energies equal to the Fermi energy. At high magnetic fields, the magnetic moment of the two lowest states differs only by the nuclear magnetic moment, which is three orders of magnitude smaller than the electron's magnetic moment. We thus estimate the decoherence rate to be a thousand times smaller than the Fermi energy divided by $\hbar$. For a typical Fermi energy of $\hbar \times 100$ kHz, we thus expect a decoherence time of 10 ms, in agreement with observations.

2˙4. Using and characterizing Feshbach resonances. – Feshbach resonances are crucial for realizing strongly interacting Fermi systems. In this section, we present the Feshbach resonance as an experimental tool to prepare and analyze such systems. This section assumes a basic understanding of the physics of a Feshbach resonance. A detailed discussion of the underlying concepts and a theoretical description of Feshbach resonances can be found in chapter **5**.

2˙4.1. High magnetic fields. In ^{6}Li, the broad Feshbach resonance between the lowest two hyperfine states lies at 834 G [135]. To access the BEC-BCS crossover, magnetic fields of about 1000 G or more are necessary. To generate these fields with sufficient homogeneity while maintaining good optical access requires a careful design, usually with some compromises.

If magnetic field coils with N windings are placed in Helmholtz configuration outside the vacuum chamber or glass cell of typical diameter d = 3 cm, a current of about $I \sim Bd/\mu_0 N \sim 3000$ A/N is required. For such current densities, water cooling is essential. For a given total coil cross section A, the coil resistance is $R = \rho N^2 (2\pi d)/A$, with $\rho = 1.7 \cdot 10^{-8}$ Ωm the resistivity of copper. The required electric power is $P = RI^2 = E_B/\tau$, where $E_B = B^2 d^3/2\mu_0$ is the magnetic energy of a homogeneous field B stored in a volume d^3, and $\tau \sim \mu_0 A/\rho$ is the $1/e$ decay time of the field energy if the coils were shorted (τ = coil inductance/resistance). Both τ and P are independent of the number of windings N. The division of the designated volume of copper into wires determines the voltage and current of the power supply at constant power.

As the required magnetic field and the dimension d are determined by design constraints, the only variable here is the total cross section of the coils A which is often chosen to be a fraction of d^2. For $A = (1 \, \text{cm})^2$, a power of $P \sim 300$ W is dissipated in each coil and the time constant $\tau \sim 2$ ms. The time constant gives the fastest possible magnetic field ramp-up time, unless the power supply has a higher maximum power than the power P for steady operation. Fortunately, the field decay time can be reduced by using a "ring-down" resistance in parallel with the coil. A diode ensures that this
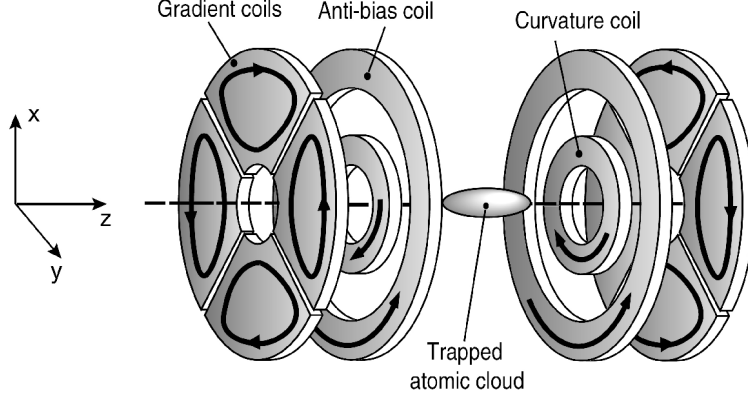
Fig. 6. – Magnetic trap in the MIT experiment, used for sympathetic cooling of ^{6}Li with ^{23}Na. The trap consists of a "curvature coil" that produces an axially confining potential. Its offset magnetic field is cancelled to about 0.5 G by the "anti-bias coil". Radial confinement is provided by the gradient coils which are wound in "cloverleaf" configuration. They replace the four Ioffe bars in a standard Ioffe-Pritchard trap. After the fermions are loaded into a single-beam optical trap, the anti-bias coils access the wide Feshbach resonance between the two lowest hyperfine states of ^{6}Li at 834 G.

ring-down path is opened once the power supply is switched off.

Fig. 6 shows the magnetic field configuration used in the MIT experiment. It allows for independent control of the bias field, the magnetic field curvature, and the radial gradient through the use of independent coils. The "cloverleaf" coils are needed for tight radial confinement during the sympathetic cooling stage of ^{6}Li with ^{23}Na in the magnetic trap. In order to tune the interatomic interactions across the Feshbach resonance, the bias field should be an independent parameter. This is accomplished by arranging a pair of coils as close as possible to the Helmholtz configuration. Our "Feshbach" coils (which also serve as "anti-bias" coils [9] during magnetic trapping) generate a residual magnetic field curvature that corresponds to an axial trapping frequency of 11.0 Hz for ^{6}Li at 834 G (resonance). If necessary we can compensate for this curvature by using the "curvature" coils. In practice, these two pairs of coils contribute both to curvature and bias field, and controlling the two currents independently allows a wide range of possible values. In most of our experiments, the "curvature" coils provide the bulk of the axial confinement. Thus, varying the bias field with the "Feshbach" coils between $B_0 = 700$ G to $B_0 = 1000$ G changes the axial trap frequency by only 0.5 Hz around the value at the Feshbach resonance ($\omega_z/2\pi = 22.8$ Hz).

2`4.2. Methods for making molecules.** Molecules are one form of pairing, and therefore play a major role in studying pairing between fermions. Many of our experiments use a purely molecular cloud as an intermediate step. Several methods have been demonstrated to create molecules from ultracold atoms:

36
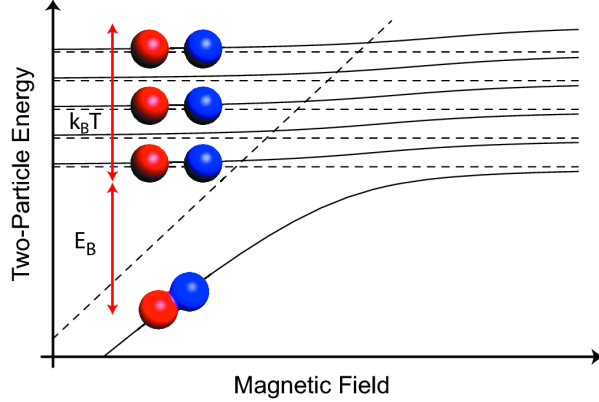
Fig. 7. – Creating molecules via three-body collisions. A molecular state is coupled to the continuum. As the gas is cooled on the molecular side, the Feshbach molecular state is populated via three-body collisions. If the binding energy is not much larger than k_B times the temperature, the energy carried away by the third body does not substantially heat the sample. For fermionic particles, further decay into lower lying vibrational states is strongly suppressed due to Pauli blocking.

- Photoassociation. In photoassociation two colliding atoms are optically excited to a bound state, which is electronically excited. By using a second step or a Raman transition, the electronic ground state can be accessed, usually with high vibrational excitation. This method is discussed in other recent reviews [136, 137]. So far, the phase space density of molecular clouds has been limited by heating from near resonant light and collisions involving the electronically excited intermediate state, or the vibrationally excited final state.

- Three-body recombination near a Feshbach resonance.

- Coherent two-body transfer near a Feshbach resonance via (1) a magnetic field sweep, (2) RF association, and (3) magnetic field modulation. Note that many theoretical descriptions of photoassociation are directly applicable to Feshbach resonances, as they can be regarded as photoassociation resonances with zero frequency photons. Sweeps of the magnetic field across the Feshbach resonance are equivalent to frequency sweeps across the photoassociation resonance.

In a three-body recombination, two of the colliding atoms form a molecule, the third particle (atom or molecule) carrying away the leftover energy and momentum. This process preferentially populates the most weakly bound molecular states. Their binding energies lie between zero and $\approx -160\,\hbar^2/mr_0^2$ (for an asymptotic van-der-Waals potential $V(r) \sim -C_6/r^6$), depending on rotational quantum numbers and boundary conditions at the inner turning point of the potential [138, 139]. With the van-der-Waals range $r_0 = (mC_6/\hbar^2)^{1/4} \approx 60\,a_0$ for ^{6}Li, these binding energies can be up to k_B times 1 K.
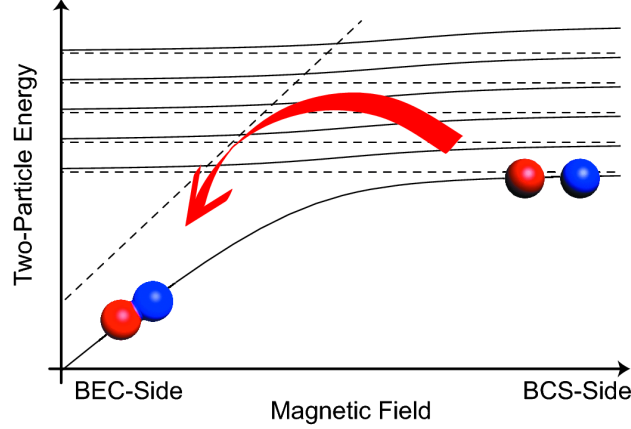
Fig. 8. – Creating molecules via magnetic field ramps. A magnetic field sweep can transfer unbound atoms adiabatically into the molecular state, much like a two-level Landau-Zener transition.

The released energy in such a collision heats up the cloud, leading to trap loss (hence the name "bad collisions"). However, in the case of the very weakly bound molecular state on the molecular side of a Feshbach resonance (scattering length $a > 0$), the binding energy can be on the order of the temperature, and molecules can efficiently form without severe heating and trap loss (Fig. 7). Subsequently, leftover atoms can be evaporated from the optical trap. This process is very efficient, since weakly bound molecules have twice the atomic polarizability, hence the optical trap is twice as deep for molecules than it is for single atoms.

The Feshbach molecules are in the highest vibrational state of the interatomic potential (see chapter **5**). They are only stable if the decay into lower lying vibrational levels is slow. It turns out that for fermions this decay is suppressed by the Pauli principle (see section **5**·1).

Producing molecules coherently by a magnetic field sweep is reversible and does not generate heat. It exploits the tunability of the Feshbach molecular state: Starting with unbound atoms in the continuum, one can sweep the magnetic field across the resonance and form a bound molecule (Fig. 8). Some aspects of this sweep can be described as a two-level Landau-Zener sweep through an avoided crossing. For a coupling matrix element V between two "bare" states, $|a\rangle$ and $|b\rangle$, and an energy sweep rate $\dot{E}$, one finds [140]

$$(13) \qquad P_{|a\rangle \to |b\rangle} = 1 - e^{-c\frac{|V|^2}{\hbar \dot{E}}}$$

for the probability $P_{|a\rangle \to |b\rangle}$ to make a transition from $|a\rangle$ to $|b\rangle$ as the bare state energies are swept through resonance. Here c is a numerical constant on the order of 1.

In the case of Feshbach resonances, the two "levels" are the molecular state and the state of two unbound atoms. V is the coupling matrix element between these states, $V = \sqrt{N/\Omega}\, g_0$, an expression that we will discuss in chapter **5**. The number N of atom pairs that appears in $|V|^2$ accounts for the fact that each spin up atom has N chances to form a molecule with a spin down atom per quantization volume Ω. Alternatively, one can consider two-body physics in a box of volume Ω/N, which emphasizes the local picture of two atoms forming a molecule.

If we take the simple Feshbach model of chapter **5**, we can replace $g_0^2 = \frac{4\pi\hbar^2}{m} a_{\mathrm{bg}}\, \Delta\mu\Delta B$, with a_{bg} the background scattering length, $\Delta\mu$ the difference in magnetic moments between the molecular state and two free atoms, and ΔB describing the width of the Feshbach resonance. The bare state energies are tuned via the magnetic field, so $\dot{E} = \Delta\mu\,\dot{B}$. We then have

$$(14) \qquad P_{\mathrm{atoms}\rightarrow\mathrm{molecules}} \simeq 1 - \exp\left(-A\frac{n}{\dot{B}}\right)$$

with $A = c\frac{4\pi\hbar a_{\mathrm{bg}}\Delta B}{m}$. The higher the density and the slower the magnetic field ramp across resonance, the more efficient is the production of molecules [141, 142].

The schematic figure of the Feshbach resonance (Fig. 8) suggests that the simple two-state picture applies only to the lowest state of relative motion between the two atoms. Excited states of relative motion on the BCS side are adiabatically connected to the next lower lying state of relative motion on the BEC side. Therefore, the Landau-Zener probability discussed above should have a prefactor which is the probability for two atoms to be in the same phase space cell, proportional to the phase space density. Indeed, it has been experimentally verified in [141] that the efficiency of forming molecules during a slow adiabatic sweep increases monotonously with the phase space density and that it can exceed 50 % for both bosonic and fermionic thermal clouds (up to 90% transfer was achieved for ^{40}K).

The coherent conversion of two atoms into molecules can be accomplished not only by sweeping the Feshbach field, but also by modulating the magnetic field close to the Feshbach resonance, at a frequency corresponding to the molecular binding energy [143, 86]. Yet another method is to drive a free-bound RF transition [103], where initially one of the free atoms occupies a different hyperfine state.

2˙4.3. Observation of Feshbach resonances. A Feshbach resonance is an "intimate" encounter between two atoms, which collide and temporarily form a molecule before they separate again. Many collisional processes are enhanced and have been used to locate the magnetic field position of these resonances.

- Trap loss by enhanced inelastic collisions. The first observations of Feshbach resonances were made by monitoring loss due to three-body recombination [7] and due to an enhanced photoassociation rate [8]. The broad Feshbach resonance in ^{6}Li was mapped out using trap loss [56]. However, since the molecules formed in three-body recombination are long-lived close to resonance, the center of the loss

feature was found at fields well below the Feshbach resonance. In addition, an unpredicted narrow Feshbach resonance at 543 Gauss was found [56, 16, 144]. Trap loss spectroscopy is usually applied to find new resonances and has been used, for example, to discover p-wave Feshbach resonances in ^{40}K [145] and ^{6}Li [146, 144] and interspecies Feshbach resonances [147, 101].

- Rapid thermalization. The increased scattering length leads to rapid thermalization of the gas. This method was used to study the resonance in ^{85}Rb [148], and in ^{40}K [57]. The absence of thermalization was used to locate the position of the zero-crossing of the scattering length in ^{6}Li at 528 G [58, 59].

- Change of interaction energy. For Bose-Einstein condensates, this is observed by the change in mean field energy and therefore the size of the cloud, either in trap or in ballistic expansion [7, 11]. For fermions, the change of the interaction energy has been monitored via clock shifts (see section **7**'2.4). The size of the fermionic cloud varies smoothly and monotonously across resonance, a direct consequence of the smooth change of the cloud's energy in the BEC-BCS crossover (see chapter **4**).

- RF spectroscopy of Feshbach molecules. Using RF spectroscopy, one can determine the onset of molecular dissociation, and then, by extrapolation, find the value of the magnetic field at which the molecular binding energy vanishes [135, 61] . The most precise value for the broad ^{6}Li Feshbach resonance was derived from RF spectroscopy between weakly bound molecular states using a multi-channel scattering model [135].

- Threshold for molecule formation. When the magnetic field is swept across the Feshbach resonance, molecules will appear with a sharp onset at the resonance.

- Threshold for molecule dissociation. Feshbach molecules start to dissociate when the magnetic field is raised to a value above the Feshbach resonance.

Since the last two methods are directly related to the formation and detection of molecules, we discuss them in more detail.

To observe the onset of molecule formation, one prepares a Fermi mixture on the "BCS"-side of the Feshbach resonance, where no two-body molecular bound state exists in vacuum (see chapter **5**). As the magnetic field is swept across the resonance, molecules will form and, accordingly, the signal from unbound atoms will diminish (Fig. 9) [61, 62, 147]. From Fig. 9 we determine a value of $B_0 = 838 \pm 27$ G for the position of the resonance. The loss of atomic signal is reversible: Ramping back across the resonance will dissociate the molecules, and reestablish all or most of the atomic signal [61, 15, 16, 17, 62, 63, 64].

In fact, the dissociation method gives a more accurate determination of the location of the Feshbach resonance [69, 70]. To avoid effects due to the high density in the trap (i.e. many-body physics), in [70] the molecular cloud is expanded to a 1000 times lower density, about 10^{10} cm^{-3}. Then the magnetic field is ramped to a value B_{test}. If B_{test} lies
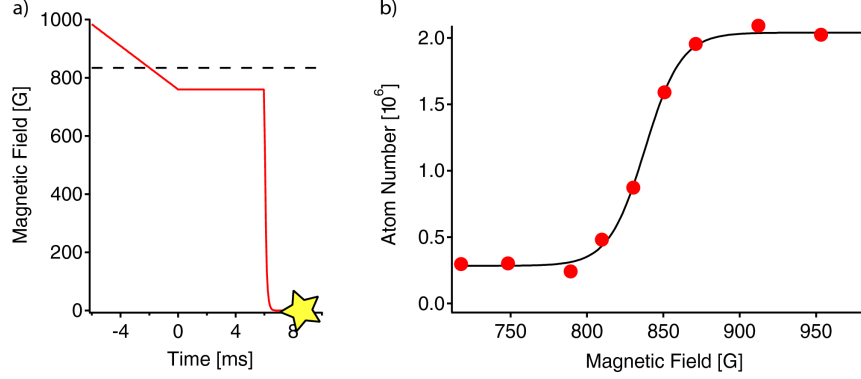
Fig. 9. – Molecule formation by magnetic field sweep across the Feshbach resonance. a) Experimental procedure. A Fermi mixture prepared on the BCS-side of the Feshbach resonance is swept across resonance (shown as the dashed line) to form molecules. The gas is released from the trap at the end point of the ramp at time $t = 0$ ms. Zero-field imaging, indicated by the star, detects the leftover atoms. b) Atomic signal vs end point of the magnetic field sweep. The line is a fit to an error function, whose center is determined to be 838 ± 27 G, with an uncertainty given by the 10%-90% width (54 G).

above the Feshbach resonance, the molecules will dissociate into unbound atoms, which are subsequently detected at low field.

The very sharp onset of the atomic signal at $B_{\text{test}} = 821 \pm 1$ G is striking (see Fig. 10) and suggests this magnetic field value as the position of the Feshbach resonance. However, via molecular RF spectroscopy the location of the Feshbach resonance has been determined to lie at 834.1 ± 1.5 G [135]. The reason for this discrepancy is probably that molecules at threshold are extremely fragile and might break apart before the resonance is reached, thus shifting the observed threshold to lower values. See Ref. [144] for a discussion and characterization of such shifts. RF spectroscopy addresses more tightly bound molecules and identifies the resonance by extrapolation, thus avoiding stability issues very close to resonance.

From Fig. 10 we can directly see that before dissociation, more than 99% of the gas exists in form of molecules. The reason is that this molecular cloud was formed via the three-body process, by simply cooling the gas at the fixed field of 780 G (the BEC-side of the resonance). The lifetime of the weakly bound molecules is so long, and the binding energy is so small, that losses and heating are negligible, and, after evaporation of leftover unbound atoms, essentially all particles are bound into molecules.

2˙4.4. Determination of the coupling strength of Feshbach resonances. The "strength" of a Feshbach resonance is determined by the square of the matrix element which couples the closed and open channels, proportional to $g_0^2 = \frac{4\pi\hbar^2}{m} a_{\text{bg}} \Delta\mu\Delta B$ (see section **2**˙4.2 and chapter **5**). This expression depends on the background scattering length only because of
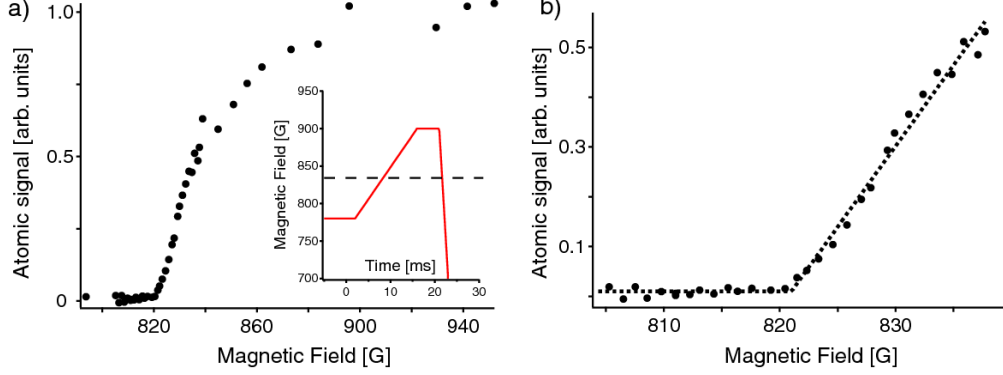
Fig. 10. – Locating the Feshbach resonance by molecule dissociation. The experimental procedure is shown in the inset. A molecular cloud is prepared on the BEC-side of the Feshbach resonance, at 780 G, and released from the trap at $t = 0$ ms. After some expansion, the field is ramped to a test value around resonance (shown as the dashed line), held constant and is finally brought to zero field, where only unbound atoms are imaged. a) The atomic signal as a function of the test field shows a sharp threshold behavior at 821 ± 1 G, where the uncertainty is the statistical error of a threshold fit, shown in b).

the definition of ΔB in the formula for the scattering length $a(B) = a_{\mathrm{bg}} \left(1 - \frac{\Delta B}{B - B_0} \right)$. A Feshbach resonance with the same strength but on top of a larger background scattering length then has a narrower width ΔB. So one way to determine the strength of a Feshbach resonance is by measuring or knowing a_{bg}, $\Delta \mu$ and ΔB.

The matrix element can be measured more directly from the dynamics of molecule dissociation and formation. When Feshbach molecules in ^{23}Na were dissociated with variable field ramp, the kinetic energy of the fragments was shown to increase with the ramp speed [149]. This reflects the finite lifetime of the Feshbach molecules, which are "ramped up" in energy for about one lifetime, before they decay through their coupling to the open channel. This method was also applied to ^{87}Rb [150].

Here we describe experiments using the reverse process, i.e. the formation of molecules by a variable field ramp, as introduced in section **2**.4.2 above. Fig. 11 demonstrates the extremely strong coupling strength of the ^{6}Li Feshbach resonance. In this experiment, a Fermi mixture is released from the trap at $B = 840$ G, slightly above the Feshbach resonance. When the magnetic field is suddenly switched off at the same time (at an initial slew rate of $\dot{B} = 30\,\mathrm{G}/\mu\mathrm{s}$), almost the entire atomic signal vanishes, i.e. the conversion into molecules is almost 95%. The ^{6}Li Feshbach resonance is so strong that the quantitative conversion from trapped fermions into molecules during a Feshbach sweep can only be avoided by using small magnetic field coils with low self-inductance and correspondingly fast switch-off time [15].

However, when we allow the gas to expand and lower its density before the sweep, then the conversion to molecules is only partial, and we can determine the strength of
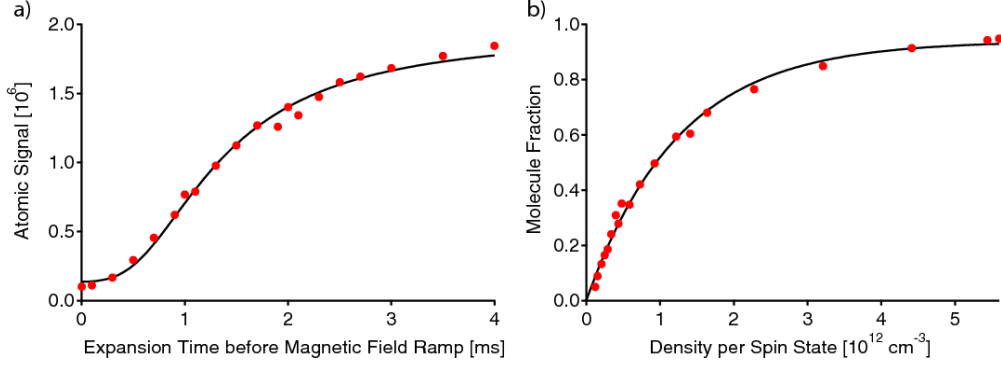
Fig. 11. – Revival of the atomic signal during expansion and strength of Feshbach coupling. a) The magnetic field is switched off after varying expansion times for a cloud released at 840 G. The field ramp creates molecules more efficiently at the high densities of the trap than at low densities after long expansion. In b), all of the atomic signal loss is interpreted as molecular conversion and plotted as a function of density. The density was calibrated by imaging the cloud at high field for varying expansion times. All fits are for the simple Landau-Zener-model described in the text.

the Feshbach coupling. In Fig. 11 b) we interpret all the disappeared atomic signal as conversion into the weakly-bound molecular state neglecting other loss-channels like unobserved molecular states. The conversion efficiency decreases with decreasing density and can be fit using the simple the Landau-Zener formula Eq. 14. We find that the constant A in Eq. 13 is $A \approx 24 \, \mathrm{G}/(10^{12} \, \mathrm{cm}^{-3} \, \mu\mathrm{s})$ with a relative error of 50% due to the uncertainty in the atom number.

The theoretical prediction is Eq. 14 with $c = 2\pi$ [151]. With the parameters for ^{6}Li we find

$$(15) \qquad A = \frac{8\pi^2 \hbar a_{\mathrm{bg}} \Delta B}{m} = 19 \, \frac{\mathrm{G}}{10^{12} \, \mathrm{cm}^{-3} \, \mu\mathrm{s}}$$

For comparison, for the ^{40}K Feshbach resonance at $B = 224.2 \, \mathrm{G}$ used in some experiments the prediction is $A = 0.011 \, \frac{\mathrm{G}}{10^{12} \, \mathrm{cm}^{-3} \, \mu\mathrm{s}}$ ($a_{\mathrm{bg}} = 174 \, a_0, \Delta B = 9.7 \, \mathrm{G}$ [131]). This is not far from the value $A \approx 0.004 \frac{\mathrm{G}}{10^{12} \, \mathrm{cm}^{-3} \, \mu\mathrm{s}}$ one extracts from the measurement in [61] ($0.05 \, \mathrm{G}/\mu\mathrm{s}$ was the ramp speed that resulted in a $1/e$ transfer of molecules, at a peak density of $n_{\mathrm{pk}} = 1.4 \times 10^{13} \, \mathrm{cm}^{-3}$). The broad resonance in ^{6}Li can efficiently convert atoms into molecules at 2,000 times faster sweep rates.

The good agreement with the simple Landau-Zener model might be fortuitous. Ref. [141] points out that the conversion efficiency must depend on the phase space density and presents data which, in the case of ^{85}Rb, disagree with simple theoretical predictions by a factor of eight.

43

2˙4.5. *The rapid ramp technique.* So far, we have discussed the time scale for two-body physics, namely the association of two atoms into a molecule. For isolated atom pairs, this process is independent of the total momentum of the pair, which is preserved due to Galilean invariance. In a many-body system, fermion pairs interact and collide, and their momentum changes. If the two-body time scale is faster than the many-body time scale, there is an interesting window of ramp rates for the sweep across the Feshbach resonance: One can be slow enough to quantitatively convert atom pairs into molecules, but also fast enough such that the momentum distribution of the final molecules reflects the momentum distribution of the fermion pairs prior to the sweep (see Fig. 12).

This method was introduced by the JILA group [69], and later adapted to ^{6}Li by our group [70]. It made it possible to analyze the momentum distribution of fermion pairs across the whole BEC-BCS crossover and detect the pair condensate (see chapter **6**).
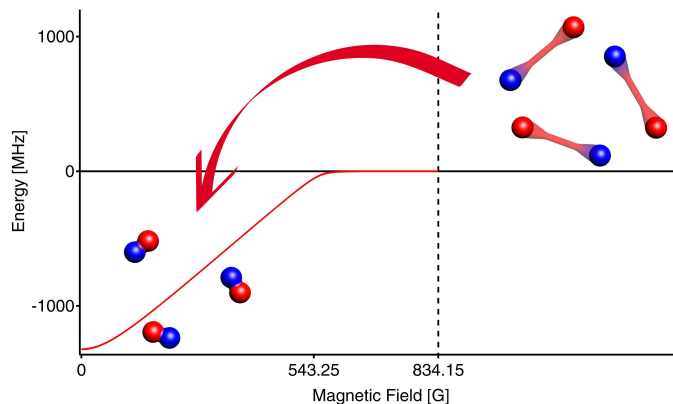
Fig. 12. – Rapid ramp to the molecular side to observe pair condensation. Immediately after switching off the trapping beam, the magnetic field is ramped to zero field. This converts long-range pairs into stable, tightly bound molecules, preserving the momentum distribution of the original pairs.

The problem with the rapid ramp technique is that it is not clear what the many-body time scale is. In particular, one wants to rule out that the pair momentum distribution changes during the sweep or that a condensate is formed while ramping. We address this question by listing several time scales of the system (table III). For theoretical modelling of the ramp process, see refs. [152, 153, 154, 155]. The final demonstration that the rapid ramp does preserve the absence or presence of a pair condensate before the sweep has to come from experiment (see section **6**˙4.2).

The fastest timescale, given by $\hbar$ divided by the Feshbach coupling strength, governs the two-body physics (in the Landau-Zener picture, this is the inverse of the anti-crossing gap). The timescale at which the magnetic field sweeps through the anti-crossing is given in the second line of Table III. As pointed out above, in the MIT experiment, even switching off the current through the Feshbach coil is still slower than the in-trap

Time scale	Formula	Value
Two-body physics	$\hbar/g_0\sqrt{2\pi n}$	20 ns
Magnetic field ramp through anti-crossing	$g_0\sqrt{2\pi n}/\Delta\mu\dot{B}$	80 ns
Inverse Fermi energy	$\hbar/E_F$	3 μs
Time required to leave strongly interacting region	$\delta B/\dot{B}$	3 μs
Evolution of the gap at $k_F|a| = 2$	$\Delta/\dot{\Delta}$	10 μs
Gap at $k_F|a| = 2$	$\hbar/\Delta$	15 μs
Inverse collision rate at unitarity and $T/T_F = 0.1$	$\approx 0.23\,\hbar E_F/(k_B T)^2$ [156]	70 μs
Growth time of a pair condensate at $k_F|a| = 2$	$\approx \hbar E_F/\Delta^2$ [157]	75 μs
Radial trapping period	$2\pi/\omega_r$	2 ms

TABLE III. – *Time scales involved in the rapid ramp technique. The given values are typical for the MIT experiment and assume a density of* $1.5 \cdot 10^{13}\,\mathrm{cm}^{-3}$.

two-body time scale, resulting in conversion efficiencies into molecules of larger than 90%.

The next fastest time scale is set by the Fermi energy, which in the unitarity regime on resonance would set the timescale for collisions in the normal Fermi gas, were it not for Pauli blocking. Indeed, if we multiply the local density n with the rms velocity in the Fermi-Dirac distribution $\propto v_F$ and with the unitarity limited cross section for elastic collisions $\sim 4\pi/k_F^2$, we obtain a "classical" collision rate of $\sim E_F/\hbar$. Also, the Fermi energy should set the time scale at which local fluctuations of the gas density can "heal", as the local chemical potential on resonance is given by $\mu \approx 0.5 E_F$. As the gas is brought into the weakly interacting regime on the BEC-side, where $k_F a < 1$, this many-body relaxation rate $\mu/\hbar$ should decrease to the smaller mean-field rate of a molecular BEC. It is thus interesting to know whether the ramp is adiabatic with respect to this local "healing" or relaxation, averaged over the sweep. If we use $\hbar/E_F$ as an upper bound for the relaxation rate around resonance, and neglect relaxation outside this region, the relevant scale is the time it takes to leave the strongly interacting regime. For typical parameters in our experiment, $k_F a \approx 1$ around 750 G, $\delta B \sim 85$ G away from resonance, and the time scale is $\sim \delta B/\dot{B}$.

The time it takes to leave the unitarity limited region in our gas is on the order of the Fermi time scale, and should be smaller than the inverse collision rate. This would mean that the original momentum distribution of fermion pairs is "frozen in" during the ramp, and the momentum distribution of the molecules at the end of the sweep reflects that of the fermion pairs on the BCS-side. However, since a collisional model for a weakly interacting gas should not be taken too seriously to estimate the relaxation time, experimental tests were required, which will be discussed in section **6**˙4.2.

The ramp is non-adiabatic with respect to the time scale of the gap, which is forced to evolve faster than it can adiabatically respond to the change in interaction strength, $\dot{\Delta}/\Delta \gtrsim \Delta/\hbar$. On the BCS-side of the resonance, the average binding energy of pairs is $\frac{3}{4}\Delta^2/E_F$. The last condition implies that pairs cannot adiabatically adjust their size during the fast ramp. On the BEC-side, the pair binding energy evolves into the molecular binding energy, $E_B = -\hbar^2/ma^2$. If one ramps far enough on the molecular side, a

becomes so small and E_B becomes so large that the molecular state can follow the ramp adiabatically. This observation is used in [154] to split the discussion of the field ramp into a "sudden" and an "adiabatic" part, connected at the scattering length a^* for which $\dot{E}_B/E_B = E_B/\hbar$. The "sudden" part is then modelled as a projection of the initial to the final pair wave function. One finds $a^* = (A/16\pi^2\dot{B})^{1/3}$, with A given by Eq. 15, and $k_F a^* = (3An/16\dot{B})^{1/3}$, which is just the third root of the Landau-Zener parameter entering Eq. 14. The latter is $\gtrsim 1$ if the molecule conversion is efficient, as it is in our case, directly implying that the "sudden" to "adiabatic" transition still occurs in the strongly interacting regime, $k_F a^* \gtrsim 1$. The ramp time needed to enter the adiabatic regime is thus smaller or about equal to the time required to leave the unitarity region.

Finally, there is the relaxation time scale of the gas in response to a change in the particle distribution. In a normal Fermi gas of N particles at temperatures $T \ll T_F$, relaxation occurs via collisions of particles close to the Fermi surface, of number NT/T_F. Pauli blocking reduces the available final states for collisions by another factor of T/T_F, giving a relaxation time $\tau_R \approx \hbar E_F/(k_B T)^2$. In general, if the Fermi surface is smeared over an energy width ΔE, the relaxation time is $\tau \approx \hbar E_F/\Delta E^2$. In the case of a (BCS-type) superfluid, $\Delta E = \Delta$, and the relaxation time thus scales as $\tau_R = \hbar E_F/\Delta^2$ [158].

2˙5. *Techniques to observe cold atoms and molecules.* –

2˙5.1. Basics. The basic techniques of imaging ultracold fermions are identical to those for imaging bosons, which were described in great detail in the 1999 Varenna lecture notes [9]. The two main techniques are absorption and dispersive imaging. In absorption imaging, a laser beam tuned to the atomic resonance is absorbed by the atoms, whose shadow image is recorded on a CCD-camera. It is often applied after expansion of the cloud from the atom trap, as the optical density of the trapped cloud is so high that the absorption is strongly saturated. Detuning the laser frequency to avoid strong absorption often results in image distortions due to dispersive effects. Dispersive imaging relies on the phase shift that atoms impart on the laser light and is usually implemented with a sufficiently large detuning δ so that the phase shift is on the order of unity.

Both types of imaging heat the sample by the recoil of Rayleigh scattered photons. However, in dispersive imaging, the signal is due to forward scattering which is enhanced similarly to superradiance. As a result, for the same amount of heating, the number of signal photons is larger than in absorption imaging by the resonant optical density divided by four [9]. This factor can be big (on the order of one hundred) for large trapped clouds and has made it possible to take several dispersive images of the same sample without noticeable smearing (so-called non-destructive imaging).

With regard to imaging, the main difference between experiments on ultracold fermions and bosons is that typically, in the boson case one deals with a single spin state (an exception are experiments on spinor-BEC [159, 160, 161, 162]), while in Fermi gases at least two hyperfine states are involved. Especially for the study of imbalanced Fermi systems where the spatial profile is different for the two components, double-shot imaging techniques are essential. In such techniques, an image of one spin state is rapidly

succeeded by an image of the second state. In case of residual off-resonant absorption of the first imaging light pulse, the second image has to be taken after less then a few tens of μs, to avoid blurring as atoms move due to photon recoil. Current CCD cameras allow rapid successive exposure by shifting each pixel row of the first image underneath a mask, where it is safely stored during the second exposure. Both absorption imaging [79] and dispersive imaging [80] have been used in this way. Another technique that has been employed for RF spectroscopy [127] was to use several independent laser beams, each resonant with a different atomic transition, that were simultaneously recorded on different parts of the CCD chip.

The probe frequency in dispersive imaging can be chosen to record a weighted sum of the column densities of the two components. In particular, by adjusting the laser detuning to lie in between the two resonance frequencies, phase-contrast imaging [9] then records directly the density difference [80] without the need of subtracting two large signals. Since spin polarization is proportional to the density difference, this technique was crucial in the study of imbalanced Fermi systems [80] (see Fig. 13).

2˙5.2. Tomographic techniques. Both absorption and dispersive imaging integrate along the line-of-sight and provide information about the column densities. However, by taking such projections along an infinite number of angles, one can reconstruct the three-dimensional density distribution tomographically using the so-called inverse Radon transformation.

If the sample has cylindrical symmetry, then one line-of-sight integrated image $n(x, z)$ is sufficient for the reconstruction of the atomic density $n(r, z)$ using the inverse Abel transform [163]

$$(16) \qquad n(r, z) = -\frac{1}{\pi} \int_r^\infty \mathrm{d}x \, \frac{1}{\sqrt{x^2 - r^2}} \frac{\mathrm{d}n(x, z)}{\mathrm{d}x}$$

This transformation takes the derivative of the column density image, and so-to-speak inverts the line-of-sight integration. In particular, discontinuous jumps in the three dimensional density appear as kinks (jumps in the derivative) of the column density.

The derivative is sensitive to noise. Due to the derivative in Eq. 16, this technique requires a very good signal-to-noise ratio. Reducing noise by averaging (blur filter) is not an option if high spatial resolution has to be maintained, i.e. for the reconstruction of sharp phase boundaries.

The inverse Abel transformation has been used to reconstruct the propagation of phonons in a Bose-Einstein condensate [164], and to reconstruct s- and d-wave scattering halos in the collision of two Bose-Einstein condensates [165, 166]. Tomographic reconstruction was essential in distinguishing fermionic superfluids with equal densities of the two components from polarized superfluids (which have a density imbalance) [80]. The signal-to-noise was high enough to identify sharp phase boundaries between the superfluid and the normal phase in the reconstructed images, characteristic for a first-order phase transition [82].
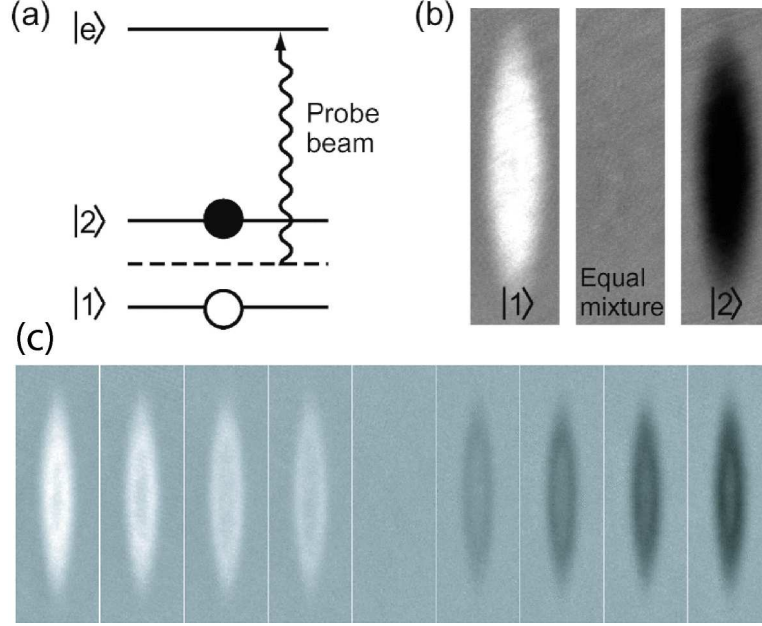
Fig. 13. – In-situ phase-contrast imaging of the density difference of two spin states of ^{6}Li at the 834 G Feshbach resonance. (a) The probe beam is tuned to the red of the resonance for state 1, and to the blue for state 2. The resulting optical signal in the phase-contrast image is proportional to the density difference of the atoms in the two states. (b) Phase-contrast images of trapped atomic clouds in state $|1\rangle$(left) and state $|2\rangle$(right) and of an equal mixture of the two states (middle). (c) The imbalance in the populations N_1, N_2 of the two states, defined as $(N_1 - N_2)/(N_1 + N_2)$, was chosen to be -50, -37, -30, -24, 0, 20, 30, 40 and 50%. The observation of a distinctive core shows the shell structure of the cloud caused by phase separation. The height of each image is about 1 mm. See Ref. [80] for further details.

Tomographic reconstruction has been extended to RF spectroscopy. RF spectra have usually been recorded for the whole cloud. However, using sufficiently short RF pulses followed immediately by spatial imaging of the cloud, it has been possible to record the spatial distribution of the RF induced changes in the population of the initial or final state [127, 134]. When many such images are recorded for different RF frequencies, and processed with an inverse Abel transformation, one obtains local RF spectra [134]. These spectra are no longer affected by inhomogeneous broadening due to the spatially varying density, and one even obtains a series of spectra each at a different local density. This method was developed to reveal a gap in the RF spectrum of a fermionic superfluid and to observe its homogeneous width and line shape [134].

2˙5.3. Distinguishing atoms from molecules. On the BEC side of the Feshbach resonance, molecules are stable, and in order to verify the presence of molecules or to

quantitatively characterize the system, it became necessary to distinguish atomic from molecular densities.

The following properties of these Feshbach molecules are important for their detection. (1) The molecules are stable on the BEC side, not too far away from the Feshbach resonance, and are dissociated by sweeping the magnetic field across it. (2) Close to the Feshbach resonance, the size of the molecules is approximately given by the atomic scattering length a and can become very large. Here, the molecular wave function has "open channel" character, i.e. the molecule is formed out of the same continuum of states in which two free atoms collide in. (3) As a consequence, the Feshbach molecule can be regarded as "two atoms on a stick", and the frequency for resonant transitions is very close to the atomic frequencies. More precisely, the molecules are expected to absorb most strongly near the outer turning point R. The excited state potential is split by the resonant van der Waals interaction $\zeta\hbar\Gamma(\lambda/2\pi R)^3$ where λ is the resonant wavelength and ζ is $\pm(3/4)$ or $\pm(3/2)$ for different excited molecular states. Therefore, as long as $a \gtrsim \lambda/2\pi$, the Feshbach molecules resonate at the atomic transition frequencies. For $a \lesssim \lambda/2\pi$, the molecules should be almost transparent at the atomic resonances. (4) Sufficiently far away from the resonance, the Feshbach molecules assume more and more closed channel character, and due to the different hyperfine interaction in the closed channel, have a magnetic moment different from the free atoms.

Various methods use these properties to obtain the molecular populations:

- Subtract from the signal of (atoms+molecules) the signal of (atoms only). The atoms only signal is obtained by sweeping to low or zero magnetic field, where the molecules no longer absorb at the atomic resonance. The field ramp needs to be slow compared to two-body timescales (i.e. should not "rip" the molecule apart), but fast compared to losses. The atoms+molecules signal is obtained either at a magnetic field close to resonance [66] or after a sweep across the resonance, which dissociates the molecules [61, 15, 62, 63, 64, 17, 66].

- Distinguish molecules by Stern-Gerlach separation. In ballistic expansion at magnetic fields sufficiently far away from the Feshbach resonance, molecules can be spatially separated from the atoms and distinguished on absorption images. This technique was used to detect molecules formed of bosonic atoms [62, 63, 64]. For ^{6}Li, it was used to measure the magnetic moment and hence the contribution of the closed channel to the Feshbach molecule [17].

- Distinguish molecules by RF spectroscopy. The molecular RF spectrum is shifted from the atomic line by the molecular binding energy. Therefore, an RF pulse populating an unoccupied state [61] can be tuned to either spin flip atoms or dissociate molecules. Imaging light in resonance with this initially unoccupied state can record the molecular population.

In most of our studies at MIT in the BEC-regime of the Feshbach resonance, the temperature of the cloud was so low that it consisted purely of molecules, i.e. we then

did not discern any atomic population using the first of the methods listed above [66]. Therefore, we routinely image the whole cloud at fields slightly below the Feshbach resonance knowing that this (atoms+molecules) signal is purely molecular.

3. – Quantitative analysis of density distributions

The purpose of imaging and image processing is to record density distributions of the atomic cloud, either trapped or during ballistic expansion. All our knowledge about the properties of cold atom systems comes from the analysis of such images. They are usually compared to the results of models of the atomic gas. Some models are exact (for the ideal gas), others are phenomenological or approximations. Many important models for bosonic atoms have been presented in our 1999 Varenna notes. Here we discuss important models for fermions, which allow us to infer properties of the system from recorded (column) density distributions.

3˙1. *Trapped atomic gases.* –

3˙1.1. Ideal Bose and Fermi gases in a harmonic trap. The particles in an atom trap are isolated from the surroundings, thus the atom number N and total energy content E_{tot} of the atomic cloud is fixed. However, it is convenient to consider the system to be in contact with a reservoir, with which it can exchange particles and energy (grand canonical ensemble). For non-interacting particles with single-particle energies E_i, the average occupation of state i is

$$(17) \qquad \langle n_i \rangle = \frac{1}{e^{(E_i - \mu)/k_B T} \mp 1}$$

with the upper sign for bosons, the lower sign for fermions. These are the Bose-Einstein and Fermi-Dirac distributions, respectively. For a fixed number of particles N one chooses the chemical potential μ such that $N = \langle N \rangle = \sum_i \langle n_i \rangle$.

Let us now apply these distributions to particles confined in a harmonic trap, with trapping potential

$$(18) \qquad V(\mathbf{r}) = \frac{1}{2} m(\omega_x^2 x^2 + \omega_y^2 y^2 + \omega_z^2 z^2)$$

We assume that the thermal energy $k_B T \equiv 1/\beta$ is much larger than the quantum mechanical level spacings $\hbar\omega_{x,y,z}$ (Thomas-Fermi approximation). In this case, the occupation of a phase space cell $\{\mathbf{r}, \mathbf{p}\}$ (which is the phase-space density times h^3) is given by Eq. 17

$$(19) \qquad f(\mathbf{r}, \mathbf{p}) = \frac{1}{e^{(\frac{\mathbf{p}^2}{2m} + V(\mathbf{r}) - \mu)/k_B T} \mp 1}$$

The density distribution of the thermal gas is

$$n_{th}(\mathbf{r}) = \int \frac{\mathrm{d}^3 \mathbf{p}}{(2\pi\hbar)^3} \, f(\mathbf{r}, \mathbf{p})$$

$$(20) \qquad \qquad = \pm \frac{1}{\lambda_{dB}^3} \, \mathrm{Li}_{3/2} \left(\pm e^{\beta(\mu - V(\mathbf{r}))} \right)$$

where $\sqrt{\frac{2\pi\hbar^2}{mk_BT}}$ is the de Broglie wavelength. $\mathrm{Li}_n(z)$ is the nth-order Polylogarithm, defined as

$$(21) \qquad \mathrm{Li}_n(z) \equiv \frac{1}{\pi^n} \int \mathrm{d}^{2n}r \frac{1}{e^{\mathbf{r}^2}/z - 1} \stackrel{n \neq 0}{=} \frac{1}{\Gamma(n)} \int_0^\infty \mathrm{d}q \frac{q^{n-1}}{e^q/z - 1}$$

where the first integral is over $2n$ dimensions, $\mathbf{r}$ is the radius vector in $2n$ dimensions, n is any positive half-integer or zero and $\Gamma(n)$ is the Gamma-function ([5]). Note that expression 20 is correct for any potential $V(\mathbf{r})$. The constraint on the number of thermal particles is

$$(23) \qquad N_{th} = \int \mathrm{d}^3\mathbf{r}\, n_{th}(\mathbf{r})$$

For a harmonic potential (18), we obtain

$$(24) \qquad N_{th} = \pm \left(\frac{k_BT}{\hbar\bar{\omega}}\right)^3 \mathrm{Li}_3(\pm e^{\beta\mu})$$

with $\bar{\omega} = (\omega_x\omega_y\omega_z)^{1/3}$ the geometric mean of the trapping frequencies.

In the classical limit at high temperature, we recover the Maxwell-Boltzmann result of a gaussian distribution,

$$(25) \qquad n_{cl}(\mathbf{r}) = \frac{N}{\pi^{3/2}\sigma_x\sigma_y\sigma_z}e^{-\sum_i x_i^2/\sigma_{x_i}^2} \qquad \text{with } \sigma_{x,y,z}^2 = \frac{2k_BT}{m\omega_{x,y,z}^2}$$

The regime of quantum degeneracy is reached when $\lambda_{dB} \approx n^{-1/3}$, or when the temperature $T \approx T_{\deg}$. The degeneracy temperature $T_{\deg} = \frac{\hbar^2}{2mk_B}n^{2/3}$ is around or below one μK for typical experimental conditions.

For **bosons**, it is at this point that the ground state becomes macroscopically occupied and the condensate forms. The density profile of the ideal gas condensate is given by the

---

([5]) The Polylogarithm appears naturally in integrals over Bose-Einstein or Fermi-Dirac distributions. Some authors [167] use different functions for bosons $g_n(z) = \mathrm{Li}_n(z)$ and for fermions $f_n(z) = -\mathrm{Li}_n(-z)$. The Polylogarithm can be expressed as a sum $\mathrm{Li}_n(z) = \sum_{k=1}^\infty \frac{z^k}{k^n}$ which is often used as the definition of the Polylogarithm. This expression is valid for all complex numbers n and z where $|z| \leq 1$. The definition given in the text is valid for all $z \leq l$.

Special cases: $\mathrm{Li}_0(z) = \frac{1}{1/z-1}$, $\mathrm{Li}_1(z) = -\ln(1-z)$. $f(\mathbf{r}, \mathbf{p})$ can be written as $\pm\mathrm{Li}_0(\pm \exp[\beta(\mu - \frac{\mathbf{p}^2}{2m} - V(\mathbf{r}))])$. When integrating density distributions to obtain column densities, a useful formula is:

$$(22) \qquad \int_{-\infty}^\infty dx\, \mathrm{Li}_n(z\, e^{-x^2}) = \sqrt{\pi}\, \mathrm{Li}_{n+1/2}(z).$$

Limiting values: $\mathrm{Li}_n(z) \stackrel{z \ll 1}{\to} z$ and $-\mathrm{Li}_n(-z) \stackrel{z \to \infty}{\to} \frac{1}{\Gamma(n+1)} \ln^n(z)$.

square of the harmonic oscillator ground state wave function:

$$(26) \qquad n_c(\mathbf{r}) = \frac{N_0}{\pi^{3/2} d_x d_y d_z} e^{-\sum_i x_i^2/d_{x_i}^2}$$

where $d_{x_i} = \sqrt{\frac{\hbar}{m\omega_{x_i}}}$ are the harmonic oscillator lengths. The density profile of the thermal, non-condensed component can be obtained from Eq. 20 if the chemical potential μ is known. As the number of condensed bosons N_0 grows to be significantly larger than 1, the chemical potential $\mu \approx -\frac{k_B T}{N_0}$ (from Eq. 17 for $E_0 = 0$) will be much closer to the ground state energy than the first excited harmonic oscillator state. Thus we set $\mu = 0$ in the expression for the non-condensed density n_{th} and number N_{th} and obtain

$$(27) \qquad n_{th}(\mathbf{r}) = \frac{1}{\lambda_{dB}^3} \mathrm{Li}_{3/2}(e^{-V(\mathbf{r})/k_B T})$$

$$(28) \qquad N_{th} = N(T/T_C)^3 \qquad \text{for } T < T_C$$

with the critical temperature for Bose-Einstein condensation in a harmonic trap

$$(29) \qquad T_C \equiv \hbar\bar{\omega}\, (N/\zeta(3))^{1/3} = 0.94\, \hbar\bar{\omega} N^{1/3}$$

where $\zeta(3) = \mathrm{Li}_3(1) \approx 1.202$. At $T = T_C$, the condition for Bose condensation is fulfilled in the center of the trap, $n = \mathrm{Li}_{3/2}(1)/\lambda_{dB}^3 = 2.612/\lambda_{dB}^3$. For lower temperatures, the maximum density of the thermal cloud is "quantum saturated" at the critical value $n_{th} = 2.612/\lambda_{dB}^3 \propto T^{3/2}$. The condensate fraction in a harmonic trap is given by

$$(30) \qquad N_0/N = 1 - (T/T_C)^3$$

For $T/T_C = 0.5$ the condensate fraction is already about 90%.

For **fermions**, the occupation of available phase space cells smoothly approaches unity without any sudden transition:

$$(31) \qquad f(\mathbf{r}, \mathbf{p}) = \frac{1}{e^{(\frac{\mathbf{p}^2}{2m}+V(\mathbf{r})-\mu)/k_B T} + 1} \overset{T\to 0}{\longrightarrow} \begin{cases} 1, & \frac{\mathbf{p}^2}{2m} + V(\mathbf{r}) < \mu \\ 0, & \frac{\mathbf{p}^2}{2m} + V(\mathbf{r}) > \mu \end{cases}$$

Accordingly, also the density profile changes smoothly from its gaussian form at high temperatures to its zero temperature shape:

$$n_F(\mathbf{r}) = \int \frac{\mathrm{d}^3\mathbf{p}}{(2\pi\hbar)^3} f(\mathbf{r}, \mathbf{p}) \overset{T\to 0}{\longrightarrow} \int_{|\mathbf{p}|<\sqrt{2m(\mu-V(\mathbf{r}))}} \frac{\mathrm{d}^3\mathbf{p}}{(2\pi\hbar)^3}$$

$$(32) \qquad = \frac{1}{6\pi^2} \left(\frac{2m}{\hbar^2}\right)^{3/2} (\mu - V(\mathbf{r}))^{3/2}.$$

From Eq. 31 we observe that at zero temperature, μ is the energy of the highest

53

occupied state of the non-interacting Fermi gas, also called the Fermi energy E_F. The (globally) largest momentum is $p_F \equiv \hbar k_F \equiv \sqrt{2mE_F}$, the Fermi momentum. *Locally*, at position $\mathbf{r}$ in the trap, it is $p_F(\mathbf{r}) \equiv \hbar k_F(\mathbf{r}) \equiv \sqrt{2m\epsilon_F(\mathbf{r})} \equiv \hbar(6\pi^2 n_F(\mathbf{r}))^{1/3}$ with the local Fermi energy $\epsilon_F(\mathbf{r})$ which equals $\mu(\mathbf{r}, T = 0) = E_F - V(\mathbf{r})$. The value of E_F is fixed by the number of fermions N, occupying the N lowest energy states of the trap. For a harmonic trap we obtain

$$N = \int \mathrm{d}^3\mathbf{r}\, n_F(\mathbf{r}) = \frac{1}{6}\left(\frac{E_F}{\hbar\bar{\omega}}\right)^3$$

(33)
$$\Rightarrow E_F = \hbar\bar{\omega}(6N)^{1/3}$$

and for the zero-temperature profile

(34)
$$n_F(\mathbf{r}) = \frac{8}{\pi^2}\frac{N}{R_{Fx}R_{Fy}R_{Fz}}\left[\max\left(1 - \sum_i \frac{x_i^2}{R_{Fi}^2}, 0\right)\right]^{3/2}$$

with the Fermi radii $R_{Fx,y,z} = \sqrt{\frac{2E_F}{m\omega_{x,y,z}^2}}$. The profile of the degenerate Fermi gas has a rather flat top compared to the gaussian profile of a thermal cloud, as the occupancy of available phase space cells saturates at unity.

At finite $T \lesssim T_F$, we can understand the shape of the cloud by comparing $k_B T$ with the local Fermi energy $\epsilon_F(\mathbf{r})$. For the outer regions in the trap where $k_B T \gg \epsilon_F(\mathbf{r})$, the gas shows a classical (Boltzmann) density distribution $n(\mathbf{r}) \propto e^{-\beta V(\mathbf{r})}$. In the inner part of the cloud where $k_B T \ll \epsilon_F(\mathbf{r})$, the density is of the zero-temperature form $n(\mathbf{r}) \propto (E_F - V(\mathbf{r}))^{3/2}$. The Polylogarithm smoothly interpolates between the two regimes. We notice here the difficulty of thermometry for very cold Fermi clouds: Temperature only affects the far wings of the density distribution. While for thermal clouds above T_F, the size of the cloud is a direct measure of temperature, for cold Fermi clouds one needs to extract the temperature from the shape of the distribution's wings.

Note that the validity of the above derivation required the Fermi energy E_F to be much larger than the level spacing $\hbar\omega_{x,y,z}$. For example, in very elongated traps and for low atom numbers one can have a situation where this condition is violated in the tightly confining radial dimensions.

3˙1.2. Trapped, interacting Fermi mixtures at zero temperature. We now consider the case of N fermionic atoms equally populating two hyperfine states ("spin up" and "spin down"). Atoms in different spin states interact via s-wave collisions characterized by the scattering length a. A dimensionless parameter measuring the strength and sign of the interaction strength is $1/k_F a$, essentially the ratio of the interparticle spacing to the scattering length. For weak attractive interactions, $1/k_F a \to -\infty$, the ground state of the system is a BCS superfluid (see chapter **4**). As the magnitude of the scattering length increases to a point where $a \to \mp\infty$ diverges (thus $1/k_F a \to 0$), a two-body molecular bound state enters the interparticle potential. For weak repulsive interactions,
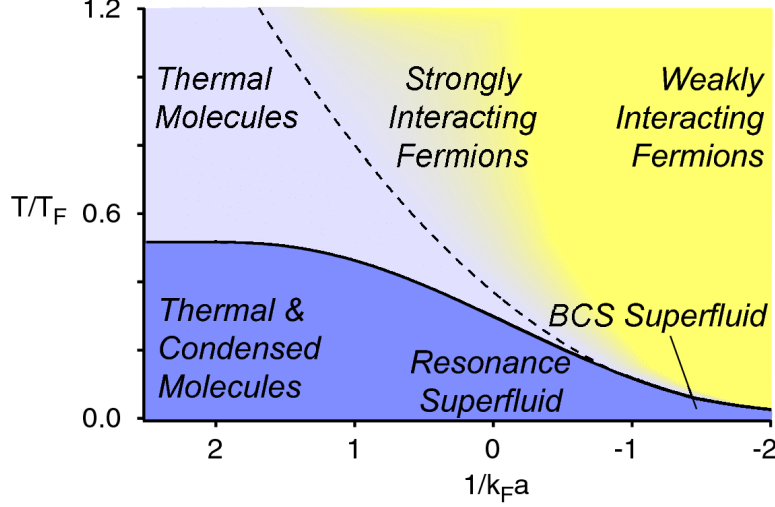
Fig. 14. – Phase diagram of interacting Fermi mixtures in a harmonic trap, as a function of temperature and interaction strength $1/k_F a$. Shown is the critical temperature T_C for the formation of a superfluid as a function of $1/k_F a$ (full line) as well as the characteristic temperature T^* at which fermion pairs start to form (dashed line), after [168]. The shading indicates that pair formation is a smooth process, not a phase transition.

$1/k_F a \rightarrow +\infty$, the ground state of the system is then a Bose-Einstein condensate of weakly-interacting molecules of mass $M = 2m$, in which two fermions of opposite spin are tightly bound.

Fig. 14 summarizes the different regimes within this BEC-BCS crossover. We see that the character of the Fermi mixture drastically changes as a function of temperature and interaction strength. For temperatures $T \gg T^*$ fermions are unpaired, and a free Fermi mixture exists on the BEC- and the BCS-side of the phase diagram. On resonance, the mixture might still be strongly interacting even at high temperatures, thus possibly requiring an effective mass description of the interacting gas. The density distribution will have the same shape as a free Fermi gas at all interaction strengths. Below T^*, fermion pairs start to form. On the BEC-side, where fermions are tightly bound, the thermal distribution should now be that of a gas of bosons with mass $M = 2m$. As a consequence, the cloud will shrink. Below T_C, we will finally observe a superfluid, condensed core, surrounded by a thermal cloud of molecules in the BEC-limit, or of unpaired fermions in the BCS-limit.

In general, the calculation of density distributions in the strongly interacting regime is a difficult affair. Simple expressions for the densities can be derived for superfluid gases at zero temperature, for molecular gases on the "BEC"-side at large and positive $1/k_F a$, for weakly interacting Fermi gases on the "BCS"-side for large and negative $1/k_F a$, and in the classical limit at high temperatures.

55

BEC limit. The molecular Bose-Einstein condensate is described by a many-body wave function $\psi(\mathbf{r})$ which obeys the Gross-Pitaevskii equation [169]

$$(35) \qquad \left(-\frac{\hbar^2 \nabla^2}{2M} + V_M(\mathbf{r}) + g \left| \psi(\mathbf{r}, t) \right|^2 \right) \psi(\mathbf{r}, t) = i\hbar \frac{\partial}{\partial t} \psi(\mathbf{r}, t)$$

where $V_M(\mathbf{r})$ is the trapping potential experienced by the molecules, and $g = \frac{4\pi\hbar^2 a_M}{M}$ describes the intermolecular interactions. We can identify $|\psi|^2$ with the condensate density n_c, which for weak interactions and at zero temperature equals the density of molecules n_M. The validity of Eq. 35 is limited to *weakly interacting* gases of molecules, for which the gas parameter $n_M a_M^3 \approx (\frac{k_F a}{6.5})^3 \ll 1$. In typical experiments on BECs of bosonic atoms, the corresponding condition is very well fulfilled. For a sodium BEC with $n \approx 10^{14} \, \text{cm}^{-3}$ and $a = 3.3 \, \text{nm}$, we have $na^3 \approx 4 \cdot 10^{-6}$. However, for molecular condensates near a Feshbach resonance, this condition can be easily violated (see chapter **6**).

In equilibrium, the ground-state wave function is $\psi(\mathbf{r}, t) = e^{-i\mu_M t/\hbar} \psi(\mathbf{r})$, where μ_M is the ground state energy and is identified with the molecular chemical potential, and $\psi(\mathbf{r})$ is a solution of the stationary Gross-Pitaevskii equation

$$(36) \qquad \left(-\frac{\hbar^2 \nabla^2}{2M} + V_M(\mathbf{r}) + g \left| \psi(\mathbf{r}) \right|^2 \right) \psi(\mathbf{r}) = \mu_M \psi(\mathbf{r})$$

In the *ideal gas limit*, $gn_c \ll \hbar\omega_{x,y,z}$, we recover the harmonic oscillator result for the condensate's density distribution $n_c(\mathbf{r})$. In the *Thomas-Fermi limit*, on the other hand, interactions dominate over the kinetic energy of the condensate wave function, $gn_c \gg \hbar\omega_{x,y,z}$. Already for weakly interacting alkali gases, this condition is very well fulfilled, with typical interaction energies of $gn_c \sim k_B \times 150 \, \text{nK}$ and $\hbar\omega_r \approx k_B \times 5 \, \text{nK}$. In this approximation we obtain the condensate density $n_c(\mathbf{r}) = |\psi(\mathbf{r})|^2$:

$$(37) \qquad n_c(\mathbf{r}) = \max \left(\frac{\mu_M - V_M(\mathbf{r})}{g}, 0 \right)$$

Thus, a condensate in the Thomas-Fermi approximation "fills in" the bottom of the trapping potential up to an energy μ_M, which is determined by the total number of molecules, $N_M = N/2 = \int \mathrm{d}^3\mathbf{r} \, n_c(\mathbf{r})$. Taking $V_M(\mathbf{r}) = 2V(\mathbf{r})$ with the harmonic trapping potential for single atoms in Eq. 18, one obtains a parabolic density profile,

$$(38) \qquad n_c(\mathbf{r}) = \frac{15}{8\pi} \frac{N_M}{R_x R_y R_z} \max \left(1 - \sum_i \frac{x_i^2}{R_i^2}, 0 \right)$$

where the *Thomas-Fermi radii* $R_i = \sqrt{\frac{2\mu_M}{M\omega_i^2}}$ give the half-lengths of the trapped conden-

sate where the density vanishes. The chemical potential is given by

$$(39) \qquad \mu_M = \frac{1}{2} \hbar \bar{\omega} \left(\frac{15 N_M a_M}{\bar{d}_{h.o.}} \right)^{2/5}$$

where $\bar{d}_{h.o.} = (d_x d_y d_z)^{1/3} = \sqrt{\hbar/M\bar{\omega}}$ is the geometric mean of the harmonic oscillator lengths for molecules.

Interactions thus have a major effect on the shape of the Bose-Einstein condensate, changing the density profile from the gaussian harmonic oscillator ground state wave function to a broad parabola, as a result of the interparticle repulsion. The characteristic size of the condensate is no longer given by the harmonic oscillator length but by the generally much larger Thomas-Fermi radius $R_{x,y,z} = d_{x,y,z} \sqrt{\frac{\bar{\omega}}{\omega_{x,y,z}}} \left(\frac{15 N_M a_M}{\bar{d}_{h.o.}} \right)^{1/5}$. Also the aspect ratio changes, for example in the x-y plane from $\frac{d_x}{d_y} = \sqrt{\frac{\omega_y}{\omega_x}}$ to $\frac{R_x}{R_y} = \frac{\omega_y}{\omega_x}$. Nevertheless, weakly interacting condensates are still considerably smaller in size than a thermal cloud at $k_B T > \mu_M$, and more dense. This leads to the clear separation between the dense condensate in the center of the cloud and the large surrounding thermal cloud, the "smoking gun" for Bose-Einstein condensation (both in the trapped and in the expanding cloud, see section **3**˙2 below). In the case of strong interactions, when the chemical potential μ_M becomes comparable to $k_B T_C$, this direct signature of condensation will be considerably weaker. In this regime we also have to account for the mutual repulsion between the thermal cloud and the condensate (see section **3**˙3.3 below).

BCS limit. In the weakly interacting BCS limit ($1/k_F a \to -\infty$), pairing of fermions and superfluidity have very small effects on the density profile of the gas. The sharp Fermi surface in k-space at k_F is modified only in an exponentially narrow region of width $\sim k_F \exp(-\frac{\pi}{2k_F|a|})$. The density, i.e. the integral over occupied k-states, is thus essentially identical to that of a non-interacting Fermi gas. The result is Eq. 34 with the number of spin-up (spin-down) atoms $N_{\uparrow,\downarrow} = N/2$ and Fermi energy $E_F = \hbar\bar{\omega}(6N_{\uparrow,\downarrow})^{1/3} = \hbar\bar{\omega}(3N)^{1/3}$. As one approaches the strongly interacting regime $1/k_F a \approx -1$, it is conceivable that the formation of the superfluid leaves a distinct trace in the density profile of the gas, as this is the situation in the BEC-limit, and the crossover between the two regimes is smooth. Indeed, several theoretical studies have predicted kinks in the density profiles signalling the onset of superfluidity [170, 168, 45, 171]. We were able to observe such a direct signature of condensation on resonance ($1/k_F a = 0$) and on the BCS-side ($1/k_F a < 0$) in unequal Fermi mixtures (see section **7**˙3.2). In equal mixtures, we detected a faint but distinct deviation from the Thomas-Fermi profile on resonance (see **6**˙5.1).

Unitarity. The regime on resonance ($1/k_F a = 0$) deserves special attention. The scattering length diverges and leaves the interparticle distance $n^{-1/3} \sim 1/k_F$ as the only relevant length scale. Correspondingly, the only relevant energy scale is the Fermi en-

$\frac{1}{k_F a}$	BEC-limit ∞	Unitarity 0	BCS-limit $-\infty$
γ (in $\mu \propto n^\gamma$)	1	$2/3$	$2/3$
$n_\uparrow(\mathbf{r})/n_\uparrow(\mathbf{0})$	$1-\sum_i \frac{x_i^2}{R_i^2}$	$(1-\sum_i \frac{x_i^2}{R_{Ui}^2})^{3/2}$	$(1-\sum_i \frac{x_i^2}{R_{Fi}^2})^{3/2}$
$n_\uparrow(\mathbf{0})$	$\frac{15}{8\pi}\frac{N_\uparrow}{R_x R_y R_z}$	$\frac{8}{\pi^2}\frac{N_\uparrow}{R_{Ux}R_{Uy}R_{Uz}}$	$\frac{8}{\pi^2}\frac{N_\uparrow}{R_{Fx}R_{Fy}R_{Fz}}$
Radii	$R_i=\sqrt{\frac{2\mu M}{M\omega_i^2}}$	$R_{Ui}=\xi^{1/4}R_{Fi}$	$R_{Fi}=\sqrt{\frac{2E_F}{m\omega_i^2}}$

TABLE IV. – *Zero-temperature density profiles of a trapped, interacting Fermi mixture in the BEC-BCS crossover. The density is zero when the expressions are not positive. For definitions see the text.*

ergy $\epsilon_F = \hbar^2 k_F^2/2m$. The regime is thus said to be universal. The chemical potential μ can then be written as a universal constant times the Fermi energy: $\mu = \xi\epsilon_F$. In the trapped case, we can use this relation locally (local density approximation) and relate the local chemical potential $\mu(\mathbf{r}) = \mu - V(\mathbf{r})$ to the local Fermi energy $\epsilon_F(\mathbf{r}) \equiv \hbar^2 k_F(\mathbf{r})^2/2m \equiv \frac{\hbar^2}{2m}(6\pi^2 n_\uparrow(\mathbf{r}))^{2/3}$, where $n_\uparrow(\mathbf{r})$ is the density of atoms in one spin state. We then directly obtain a relation for the density profile $n_{\uparrow U}(\mathbf{r})$ of the unitary Fermi gas:

$$n_{\uparrow U}(\mathbf{r}) = \frac{1}{6\pi^2}\left(\frac{2m}{\xi\hbar^2}\right)^{3/2}(\mu - V(\mathbf{r}))^{3/2}.$$

The constraint from the number of particles in spin up, $N_\uparrow = N/2$, determines μ:

$$N_\uparrow = \int \mathrm{d}^3\mathbf{r}\, n_{\uparrow U}(\mathbf{r}) = \frac{1}{6}\left(\frac{\mu}{\sqrt{\xi}\hbar\bar{\omega}}\right)^3$$

(40)
$$\Rightarrow \mu = \sqrt{\xi}E_F.$$

The density profile becomes

(41)
$$n_{\uparrow U}(\mathbf{r}) = \frac{8}{\pi^2}\frac{N_\uparrow}{R_{Ux}R_{Uy}R_{Uz}}\left[\max\left(1 - \sum_i \frac{x_i^2}{R_{Ui}^2}, 0\right)\right]^{3/2}$$

with the radii $R_{Ux,y,z} = \xi^{1/4}R_{Fx,y,z}$. Table IV summarizes the various density profiles of interacting Fermi mixtures.

Remarkably, the functional form $n_{\uparrow U}(\mathbf{r}) \propto (\mu - V(\mathbf{r}))^{3/2}$ is identical to that of a non-interacting Fermi gas. The underlying reason is that the equation of state $\mu \propto n^{2/3}$ has the same power-law form as for non-interacting fermions. The universal constant ξ simply rescales the radii (by a factor $\xi^{1/4}$) and the central density (by a factor $\xi^{-3/4}$). One thus has direct experimental access to the universal constant ξ by measuring the size of the cloud at unitarity (see section **7**˙1.1).

3˙2. *Expansion of strongly interacting Fermi mixtures.* – Intriguingly rich physics can be uncovered by the simple release of ultracold gases from their confining trap. From the size of the expanded cloud and the known time-of-flight one directly obtains the energy content of the gas: the temperature in the case of thermal clouds, the Fermi energy for non-interacting degenerate Fermi gases, the mean-field energy for Bose-Einstein condensates. In the case of free ballistic expansion, where no collisions occur during expansion, the density distribution of the expanded cloud directly reveals the original momentum distribution of the particles in the trap. Thermal clouds will become spherical after ballistic expansion, reflecting their isotropic momentum distribution in the trap. The expansion of Bose-Einstein condensates is not ballistic but mean-field driven, leading to superfluid hydrodynamic expansion. As mean-field energy is preferentially released in the direction(s) of tight confinement, this allows for the famous "smoking gun" signature of Bose-Einstein condensation: inversion of the condensate's aspect ratio after expansion out of an anisotropic trap. In strongly interacting gases the normal, uncondensed cloud can be collisionally dense, and will expand according to classical hydrodynamics. As particles will preferentially leave the cloud along the narrower dimensions, where they undergo fewer collisions, this also leads to an inversion of the cloud's initial aspect ratio. It is thus no longer a "smoking gun" for condensation, but merely for strong interactions. Expansion is also useful to measure correlations in momentum space [172]. Finally, in the case of harmonic trapping, expansion of a superfluid cloud can often be described as a "magnifying glass", a mere scaling of the density distribution in the trap. This allows for example to observe quantized vortices [68], which are too small to be observable in the trap. In this section, we show how quantitative information can be derived from images of expanding clouds.

3˙2.1.   Free ballistic expansion. Let us consider the expansion of a non-condensed thermal cloud. If the mean free path λ_c between collisions is longer than the size of the trapped cloud R, we can neglect collisions during expansion, which is hence ballistic. The collision rate is $\Gamma = n\sigma v$, with density n, collisional cross section σ and thermal (root mean square) velocity v, which gives $\lambda_c = v/\Gamma = 1/n\sigma$. As $R = v/\omega$ for a harmonic trap, the condition $\lambda_c \gg R$ is equivalent to having $\Gamma \ll \omega$, that is, the mean time interval between collisions should be larger than a period of oscillation in the trap.

This condition can be fulfilled for the cloud of uncondensed molecules in the BEC limit where $1/k_F a \gg 1$ and collisions are negligible (this has been the case also for atomic BECs with the exception of very large thermal clouds, see [173, 174]), and for the cloud of unpaired fermions in the BEC- and in the BCS-limit for $k_F|a| \ll 1$ (the exact criterion is still $\Gamma \ll \omega$). For molecules with mass M, we need to replace $m \to M$ in the following discussion.

In the ballistic case, a particle initially at point $\mathbf{r}_0$ in the trap, will reach point $\mathbf{r} = \mathbf{r}_0 + \frac{\mathbf{p}_0}{m}t$ after expansion time t. We obtain the density at point $\mathbf{r}$ at time t by adding the contributions from particles at all points $\mathbf{r}_0$ that had the correct initial momentum

$\mathbf{p}_0 = m(\mathbf{r} - \mathbf{r}_0)/t$. In terms of the semi-classical distribution $f(\mathbf{r}, \mathbf{p})$, Eq. 19, this is

$$
\begin{aligned}
n(\mathbf{r}, t) &= \int d^3\mathbf{r}_0 \int \frac{d^3\mathbf{p}_0}{(2\pi\hbar)^3} \, f(\mathbf{r}_0, \mathbf{p}_0) \, \delta\left(\mathbf{r} - \mathbf{r}_0 - \frac{\mathbf{p}_0}{m}t\right) \\
&= \int \frac{d^3\mathbf{p}_0}{(2\pi\hbar)^3} \, f\left(\mathbf{r} - \frac{\mathbf{p}_0}{m}t, \mathbf{p}_0\right) \\
&= \int \frac{d^3\mathbf{p}_0}{(2\pi\hbar)^3} \left\{\exp\left[\beta\frac{\mathbf{p}_0^2}{2m} + \beta V\left(\mathbf{r} - \frac{\mathbf{p}_0}{m}t\right) - \beta\mu\right] \mp 1\right\}^{-1}
\end{aligned}
$$

(42)

The integral can be carried out analytically in the case of a harmonic potential (Eq. 18):

$$
\begin{aligned}
n(\mathbf{r}, t) &= \int \frac{d^3\mathbf{p}_0}{(2\pi\hbar)^3} \left\{\exp\left[\beta\sum_i \left(1 + \omega_i^2 t^2\right)\frac{p_{0i}^2}{2m} + \beta\sum_i \frac{1}{2}m\frac{\omega_i^2 x_i^2}{1 + \omega_i^2 t^2} - \beta\mu\right] \mp 1\right\}^{-1} \\
&= \pm\frac{1}{\lambda_{dB}^3}\prod_i \frac{1}{\sqrt{1 + \omega_i^2 t^2}} \, \text{Li}_{3/2}\left[\pm\exp\left(\beta\mu - \beta\sum_i \frac{1}{2}m\frac{\omega_i^2 x_i^2}{1 + \omega_i^2 t^2}\right)\right]
\end{aligned}
$$

Note that this has the same form as the density distribution in the trap, but with spatial dimension $i = x, y, z$ rescaled by the factor $b_i(t) = \sqrt{1 + \omega_i^2 t^2}$. Ballistic expansion of a thermal (bosonic or fermionic) cloud from a harmonic trap is thus a scaling transformation:

(43)
$$
n(\mathbf{r}, t) = \frac{1}{\mathcal{V}(t)} \, n\left(\frac{x}{b_x(t)}, \frac{y}{b_y(t)}, \frac{z}{b_z(t)}, t = 0\right)
$$

where the unit volume scales as $\mathcal{V}(t) = b_x b_y b_z$. After an expansion time long compared to the trapping periods ($t \gg 1/\omega_i$), we have

(44)
$$
n(\mathbf{r}, t \gg 1/\omega_i) = \pm\frac{1}{\lambda_{dB}^3}\frac{1}{(\bar{\omega}t)^3} \, \text{Li}_{3/2}\left[\pm\exp\left(\beta\mu - \beta\frac{1}{2}m\frac{\mathbf{r}^2}{t^2}\right)\right]
$$

As expected, we obtain an isotropic density profile, reflecting the original isotropic momentum distribution of the trapped gas. Importantly, the *shape* of the density profile, i.e. its variation with $\mathbf{r}$, becomes insensitive to the trapping potential. Eq. 44 thus holds for a general trapping geometry, for expansion times long compared to the longest trapping period. Even if the trapping potential is not known in detail, one can still determine the cloud's temperature and even decide whether the gas is degenerate. Note that the *momentum distribution* at point $\mathbf{r}$ after long expansion times $t \gg 1/\omega_i$ has become

anisotropic:

$$f(\mathbf{r}, \mathbf{p}_0, t) = \int d^3\mathbf{r}_0 \, f(\mathbf{r}_0, \mathbf{p}_0) \, \delta\left(\mathbf{r} - \mathbf{r}_0 - \frac{\mathbf{p}_0}{m}t\right)$$

$$= f\left(\mathbf{r} - \frac{\mathbf{p}_0}{m}t, \mathbf{p}_0\right)$$

$$(45) \qquad \overset{t \gg 1/\omega_i}{\to} = \left(\exp\left[\beta\left(\sum_i \omega_i^2 t^2 \frac{(p_{0i} - m\frac{x_i}{t})^2}{2m} + \frac{1}{2}m\frac{\mathbf{r}^2}{t^2} - \mu\right)\right] \mp 1\right)^{-1}$$

The momentum distribution at point $\mathbf{r}$ is ellipsoidal, centered at $\bar{\mathbf{p}} = m\frac{\mathbf{r}}{t}$, and with characteristic widths $\Delta p_i \propto m\frac{\Delta x_i}{t} \propto \frac{1}{\omega_i}$ directly mirroring the ellipsoidal atomic distribution in the trap.

Ballistic expansion into a saddle potential. In many experiments, atoms are released from an optical trap, but magnetic fields (Feshbach fields) are still left on. In general, these magnetic fields are inhomogeneous, either due to technical limitations, or deliberately, e.g. in case of the optical-magnetic hybrid trap discussed in section **2**˙2.2. We focus here on the important case of a magnetic field created by pair of coils which generates a saddle point potential.

So we assume that at $t > 0$, the gas is not released into free space, but into a new potential. We define $V(\mathbf{r}, t > 0) = \frac{1}{2}m\left(\omega_{Sx}^2 x^2 + \omega_{Sz}^2 y^2 + \omega_{Sz}^2 z^2\right)$, and can describe expansion into anticonfining potentials with imaginary frequencies. For example, for the magnetic saddle potentials relevant for the MIT experiments, the radial dimension is anticonfining and $\omega_{Sx,y} = i\frac{1}{\sqrt{2}}\omega_{Sz}$. In the potential $V(\mathbf{r}, t > 0)$, particles with initial position $\mathbf{r}_0$ and momentum $\mathbf{p}_0$ will reach the point $\mathbf{r}$ with $x_i = \cos(\omega_{Si}t)x_{0i} + \frac{1}{\omega_{Si}}\sin(\omega_{Si}t)\frac{p_{0i}}{m}$ after expansion time t. The calculation of the density profile is fully analogous to the case of free expansion, after the change of variables $x_{0i} \to \tilde{x}_{0i}/\cos(\omega_{Si}t)$ and the substitution $t \to \sin(\omega_{Si}t)/\omega_{Si}$. We again obtain a scaling transformation, Eq. 43, but for this case with scaling parameters $b_i(t) = \sqrt{\cos^2(\omega_{Si}t) + \frac{\omega_i^2}{\omega_{Si}^2}\sin^2(\omega_{Si}t)}$. For expansion into the magnetic saddle potential, this gives $b_\perp(t) = \sqrt{\cosh^2(\frac{1}{\sqrt{2}}\omega_{Sz}t) + \frac{2\omega_\perp^2}{\omega_{Sz}^2}\sinh^2(\frac{1}{\sqrt{2}}\omega_{Sz}t)}$ and $b_z(t) = \sqrt{\cos^2(\omega_{Sz}t) + \frac{\omega_z^2}{\omega_{Sz}^2}\sin^2(\omega_{Sz}t)}$. For the MIT trap, the initial axial trapping potential is dominated by the magnetic field curvature, while the initial radial potential is almost entirely due to the optical trap. After switching off the optical trap, we have $\omega_{Sz} = \omega_z$ and $\omega_{Sx} = i\frac{1}{\sqrt{2}}\omega_z$. In this case, $b_z(t) = 1$ and the cloud expands only into the radial direction.

3˙2.2. Collisionally hydrodynamic expansion. If the mean free path λ_c is short compared to the cloud size, the gas is in the hydrodynamic regime, and collisions during expansion can no longer be neglected. Collisions will tend to reestablish local thermal equilibrium, in particular an isotropic momentum distribution. For anisotropic traps,

this directly leads to anisotropic expansion, in strong contrast to the ballistic case: Particles trying to escape in one direction suffer collisions that redistribute their momenta equally in all directions. The escape is hindered more for the weakly confined directions where the cloud is long initially and particles can undergo more collisions. For cylindrically symmetric clouds, this leads to an inversion of the aspect ratio of the cloud during expansion.

Hydrodynamic expansion can take place for $1/k_F|a| < 1$, which includes (for $a > 0$) strongly interacting clouds of uncondensed molecules, and (for $a < 0$) a strongly interacting, normal Fermi mixture. There is no sharp boundary between molecular hydrodynamics and fermionic hydrodynamics, since $1/k_F|a| < 1$ is the strongly interacting regime where many-body physics dominates and the single-particle description (molecules in one limit, unbound fermions in the other) is no longer valid.

In the hydrodynamic regime, the evolution of the gas is governed by the continuity equation for the density $n(\mathbf{r}, t)$ and, neglecting friction (viscosity), the Euler equation for the velocity field $\mathbf{v}(\mathbf{r}, t)$:

$$(46) \qquad \frac{\partial n}{\partial t} + \nabla \cdot (n\mathbf{v}) = 0$$

$$(47) \qquad m\frac{d\mathbf{v}}{dt} = m\frac{\partial \mathbf{v}}{\partial t} + m(\mathbf{v} \cdot \nabla)\mathbf{v} = -\nabla V(\mathbf{r}, t) - \frac{1}{n}\nabla P(\mathbf{r}, t)$$

where P is the pressure. Friction is negligible deep in the hydrodynamic regime, when the mean free path approaches zero. The Euler equation is simply Newton's law for the collection of gas particles at $\mathbf{r}$. In steady state, we recover the equilibrium solution

$$(48) \qquad \nabla P_0(\mathbf{r}) = n_0(\mathbf{r})\nabla\mu_0(\mathbf{r}) = -n_0(\mathbf{r})\nabla V(\mathbf{r}, 0)$$

where we have used the expression for the local chemical potential $\mu_0(\mathbf{r}) = \mu - V(\mathbf{r})$.

Scaling solution for harmonic potentials. In the case of free expansion, the potential $V(\mathbf{r}, t)$ is the initial harmonic trapping potential for $t < 0$, with radial and axial trapping frequencies $\omega_\perp(0)$ and $\omega_z(0)$, and zero for $t > 0$. We can more generally consider here an arbitrary time variation $\omega_\perp(t)$ and $\omega_z(t)$ of the trapping frequencies. For this case, the Euler equation allows a simple scaling solution for the coordinates and velocities [175]

$$x_i(t) = b_i(t)\, x_{0i}$$
$$(49) \qquad v_i(t) = \frac{\dot{b}_i}{b_i}\, x_i(t)$$

with initial conditions $b_i(0) = 1$ and $\dot{b}_i(0) = 0$. The unit volume scales as $\mathcal{V}(t) = b_x\, b_y\, b_z$, the density varies as $n(\mathbf{r}, t) = n_0(\mathbf{r}_0)/\mathcal{V}$, where the fluid element at initial position $\mathbf{r}_0$ has propagated to $\mathbf{r}$ at time t.

Pressure. The thermodynamic properties of a simple fluid or gas only depend on three variables, that are, in the grand canonical description, the temperature T, the chemical potential μ and the volume V. From the grand canonical partition function Z, one obtains in this case the pressure $P = k_B T \frac{\ln Z}{V}$. For a non-interacting, ideal gas of bosons or fermions, the average energy is $E = \frac{3}{2} k_B T \ln Z$, leading to the relation $PV = \frac{2}{3} E$. This equation is no longer true for an interacting gas, for example the van der Waals gas. It is very remarkable, then, that this relation nevertheless holds also for the strongly interacting, unitary gas on resonance, for all temperatures [45, 176] ([6]). Under an adiabatic expansion, the energy E changes according to $dE = -PdV$. Hence $\frac{3}{2} d(PV) = \frac{3}{2}(VdP + PdV) = -PdV$, which leads to the law $PV^{5/3} = \text{const}$ for adiabatic expansion. The pressure thus scales as $\mathcal{V}^{-5/3}$, and the force, using Eq. 48,

$$-\frac{1}{n}\frac{\partial}{\partial x_i}P(\mathbf{r},t) = -\frac{\mathcal{V}}{n_0}\frac{1}{b_i}\frac{\partial}{\partial x_{0i}}\frac{P_0(\mathbf{r}_0)}{\mathcal{V}^{5/3}} = \frac{1}{b_i \mathcal{V}^{2/3}}\frac{\partial}{\partial x_{i0}}V(\mathbf{r}_0,0)$$

(50)
$$= \frac{1}{b_i \mathcal{V}^{2/3}}m\omega_i^2(0)x_{i0}$$

The Euler equations then reduce to equations for the scaling parameters $b_i(t)$, which can be solved numerically:

(51)
$$\ddot{b}_i = -\omega_i^2(t)\,b_i + \frac{\omega_i^2(0)}{b_i \mathcal{V}^{2/3}}$$

In the following section we will see that superfluid hydrodynamics leads to very similar scaling equations, with the exponent $2/3$ for the volume scaling parameter $\mathcal{V}$ replaced by the parameter γ in the equation of state of the superfluid $\mu(n) = n^\gamma$. The discussion of free expansion, the long-time behavior, inversion of the aspect ratio etc. will be identical for superfluid hydrodynamics, so we defer the topic until the next section.

From ballistic to hydrodynamic expansion. The regime in between ballistic, collisionless expansion and pure hydrodynamic, collisional expansion can be treated approximately. For the effects of interactions on a classical gas, see [177, 178], for the case of Fermi gases with attractive interactions, see [179].

3˙2.3. Superfluid hydrodynamic expansion. In the simplest (scalar) case, a superfluid is described by a macroscopic, complex order parameter $\psi(\mathbf{r},t) = \sqrt{n(\mathbf{r},t)}e^{i\phi(\mathbf{r},t)}$ parameterized by the *superfluid density* $n(\mathbf{r},t)$ and a phase $\phi(\mathbf{r},t)$. The dynamics of the order

---

([6]) On resonance, universality requires that the energy $E = N\epsilon_F f(T/T_F)$ with a universal function f. Entropy can only be a function of T/T_F, so adiabaticity requires this ratio to be constant. The pressure is then $P = -\partial E/\partial V|_{S,N} = -Nf(T/T_F)\partial\epsilon_F/\partial V = \frac{2}{3}E/V$.

parameter are well described by a time-dependent Schrödinger equation of the type

$$(52) \qquad i\hbar \frac{\partial}{\partial t}\psi(\mathbf{r}, t) = \left(-\frac{\hbar^2}{2m}\nabla^2 + V(\mathbf{r}, t) + \mu(n(\mathbf{r}, t)) \right) \psi(\mathbf{r}, t)$$

where $\mu(n)$ is the chemical potential given by the equation of state of the superfluid. In the case of weakly interacting BECs, this is the Gross-Pitaevskii equation for the condensate wave function from section **3**˙1.2. For fermionic superfluids, a formally similar equation is the Ginzburg-Landau equation, which is however valid only close to T_C. Rewriting Eq. 52 in terms of the superfluid density n and velocity $\mathbf{v}$, neglecting the curvature $\nabla^2 \sqrt{n}$ of the magnitude of ψ and using the fact that the superfluid is irrotational $\nabla \times \mathbf{r} = 0$, we arrive again at the continuity equation and the Euler equation for classical inviscous flow:

$$(53) \qquad \frac{\partial n}{\partial t} + \nabla \cdot (n\mathbf{v}) = 0$$

$$(54) \qquad m\frac{\partial \mathbf{v}}{\partial t} + m(\mathbf{v} \cdot \nabla)\mathbf{v} = -\nabla\left(V + \mu(n)\right)$$

The validity of these hydrodynamic equations is restricted to superfluids whose healing length is much smaller than the sample size and thus, for fermionic superfluids in a harmonic trap, for a superfluid gap larger than the harmonic oscillator energies $\hbar\omega_{x,y,z}$ [179]. For a power-law equation of state $\mu(n) \propto n^\gamma$, the equations allow a scaling solution for (possibly time-varying) harmonic potentials. The scaling parameters $b_i(t)$ are given by the differential equations [180, 175, 179, 181]

$$(55) \qquad \ddot{b}_i = -\omega_i^2(t)\,b_i + \frac{\omega_i^2(0)}{b_i \mathcal{V}^\gamma}$$

Important limiting cases in the BEC-BCS crossover are:

- BEC-limit $(1/k_F a \gg 1)$: Here, the mean-field repulsion between molecules leads to a chemical potential per fermion $\mu(n) = \frac{\pi\hbar^2 a_M n}{m}$, so $\gamma = 1$.

- BCS-limit $(1/k_F a \ll -1)$: In the BCS-limit, the dominant contribution to the chemical potential comes from the kinetic energy of the constituent fermions, given by the Fermi energy. So here $\mu(n) = \epsilon_F \propto n^{2/3}$ and $\gamma = 2/3$.

- Unitarity limit $(1/k_F a = 0)$: In the unitarity limit, the only remaining energy scale is the Fermi energy. One necessarily has $\mu(n) \propto \epsilon_F \propto n^{2/3}$ and $\gamma = 2/3$, just as in the BCS-limit.

Note that the scaling laws for the BCS- and the unitarity limit [182] are identical to those found for a collisionally hydrodynamic gas in section **3**˙2.2. For a derivation of superfluid hydrodynamics in the BCS-limit, we refer the reader to the contribution of Y. Castin to these lecture notes.
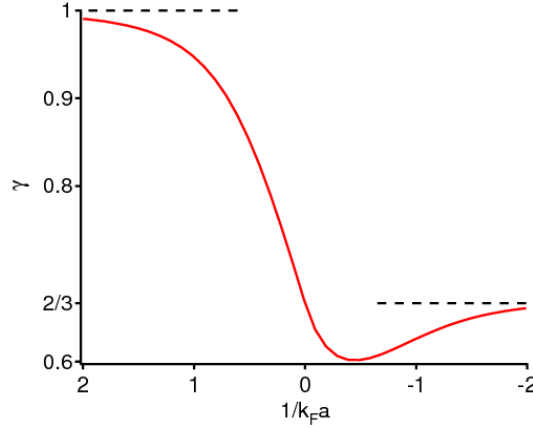
Fig. 15. – The exponent γ as a function of the interaction parameter $1/k_F a$. γ approximately describes the superfluid equation of state $\mu(n) \sim n^\gamma$ in the BEC-BCS crossover. A similar figure can be found in [181].

The Leggett ansatz (see section 4˙4) allows to interpolate between the BEC- and the BCS-regime and gives a chemical potential $\mu(n)$ that correctly captures the physics in the two limits. With its help, we can define an effective exponent $\gamma = \frac{n}{\mu} \frac{\partial \mu}{\partial n}$ and write $\mu(n) \simeq n^\gamma$, assuming that γ varies slowly with the interaction parameter $1/k_F a$. This exponent, shown in Fig. 15, attains the correct limiting values in the BEC- and the BCS-limit, as well as on resonance, so we may use it for the present purpose as an approximate description of the gas' equation of state throughout the crossover.

In-trap density profile. The in-trap density profile of the superfluid at zero temperature can be deduced from the Euler equations in steady state. Neglecting kinetic energy $\frac{1}{2} m \mathbf{v}^2$ (Thomas-Fermi approximation), the equation simply reads $V(\mathbf{r}) + \mu(n(\mathbf{r})) = $ const. $= \mu(n(\mathbf{0}))$. For the power-law equation of state $\mu(n) \propto n^\gamma$, we directly obtain

(56) $$n(\mathbf{r}) \propto (\mu(n(\mathbf{0})) - V(\mathbf{r}))^{1/\gamma}$$

for $\mu(n(\mathbf{0})) > V(\mathbf{r})$ and zero otherwise. For a BEC and harmonic trapping, we recover the inverted parabola, Eq. 38, for a BCS superfluid in the limit of weak interactions the density distribution of an ideal Fermi gas, Eq. 34. Note that in the crossover $1/k_F |a| \lesssim 1$, the correct calculation of the density profile is less straightforward, as the parameter $1/k_F(\mathbf{r})a$ depends on position, and the equation of state varies across the cloud. The power-law approach, using a fixed $\gamma = \gamma(1/k_F(\mathbf{0})a)$, will only provide an approximate description. Fortunately, on resonance evidently $1/k_F(\mathbf{r})a = 0$ across the entire cloud, and the power-law equation of state becomes exact at $T = 0$.

65

Free expansion out of a cylindrically symmetric trap. In this case $\omega_i(t > 0) = 0$, and $\omega_x(0) = \omega_y(0) \equiv \omega_\perp$. We have

$$(57) \qquad \ddot{b}_\perp = \frac{\omega_\perp^2}{b_\perp^{2\gamma+1} b_z^\gamma}$$

$$(58) \qquad \ddot{b}_z = \frac{\omega_z^2}{b_\perp^{2\gamma} b_z^{\gamma+1}}$$

The MIT trap is cigar-shaped, with an aspect ratio of short to long axes $\epsilon = \omega_z/\omega_\perp \ll 1$. In such a case, expansion is fast in the radial, initially tightly confined dimensions, whereas it is slow in the z-direction. For times short compared to $\tau_\epsilon = \frac{1}{\omega_z \epsilon}$, many axial trapping periods, we can set $b_z \approx 1$ on the right side of Eqs. 57 and 58, decoupling the transverse from the axial expansion. For $\gamma = 1$, the case of a Bose-Einstein condensate of tightly bound molecules, the simplified equations for $t \ll \tau_\epsilon$ have an analytic solution [180, 175]: $b_\perp(t) = \sqrt{1 + \omega_\perp^2 t^2}$ and $b_z(t) = 1 + \epsilon^2 \left(\omega_\perp t \arctan(\omega_\perp t) - \ln \sqrt{1 + \omega_\perp^2 t^2} \right)$. For long times t, the expansion is linear in time: $b_\perp(t) = \omega_\perp t$ for $t \gg 1/\omega_\perp$ and $b_z(t) = (\pi/2)\epsilon^2 \omega_\perp t$ for $t \gg \tau_\epsilon$. Note that the radial expansion accidentally follows the same scaling law as that of a ballistically expanding normal cloud.

The general behavior of the expanding gas is the same for all relevant γ. Driven either by repulsive interactions (BEC-case) or by kinetic energy (BCS-case), the gas first expands radially at constant acceleration $\ddot{R}_\perp(t \ll 1/\omega_\perp) = R_\perp(0)\omega_\perp^2$, and over a radial trapping period reaches a final expansion velocity $\dot{R}(t \gg 1/\omega_\perp) \approx \omega_\perp R_\perp(0)$. The axial size grows as $b_z(t) - 1 \approx \epsilon^2 \omega_\perp t$, leading to an inversion of the cloud's aspect ratio from initially ϵ to $\sim 1/\epsilon$. This inversion is in contrast to the isotropic aspect ratio of a ballistically expanding gas, and is thus characteristic for hydrodynamic expansion, which can be of collisional *or* of superfluid origin. Fig. 16 and table V summarize the time evolution of the cloud's radii and aspect ratios for $\gamma = 1$ (BEC) and $\gamma = 2/3$ (BCS and Unitarity), while Fig. 17 compares the long-time behavior of the velocities and aspect ratios across the BEC-BCS crossover. For expansion out of an elongated cigar-shaped trap and $\gamma = 2/3$, which holds in the BCS-limit, at unitarity, but also for a collisionally hydrodynamic gas, the asymptotic expansion velocity is $v_\perp = \sqrt{\frac{3}{2}}\omega_\perp R_\perp(0) \approx 1.22\, \omega_\perp R_\perp(0)$. This can be understood by noting that the cloud's kinetic energy, initially distributed isotropically, is released only into the radial direction during hydrodynamic expansion, so $\frac{1}{2}mv_\perp^2 = \frac{3}{2}\mu = \frac{3}{4}m\omega_\perp^2 R_\perp(0)^2$.

Hydrodynamic expansion into a saddle potential. As discussed in section **3**.2.1, expansion may not occur into free space, but into an inhomogeneous magnetic field which is often described by a saddle potential.

The Euler equations (55) now read for $t > 0$

$$(59) \qquad \ddot{b}_i = -\omega_{S,i}^2\, b_i + \frac{\omega_i^2(0)}{b_i \mathcal{V}^\gamma}$$

66
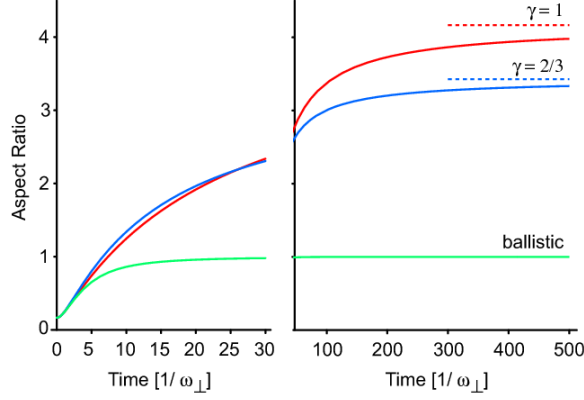
Fig. 16. – Aspect ratio $\epsilon(t) = R_x(t)/R_z(t)$ as a function of time for the MIT trap ($\epsilon = 1/6$) in ballistic, collisional or superfluid hydrodynamic expansion ($\gamma = 2/3$) and superfluid hydrodynamic expansion of a molecular BEC ($\gamma = 1$).

Here, $\omega_{S,i}$ are the real or imaginary frequencies characterizing the saddle point potential. These equations typically need to be solved numerically. For a Bose-Einstein condensate of molecules expanding from long cigar-shaped traps ($\epsilon \ll 1$), the *radial* equation again allows for an analytic solution identical to that for a ballistically expanding, non-
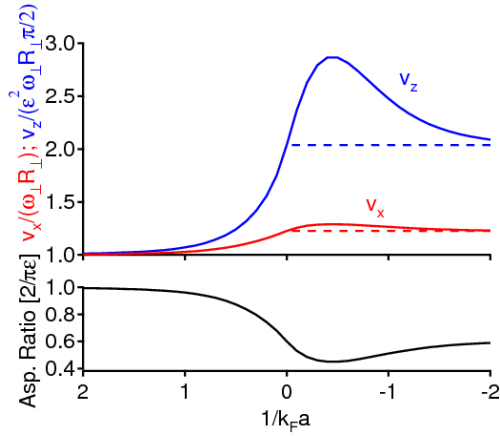
Fig. 17. – Asymptotic velocities and aspect ratio for hydrodynamic expansion out of a very elongated cigar-shaped trap ($\epsilon = \omega_z/\omega_x \ll 1$), as a function of the interaction parameter $1/k_F a$. The dashed lines show the asymptotic values in the BCS-limit. A similar figure can be found in [181].

67

	Ballistic	Hydrodynamic (BEC)	(BCS, unitarity, collisional)
$b_\perp(t)$	$\sqrt{1+\omega_\perp^2 t^2}$	$\sqrt{1+\omega_\perp^2 t^2}$	$\sim 1.22\,\omega_\perp t$
$b_z(t)$	$\sqrt{1+\omega_z^2 t^2}$	$1+\epsilon^2(\omega_\perp t \arctan(\omega_\perp t)$ $-\ln\sqrt{1+\omega_\perp^2 t^2})$	$\sim 2.05\,\frac{\pi}{2}\epsilon^2\omega_\perp t$
AR	1	$\frac{2}{\pi}\frac{1}{\epsilon}$	$\sim 0.60\,\frac{2}{\pi}\frac{1}{\epsilon}$

TABLE V. – *Comparison between ballistic and hydrodynamic expansion. Formulas for hydrodynamic expansion assume a long cigar-shaped trap ($\epsilon = \omega_z/\omega_x \ll 1$), formulas for the aspect ratio (AR) and for the BCS, Unitarity, collisional limit give the asymptotic behavior. The formula for BEC-expansion is valid at short times $t \ll \omega_\perp/\omega_z^2$, but also captures the correct long time limit.*

interacting gas. One obtains

$$(60) \qquad b_\perp(t) = \sqrt{\cosh^2\left(\frac{1}{\sqrt{2}}\omega_{Sz}t\right) + \frac{2\omega_\perp^2}{\omega_{Sz}^2}\sinh^2\left(\frac{1}{\sqrt{2}}\omega_{Sz}t\right)}.$$

However, the *axial* cloud size behaves drastically different from a non-interacting cloud. For $\omega_{Sz} = \omega_z$, the axial cloud size of a non-interacting gas would never change ($b_z(t) = 1$), whereas a hydrodynamic gas, released into the radial dimensions, will start to *shrink* axially under the influence of the confining axial potential. The cloud's energy (interaction energy for a BEC, kinetic energy for a BCS superfluid) escapes radially, hence there is not sufficient pressure to maintain the axial cloud size.

Further discussions of superfluid hydrodynamics and scaling transformations can be found in the contributions of Y. Castin and S. Stringari to these proceedings.

3'3. Fitting functions for trapped and expanded Fermi gases. – In the preceding sections we derived the 3D density distribution of a Fermi mixture in various regimes. However, all imaging techniques record column densities, density profiles integrated along the line of sight (the z-axis in the following).

For condensed gases, where $n(\mathbf{r}) \approx n(\mathbf{0})\,(1 - V(\mathbf{r})/\mu)^{1/\gamma}$, one obtains the column density

$$(61) \qquad n_{2\mathrm{D,c}}(x,y) = n_c\left(1 - \frac{x^2}{R_x^2} - \frac{y^2}{R_y^2}\right)^{\frac{1}{\gamma}+\frac{1}{2}}$$

For thermal Bose (molecular) and Fermi clouds, we have

$$(62) \qquad n_{2\mathrm{D}}(x,y) = n_{2\mathrm{D,0}}\,\mathrm{Li}_2\left(\pm\exp\left[\beta\mu - \beta\frac{1}{2}m(\omega_x^2 x^2 + \omega_y^2 y^2)\right]\right) / \mathrm{Li}_2\left(\pm e^{\beta\mu}\right)$$

In the following, we will discuss the fitting functions valid in the different regimes of interaction, and the derived quantities.

3˙3.1. Non-interacting Fermi gases.

Cloud size. In the classical regime at $T/T_F \gg 1$, the characteristic cloud size is given by the gaussian radius $\sigma_i = \sqrt{\frac{2k_B T}{m\omega_i^2}}$. In the degenerate regime, however, the cloud size saturates at the Fermi radius $R_{Fi} = \sqrt{\frac{2E_F}{m\omega_i^2}}$. It is thus convenient to define a fit parameter that interpolates between the two limits:

$$R_i^2 = \frac{2k_B T}{m\omega_i^2} f(e^{\mu\beta}) \rightarrow \left\{ \begin{array}{ll} \sigma_i, & T/T_F \gg 1 \\ R_{Fi}, & T/T_F \ll 1 \end{array} \right.$$

(63) $$\text{where } f(x) = \frac{\text{Li}_1(-x)}{\text{Li}_0(-x)} = \frac{1+x}{x} \ln(1+x)$$

For all temperatures, R_i is thus directly related to the physical size of the cloud, and thus a better choice as a fit parameter than σ_i, which goes to zero at $T = 0$, or $\sqrt{\frac{2\mu}{m\omega_i^2}}$, which goes to zero around $T/T_F = 0.57$. Numerically, using R_i is easier to implement than using the root mean square radius of the cloud

(64) $$\langle x_i^2 \rangle = \frac{k_B T}{m\omega_i^2} \frac{\text{Li}_4(-e^{\mu\beta})}{\text{Li}_3(-e^{\mu\beta})}$$

Fitting function. The fit function used for the density profiles of Fermi clouds is then in 2D

(65) $$n_{2D}(x,y) = n_{2D,0} \frac{\text{Li}_2\left(\pm \exp\left[q - \left(\frac{x^2}{R_x^2} + \frac{y^2}{R_y^2}\right) f(e^q)\right]\right)}{\text{Li}_2\left(\pm e^q\right)}$$

and for 1D

(66) $$n_{1D}(x) = n_{1D,0} \frac{\text{Li}_{5/2}\left(\pm \exp\left[q - \frac{x^2}{R_x^2} f(e^q)\right]\right)}{\text{Li}_{5/2}\left(\pm e^q\right)}.$$

The parameter $q = \mu\beta$, the logarithm of the fugacity, determines the *shape* of the cloud. For a small fugacity (large and negative q), the above functions reduce to the simple gaussian distribution of thermal clouds. For high fugacity (large and positive q), they tend to the zero-temperature distribution $n_{2D,0}(1 - \frac{x^2}{R_{Fx}^2})^2$ (in 2D) and $n_{1D,0}(1 - \frac{x^2}{R_{Fx}^2})^{5/2}$ (in 1D).

Derived quantities. Degeneracy The degeneracy parameter T/T_F can be calculated by combining Eq. 24 with Eq. 33:

(67) $$\frac{T}{T_F} = [-6\,\text{Li}_3(-e^q)]^{-1/3}$$

69

This parameter depends only on the *shape* of the cloud. A characteristic point where shape deviations due to quantum statistics start to play a role is the point where μ changes sign, and we see from Eq. 67 that this occurs at $T/T_F \approx 0.57$. Many non-ideal aspects of imaging, such as finite resolution, out of focus imaging, saturation, heating of the cloud by the probe pulse etc., tend to wash out the non-gaussian features of a highly degenerate Fermi cloud and hence lead to a larger value of T/T_F. However, dispersive effects due to non-resonant imaging light can potentially mimic sharp edges of the cloud, which the fitting routine would then falsely interpret to result from a very low T/T_F. It is clear that care has to be taken when determining the degeneracy parameter from the shape of the cloud alone.

Temperature. The size of the cloud and the shape parameter q give the temperature as

$$(68) \qquad k_B T = \frac{1}{2} m \omega_i^2 \frac{R_i^2}{b_i(t)^2} \frac{1}{f(e^q)}$$

where we have used the expansion factor $b_i(t)$ from section **3**˙2. We recall that $b_i(t) = \sqrt{1 + \omega_i^2 t^2}$ for the free expansion of a non-interacting Fermi gas. For low temperatures $T \ll T_F$, $f(e^{\mu\beta}) \to \mu\beta = \mu/k_B T$ and $R_i = b_i(t) R_{Fi}$. In this case, temperature only affects the wings of the density distribution, where the *local* $T/T_F(\mathbf{r})$ is still large. In fact,

$$(69) \qquad n_{1D}(x) \propto \begin{cases} (1 - \frac{x^2}{R_{Fx}^2})^{5/2} & \text{for } x \ll R_{Fx} \\ e^{-\frac{x^2}{\sigma_x^2}} & \text{for } x \gg R_{Fx}, \end{cases}$$

and we see that temperature only affects the cloud's wings beyond the zero-temperature Fermi radius. Thermometry of very low temperature Fermi clouds is thus difficult, limited by the signal-to-noise ratio in the low-density wings of the distribution. This is different from thermometry of thermal clouds at high temperature $T \gg T_F$, where the entire size of the cloud σ_i directly gives the temperature.

Because of the sensitivity to the cloud's wings, thermometry is more robust when the full 2D distribution is used for the fit. Alternatively, one can rely on the known trapping geometry plus the local density approximation and perform an average over the elliptical equipotential lines in the x-y plane (line of sight integration necessarily mixes points at different values of the potential energy.) As the number of points included in the average grows with the distance from the cloud's center, the signal-to-noise will actually be best in the wings. Such an average is superior to a simple integration along the x-axis, for example, as this will more strongly mix regions that have different local T/T_F.

The ideal gases (Fermi, Bose, Boltzmann) are the only systems for which we have an exact description. Therefore, they are attractive as a thermometer, when brought in contact with strongly interacting systems. This concept has been recently carried out by determining absolute temperatures for imbalanced Fermi gases at unitarity [82].

In these systems, for sufficiently high imbalance, the majority cloud extends beyond the minority cloud, and is (locally) an ideal gas. Therefore, in Ref. [82] the spatial wings of these clouds could be fitted with the functions for the ideal Fermi gas discussed in this section, and absolute temperatures for the superfluid phase transition could be determined. The fitting of the majority wings had to be done with in-trap profiles, which required to address the effect of anharmonicities of the optical trapping potential. Usually, for thermometry, ballistic expansion is preferable since velocity distributions are independent of the shape of the trapping potential. However, in the case of imbalanced Fermi gases, the atoms in the wings can collide with the strongly interacting core during expansion, modifying their velocity distribution.

Another way to perform ideal gas thermometry is done by converting the sample to a non-interacting system by sweeping sufficiently far away from the Feshbach resonance. If such magnetic field sweeps are adiabatic, they conserve entropy (but not temperature). By fitting the spatial profiles of the non-interacting cloud, the entropy S of the strongly interacting system can be determined. If it is possible to vary the energy of the strongly interacting system in a controlled way (e.g. by using the virial theorem at unitarity [45, 176] or by providing controlled heating [72]), one can determine the derivative dS/dE which is equal to the inverse absolute temperature. So far this method could be implemented only for a balanced Fermi system at unitarity [183] and, due to the need of determining a derivative, could only provide temperatures averaged over a range of energies.

Number of atoms and Fermi energy. The number of atoms in the observed spin state can be obtained from the total absorption recorded in the cloud's CCD image. The transmission of resonant light at pixel (x, y) is given by $\tilde{T}(x, y) = e^{-\sigma_0 \int n_{3D}(x,y,z)\,dz}$, where σ_0 is the resonant atom-photon cross section for light absorption. Thus, the number of atoms is

$$(70) \qquad N_\uparrow = \frac{A}{M\sigma_0} \sum_{pixels} -\ln(\tilde{T}(x,y))$$

where A is the area per pixel and M the optical magnification.

Typically, the fitting functions are applied to the optical density $\sigma_0 \int_z n_{3D}(x,y,z) = -\ln\left(\tilde{T}(x,y)\right)$. The fit parameter $n_{2D,0}$ thus measures the peak optical density of the cloud, while the radii $\tilde{R}_x$ and $\tilde{R}_y$ have units of camera pixels. The number of atoms described by the fitting function is thus given by

$$
\begin{aligned}
N_{\text{fit}} &= \frac{A}{M\sigma_0} \pi\, n_{2D,0}\, \tilde{R}_x \tilde{R}_y \frac{\text{Li}_3(-e^q)}{\text{Li}_2(-e^q)} \frac{\text{Li}_0(-e^q)}{\text{Li}_1 - e^q} \\
(71) \qquad &\to \frac{A}{\sigma_0} \begin{cases} \frac{\pi}{3} n_{2D,0}\, \tilde{R}_{Fx} \tilde{R}_{Fy}, & T \ll T_F \\ \pi\, n_{2D,0}\, \tilde{\sigma}_x \tilde{\sigma}_y, & T \gg T_F. \end{cases}
\end{aligned}
$$

From the number of atoms and the trapping frequencies, one can calculate the Fermi energy $k_B T_F$:

$$(72) \qquad k_B T_F = \hbar \bar{\omega} (6 N_{\text{fit}})^{1/3}$$

An independent determination of the Fermi energy is provided by the measured (physical) size of the cloud R_i for highly degenerate clouds. For $T \to 0$, $R_i \approx b_i(t) R_{Fi}$ and thus $k_B T_F = \frac{1}{2} m \omega_i^2 \frac{R_i^2}{b_i(t)^2}$. As only the trapping frequencies and the magnification of the imaging system enter into this equation, this relation allows a calibration of the light absorption cross section which may be reduced from the resonant cross section by detuning, non-ideal polarization of the probe light, and saturation.

For arbitrary temperature, the shape parameter q enters the relation for the Fermi energy:

$$(73) \qquad k_B T_F = k_B T \frac{T_F}{T} = \frac{1}{2} m \omega_i^2 \frac{R_i^2}{b_i(t)^2} \frac{(-6 \operatorname{Li}_3(-e^q))^{1/3}}{f(e^q)}$$

3˙3.2. Resonantly interacting Fermi gases. The calculation of density profiles of interacting gases is delicate. Already above the superfluid transition temperature, attractive interactions lead to a shrinking of the cloud. Since interactions (parameterized by the local $k_F a$) vary across the cloud, there is a priori no simple analytical function describing interacting Fermi gases. Experimentally, it turns out that the difference in the *shape* of a (balanced) interacting and a non-interacting Fermi mixture is minute around resonance and on the BCS-side. Especially for the resonant case $(1/k_F a = 0)$, this has led to the common practice of using the shape of the non-interacting Fermi gas as fitting function, and quote an effective temperature $\tilde{T}$ and effective degeneracy $\frac{\tilde{T}}{T_F}$ of resonantly interacting clouds [60, 72]. In fact, universality on resonance implies that the gas' chemical potential must be $\mu(\mathbf{r}) = \xi(T/T_F) \epsilon_F(\mathbf{r})$, with a universal function $\xi(T/T_F)$ which only depends on the reduced temperature T/T_F [45]. The zero-temperature limit of $\xi \equiv \xi_0$ has been subject of extensive experimental and theoretical studies (see section **7˙1.1**), and its value is $\xi(0) \approx 0.42$. At $T = 0$, we have for a trapped gas $\mu(\mathbf{r}) = \mu_0 - V(\mathbf{r}) = \xi_0 \epsilon_F(\mathbf{r}) \propto n^{2/3}(\mathbf{r})$. The density profile will then have the exact same shape as a non-interacting Fermi gas, with a renormalized Fermi temperature. However, for finite temperature, $\xi(T/T_F)$ differs from the temperature dependence of a non-interacting gas [184], and there is no a priori reason that the shape of the cloud at unitarity should be similar to that of a non-interacting Fermi gas. It turns out that the difference is very small.

The shape similarity was an important issue in the quest for superfluidity in Fermi gases. In the case of weakly interacting BECs, condensation is apparent from the sudden appearance of a dense, central core in midst of a large thermal cloud. In contrast to that, Fermi gases do not show such a signature, at least at first sight (see Fig. 18), and different detection methods for superfluidity were explored.

The only loophole that may allow seeing a signature of superfluidity in the spatial
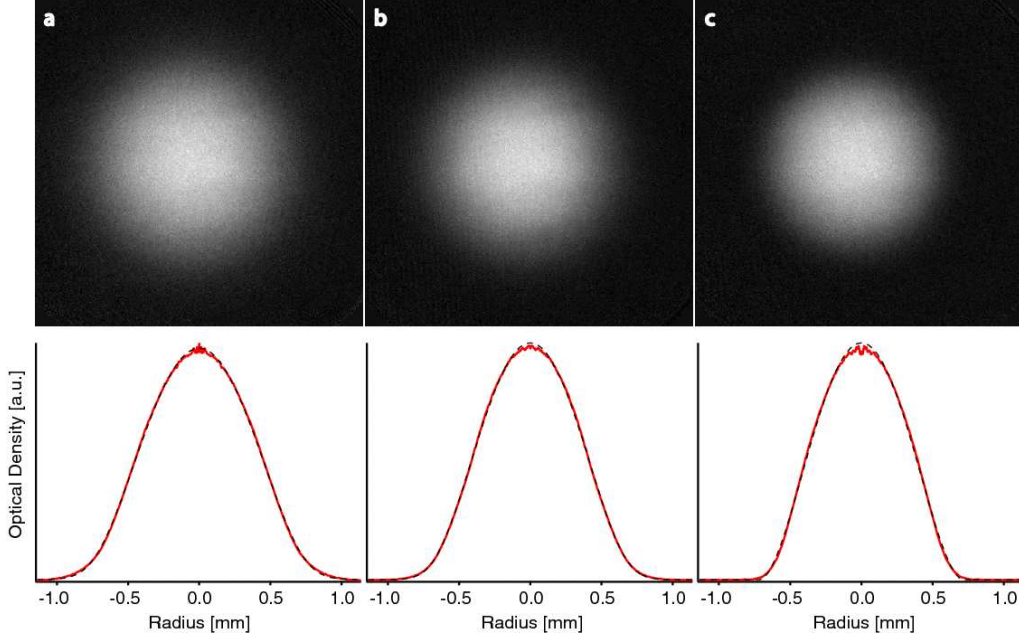
Fig. 18. – The absence of a signature of condensation in the spatial profile of strongly interacting Fermi gases. Shown are high-resolution images of spin up atoms in a resonantly interacting, equal mixture of spin up and spin down for different temperatures. The lower graphs show azimuthally averaged radial profiles (noise level well below 1% of the maximum optical density). All three clouds are very well fit using a finite-temperature Thomas-Fermi distribution (with fugacity $e^{\mu/k_B\widetilde{T}}$, central density n_0 and mean square radius $< r^2 >$ as free parameters, see Eq. 62). However, the empirical temperatures of $\widetilde{T}/T_F = 0.22$ (a), 0.13 (b) and 0.075 (c) determined from the profiles' wings indicate that at least clouds b and c should be in the superfluid regime. Trap parameters $\nu_r = 162$ Hz, $\nu_z = 22.8$ Hz, 10 ms time of flight, expansion factor 13.9, atom numbers N per spin state were 10.2 (a), 9.5 (b) and 7.5 $\times 10^6$.

profile of balanced Fermi gases would be a rapid variation of $\xi(T/T_F)$ around the critical temperature T_C. This would translate into a sudden variation of the density at the interface between the normal and superfluid region, e.g. where the gas is locally critical, $T = T_C(\mathbf{r})$.

We have indeed found a faint signature of condensation in density profiles of the unitary gas on resonance after expansion. These results will be presented in section **6**˙5.1. Note that the observation of such a feature in the density profiles draws into question the common practice of determining an "effective temperature" from density profiles at unitarity using the ideal gas fitting function. In contrast to balanced Fermi mixtures, a striking signature of condensation can be observed in the density profiles of mixtures with *imbalanced* populations of spin up and spin down fermions. This will be discussed in section **6**˙5.2.

73

3˙3.3. Molecular clouds. In partially condensed molecular gases that are weakly inter-
acting, one can neglect the mutual repulsion between the condensate and the surrounding
thermal cloud of molecules. The density distribution is typically well-fit by a bimodal
sum of an inverted parabola for the condensate

$$(74) \qquad n_c(x,y) = n_{c0}\left(1 - \frac{x^2}{R_{cx}^2} - \frac{y^2}{R_{cy}^2}\right)$$

and a Bose-function for the thermal cloud, as in Eq. 62, with the parameter $q = \mu\beta$
often left as an adjustable parameter (instead of fixing it via the condensate's chemical
potential $\mu = gn_{c0}$):

$$(75) \qquad n_{th}(x,y) = n_{th0}\,\mathrm{Li}_2\left(\exp\left[q - \frac{x^2}{R_{th,x}^2} - \frac{y^2}{R_{th,y}^2}\right]\right)/\mathrm{Li}_2(\exp[q])$$

For practical purposes, this is often simplified by a gaussian, as if $q \ll 0$. Then $n_{th} \approx$
$n_{th0}\,\exp\left(-\frac{x^2}{R_{th,x}^2} - \frac{y^2}{R_{th,y}^2}\right)$.

Once the condensate mean-field $2gn_c$ (with $g = \frac{4\pi\hbar^2 a_M}{M}$) experienced by thermal
molecules is no longer small compared to $k_B T$, the mutual repulsion can no longer be
neglected. The thermal molecules will then experience a "Mexican-hat" potential, the
sum of the confining harmonic potential $V_M(\mathbf{r})$, and the repulsion from the condensate
$2gn_c(\mathbf{r})$ and from the surrounding thermal cloud, $2gn_{th}(\mathbf{r})$. The thermal molecules them-
selves will in turn repel the condensate. The situation can be captured by two coupled
equations for the condensate (in Thomas-Fermi approximation) and the thermal cloud:

$$gn_c(\mathbf{r}) = \mathrm{Max}\,(\mu - V_M(\mathbf{r}) - 2gn_{th}(\mathbf{r}), 0)$$
$$n_{th}(\mathbf{r}) = \frac{1}{\lambda_M^3}\,\mathrm{Li}_{3/2}(e^{\beta(\mu - V_M(\mathbf{r}) - 2gn_c(\mathbf{r}) - 2gn_{th}(\mathbf{r}))})$$
$$(76) \qquad\qquad = \frac{1}{\lambda_M^3}\,\mathrm{Li}_{3/2}(e^{-\beta|\mu - V_M(\mathbf{r}) - 2gn_{th}(\mathbf{r})|})$$

where λ_M is the thermal de Broglie wavelength for molecules. In the case of weakly
interacting Bose gases, one can neglect the mean field term $2gn_{th}(\mathbf{r})$ [185].

Note that these coupled equations are only an approximative way to describe the
strongly correlated gas. The mean field approximation for the thermal molecules ne-
glects phonons and other collective excitations. The above equations can be solved
numerically. In the limit of strong interactions, the condensate almost fully expels the
thermal molecules from the trap center, so that the thermal cloud forms a shell around
the condensate.

The practical implication of this discussion is that there is no simple analytic expres-
sion for the density distribution of partially condensed clouds in the strongly interacting
regime. For fitting purposes one may still choose for example the bimodal fit of Eq. 75,

but one must be aware that quantities like the "condensate fraction" thus obtained depend on the model assumed in the fit. For tests of many-body calculations, the full density distributions should be compared to those predicted by theory.

Derived quantities. Temperature.

For weakly interacting Bose gases, Eq. 75 holds and the temperature is given by

$$(77) \qquad k_B T = \frac{1}{2} m \omega_i^2 \frac{R_{th,i}^2}{b_i(t)^2}$$

where $b_i(t) = \sqrt{1 + \omega_i^2 t^2}$ is the expansion factor of the thermal gas. To ensure model-independent results, only the thermal gas should be included in the fit, not the condensed core. For strongly interacting clouds, temperature can in principle still be obtained from the thermal wings of the *trapped* molecular distribution, which is gaussian at distances $\mathbf{r}$ for which $V_M(\mathbf{r}) \gg \mu$. However, a possible systematic correction can occur in expansion due to interactions of molecules in the wings with the core, which may be either condensed or strongly interacting.

Note that unless the whole cloud is deep in the hydrodynamic regime, there is no simple scaling law for the expansion of such strongly interacting molecular gases. Absolute thermometry of strongly interacting, balanced gases is still a challenging problem.

Chemical potential

In a confining potential, and at zero temperature, the chemical potential is given by the size of the condensate, as $V(\mathbf{r}) = \mu$. It can be expressed by the fit parameters according to Eq. 74 as

$$(78) \qquad \mu = \frac{1}{2} m \omega_i^2 \frac{R_{c,i}^2}{b_i(t)^2}$$

with $b_i(t)$ the expansion factor for superfluid hydrodynamic expansion into direction i. At finite temperatures and for strong interactions, the thermal cloud will mostly reside outside the condensate and can affect the actual or fitted condensate size.

Condensate fraction

In the field of dilute atomic gases, the condensate fraction is a key quantity to characterize the superfluid regime. In contrast to superfluid helium and superconductors, gaseous condensates can be directly observed in a dramatic way. However, unless interactions are negligible, the determination of the condensate fraction is model dependent. For weakly interacting gases (or those obtained after a rapid ramp into the weakly interacting regime), the density distribution can typically be well fit with the bimodal distribution of Eqs. 74 and 75. A robust way to define a "condensate fraction" is then to ascribe the total number of molecules in the narrower distribution to the condensate. For strong interactions however, the mean-field repulsion of thermal and condensed molecules (see above) will lead to the expulsion of a large part of thermal molecules from the condensate. In addition, low-energy excitations such as phonons, as well as quantum

depletion will modify the non-condensed fraction at the position of the condensate, and the fitted condensate fraction depends on the form of the fitting function for the bimodal fit. In these cases, it is better to directly compare density distributions with theoretical predictions.

4. – Theory of the BEC-BCS crossover

4˙1. *Elastic collisions*. – Due to their diluteness, most properties of systems of ultra-cold atoms are related to two-body collisions. If we neglect the weak magnetic dipole interaction between the spins, the interatomic interaction is described by a central potential $V(r)$. At large distances from each other, atoms interact with the van der Waals-potential $-C_6/r^6$ as they experience each other's fluctuating electric dipole[7]. At short distances on the order of a few Bohr radii a_0, the two electron clouds strongly repel each other, leading to "hard-core" repulsion. If the spins of the two valence electrons (we are considering alkali atoms) are in a triplet configuration, there is an additional repulsion due to Pauli's exclusion principle. Hence, the triplet potential $V_T(r)$ is shallower than the singlet one $V_S(r)$. The exact inclusion of the interatomic potential in the description of the gas would be extremely complicated. However, the gases we are dealing with are ultracold and ultradilute, which implies that both the de Broglie wavelength λ_{dB} and the interparticle distance $n^{-1/3} \sim 5\,000 - 10\,000\,a_0$ are much larger than the range of the interatomic potential r_0 (on the order of the van der Waals length $r_0 \sim \left(\mu C_6/\hbar^2\right) \sim 50\,a_0$ for ^{6}Li). As a result, scattering processes never explore the fine details of the short-range scattering potential. The entire collision process can thus be described by a single quantity, the *scattering length*.

Since the description of Feshbach resonances and of the BCS-BEC crossover require the concept of the effective range and renormalization of the scattering length, we quickly summarize some important results of scattering theory.

The Schrödinger equation for the reduced one-particle problem in the center-of-mass frame of the colliding atoms (with reduced mass $m/2$, distance vector r, and initial relative wave vector $\mathbf{k}$) is

$$(79) \qquad (\nabla^2 + k^2)\Psi_{\mathbf{k}}(\mathbf{r}) = v(r)\Psi_{\mathbf{k}}(\mathbf{r}) \quad \text{with } k^2 = \frac{mE}{\hbar^2} \quad \text{and } v(r) = \frac{mV(r)}{\hbar^2}$$

Far away from the scattering potential, the wave function $\Psi_{\mathbf{k}}(\mathbf{r})$ is given by the sum of the incident plane wave $e^{i\mathbf{k}\cdot\mathbf{r}}$ and an outgoing scattered wave:

$$(80) \qquad \Psi_{\mathbf{k}}(\mathbf{r}) \sim e^{i\mathbf{k}\cdot\mathbf{r}} + f(\mathbf{k'},\mathbf{k})\frac{e^{ikr}}{r}$$

$f(\mathbf{k'},\mathbf{k})$ is the scattering amplitude for scattering an incident plane wave with wave vector $\mathbf{k}$ into the direction $\mathbf{k'} = k\,\mathbf{r}/r$ (energy conservation implies $k' = k$).

Since we assume a central potential, the scattered wave must be axially symmetric with respect to the incident wave vector $\mathbf{k}$, and we can perform the usual expansion into partial waves with angular momentum l [186]. For ultracold collisions, we are interested in describing the scattering process at *low momenta* $k \ll 1/r_0$, where r_0 is the range of the

---

[7] For distances on the order of or larger than the characteristic wavelength of radiation of the atom, $\lambda \gg r_0$, retardation effects change the potential to a $-1/r^7$ law.

interatomic potential. In the absence of resonance phenomena for $l \neq 0$, *s-wave scattering* $l = 0$ is dominant over all other partial waves (if allowed by the Pauli principle):

$$(81) \qquad f \approx f_s = \frac{1}{2ik}(e^{2i\delta_s} - 1) = \frac{1}{k \cot \delta_s - ik}$$

where f_s and δ_s are the *s*-wave scattering amplitude and phase shift, resp. [186]. Time-reversal symmetry implies that $k \cot \delta_s$ is an even function of k. For low momenta $k \ll 1/r_0$, we may expand it to order k^2:

$$(82) \qquad k \cot \delta_s \approx -\frac{1}{a} + r_{\text{eff}} \frac{k^2}{2}$$

which defines the *scattering length*

$$(83) \qquad a = - \lim_{k \ll 1/r_0} \frac{\tan \delta_s}{k},$$

and the effective range r_{eff} of the scattering potential. For example, for a spherical well potential of depth $V \equiv \hbar^2 K^2/m$ and radius R, $r_{\text{eff}} = R - \frac{1}{K^2 a} - \frac{1}{3}\frac{R^3}{a^2}$, which deviates from the potential range R only for $|a| \lesssim R$ or very shallow wells. For van der Waals potentials, r_{eff} is of order r_0 [187]. With the help of a and r_{eff}, f is written as [186]

$$(84) \qquad f(k) = \frac{1}{-\frac{1}{a} + r_{\text{eff}} \frac{k^2}{2} - ik}$$

In the limit $k|a| \ll 1$ and $|r_{\text{eff}}| \lesssim 1/k$, f becomes independent on momentum and equals $-a$. For $k|a| \gg 1$ and $r_{\text{eff}} \ll 1/k$, the scattering amplitude is $f = \frac{i}{k}$ and the cross section for atom-atom collisions is $\sigma = \frac{4\pi}{k^2}$. This is the so-called unitarity limit. Such a divergence of a occurs whenever a new bound state is supported by the potential (see section **5**˙2).

4˙2. *Pseudo-potentials*. – If the de Broglie wavelength $\frac{2\pi}{k}$ of the colliding particles is much larger than the fine details of the interatomic potential, $1/k \gg r_0$, we can create a simpler description by modifying the potential in such a way that it is much easier to manipulate in the calculations, but still reproduces the correct *s*-wave scattering. An obvious candidate for such a "pseudo-potential" is a delta-potential $\delta(\mathbf{r})$.

However, there is a subtlety involved which we will address in the following. The goal is to find an expression for the scattering amplitude f in terms of the potential $V(r) = \frac{\hbar^2 v(r)}{m}$, so that we can try out different pseudo-potentials, always ensuring that $f \rightarrow -a$ in the *s*-wave limit. For this, let us go back to the Schrödinger equation Eq. 79. If we knew the solution to the following equation:

$$(85) \qquad (\nabla^2 + k^2)G_k(\mathbf{r}) = \delta(\mathbf{r})$$

we could write an integral equation for the wave function $\Psi_{\mathbf{k}}(\mathbf{r})$ as follows:

$$(86) \qquad \Psi_{\mathbf{k}}(\mathbf{r}) = e^{i\mathbf{k}\cdot\mathbf{r}} + \int d^3 r' G_k(\mathbf{r} - \mathbf{r}')v(\mathbf{r}')\Psi_{\mathbf{k}}(\mathbf{r}')$$

This can be simply checked by inserting this implicit solution for $\Psi_{\mathbf{k}}$ into Eq. 79. $G_k(\mathbf{r})$ can be easily obtained from the Fourier transform of Eq. 85, defining $G_k(\mathbf{p}) = \int d^3 r e^{-i\mathbf{p}\cdot\mathbf{r}}G_k(\mathbf{r})$:

$$(87) \qquad (-p^2 + k^2)G_k(\mathbf{p}) = 1$$

The solution for $G_k(\mathbf{r})$ is

$$(88) \qquad G_{k,+}(\mathbf{r}) = \int \frac{d^3 p}{(2\pi)^3} \frac{e^{i\mathbf{p}\cdot\mathbf{r}}}{k^2 - p^2 + i\eta} = -\frac{1}{4\pi}\frac{e^{ikr}}{r}$$

where we have chosen (by adding the infinitesimal constant $i\eta$, with $\eta > 0$ in the denominator) the solution that corresponds to an outgoing spherical wave. $G_{k,+}(\mathbf{r})$ is the *Green's function* of the scattering problem. Far away from the origin, $|\mathbf{r} - \mathbf{r}'| \sim r - \mathbf{r}' \cdot \mathbf{u}$, with the unit vector $\mathbf{u} = \mathbf{r}/r$, and

$$(89) \qquad \Psi_{\mathbf{k}}(\mathbf{r}) \sim e^{i\mathbf{k}\cdot\mathbf{r}} - \frac{e^{ikr}}{4\pi r}\int d^3 r' e^{-i\mathbf{k}'\cdot\mathbf{r}'}v(\mathbf{r}')\Psi_{\mathbf{k}}(\mathbf{r}')$$

where $\mathbf{k}' = k\mathbf{u}$. With Eq. 80, this invites the definition of the scattering amplitude via

$$(90) \qquad f(\mathbf{k}', \mathbf{k}) = -\frac{1}{4\pi}\int d^3 r\, e^{-i\mathbf{k}'\cdot\mathbf{r}}v(\mathbf{r})\Psi_{\mathbf{k}}(\mathbf{r})$$

Inserting the exact formula for $\Psi_{\mathbf{k}}(\mathbf{r})$, Eq. 86, combined with Eq. 88, leads to an integral equation for the scattering amplitude

$$(91) \qquad f(\mathbf{k}', \mathbf{k}) = -\frac{v(\mathbf{k}' - \mathbf{k})}{4\pi} + \int \frac{d^3 q}{(2\pi)^3} \frac{v(\mathbf{k}' - \mathbf{q})f(\mathbf{q}, \mathbf{k})}{k^2 - q^2 + i\eta}$$

where $v(\mathbf{k})$ is the Fourier transform of the potential $v(\mathbf{r})$ (which we suppose to exist). This is the Lippmann-Schwinger equation, an exact integral equation for f in terms of the potential v, useful to perform a perturbation expansion. Note that it requires knowledge of $f(\mathbf{q}, \mathbf{k})$ for $q^2 \neq k^2$ ("off the energy shell"). However, the dominant contributions to the integral do come from wave vectors $\mathbf{q}$ such that $q^2 = k^2$. For low-energy s-wave scattering, $f(\mathbf{q}, \mathbf{k}) \to f(k)$ then only depends on the magnitude of the wave vector $\mathbf{k}$. With this approximation, we can take $f(k)$ outside the integral. Taking the limit

$k \ll 1/r_0$, dividing by $f(k)$ and by $v_0 \equiv v(\mathbf{0})$, we arrive at

$$(92) \qquad \frac{1}{f(k)} \approx -\frac{4\pi}{v_0} + \frac{4\pi}{v_0} \int \frac{d^3q}{(2\pi)^3} \frac{v(-\mathbf{q})}{k^2 - q^2 + i\eta}$$

If we only keep the first order in v, we obtain the scattering length in *Born approximation*, $a = \frac{v_0}{4\pi}$. For a delta-potential $V(\mathbf{r}) = V_0 \, \delta(\mathbf{r})$, we obtain to first order in V_0

$$(93) \qquad V_0 = \frac{4\pi\hbar^2 a}{m}$$

However, already the second order term in the expansion of Eq. 92 would not converge, as it involves the divergent integral $\int \frac{d^3q}{(2\pi)^3} \frac{1}{q^2}$. The reason is that the Fourier transform of the δ-potential does not fall off at large momenta. Any physical potential *does* fall off at some large momentum, so this is not a "real" problem. For example, the van-der-Waals potential varies on a characteristic length scale r_0 and will thus have a natural momentum cut-off $\hbar/r_0$. A proper regularization of contact interactions employs the pseudo-potential [167] $V(\mathbf{r})\psi(\mathbf{r}) = V_0\delta(\mathbf{r})\frac{\partial}{\partial r}(r\psi(\mathbf{r}))$. It leads exactly to a scattering amplitude $f(k) = -a/(1 + ika)$ if $V_0 = \frac{4\pi\hbar^2 a}{m}$.

Here we will work with a Fourier transform that is equal to a constant V_0 at all relevant momenta in the problem, but that falls off at very large momenta, to make the second order term converge. The exact form is not important. If we are to calculate physical quantities, we will replace V_0 in favor of the observable quantity a using the formal prescription

$$(94) \qquad \frac{1}{V_0} = \frac{m}{4\pi\hbar^2 a} - \frac{m}{\hbar^2} \int \frac{d^3q}{(2\pi)^3} \frac{1}{q^2}$$

We will always find that the diverging term is exactly balanced by another diverging integral in the final expressions, so this is a well-defined procedure [188, 189].

Alternatively, one can introduce a "brute force" energy cut-off $E_R = \hbar^2/mR^2$ (momentum cut-off $\hbar/R$), taken to be much larger than typical scattering energies. Eq. 92 then gives

$$(95) \qquad \frac{1}{f(k)} \approx -\frac{4\pi}{v_0} - \frac{2}{\pi}\frac{1}{R} + \frac{2R}{\pi}k^2 - ik$$

This is now exactly of the form Eq. 84 with the scattering length

$$(96) \qquad a = \frac{\pi}{2}\frac{R}{1 + \frac{2\pi^2 R}{v_0}}$$

For any physical, given scattering length a we can thus find the correct strength v_0 that reproduces the same a (provided that we choose $R \ll a$ for positive a). This approach

implies an effective range $r_{\text{eff}} = \frac{4}{\pi}R$ that should be chosen much smaller than all relevant distances. Note that as a function of v_0, only one pole of a and therefore only one bound state is obtained, at $v_0 = -2\pi^2 R$.

This prompts us to discuss the relation between Eq. 94 and Eq. 91: The Lippmann-Schwinger equation is an exact reformulation of Schrödinger's equation for the scattering problem. One can, for example, exactly solve for the scattering amplitude in the case of a spherical well potential [190]. In particular, all bound states supported by the potential are recovered. However, to arrive at Eq. 94, one ignores the oscillatory behavior of both $v(\mathbf{q})$ and $f(\mathbf{q}, \mathbf{k})$ and replaces them by $\mathbf{q}$-independent constants. As a result, Eq. 94, with a cut-off for the diverging integral at a wave vector $1/R$, only allows for *one* bound state to appear as the potential strength is increased (see Eq. 96).

We will analyze this approximation for a spherical well of depth V and radius R. The true scattering length for a spherical well is given by [186]

$$(97) \qquad \frac{a}{R} = 1 - \frac{\tan(KR)}{KR}$$

with $K^2 = mV/\hbar^2$. which one can write as

$$(98) \qquad \frac{a}{R} = 1 - \frac{\prod_{n=1}^{\infty}(1 - \frac{K^2 R^2}{n^2 \pi^2})}{\prod_{n=1}^{\infty}(1 - \frac{4K^2 R^2}{(2n-1)^2 \pi^2})} \qquad \begin{array}{l} \leftarrow \text{Zeros of a-R} \\ \leftarrow \text{Resonances of } a \end{array}$$

In contrast, Eq. 94 with $V_0 = -\frac{4\pi}{3}V R^3$ and the "brute force" cut-off at $1/R$ gives

$$(99) \qquad \frac{a}{R} = \frac{K^2 R^2}{\frac{2}{\pi}K^2 R^2 - 3}$$

The sudden cut-off strips the scattering length of all but one zero (at $V = 0$) and of all but one resonance. For a shallow well that does not support a bound state, the scattering length still behaves correctly as $a = -\frac{1}{3}\frac{V}{E_R}R$. However, the sudden cut-off $v(\mathbf{q}) \approx$ const. for $q \leq \frac{1}{R}$ and 0 beyond results in a shifted critical well depth to accommodate the first bound state, $V = \frac{3\pi}{2}E_R$, differing from the exact result $V = \frac{\pi^2}{4}E_R$. This could be cured by adjusting the cut-off. But for increasing well depth, no new bound state is found and a saturates at $\sim R$, contrary to the exact result.

At first, such an approximation might be unsettling, as the van-der-Waals potentials of the atoms we deal with contain many bound states. However, the gas is in the ultracold regime, where the de Broglie-wavelength is much larger than the range r_0 of the potential. The short-range physics, and whether the wave function has one or many nodes within r_0 (i.e. whether the potential supports one or many bound states), is not important. All that matters is the phase shift δ_s *modulo* 2π that the atomic wave packets receive during a collision. We have seen that with a Fourier transform of the potential that is constant up to a momentum cut-off $\hbar/R$, we can reproduce any low-energy scattering behavior, which is described by the scattering length a. We can even realize a wide

81

range of combinations of a and the effective range r_{eff} to capture scattering at finite values of k. An exception is the situation where $0 < a \lesssim r_{\text{eff}}$ or potentials that have a negative effective range. This can be cured by more sophisticated models (see the model for Feshbach resonances in chapter **5**).

4˙3. *Cooper instability in a Fermi gas with attractive interactions*. – In contrast to bosons, the non-interacting Fermi gas does not show any phase transition down to zero temperature. One might assume that this qualitative fact should not change as interactions are introduced, at least as long as they are weak. This is essentially true in the case of repulsive interactions (^{8}). For attractive interactions, the situation is, however, dramatically different. Even for very weak attraction, the fermions form pairs and become superfluid, due to a generalized from of pair condensation.

The idea of pairing might be natural, as tightly bound pairs of fermions can be regarded as point-like bosons, which should form a Bose-Einstein condensate. However, for weak attractive interaction – as is the case for the residual, phonon-induced electron-electron interaction in metals – it is not evident that a paired state exists. Indeed, we will see in the following that in three dimensions there is no bound state for two isolated particles and arbitrarily weak interaction. However, by discussing exact solutions in 1D and 2D, where bound states exist for weak interactions, we gain insight into how a modified density of states will lead to bound states even in 3D – this is the famous Cooper instability.

4˙3.1. Two-body bound states in 1D, 2D and 3D. Localizing a quantum-mechanical particle of mass $\mu = m/2$ to a certain range R leads to an increased momentum uncertainty of $p \sim \hbar/R$ at a kinetic energy cost of about $E_R = p^2/m = \hbar^2/mR^2$. Clearly, a shallow potential well of size R and depth V with $V/E_R \equiv \epsilon \ll 1$ cannot confine the particle within its borders. But we can search for a bound state at energy $|E_B| \ll E_R$ of much larger size $r_B = 1/\kappa \equiv \sqrt{\hbar^2/m|E_B|} \gg R$.

- **1D**: The bound state wave function far away from the well necessarily behaves like $e^{\pm\kappa x}$ for negative (positive) x (see Fig. 19a). As we traverse the well, the wave function has to change its slope by 2κ over a range R. This costs kinetic energy $\approx \hbar^2\kappa/mR$ that has to be provided by the potential energy $-V$. We deduce that $\kappa \approx mRV/\hbar^2 = \epsilon/R$, where $\epsilon = V/E_R$ is a small number for a weak potential. The size of the bound state $r_B \approx R/\epsilon$ is indeed much larger than the size of the well, and the bound state energy $E_B \approx -E_R\,\epsilon^2/2$ depends quadratically on the weak attraction $-V$. Importantly, we can *always* find a bound state even for arbitrarily weak (purely) attractive potentials.
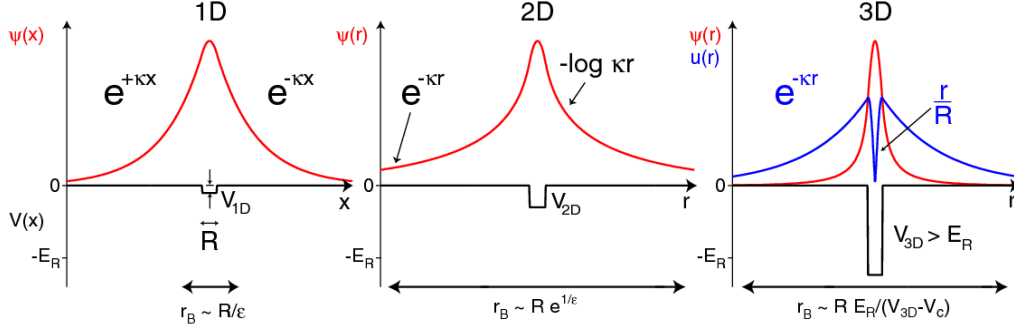
Fig. 19. – Bound state wave functions in 1D, 2D and 3D for a potential well of size R and depth V. In 1D and 2D, bound states exist for arbitrarily shallow wells. In terms of the small parameter $\epsilon = V/E_R$ with $E_R = \hbar^2/mR^2$, the size of the bound state in 1D is R/ϵ. In 2D, the bound state is exponentially large, of size $Re^{-1/\epsilon}$. In 3D, due to the steep slope in $u(r) = r\psi(r)$, bound states can only exist for well depths V_{3D} larger than a certain threshold $V_c \approx E_R$. The size of the bound state diverges as $RE_R/(V_{3D} - V_c)$ for $V_{3D} > V_c$.

- **2D**: For a spherically symmetric well, the Schrödinger equation for the radial wave function $\psi(r)$ *outside* the well reads $\frac{1}{r}\partial_r(r\partial_r\psi) = \kappa^2\psi$. The solution is the modified Bessel function which vanishes like $e^{-\kappa r}$ as $r \gg 1/\kappa$ (see Fig. 19b). For $R \ll r \ll 1/\kappa$, we can neglect the small bound state energy $E_B \propto -\kappa^2$ compared to the kinetic energy and have $\partial_r(r\psi') = 0$ or $\psi(r) \approx \log(\kappa r)/\log(\kappa R)$, where $1/\kappa$ is the natural scale of evolution for $\psi(r)$ and we have normalized ψ to be of order 1 at R. Note that in 2D, it is not the change in the slope ψ' of the wave function which costs kinetic energy, but the change in $r\psi'$. *Inside* the well, we can assume $\psi(r)$ to be practically constant as $V \ll E_R$. Thus, $r\psi'$ changes from $\approx 1/\log \kappa R$ (outside) to ≈ 0 (inside) over a distance R. The corresponding kinetic energy cost is $\frac{\hbar^2}{mr}\partial_r(r\psi')/\psi \approx \hbar^2/mR^2 \log(\kappa R) = E_R/\log(\kappa R)$, which has to be provided by the potential energy $-V$. We deduce $\kappa \approx \frac{1}{R}e^{-cE_R/V}$ and $E_B \approx -E_R e^{-2cE_R/V}$ with c on the order of 1. The particle is extremely weakly bound, with its bound state energy depending exponentially on the shallow potential $-V$. Accordingly, the size of the bound state is exponentially large, $r_B \approx R e^{cE_R/V}$. Nevertheless, we can *always* find this weakly bound state, for arbitrarily small attraction.

- **3D**: For a spherically symmetric well, the Schrödinger equation for the wave function ψ transforms into an effective one-dimensional problem for the wave function $u = r\psi$ (see Fig. 19c). We might now be tempted to think that there must always be a bound state in 3D, as we already found this to be the case in 1D. However, the boundary condition on $u(r)$ is now to vanish linearly at $r = 0$, in order for $\psi(0)$ to be finite. Outside the potential well, we still have $u \propto e^{-\kappa r}$ for a bound state. Inside the well the wave function must fall off to zero at $r = 0$ and necessarily has to change its slope from $-\kappa$ outside to $\sim 1/R$ inside the well over a distance

	1D	2D	3D
V	$\ll E_R$	$\ll E_R$	$> V_c \approx E_R$
$\psi(r > R)$	e^{-r/r_B}	$K_0(\frac{r}{r_B}) = \begin{cases} -\log r/r_B, & R \ll r \ll r_B \\ e^{-r/r_B}, & r \gg r_B \end{cases}$	$\frac{e^{-r/r_B}}{r}$
r_B	$R\frac{E_R}{V}$	$R\,e^{cE_R/V}$	$R\frac{E_R}{V-V_c}$
$E_B = -\frac{\hbar^2}{mr_B^2}$	$-V^2/E_R$	$-E_R e^{-2cE_R/V}$	$-(V-V_c)^2/E_R$

TABLE VI. – *Bound states in 1D, 2D and 3D for a potential well of size R and depth V. $\psi(r > R)$ is the wave function outside the well, r_B is the size of the bound state, and E_B its energy $(E_R = \hbar^2/mR^2)$.*

R. This costs the large kinetic energy $\sim \hbar^2 u''/2mu \approx \hbar^2/mR^2 = E_R$. If the well depth V is smaller than a *critical depth* V_c on the order of E_R, the particle cannot be bound. At $V = V_c$, the first bound state enters at $E = 0$. As $\kappa = 0$, u is then constant outside the well. If the potential depth is further increased by a small amount $\Delta V \ll V_c$, u again falls off like $e^{-\kappa r}$ for $r > R$. This requires an additional change in slope by κ over the distance R, provided by ΔV. So we find analogously to the 1D case $\kappa \sim mR\Delta V/\hbar^2$. Hence, the bound state energy $E_B \approx -\Delta V^2/E_R$ is quadratic in the "detuning" $\Delta V = (V - V_C)$, and the size of the bound state diverges as $r_B \approx RE_R/(V - V_C)$. We will find exactly the same behavior for a weakly bound state when discussing Feshbach resonances in chapter **5**.

The analysis holds for quite general shapes $V(r)$ of the (purely attractive) potential well (in the equations, we only need to replace V by its average over the well - if it exists -, $\frac{1}{R} \int_{-\infty}^{\infty} V(x)dx$ in 1D, $\frac{1}{R^2} \int_0^{\infty} rV(r)dr$ in 2D etc.). Table VI summarizes the different cases.

Applying these results to the equivalent problem of two interacting particles colliding in their center-of-mass frame, we see that in 1D and 2D, two isolated particles can bind for an arbitrarily weak purely attractive interaction. Hence in 1D and 2D, pairing of fermions can be understood already at the two-particle level. Indeed, one can show that the existence of a two-body bound state for isolated particles in 2D is a necessary and sufficient condition for the instability of the many-body Fermi sea (Cooper instability, see below) [193]. In 3D, however, there is a threshold interaction below which two isolated particles are unbound. We conclude that if pairing and condensation occur for arbitrarily weak interactions in 3D, then this must entirely be due to many-body effects.

4˙3.2. *Density of states.* What physical quantity decides whether there are bound states or not? To answer this question, we formulate the problem of two interacting particles of mass m in momentum space. This allows a particularly transparent treatment for all three cases (1D, 2D, 3D) at once, and identifies the *density of states* in the different dimensions as the decisive factor for the existence of bound states.

	1D	2D	3D
$\frac{\hbar^2}{m\Omega}\rho(\epsilon)$	$\frac{1}{\pi}\sqrt{\frac{\hbar^2}{2m\epsilon}}$	$\frac{1}{2\pi}$	$\frac{1}{2\pi^2}\sqrt{\frac{2m\epsilon}{\hbar^2}}$
$\frac{1}{|V_0|} = \frac{1}{\Omega}\int_{\epsilon<E_R}d\epsilon\frac{\rho_n(\epsilon)}{2\epsilon+|E|}$	$\sqrt{\frac{m}{4\hbar^2|E|}}$	$\frac{m}{4\pi\hbar^2}\log\frac{2E_R+|E|}{|E|}$	$\frac{1}{2\pi^2}\frac{m^{3/2}}{\hbar^3}(\sqrt{2E_R}-\frac{\pi}{2}\sqrt{|E|})$
$E = -\frac{\hbar^2\kappa^2}{m}$	$-\frac{m}{4\hbar^2}V_0^2$	$-2E_R\,e^{-\frac{4\pi\hbar^2}{m|V_0|}}$	$-\frac{8}{\pi^2}E_R\frac{(|V_0|-V_{0c})^2}{|V_0|^2} = -\hbar^2/ma^2$

TABLE VII. – *Link between the density of states and the existence of a bound state for arbitrarily weak interaction. The table shows the density of states, $\rho(\epsilon)$, the equation relating the bound state energy E to V_0, and the result for E. It is assumed that $E_R \gg |E|$. To compare with table VI note that $|V_0| \sim VR^n$. $V_{0c} = \sqrt{2}\,\pi^2 E_R R^3$ is the threshold interaction strength for the 3D case. The formula for the 3D bound state energy follows from the renormalization procedure outlined in section 4'2, when expressing V_0 in terms of the scattering length a using Eq. 94.*

Searching for a shallow bound state of energy $E = -\frac{\hbar^2\kappa^2}{m}$ ($m/2$ is the reduced mass), we start by writing the Schrödinger equation for the relative wave function $\frac{\hbar^2}{m}(\nabla^2 - \kappa^2)\psi = V\psi$ in (n-dimensional) momentum space:

$$(100) \qquad \psi_\kappa(\mathbf{q}) = -\frac{m}{\hbar^2}\frac{1}{q^2+\kappa^2}\int\frac{d^nq'}{(2\pi)^n}V(\mathbf{q}-\mathbf{q}')\psi_\kappa(\mathbf{q}')$$

For a short-range potential of range $R \ll 1/\kappa$, $V(\mathbf{q})$ is practically constant, $V(\mathbf{q}) \approx V_0$, for all relevant q, and falls off to zero on a large q-scale of $\approx 1/R$. For example, for a potential well of depth V and size R, we have $V_0 \sim -VR^n$. Thus,

$$(101) \qquad \psi_\kappa(\mathbf{q}) \approx -\frac{mV_0}{\hbar^2}\frac{1}{q^2+\kappa^2}\int_{q'\lesssim\frac{1}{R}}\frac{d^nq'}{(2\pi)^n}\psi_\kappa(\mathbf{q}')$$

We integrate once more over $\mathbf{q}$, applying the same cut-off $1/R$, and then divide by the common factor $\int_{q\lesssim\frac{1}{R}}\frac{d^nq}{(2\pi)^n}\psi_\kappa(\mathbf{q})$. We obtain the following equation for the bound state energy E:

$$(102) \qquad -\frac{1}{V_0} = \frac{m}{\hbar^2}\int_{q\lesssim\frac{1}{R}}\frac{d^nq}{(2\pi)^n}\frac{1}{q^2+\kappa^2} = \frac{1}{\Omega}\int_{\epsilon<E_R}d\epsilon\frac{\rho_n(\epsilon)}{2\epsilon+|E|}$$

with the density of states in n dimensions $\rho_n(\epsilon)$, the energy cut-off $E_R = \hbar^2/mR^2$ and the volume Ω of the system (note that V_0 has units of energy times volume). The question on the existence of bound states for arbitrarily weak interaction has now been reformulated: As $|V_0| \to 0$, the left hand side of Eq. 102 diverges. This equation has a solution for small $|V_0|$ only if the right hand side also diverges for vanishing bound state energy $|E| \to 0$, and this involves an integral over the density of states. Table VII presents the different cases in 1D, 2D, 3D. In 1D, the integral diverges as $1/\sqrt{|E|}$, so one can always find a bound state solution. The binding energy depends quadratically on the interaction, as
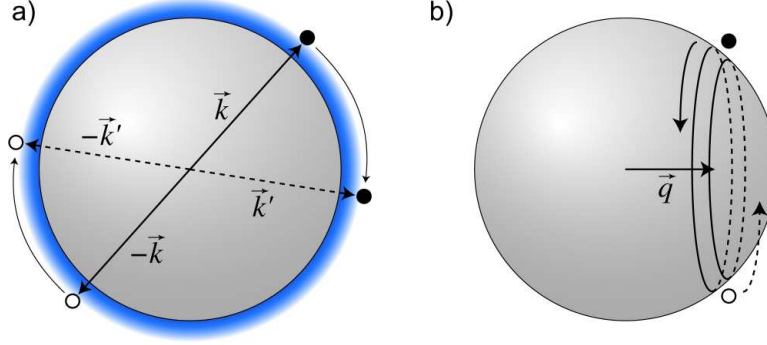
Fig. 20. – Cooper problem: Two particles scattering on top of a Fermi sea. a) Weakly interacting particles with equal and opposite momenta can scatter into final states in a narrow shell (blue-shaded) on top of the Fermi sea (gray shaded), which blocks possible final momentum states. b) For non-zero total momentum $2\mathbf{q}$, particles can scatter only in a narrow band around a circle with radius $\sqrt{k_F^2 - q^2}$.

we had found before. In 2D, where the density of states ρ_{2D} is *constant*, the integral still diverges logarithmically as $|E| \to 0$, so that again there is a solution $|E|$ for any small $|V_0|$. The binding energy now depends exponentially on the interaction and ρ_{2D}:

$$(103) \qquad\qquad E_{2D} = -2E_R\, e^{-\frac{2\Omega}{\rho_{2D}|V_0|}}$$

However, in 3D the integral is finite for vanishing $|E|$, and there is a threshold for the interaction potential to bind the two particles.

These results give us an idea why there might be a paired state for two fermions immersed in a medium, even for arbitrarily weak interactions: It could be that the density of available states to the two fermions is altered due to the presence of the other atoms. This is exactly what happens, as will be discussed in the next section.

4˙3.3. Pairing of fermions – The Cooper problem. Consider now two weakly interacting spin 1/2 fermions not in vacuum, but on top of a (non-interacting) filled Fermi sea, the Cooper problem [33]. Momentum states below the Fermi surface are not available to the two scattering particles due to Pauli blocking (Fig. 20a). For weak interactions, the particles' momenta are essentially confined to a narrow shell above the Fermi surface. The density of states at the Fermi surface is $\rho_{3D}(E_F)$, which is a constant just like in two dimensions. We should thus find a *bound state* for the two-particle system *for arbitrarily weak attractive interaction*.

In principle, the two fermions could form a pair at any finite momentum. However, considering the discussion in the previous section, the largest binding energy can be expected for the pairs with the largest density of scattering states. For zero-momentum pairs, the entire Fermi surface is available for scattering, as we can see from Fig. 20a. If the pairs have finite center-of-mass momentum $\mathbf{q}$, the number of contributing states is

strongly reduced, as they are confined to a circle (see Fig. 20b). Consequently, pairs at rest experience the strongest binding. In the following we will calculate this energy.

We can write the Schrödinger equation for the two interacting particles as before, but now we need to search for a small binding energy $E_B = E - 2E_F < 0$ on top of the large Fermi energy $2E_F$ of the two particles. The equation for E_B is

$$(104) \qquad -\frac{1}{V_0} = \frac{1}{\Omega} \int_{E_F < \epsilon < E_F + E_R} d\epsilon \frac{\rho_{3D}(\epsilon)}{2(\epsilon - E_F) + |E_B|}$$

The effect of Pauli blocking of momentum states below the Fermi surface is explicitly included by only integrating over energies $\epsilon > E_F$.

In conventional superconductors, the natural cut-off energy E_R is given by the Debye frequency ω_D, $E_R = \hbar\omega_D$, corresponding to the highest frequency at which ions in the crystal lattice can respond to a bypassing electron. Since we have $\hbar\omega_D \ll E_F$, we can approximate $\rho_{3D}(\epsilon) \approx \rho_{3D}(E_F)$ and find:

$$(105) \qquad E_B = -2\hbar\omega_D e^{-2\Omega/\rho_{3D}(E_F)|V_0|}$$

In the case of an atomic Fermi gas, we should replace $1/V_0$ by the physically relevant scattering length $a < 0$ using the prescription in Eq. 94. The equation for the bound state becomes

$$(106) \qquad -\frac{m}{4\pi\hbar^2 a} = \frac{1}{\Omega} \int_{E_F}^{E_F + E_R} d\epsilon \frac{\rho_{3D}(\epsilon)}{2(\epsilon - E_F) + |E_B|} - \frac{1}{\Omega} \int_0^{E_F + E_R} d\epsilon \frac{\rho_{3D}(\epsilon)}{2\epsilon}$$

The right hand expression is now finite as we let the cut-off $E_R \to \infty$, the result being (one assumes $|E_B| \ll E_F$)

$$(107) \qquad -\frac{m}{4\pi\hbar^2 a} = \frac{\rho_{3D}(E_F)}{2\Omega} \left(-\log\left(\frac{|E_B|}{8E_F}\right) - 2 \right)$$

Inserting $\rho_{3D}(E_F) = \frac{\Omega m k_F}{2\pi^2 \hbar^2}$ with the Fermi wave vector $k_F = \sqrt{2mE_F/\hbar^2}$, one arrives at

$$(108) \qquad E_B = -\frac{8}{e^2} E_F \, e^{-\pi/k_F|a|}$$

The binding energies Eqs. 105 and 108 can be compared with the result for the bound state of two particles in 2D, Eq. 103. The role of the constant density of states ρ_{2D} is here played by the 3D density of states at the Fermi surface, $\rho_{3D}(E_F)$.

The result is remarkable: Two weakly interacting fermions on top of a Fermi sea form a bound state due to Pauli blocking. However, in this artificial problem we neglected the interactions between particles *in* the Fermi sea. As we "switch on" the interactions for all particles from top to the bottom of the Fermi sea, the preceding discussion indicates that the gas will reorder itself into a completely new, paired state. The Fermi sea is thus

unstable towards pairing (Cooper instability). The full many-body description of such a paired state, including the necessary anti-symmetrization of the full wave function, was achieved by Bardeen, Cooper and Schrieffer (BCS) in 1957 [34]. As we will see in the next section, the self-consistent inclusion of all fermion pairs leads to more available momentum space for pairing. The effective density of states is then twice as large, giving a superfluid gap Δ that differs from $|E_B|$ (Eq. 108) by a factor of 2 in the exponent:

$$(109) \qquad\qquad \Delta = \frac{8}{e^2} E_F \, e^{-\pi/2k_F|a|}$$

It should be noted that the crucial difference to the situation of two particles in vacuum in 3D is the constant density of states at the Fermi energy (and not the 2D character of the Fermi surface). Therefore, if we were to consider the Cooper problem in higher dimensions n and have two fermions scatter on the $(n-1)$ dimensional Fermi surface, the result would be similar to the 2D case (due to the constant density of states), and not to the case of $(n-1)$ dimensions.

The conclusion of this section is that Cooper pairing is a many-body phenomenon, but the binding of two fermions can still be understood by two-body quantum mechanics, as it is similar to two isolated particles in two dimensions. To first order, the many-body physics is not the modification of interactions, but rather the modification of the density of states due to Pauli blocking.

4˙4. *Crossover wave function*. – From section **4**˙3.1 we know that in 3D, two fermions in isolation can form a molecule for strong enough attractive interaction. The ground state of the system should be a Bose-Einstein condensate of these tightly bound pairs. However, if we increase the density of particles in the system, we will ultimately reach the point where the Pauli pressure of the fermionic constituents becomes important and modifies the properties of the system. When the Fermi energy of the constituents exceeds the binding energy of the molecules, we expect that the equation of state will be fermionic, i.e. the chemical potential will be proportional to the density to the power of 2/3. Only when the size of the molecules is much smaller than the interparticle spacing, i.e. when the binding energy largely exceeds the Fermi energy, is the fermionic nature of the constituents irrelevant – tightly bound fermions are spread out widely in momentum space and do not run into the Pauli limitation of unity occupation per momentum state.

For too weak an attraction there is no bound state for two isolated fermions, but Cooper pairs can form in the medium as discussed above. The ground state of the system turns out to be a condensate of Cooper pairs as described by BCS theory. In contrast to the physics of molecular condensates, however, the binding energy of these pairs is much less than the Fermi energy and therefore Pauli pressure plays a major role.

It was realized by Leggett [40], building upon work by Popov [37], Keldysh [38] and Eagles [39], that the crossover from the BCS- to the BEC-regime is smooth. This is somewhat surprising since the two-body physics shows a threshold behavior at a critical interaction strength, below which there is no bound state for two particles. In the presence of the Fermi sea, however, we simply cross over from a regime of tightly bound

molecules to a regime where the pairs are of much larger size than the interparticle spacing. Closely following Leggett's work [40], and its extension to finite temperatures by Nozières and Schmitt-Rink [41], we will describe the BEC-BCS crossover in a simple "one-channel" model of a potential well. Rather than the interaction strength V_0 as in section $\mathbf{4}\dot{}3.1$, we will take the scattering length a as the parameter that "tunes" the interaction. The relation between V_0 and a is given by Eq. 94 and its explicit form Eq. 96. For positive $a > 0$, there is a two-body bound state available at $E_B = -\hbar^2/ma^2$ (see table VII), while small and negative $a < 0$ corresponds to weak attraction where Cooper pairs can form in the medium. In either case, for s-wave interactions, the orbital part of the pair wave function $\varphi(\mathbf{r}_1, \mathbf{r}_2)$ will be symmetric under exchange of the paired particles' coordinates and, in a uniform system, will only depend on their distance $|\mathbf{r}_1 - \mathbf{r}_2|$. We will explore the many-body wave function

$$(110) \qquad \Psi\left(\mathbf{r}_1, \ldots, \mathbf{r}_N\right) = \mathcal{A}\left\{\varphi(|\mathbf{r}_1 - \mathbf{r}_2|)\chi_{12} \ldots \varphi(|\mathbf{r}_{N-1} - \mathbf{r}_N|)\chi_{N-1,N}\right\}$$

that describes a condensate of such fermion pairs, with the operator $\mathcal{A}$ denoting the correct antisymmetrization of all fermion coordinates, and the spin singlet $\chi_{ij} = \frac{1}{\sqrt{2}}(|\uparrow\rangle_i |\downarrow\rangle_j - |\downarrow\rangle_i |\uparrow\rangle_j)$. In the experiment, "spin up" and "spin down" will correspond to two atomic hyperfine states.

In second quantization notation we write

$$(111) \quad |\Psi\rangle_N = \int \prod_i d^3r_i \, \varphi(\mathbf{r}_1 - \mathbf{r}_2)\Psi_\uparrow^\dagger(\mathbf{r}_1)\Psi_\downarrow^\dagger(\mathbf{r}_2) \ldots \varphi(\mathbf{r}_{N-1} - \mathbf{r}_N)\Psi_\uparrow^\dagger(\mathbf{r}_{N-1})\Psi_\downarrow^\dagger(\mathbf{r}_N) |0\rangle$$

where the fields $\Psi_\sigma^\dagger(\mathbf{r}) = \sum_k c_{k\sigma}^\dagger \frac{e^{-i\mathbf{k}\cdot\mathbf{r}}}{\sqrt{\Omega}}$. With the Fourier transform $\varphi(\mathbf{r}_1 - \mathbf{r}_2) = \sum_k \varphi_k \frac{e^{i\mathbf{k}\cdot(\mathbf{r}_1 - \mathbf{r}_2)}}{\sqrt{\Omega}}$ we can introduce the pair creation operator

$$(112) \qquad\qquad b^\dagger = \sum_k \varphi_k c_{k\uparrow}^\dagger c_{-k\downarrow}^\dagger$$

and find

$$(113) \qquad\qquad |\Psi\rangle_N = b^{\dagger N/2} |0\rangle$$

This expression for $|\Psi\rangle_N$ is formally identical to the Gross-Pitaevskii ground state of a condensate of bosonic particles. However, the operators $b^\dagger$ obey bosonic commutation relations only in the limit of tightly bound pairs. For the commutators, we obtain

$$(114) \quad \left[b^\dagger, b^\dagger\right]_- = \sum_{kk'} \varphi_k \varphi_{k'} \left[c_{k\uparrow}^\dagger c_{-k\downarrow}^\dagger, c_{k'\uparrow}^\dagger c_{-k'\downarrow}^\dagger\right]_- = 0$$

$$\left[b, b\right]_- = \sum_{kk'} \varphi_k^* \varphi_{k'}^* \left[c_{-k\downarrow} c_{k\uparrow}, c_{-k'\downarrow} c_{k'\uparrow}\right]_- = 0$$

$$\left[b, b^\dagger\right]_- = \sum_{kk'} \varphi_k^* \varphi_{k'} \left[c_{-k\downarrow} c_{k\uparrow}, c_{k'\uparrow}^\dagger c_{-k'\downarrow}^\dagger\right]_- = \sum_k |\varphi_k|^2 (1 - n_{k\uparrow} - n_{k\downarrow})$$

The third commutator is equal to one only in the limit where the pairs are tightly bound and occupy a wide region in momentum space. In this case, the occupation numbers n_k of any momentum state k are very small (see section $4\dot{\,}6.3$ below), and $\left[b, b^\dagger\right]_- \approx \sum_k |\varphi_k|^2 = \int \mathrm{d}^3 r_1 \int \mathrm{d}^3 r_2 \, |\varphi(\mathbf{r}_1, \mathbf{r}_2)|^2 = 1$.

Working with the N-particle state $|\Psi\rangle_N$ is inconvenient, as one would face a complicated combinatoric problem in manipulating the sum over all the $c_k^\dagger$'s (as one chooses a certain k for the first fermion, the choices for the second depend on this k, etc.). It is preferable to use the grand canonical formalism, not fixing the number of atoms but the chemical potential μ. A separate, crucial step is to define a many-body state which is a superposition of states with different atom numbers. In the BEC limit, this is analogous to the use of coherent states (vs. Fock states) in quantum optics. Let $N_p = N/2$ be the number of pairs. Then,

$$\mathcal{N}\,|\Psi\rangle \quad = \sum_{J_{\text{even}}} \frac{N_p^{J/4}}{(J/2)!} \, |\Psi\rangle_J \quad = \sum_M \frac{1}{M!} N_p^{M/2} \, b^{\dagger\,M} \, |0\rangle = e^{\sqrt{N_p}\, b^\dagger}\, |0\rangle$$

(115)
$$= \prod_k e^{\sqrt{N_p}\, \varphi_k c_{k\uparrow}^\dagger c_{-k\downarrow}^\dagger} \, |0\rangle = \prod_k (1 + \sqrt{N_p}\, \varphi_k\, c_{k\uparrow}^\dagger c_{-k\downarrow}^\dagger)\, |0\rangle$$

The second to last equation follows since the operators $c_{k\uparrow}^\dagger c_{-k\downarrow}^\dagger$ commute for different k, and the last equation follows from $c_k^{\dagger 2} = 0$. If we choose the constant $\mathcal{N} = \prod_k \frac{1}{u_k} = \prod_k \sqrt{1 + N_p|\varphi_k|^2}$, then $|\Psi\rangle$ becomes a properly normalized state

(116)
$$|\Psi_{\text{BCS}}\rangle = \prod_k (u_k + v_k c_{k\uparrow}^\dagger c_{-k\downarrow}^\dagger)\, |0\rangle$$

with $v_k = \sqrt{N_p}\, \varphi_k u_k$ and $|u_k|^2 + |v_k|^2 = 1$. This is the famous BCS wave function, first introduced as a variational Ansatz, later shown to be the exact solution of the simplified Hamiltonian Eq. 118 (below). It is a product of wave functions referring to the occupation of pairs of single-particle momentum states, $(\mathbf{k}, \uparrow, -\mathbf{k}, \downarrow)$. As a special case, it describes a non-interacting Fermi sea, with all momentum pairs occupied up to the Fermi momentum ($u_k = 0, v_k = 1$ for $k < k_F$ and $u_k = 1, v_k = 0$ for $k > k_F$). In general, for a suitable choice of the v_k's and u_k's, it describes a "molten" Fermi sea, modified by the coherent scattering of pairs with zero total momentum. Pairs of momentum states are seen to be in a superposition of being fully empty and fully occupied. The above derivation makes it clear that this wave function encompasses the entire regime of pairing, from point bosons (small molecules) to weakly and non-interacting fermions.

$4\dot{\,}5$. *Gap and number equation.* – The variational parameters u_k and v_k are derived in the standard way by minimizing the free energy $E - \mu N = \left\langle \hat{H} - \mu \hat{N} \right\rangle$. The many-body Hamiltonian for the system is

(117)
$$\hat{H} = \sum_{k,\sigma} \epsilon_k c_{k\sigma}^\dagger c_{k\sigma} + \frac{V_0}{\Omega} \sum_{k,k',q} c_{k+\frac{q}{2}\uparrow}^\dagger c_{-k+\frac{q}{2}\downarrow}^\dagger c_{k'+\frac{q}{2}\downarrow} c_{-k'+\frac{q}{2}\uparrow}$$

90

The dominant role in superfluidity is played by fermion pairs with zero total momentum. Indeed, as we have seen in section **4·3.3**, Cooper pairs with zero momentum have the largest binding energy. Therefore, we simplify the mathematical description by neglecting interactions between pairs at finite momentum, i.e. we only keep the terms for $\mathbf{q} = 0$. This is a very drastic simplification, as hereby density fluctuations are eliminated. It is less critical for charged superfluids, where density fluctuations are suppressed by Coulomb interactions. However, for neutral superfluids, sound waves (the Bogoliubov-Anderson mode, see section **4·7.3**) are eliminated by this approximation. The approximate Hamiltonian ("BCS Hamiltonian") reads

$$(118) \qquad \hat{H} = \sum_{k,\sigma} \epsilon_k c_{k\sigma}^\dagger c_{k\sigma} + \frac{V_0}{\Omega} \sum_{k,k'} c_{k\uparrow}^\dagger c_{-k\downarrow}^\dagger c_{k'\downarrow} c_{-k'\uparrow}$$

The free energy becomes

$$(119) \qquad \mathcal{F} = \left\langle \hat{H} - \mu\hat{N} \right\rangle = \sum_k 2\xi_k v_k^2 + \frac{V_0}{\Omega} \sum_{k,k'} u_k v_k u_{k'} v_{k'}$$

$$\text{with } \xi_k = \epsilon_k - \mu$$

Minimizing $E - \mu N$ leads to

$$v_k^2 = \frac{1}{2}\left(1 - \frac{\xi_k}{E_k}\right)$$

$$u_k^2 = \frac{1}{2}\left(1 + \frac{\xi_k}{E_k}\right)$$

$$(120) \qquad \text{with } E_k = \sqrt{\xi_k^2 + \Delta^2}$$

where Δ is given by the *gap equation* $\Delta \equiv \frac{V_0}{\Omega} \sum_k \left\langle c_{k\uparrow} c_{-k\downarrow} \right\rangle = -\frac{V_0}{\Omega} \sum_k u_k v_k = -\frac{V_0}{\Omega} \sum_k \frac{\Delta}{2E_k}$ or

$$(121) \qquad -\frac{1}{V_0} = \int \frac{d^3k}{(2\pi)^3} \frac{1}{2E_k}$$

Note the similarity to the bound state equation in free space, Eq. 102, and in the simplified Cooper problem, Eq. 104. An additional constraint is given by the *number equation* for the total particle density $n = N/\Omega$

$$(122) \qquad n = 2 \int \frac{d^3k}{(2\pi)^3} v_k^2$$

Gap and number equations have to be solved simultaneously to yield the two unknowns μ and Δ. We will once more replace V_0 by the scattering length a using prescription

Eq. 94, so that the gap equation becomes (compare Eq. 106)

$$(123) \qquad -\frac{m}{4\pi\hbar^2 a} = \int \frac{d^3k}{(2\pi)^3} \left(\frac{1}{2E_k} - \frac{1}{2\epsilon_k} \right)$$

where the integral is now well-defined. The equations can be rewritten in dimensionless form with the Fermi energy $E_F = \hbar^2 k_F^2/2m$ and wave vector $k_F = (3\pi^2 n)^{1/3}$ [194]

$$(124) \qquad -\frac{1}{k_F a} = \frac{2}{\pi} \sqrt{\frac{\Delta}{E_F}} \, I_1\left(\frac{\mu}{\Delta}\right)$$

$$(125) \qquad 1 = \frac{3}{2} \left(\frac{\Delta}{E_F} \right)^{3/2} I_2\left(\frac{\mu}{\Delta}\right)$$

$$(126) \qquad \text{with } I_1(z) = \int_0^\infty dx \, x^2 \left(\frac{1}{\sqrt{(x^2 - z)^2 + 1}} - \frac{1}{x^2} \right)$$

$$(127) \qquad \text{and } I_2(z) = \int_0^\infty dx \, x^2 \left(1 - \frac{x^2 - z}{\sqrt{(x^2 - z)^2 + 1}} \right)$$

This gives

$$(128) \qquad -\frac{1}{k_F a} = \frac{2}{\pi} \left(\frac{2}{3 I_2\left(\frac{\mu}{\Delta}\right)} \right)^{1/3} I_1\left(\frac{\mu}{\Delta}\right)$$

$$(129) \qquad \frac{\Delta}{E_F} = \left(\frac{2}{3 I_2\left(\frac{\mu}{\Delta}\right)} \right)^{2/3}$$

The first equation can be inverted to obtain μ/Δ as a function of the *interaction parameter* $1/k_F a$, which can then be inserted into the second equation to yield the gap Δ. The result for μ and Δ as a function of $1/k_F a$ is shown in Fig. 21. It is possible to obtain analytic expressions for the solutions in terms of complete elliptic integrals [195].

In this derivation, we have combined the simplified Hamiltonian, Eq. 118 with the BCS variational Ansatz. Alternatively one can apply a decoupling (mean field) approximation to the Hamiltonian [169]. Expecting that there will be some form of pair condensate, we assume that the pair creation and annihilation operator only weakly fluctuates around its non-zero expectation value

$$(130) \qquad C_k = \langle c_{k\uparrow} c_{-k\downarrow} \rangle = -\left\langle c_{k\uparrow}^\dagger c_{-k\downarrow}^\dagger \right\rangle$$

chosen to be real (since the relative phase of states which differ in particle number by
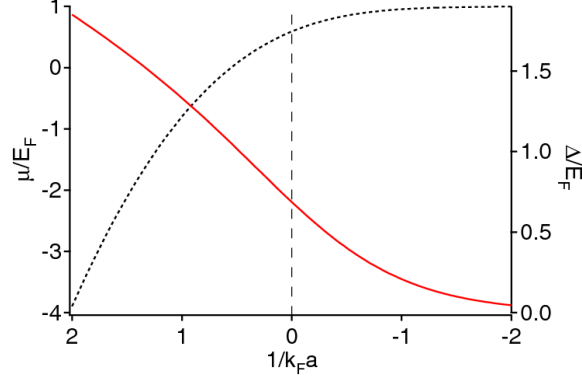
Fig. 21. – Chemical potential (dotted line) and gap (straight line, red) in the BEC-BCS crossover as a function of the interaction parameter $1/k_F a$. The BCS-limit of negative $1/k_F a$ is to the right on the graph. The resonance where $1/k_F a = 0$ is indicated by the dashed line.

two can be arbitrarily chosen). That is, we write

$$(131) \qquad c_{k\uparrow} c_{-k\downarrow} = C_k + (c_{k\uparrow} c_{-k\downarrow} - C_k)$$

with the operator in parentheses giving rise to fluctuations that are small on the scale of C_k. The gap parameter Δ is now defined as

$$(132) \qquad \Delta = \frac{V_0}{\Omega} \sum_k C_k$$

We only include terms in the interaction part of the Hamiltonian which involve the C_k's at least once. That is, we neglect the correlation of fluctuations of the pair creation and annihilation operators. One obtains

$$(133) \qquad \hat{H} = \sum_k \epsilon_k (c_{k\uparrow}^\dagger c_{k\uparrow} + c_{k\downarrow}^\dagger c_{k\downarrow}) - \Delta \sum_k \left(c_{k\uparrow}^\dagger c_{-k\downarrow}^\dagger + c_{k\downarrow} c_{-k\uparrow} + \sum_{k'} C_{k'} \right)$$

This Hamiltonian is bilinear in the creation and annihilation operators and can easily be solved by a Bogoliubov transformation [196, 197, 169] from the particle operators $c_{k\downarrow}$ and $c_{k\uparrow}$ to new quasi-particle operators $\gamma_{k\uparrow}$ and $\gamma_{k\downarrow}$:

$$(134) \qquad \gamma_{k\uparrow} = u_k c_{k\uparrow} - v_k c_{-k\downarrow}^\dagger$$
$$\gamma_{-k\downarrow}^\dagger = u_k c_{-k\downarrow}^\dagger + v_k c_{k\uparrow}$$

The u_k and v_k are determined from the requirements that the new operators fulfill fermionic commutation relations and that the transformed Hamiltonian is diagonal with

respect to the quasiparticle operators. This solution is identical to the one obtained before for the u_k and v_k, and the transformed Hamiltonian becomes

$$(135) \qquad \hat{H} - \mu\hat{N} = -\frac{\Delta^2}{V_0/\Omega} + \sum_k (\xi_k - E_k) + \sum_k E_k(\gamma_{k\uparrow}^\dagger \gamma_{k\uparrow} + \gamma_{k\downarrow}^\dagger \gamma_{k\downarrow})$$

The first two terms give the free energy $E - \mu N$ of the pair condensate, identical to Eq. 119 when the correct u_k and v_k are inserted. The third term represents the energy of excited quasi-particles, and we identify E_k as excitation energy of a quasi-particle. The superfluid ground state is the quasi-particle vacuum: $\gamma_{k\uparrow}|\Psi\rangle = 0 = \gamma_{k\downarrow}|\Psi\rangle$.

This approach via the pairing field is analogous to the Bogoliubov treatment of an interacting Bose-Einstein condensate: There, the creation and annihilation operators for atoms with zero momentum are replaced by $\sqrt{N_0}$, the square root of the number of condensed atoms (i.e. a coherent field). In the interaction term of the Hamiltonian all terms are dropped that contain less than two factors of $\sqrt{N_0}$. In other words, the Hamiltonian (Eq. 118) is solved by keeping only certain pair interactions, either by using a variational pairing wave function, or by introducing a mean pairing field. It should be noted that these approximations are not even necessary, as the BCS wave function can be shown to be the *exact* solution to the reduced Hamiltonian *Eq.* 118 [198].

4˙6. *Discussion of the three regimes – BCS, BEC and crossover*. –

4˙6.1.   BCS limit. In the BCS-limit of weak attractive interaction, $k_F a \to 0_-$, we have[9]

$$(136) \qquad \mu \approx E_F$$

$$(137) \qquad \Delta \approx \frac{8}{e^2} e^{-\pi/2k_F|a|}$$

The first equation tells us that adding a spin up and spin down particle to the system costs a Fermi energy per particle (with the implicit assumption that both a spin up and a spin down particle are added, raising the total energy by 2μ). In the weakly interacting BCS limit Pauli blocking still dominates over interactions, and hence the particles can only be added at the Fermi surface. The second equation is the classic result of BCS theory for the superfluid gap[10]. Compared to the bound state energy for a single Cooper pair on top of a non-interacting Fermi sea, Eq. 108, the gap is larger (the negative exponent is smaller by a factor of two), as the entire collection of particles now takes part in the pairing[11]. However, the gap is still exponentially small compared to

---

[9] This follows by substituting $\xi = x^2 - z$ in the integrals and taking the limit $z \to \infty$. One has $I_1(z) \approx \sqrt{z}\,(\log(8z) - 2)$ and $I_2(z) = \frac{2}{3}z^{3/2}$.

[10] The present mean field treatment does not include density fluctuations, which modify the prefactor in the expression for the gap Δ [199, 169].

[11] In the self-consistent BCS solution, not only the momentum states above the Fermi surface

the Fermi energy: Cooper pairing is fragile.

The ground state energy of the BCS state can be calculated from Eq. 119 and is

$$(138) \qquad E_{\text{G, BCS}} = \frac{3}{5} N E_F - \frac{1}{2} \rho(E_F) \Delta^2$$

The first term is the energy of the non-interacting normal state, where $\frac{3}{5} E_F$ is the average kinetic energy per fermion in the Fermi sea. The second term is the energy due to condensation, negative as it should be, indicating that the BCS state is energetically favorable compared to the normal state.

Although the total kinetic energy of the Fermi gas has been increased (by populating momentum states above E_F), the total energy is lower due to the gain in potential energy. This is valid for any kind of pairing (i.e. proton and electron forming a hydrogen atom), since the localization of the pair wave function costs kinetic energy.

The energy of the BCS state, $-\frac{1}{2} \rho(E_F) \Delta^2$ can be interpreted in two ways. One way refers to the wave function Eq. 110, which consists of $N/2$ identical fermion pairs. The energy per pair is then $-\frac{3}{4} \Delta^2 / E_F$. The other interpretation refers to the BCS wave function Eq. 116. It is essentially a product of a "frozen" Fermi sea (as $v_k \approx 1$, $u_k \approx 0$ for low values of k) with a paired component consisting of $\sim \rho(E_F) \Delta \sim N \Delta / E_F$ pairs, located in an energy shell of width Δ around the Fermi energy. They each contribute a pairing energy on the order of Δ. The second interpretation justifies the picture of a Cooper pair condensate. In the solution of the Cooper problem (section **4**˙3.3), the pair wave function has a peak occupation per momentum state of $\sim 1/\rho(E_F)\Delta$. Therefore, one can stack up $\sim \rho(E_F)\Delta$ pairs with zero total momentum without getting into serious trouble with the Pauli exclusion principle and construct a Bose-Einstein condensate consisting of $\sim \rho(E_F)\Delta$ Cooper pairs ([12]).

It depends on the experiment whether it reveals a pairing energy of $\frac{1}{2}\Delta^2/E_F$ or of Δ. In RF spectroscopy, all momentum states can be excited (see section **2**˙3), and the spectrum shows a gap of $\frac{1}{2}\Delta^2/E_F$ (see section **4**˙7.2). Tunnelling experiments in superconductors probe the region close to the Fermi surface, and show a pairing gap of Δ.

The two interpretations for the BCS energy carry along two possible choices of the pairing wave function (see section **4**˙6.3). The first one is $\varphi_k = u_k/v_k \sqrt{N_p}$, which can be shown to extend throughout the whole Fermi sea from zero to slightly above k_F, whereas the second one, $\psi(k) = u_k v_k$, is concentrated around the Fermi surface (see Fig. 25).

To give a sense of scale, Fermi energies in dilute atomic gases are on the order of a

---

contribute to pairing, but also those *below* it, in a symmetric shell around the Fermi momentum. In the Cooper problem the states below the Fermi surface were excluded, reducing the effective density of states by a factor of two.

([12]) Similarly to the fermion pairs described by the operator $b^\dagger$, the Cooper pairs from section **4**˙3.3 are not bosons, as shown by the equivalent of Eq. 114. However, if there were only a few Cooper pairs, much less than $\rho(E_F)\Delta$, the occupation of momentum states n_k would still be very small compared to 1 and these pairs would be to a good approximation bosons.

μK, corresponding to $1/k_F \sim 4\,000\, a_0$. In the absence of scattering resonances, a typical scattering length would be about $50 - 100\, a_0$ (on the order of the van der Waals-range). Even if $a < 0$, this would result in a vanishingly small gap $\Delta/k_B \approx 10^{-30} \dots 10^{-60}\,$K. Therefore, the realization of superfluidity in Fermi gases requires scattering or Feshbach resonances to increase the scattering length, bringing the gas into the strongly interacting regime where $k_F\,|a| > 1$ (see chapter **5**). In this case, the above mean field theory predicts $\Delta > 0.22\, E_F$ or $\Delta/k_B > 200\,$nK for $k_F|a| > 1$, and this is the regime where current experiments are operating.

4˙6.2. BEC limit. In the BEC limit of tightly bound pairs, for $k_F a \to 0_+$, one finds[13]

$$\text{(139)} \qquad \mu = -\frac{\hbar^2}{2ma^2} + \frac{\pi\hbar^2 a n}{m}$$

$$\text{(140)} \qquad \Delta \approx \sqrt{\frac{16}{3\pi}} \frac{E_F}{\sqrt{k_F a}}$$

The first term in the expression for the chemical potential is the binding energy per fermion in a tightly bound molecule (see table VII). This reflects again the implicit assumption (made by using the wave function in Eq. 110) that we always add *two* fermions of opposite spin at the same time to the system.

The second term is a mean field contribution describing the repulsive interaction between molecules in the gas. Indeed, a condensate of molecules of mass $m_M = 2m$, density $n_M = n/2$ and a molecule-molecule scattering length a_M will have a chemical potential $\mu_M = \frac{4\pi\hbar^2 a_M n_M}{m_M}$. Since μ_M is twice the chemical potential for each fermion, we obtain from the above expression the molecule-molecule scattering length $a_M = 2a$. However, this result is not exact. Petrov, Shlyapnikov and Salomon [200] have performed an exact calculation for the interaction between four fermions and shown that $a_M = 0.6\,a$. The present mean field approach neglects correlations between different pairs, or between one fermion and a pair. If those are included, the correct few-body physics is recovered [201, 202, 203].

The expression for the quantity Δ signifies neither the binding energy of molecules nor does it correspond to a gap in the excitation spectrum. Indeed, in the BEC-regime, as soon as $\mu < 0$, there is no longer a gap at non-zero k in the single-fermion excitation spectrum (see Fig. 23 below). Instead, we have for the quasi-particle energies $E_k = \sqrt{(\epsilon_k - \mu)^2 + \Delta^2} \approx |\mu| + \epsilon_k + \frac{\Delta^2}{2|\mu|}$. So Δ itself does not play a role in the BEC-regime, but only the combination $\Delta^2/|\mu|$ is important. As we see from Eq. 139,

$$\text{(141)} \qquad \frac{\Delta^2}{2|\mu|} = \frac{8}{3\pi}\frac{E_F^2}{k_F a}\frac{2ma^2}{\hbar^2} = \frac{4}{3\pi}\frac{\hbar^2}{m}k_F^3 a = \frac{4\pi\hbar^2}{m}n\,a$$

---

[13] This result follows from the expansion of the integrals for $z < 0$ and $|z| \to \infty$. One finds $I_1(z) = -\frac{\pi}{2}\sqrt{|z|} - \frac{\pi}{32}\frac{1}{|z|^{3/2}}$ and $I_2(z) = \frac{\pi}{8}\frac{1}{\sqrt{|z|}}$.
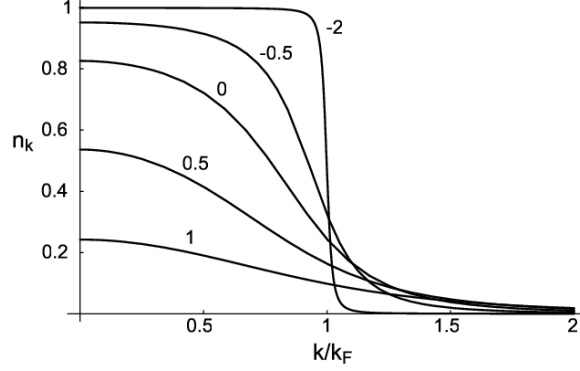
Fig. 22. – Occupation n_k of momentum states k in the BEC-BCS crossover. The numbers give the interaction parameter $1/k_F a$. After [41].

which is two times the molecular mean field. In fact, we will show in section **4˙7** that it can be interpreted here as the mean field energy experienced by a single fermion in a gas of molecules.

It might surprise that the simplified Hamiltonian Eq. 118 contains interactions between two molecules or between a molecule and a single fermion at all. In fact, a crucial part of the simplification has been to explicitly *neglect* such three- and four-body interactions. The solution to this puzzle lies in the Pauli principle, which acts as an effective repulsive interaction: In a molecule, each constituent fermion is confined to a region of size $\sim a$ around the molecule's center of mass (see next section). The probability to find another like fermion in that region is strongly reduced due to Pauli blocking. Thus, effectively, the motion of molecules is constrained to a reduced volume $\Omega' = \Omega - cN_M a_M^3$, with the number of molecules N_M and c on the order of 1. This is the same effect one has for a gas of hard-sphere bosons of size a_M, and generally for a Bose gas with scattering length a_M. An analogous argument leads to the effective interaction between a single fermion and a molecule. We see that the only way interactions between pairs, or between a pair and a single fermion, enter in the simplified description of the BEC-BCS crossover is via the anti-symmetry of the many-body wave function.

4˙6.3. Evolution from BCS to BEC. Our variational approach smoothly interpolates between the two known regimes of a BCS-type superfluid and a BEC of molecules. It is a crossover, which occurs approximately between $1/k_F a = -1$ and $+1$ and is fully continuous. The occupation of momentum states $n_k = v_k^2$ evolves smoothly from the step-function $\Theta(k_F - k)$ of a degenerate Fermi gas, broadened over a width $\Delta \ll E_F$ due to pairing, to that of N_p molecules, namely the number of molecules N_p times the probability $|\varphi_k|^2$ to find a molecule with momentum k (we have $\varphi_k = \frac{(2\pi a)^{3/2}}{\sqrt{\Omega}} \frac{1}{\pi} \frac{1}{1+k^2 a^2}$) (see Fig. 22). It is also interesting to follow the evolution of the "Cooper pair" wave
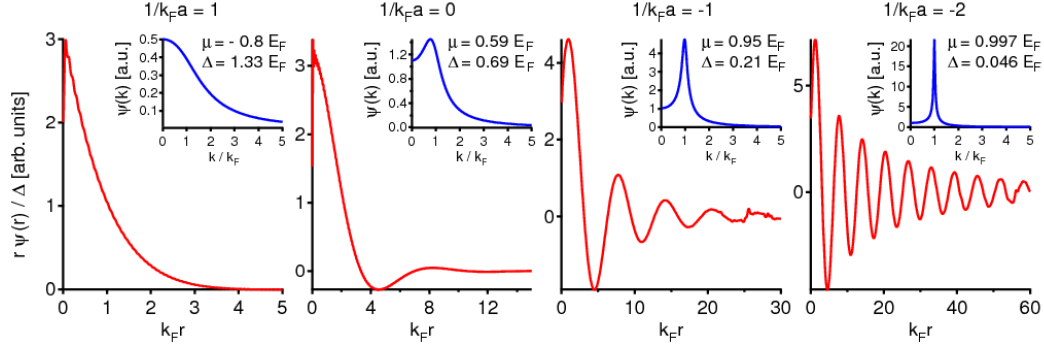
97

Fig. 23. – Evolution of the spatial pair wave function $\psi(r)$ in the BEC-BCS crossover. The inset shows the Fourier transform $\psi(k)$, showing clearly that in the BCS-limit, momentum states around the Fermi surface make the dominant contribution to the wave function. In the crossover, the entire Fermi sphere takes part in the pairing. In the BEC-limit, $\psi(k)$ broadens as the pairs become more and more tightly bound. $\psi(r)$ was obtained via numerical integration of $\int_{-\mu}^{\infty} d\xi \frac{\sin(r\sqrt{\xi+\mu})}{\sqrt{\xi^2+\Delta^2}}$ (here, $\hbar = 1 = m$), an expression that follows from Eq. 142.

function[14] both in k-space, where it is given by $\langle \Psi_{BCS}| c_{k\uparrow}^{\dagger} c_{-k\downarrow}^{\dagger} |\Psi_{BCS}\rangle = u_k v_k$, and in real space, where it is

$$\psi(\mathbf{r}_1, \mathbf{r}_2) = \langle \Psi_{BCS}| \Psi_{\uparrow}^{\dagger}(\mathbf{r}_1)\Psi_{\downarrow}^{\dagger}(\mathbf{r}_2) |\Psi_{BCS}\rangle = \frac{1}{\Omega} \sum_k u_k v_k e^{-i\mathbf{k}\cdot(\mathbf{r}_1-\mathbf{r}_2)}$$

$$(142) \qquad = \frac{1}{\Omega} \sum_k \frac{\Delta}{2E_k} e^{-i\mathbf{k}\cdot(\mathbf{r}_1-\mathbf{r}_2)}$$

In the BCS limit, the pairing occurs near the Fermi surface $k = k_F$, in a region of width $\delta k \sim \frac{\partial k}{\partial \epsilon} \delta \epsilon \approx \frac{\Delta}{\hbar v_F}$, where v_F is the velocity of fermions at the Fermi surface. Therefore, the spatial wave function of Cooper pairs has a strong modulation at the inverse wave vector $1/k_F$, and an overall extent of the inverse width of the pairing region, $\sim 1/\delta k \sim \frac{\hbar v_F}{\Delta} \gg 1/k_F$. More quantitatively, Eq. 142 gives (setting $r = |\mathbf{r}_1 - \mathbf{r}_2|$) [34]

$$(143) \qquad \psi(r) = \frac{k_F}{\pi^2 r} \frac{\Delta}{\hbar v_F} \sin(k_F r) \, K_0 \left(\frac{r}{\pi \xi_{BCS}} \right) \overset{r \to \infty}{\sim} \sin(k_F r) \, e^{-r/(\pi \xi_{BCS})}$$

where $K_0(kr)$ is the modified Bessel function that falls off as e^{-kr} at infinity. We have

[14] Note that this definition is not equal to the Fourier transform of the pair wave function $\varphi(\mathbf{r})$ introduced in Eq. 110, which would be $v_k/u_k \sqrt{N_p}$. The definition given here is the two-point correlation function. Both definitions for the Cooper pair wave function show a sharp feature, either a peak or an edge at the Fermi surface, of width $\sim \delta k$, thus giving similar behavior for the real space wave function.
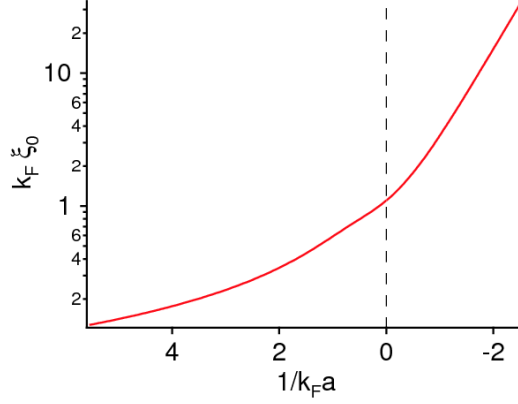
98

Fig. 24. – From tightly bound molecules to long-range Cooper pairs. Evolution of the pair size $\xi_0 = \sqrt{\frac{\langle \psi(\mathbf{r})|r^2|\psi(\mathbf{r})\rangle}{\langle \psi(\mathbf{r})|\psi(\mathbf{r})\rangle}}$ as a function of the interaction parameter $1/k_F a$. On resonance (dashed line), the pair size is on the order of the inverse wave vector, $\xi_0(0) \sim \frac{1}{k_F}$, about a third of the interparticle spacing.

encountered a similar exponential envelope function for a two-body bound state (see table VI). The characteristic size of the Cooper pair, or the *two-particle correlation length* ξ_0, can be defined as $\xi_0^2 = \frac{\langle \psi(\mathbf{r})|r^2|\psi(\mathbf{r})\rangle}{\langle \psi(\mathbf{r})|\psi(\mathbf{r})\rangle}$, and this gives indeed $\xi_0 \sim 1/\delta k$,

$$(144) \qquad \xi_0 \approx \xi_{BCS} \equiv \frac{\hbar v_F}{\pi \Delta} \gg 1/k_F \quad \text{in the BCS-limit}$$

In the BEC limit, $u_k v_k \propto \frac{1}{1+(ka)^2}$, and so

$$(145) \qquad \psi(\mathbf{r}_1, \mathbf{r}_2) \sim \frac{e^{-|\mathbf{r}_1 - \mathbf{r}_2|/a}}{|\mathbf{r}_1 - \mathbf{r}_2|}$$

which is simply the wave function of a molecule of size $\sim a$ (see table VI). The two-particle correlation length([15]) is thus $\xi_0 \sim a$. Figs. 23 and 24 summarize the evolution of the pair wave function and pair size throughout the crossover.

4'7. *Single-particle and collective excitations*. – Fermionic superfluids can be excited in two ways: Fermi-type excitations of single atoms or Bose-like excitations of fermion pairs. The first is related to pair breaking, the second to density fluctuations – sound

---

([15]) This length scale should be distinguished from the *coherence length* ξ_{phase} that is associated with spatial fluctuations of the order parameter. The two length scales coincide in the BCS-limit, but differ in the BEC-limit, where ξ_{phase} is given by the healing length $\propto \frac{1}{\sqrt{na}}$. See [204] for a detailed discussion.
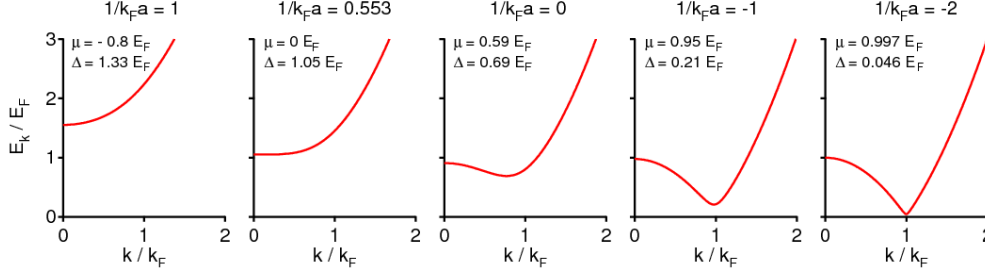
Fig. 25. – Evolution of the single-particle excitation spectrum in the BEC-BCS crossover. On the BEC-side, for $\mu < 0$, the minimum required energy to add a particle is $\sqrt{\mu^2 + \Delta^2}$ and occurs at $k = 0$. This qualitatively changes at $1/k_F a = 0.553$ where $\mu = 0$. For $\mu > 0$, the minimum energy is Δ and occurs at $k = \sqrt{2m\mu/\hbar^2}$.

waves.

4˙7.1. Single-particle excitations. The BCS-state $|\Psi_{\mathrm{BCS}}\rangle$ describes a collection of pairs, each momentum state pair $(\mathbf{k}\uparrow, -\mathbf{k}\downarrow)$ having probability amplitude u_k of being empty and v_k of being populated. We now calculate the energy cost for adding a *single* fermion in state $\mathbf{k}\uparrow$, which does not have a pairing partner, i.e. the state $-\mathbf{k}\downarrow$ is empty. This requires a kinetic energy ξ_k (relative to the chemical potential). For the other particles, the states $(\mathbf{k}\uparrow, -\mathbf{k}\downarrow)$ are no longer available, and according to Eq. 119 the (negative) pairing energy is increased by $-2\xi_k v_k^2 - 2\frac{V_0}{\Omega} u_k v_k \sum_{k'} u_{k'} v_{k'}$, which equals $-\xi_k(1 - \frac{\xi_k}{E_k}) + \frac{\Delta^2}{E_k} = E_k - \xi_k$ (see Eq. 120). The total cost for adding one fermion is thus simply $\xi_k + (E_k - \xi_k) = E_k$ (again relative to μ, i.e. this is the cost in free energy). In the same way, one calculates the cost for removing a fermion from the BCS-state (e.g. deep in the Fermi sea), and leaving behind an unpaired fermion in state $-\mathbf{k}\downarrow$. The result is again E_k. This shows that adding or removing a particle creates a quasi-particle with energy E_k, as we had found already via the Bogoliubov transformation Eq. 135. For example, the quasi-particle excitation

$$
(146) \qquad \gamma_{k\uparrow}^\dagger |\Psi_{\mathrm{BCS}}\rangle = c_{k\uparrow}^\dagger \prod_{l \neq k} \left(u_l + v_l c_{l\uparrow}^\dagger c_{-l\downarrow}^\dagger \right) |0\rangle
$$

correctly describes the removal of the momentum pair at $(\mathbf{k}\uparrow, -\mathbf{k}\downarrow)$, and the addition of a single fermion in $\mathbf{k}\uparrow$.

Fig. 25 shows the single-particle excitation energy E_k for different interaction strengths in the BEC-BCS crossover. For $\mu > 0$, the minimum energy required to remove a particle from the condensate occurs for $\xi_k = \mu$ and is Δ, which gives Δ the name of the superfluid gap. One dramatic consequence of this gap is that it prevents single fermions to enter the superfluid, resulting in phase separation in imbalanced Fermi mixtures [80]. For $\mu < 0$ the minimum energy to remove a particle becomes $\sqrt{\mu^2 + \Delta^2}$ and occurs for $k = 0$.

To excite the system without adding or removing particles can be done in two ways:

One can remove a particle, requiring an energy E_k, and add it back at energy cost $E_{k'}$, thus creating two unpaired particles with momenta k and k'. The second possibility is to excite a fermion pair in $(\mathbf{k} \uparrow, -\mathbf{k} \downarrow)$ into the state orthogonal to the ground state, which can be written

$$
(147) \qquad \gamma_{k\uparrow}^\dagger \gamma_{-k\downarrow}^\dagger |\Psi_{\text{BCS}}\rangle = (v_k - u_k c_{k\uparrow}^\dagger c_{-k\downarrow}^\dagger) \prod_{l \neq k} \left(u_l + v_l c_{l\uparrow}^\dagger c_{-l\downarrow}^\dagger \right) |0\rangle
$$

Instead of the pairing energy $\xi_k - E_k$ for that state, the energy for such an excitation is $\xi_k + E_k$, that is, this excited pair state lies an energy $2E_k$ above the BCS ground state. The minimum energy required to excite the system, without changing the particle number, is thus 2Δ in the BCS limit, and $2\sqrt{\mu^2 + \Delta^2}$ in the BEC-limit. In the latter case, from Eq. 139, one has

$$
(148) \qquad 2\sqrt{\mu^2 + \Delta^2} \approx |E_B| - \mu_M + \frac{2\Delta^2}{|E_B|}
$$

The first two terms $|E_B| - \mu_M = \hbar^2/ma^2 - \mu_M$ give the energy required to remove a molecule (the positive mean field μ_M pushes this energy closer to threshold). The last term will then correspond to the energy required to add two unpaired fermions into the system. From our discussion in section **4˙**6.2, we expect that this should cost twice the mean field energy $\mu_{\text{BF}} = \frac{4\pi\hbar^2 a_{\text{BF}} n_M}{m_{\text{BF}}}$ of a fermion interacting with a cloud of bosons, the molecules. Here, a_{BF} is the Boson-Fermion scattering length and $m_{\text{BF}} = 2m_B m_F/(m_B + m_F) = 4/3\, m$ is twice the reduced mass of the boson-fermion system. With the help of Eq. 141 we equate

$$
(149) \qquad \frac{\Delta^2}{|E_B|} = \frac{4\pi\hbar^2 a n}{m} \equiv \frac{4\pi\hbar^2 a_{\text{BF}} n_M}{m_{\text{BF}}} = \frac{3\pi\hbar^2 a_{\text{BF}} \frac{n}{2}}{m}
$$

and obtain the Boson-Fermion scattering length at the mean field level,

$$
(150) \qquad a_{\text{BF}} = \frac{8}{3}\, a
$$

The exact value $a_{\text{BF}} = 1.18\, a$ has been obtained already 50 years ago [205].

4˙7.2. RF excitation into a third state. The hyperfine structure of ultracold atoms offers more than just two states "spin up" and "spin down". This allows for a new type of single-particle excitation, not available for electrons in superconductors, namely the transfer of, say, a spin up fermion into a third, empty state, $|3\rangle$, via a radiofrequency (RF) transition (see sections **2˙**3 and **7˙**2.4). We have all the tools ready to calculate the excitation spectrum for RF spectroscopy in the case where the third state does not interact with atoms in the spin up or spin down states. Due to its long wavelength, Doppler shifts are negligible and the RF excitation flips the spin from $|\uparrow\rangle$ to $|3\rangle$ and vice versa regardless of the momentum state of the atom, and without momentum transfer.

The RF operator is thus

$$(151) \qquad \hat{V} = V_0 \sum_k c_{k3}^\dagger c_{k\uparrow} + c_{k\uparrow}^\dagger c_{k3}$$

where V_0 is the strength of the RF drive (the Rabi frequency $\omega_R = 2V_0/\hbar$) taken to be real. As the third state is initially empty, only the first part contributes when acting on the initial state. To calculate the action of the spin flip $c_{k3}^\dagger c_{k\uparrow}$ on the BCS state, we express $c_{k\uparrow} = u_k \gamma_{k\uparrow} + v_k \gamma_{-k\downarrow}^\dagger$ in terms of the Bogoliubov quasi-particle operators (Eq. 135). As the BCS-state is the quasi-particle vacuum, $\gamma_{k\uparrow} |\Psi_{\rm BCS}\rangle = 0$, and one has

$$(152) \qquad c_{k3}^\dagger c_{k\uparrow} |\Psi_{\rm BCS}\rangle = v_k c_{k3}^\dagger \gamma_{-k\downarrow}^\dagger |\Psi_{\rm BCS}\rangle \qquad \text{and thus}$$

$$(153) \qquad \hat{V} |\Psi_{\rm BCS}\rangle = V_0 \sum_k v_k c_{k3}^\dagger \gamma_{-k\downarrow}^\dagger |\Psi_{\rm BCS}\rangle$$

When the RF excitation removes the particle from the BCS state, it creates a quasi-particle with a cost in total energy of $E_k - \mu$ (see section 4.7.1). The energy cost for creating the particle in the third state is, apart from the bare hyperfine splitting $\hbar\omega_{\uparrow 3}$, the kinetic energy ϵ_k. In total, the RF photon has to provide the energy

$$(154) \qquad \hbar\Omega(k) = \hbar\omega_{\uparrow 3} + E_k + \epsilon_k - \mu$$

Fermi's Golden Rule gives now the transition rate $\Gamma(\omega)$ at which particles leave the BCS state and arrive in state $|3\rangle$ (ω is the RF frequency).

$$(155) \qquad \Gamma(\omega) \equiv \frac{2\pi}{\hbar} \sum_f \left| \left\langle f \left| \hat{V} \right| \Psi_{\rm BCS} \right\rangle \right|^2 \delta\left(\hbar\omega - E_f\right)$$

where the sum is over all eigenstates $|f\rangle$ with energy E_f (relative to the energy of the BCS state). The relevant eigenstates are just the states calculated in Eq. 152: $|k\rangle \equiv c_{k3}^\dagger \gamma_{-k\uparrow} |\Psi_{\rm BCS}\rangle$ of energy $\hbar\Omega(k)$. The sum over final states becomes a sum over momentum states, and, according to Eq. 153, the matrix element is $V_0 v_k$. The condition for energy conservation, $\hbar\omega = \hbar\Omega(k)$, can be inverted via Eq. 154 to give ϵ_k in terms of ω. The delta function then becomes $\delta(\hbar\omega - \hbar\Omega(k)) = \frac{1}{\hbar}\frac{d\epsilon_k}{d\Omega}\delta(\epsilon_k - \epsilon(\omega))$. With $\frac{d\Omega}{d\epsilon_k} = \frac{\xi_k}{E_k} + 1 = 2u_k^2$, we obtain the simple expression

$$(156) \qquad \Gamma(\omega) = \frac{\pi}{\hbar} V_0^2 \, \rho(\epsilon_k) \, \frac{v_k^2}{u_k^2} \bigg|_{\epsilon_k = \epsilon(\omega)} = \pi N_p \, V_0^2 \, \rho(\epsilon_k) \, |\varphi_k|^2 \, \big|_{\epsilon_k = \epsilon(\omega)}$$

This result shows that RF spectroscopy of the BCS state directly measures the fermion pair wave function φ_k (see Eq. 110 and Eq. 115). Note that it is $\varphi_k = v_k/u_k\sqrt{N_p}$, rather than the Cooper pair wave function $\psi_k = u_k v_k$, that appears here. While the two coincide in the BEC-limit of tightly bound molecules (apart from the normalization

with $\sqrt{N_p}$), they are quite different in the BCS regime, where φ_k extends throughout the entire Fermi sea, while ψ_k is peaked in a narrow range around the Fermi surface (see Fig. 23). This goes back to the two possible interpretations of the BCS state discussed in section 4˙6.1, either as a condensate of $N/2$ fermion pairs (Eq. 110) or as the product of a Fermi sea and a condensate of Cooper pairs (Eq. 116). In RF spectroscopy, the first point of view is the natural choice, as the RF interaction couples to all momentum states in the entire Fermi sea.

We now discuss the spectrum itself. From here on, frequencies ω are given relative to the hyperfine frequency $\omega_{\uparrow 3}$. From Eq. 154 we see that the minimum or threshold frequency required to excite a particle into state $|3\rangle$ is

(157) $\qquad \hbar\omega_{\text{th}} = \sqrt{\mu^2 + \Delta^2} - \mu \rightarrow \begin{cases} \frac{\Delta^2}{2E_F} & \text{in the BCS-limit} \\ 0.31 E_F & \text{on resonance} \\ |E_B| = \frac{\hbar^2}{ma^2} & \text{in the BEC-limit} \end{cases}$

In either limit, the threshold for RF spectroscopy thus measures the binding energy of fermion pairs (apart from a prefactor in the BCS-limit, see section 4˙6.1), and *not* the superfluid gap Δ, which would be the binding energy of Cooper pairs described by ψ_k.

To obtain the spectrum explicitly, we calculate $\epsilon(\omega) = \frac{1}{2\hbar\omega}(\hbar\omega - \hbar\omega_{\text{th}})(\hbar\omega + \hbar\omega_{\text{th}} + 2\mu)$ and $v_k^2/u_k^2\big|_{\epsilon_k = \epsilon(\omega)} = \Delta^2/(\hbar\omega)^2$. With $\rho(E_F) = 3N/4E_F$ the spectrum finally becomes

(158) $\qquad \Gamma(\omega) = \frac{3\pi}{4\sqrt{2}\hbar} \frac{N\,V_0^2\Delta^2}{E_F^{3/2}} \frac{\sqrt{\hbar\omega - \hbar\omega_{\text{th}}}}{\hbar^2\omega^2} \sqrt{1 + \frac{\omega_{\text{th}}}{\omega} + \frac{2\mu}{\hbar\omega}}$

In the BEC-limit, this reduces to (see Eq. 140)

(159) $\qquad \Gamma_{\text{BEC}}(\omega) = \frac{4}{\hbar} N_M\,V_0^2\,\sqrt{|E_B|}\frac{\sqrt{\hbar\omega - |E_B|}}{\hbar^2\omega^2}$

This is exactly the dissociation spectrum of $N_M = N/2$ non-interacting molecules (compare to the Feshbach association spectrum Eq. 219 in section 5 for $a_{\text{bg}} \rightarrow 0$). Fig. 26 shows the RF spectra for various values of the interaction strength in the BEC-BCS crossover. Qualitatively, the shape of $\Gamma(\omega)$ does not change much, always staying close to the characteristic asymmetric shape of a molecular dissociation spectrum like Eq. 159, with the pair binding energy as the only relevant energy scale. For example, the spectrum has a maximum at
(160)

$\hbar\omega_{\text{max}} = \frac{1}{3}\left(-4\mu + \sqrt{16\mu^2 + 15\Delta^2}\right) \rightarrow \begin{cases} \frac{5}{8}\frac{\Delta^2}{E_F} = \frac{5}{4}\hbar\omega_{\text{th}}, & \text{in the BCS-limit} \\ 0.40 E_F = 1.26\,\hbar\omega_{\text{th}}, & \text{on resonance} \\ \frac{8}{3}|E_B|, & \text{in the BEC-limit} \end{cases}$

which is always on the order of the fermion pair binding energy. The spectrum falls off like $1/\omega^{3/2}$ at large frequencies. This is due to the asymptotic momentum distribution
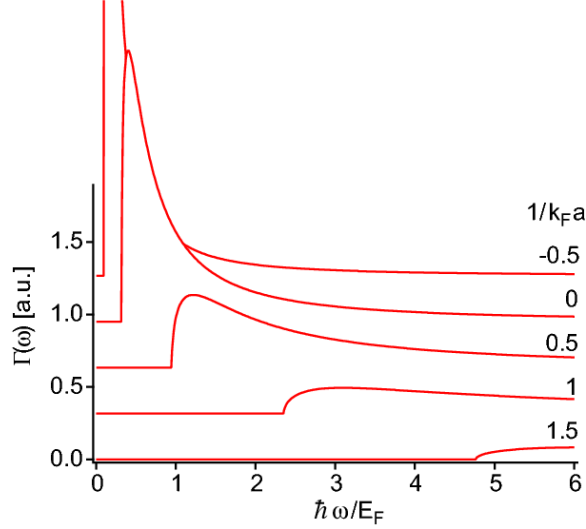
Fig. 26. – RF spectra in the BEC-BCS crossover for transitions into a third, empty and non-interacting state. The threshold changes smoothly from the binding energy of molecules in the BEC-regime to the binding energy of fermion pairs $\sim \Delta^2/E_F$ in the BCS-regime.

$v_k^2 \sim 1/k^4$. The long tails lead to a divergence of the mean transition frequency, so that the sum rule approach in **2**˙3.3 does not give a sensible result here. The divergence is removed if the third state interacts with atoms in state $|\downarrow\rangle$. Note that the BCS formalism neglects interactions between spin up and spin down that are already present in the normal state, which may contribute additional shifts and broadening of the spectra. For the superfluid ^{6}Li system in the $|1\rangle$ and $|2\rangle$ states, the accessible final state $|3\rangle$ has strong interactions with state $|1\rangle$. Therefore, the experimental spectra in the resonance region [206, 134, 77] are qualitatively different from the idealized spectra presented here (see [99]). For recent theoretical studies on RF spectroscopy, incorporating final state interactions, see [132, 133, 207].

4˙7.3. *Collective excitations.* In addition to single-particle excitations, we have to consider collective excitations related to density fluctuations or sound waves (^{16}). Sound modes have a linear dispersion relation $E_k = \hbar c_s k$. In the weakly-interacting BEC-limit, the speed of sound is given by the Bogoliubov solution $c_s = \sqrt{\mu_M/m_M} = \sqrt{4\pi\hbar^2 a_M n_M/m_M}$. For stronger interactions, the Lee-Huang-Yang expansion becomes important (Lee, Huang and Yang, 1957) which increases the speed of sound by a factor $1 + 16\sqrt{\frac{n_M a_M^3}{\pi}}$ [167]. The Bogoliubov sound mode finds its analogue in the BCS-regime, where it is called the Bogoliubov-Anderson mode, propagating at the speed of sound

---

(^{16}) The reduced BCS Hamiltonian Eq. 118 does not contain density fluctuations. One needs to work with the Hamiltonian Eq. 117.

$v_F/\sqrt{3}$, with $v_F = \hbar k_F/m$ the Fermi velocity[17]. The connection between the BEC and BCS results is smooth, as expected and found by [188, 208, 209].

Sound waves are described by hydrodynamic equations, which are identical for superfluid hydrodynamics and inviscid, classical collisional hydrodynamics. For trapped clouds of finite size, collective modes are the solutions of the hydrodynamic equations for the geometry of the trapped cloud. In a harmonic trap, the size of the cloud depends on the square root of the chemical potential (not counting binding energies), just like the speed of sound. As a result, the lowest lying collective excitations are proportional to the trap frequency and, to leading order, independent of the density and size of the cloud [210].

Modes for which the velocity field has zero divergence are called surface modes. Their frequencies are independent of the density of states and do not change across the BCS-BEC crossover, as long as the system is hydrodynamic. However, the frequencies are different from the collisionless regime (where all frequencies are integer multiples of the trap frequencies) and can be used to distinguish hydrodynamic from collisionless behavior. In contrast, compression modes depend on the compressibility of the gas and therefore on the equation of state. On both the BEC and BCS side and at unitarity, the chemical potential is proportional to a power of the density $\mu \propto n^\gamma$. The frequency of breathing modes depends on γ, which has been used to verify that $\gamma = 1$ on the BEC side and $\gamma = 2/3$ at unitarity [73, 74, 211].

For an extensive discussion of collective modes we refer to the contributions of S. Stringari and R. Grimm to these proceedings.

4˙7.4. *Landau criterion for superfluidity.* The Landau criterion for superfluidity gives a critical velocity v_c, beyond which it becomes energetically favorable to transfer momentum from the moving superfluid (or the moving object) to excitations [212]. As a result, superfluid flow is damped. Creating an excitation carrying plane-wave momentum $\hbar\mathbf{k}$ costs an energy $E_k + \hbar\mathbf{k}\cdot\mathbf{v}$ in the rest frame (Doppler shift). The minimum cost occurs naturally for creating an excitation with $\mathbf{k}$ antiparallel to the velocity $\mathbf{v}$ of the superfluid. This is only energetically favored if $E_k - \hbar k v < 0$, leading to Landau's criterion for the critical velocity:

$$(161) \qquad\qquad v_c = \min_k \frac{E_k}{\hbar k}$$

---

[17] This speed of sound can be calculated using the hydrodynamic equation $c = \sqrt{\frac{\partial P}{\partial \rho}}$, $\rho = m n$ and the pressure of a normal Fermi gas $P = \frac{2}{3}\frac{E}{V} = \frac{2}{5}E_F\, n = \frac{2}{5}\frac{\hbar^2}{2m}(3\pi^2)^{2/3}n^{5/3}$. Thus, the sound mode is already present in the normal Fermi gas, the main effect of superfluid pairing being to push low-lying single-particle excitations up in energy, which would otherwise provide damping. The low temperature limit for the normal gas is peculiar. On the one hand, the damping vanishes at zero temperature, on the other hand, the sound mode cannot propagate, as collisions are absent and the gas can no longer maintain local equilibrium.
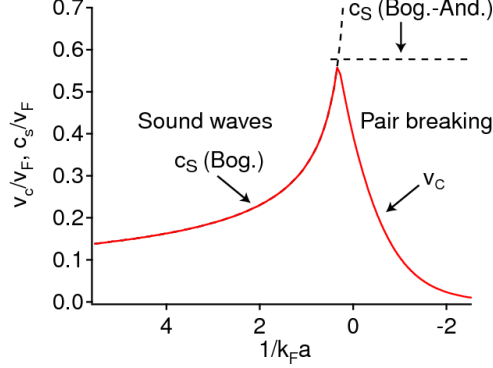
Fig. 27. – Critical velocity v_c in the BEC-BCS crossover. The relevant excitations in the BEC-regime correspond to Bogoliubov (Bog.) sound waves with speed of sound $c_s = \sqrt{\frac{\mu}{m}} = \frac{v_F}{\sqrt{3\pi}}\sqrt{k_F a}$. This sound mode eventually becomes the Bogoliubov-Anderson (Bog.-And.) mode in the BCS-regime, with $c_s = \frac{v_F}{\sqrt{3}}$. The evolution is smooth [188, 208, 209], but only the limiting cases are shown here. In the BCS-regime the excitations with the lowest critical velocity are single-particle excitations that break a Cooper pair. Here, $v_c \approx \frac{\Delta}{\hbar k_F}$. After [209].

The minimum has to be taken over all possible excitations, including single-particle excitations, collective excitations (and, for certain geometries, such as narrow channels and small moving objects, excitation of vortex pairs).

On the BCS side, the single-particle excitation spectrum derived above gives a critical velocity of

$$(162) \qquad v_{c,\mathrm{BCS}} = \min_k \frac{E_k}{\hbar k} = \sqrt{\left(\sqrt{\mu^2 + \Delta^2} - \mu\right)/m} \quad \overset{\frac{\Delta}{\mu}\to 0_+}{\to} \quad \frac{\Delta}{\hbar k_F}$$

An object that is dragged through the superfluid faster than this velocity will break fermion pairs. For sound excitations, the Landau criterion gives the speed of sound as critical velocity. In a simple approximation (neglecting possible coupling between single particle and collective excitations), the critical velocity for the superfluid is given by the smaller of the two velocities. On the BEC side, where the pairs are tightly bound, the speed of sound determines the critical velocity, whereas on the BCS side, the critical velocity comes from pair breaking.

For the BEC-side, it has been shown in [209] that for small momenta $k \ll 1/a$ that do not resolve the composite nature of the molecules, the expression for the Bogoliubov-dispersion $E_{k,\mathrm{BEC}} = \sqrt{(\frac{\hbar^2 k^2}{2m_M} + \mu_M)^2 - \mu_M^2}$ remains valid even well into the crossover region. This allows us to determine the speed of sound in an approximate way, which is shown in Fig. 27. Notable is the sharp peak in the critical velocity around resonance which reflects the rather narrow transition from a region where excitation of sound limits superfluid flow, to a region where pair breaking dominates. At the same time, the onset

106

of dissipation switches from low k's (sound) to high k's (pair breaking). It is near the Feshbach resonance that the superfluid is most stable [213, 209]. This makes the critical velocity one of the few quantities which show a pronounced peak across the BEC-BCS crossover, in contrast to the chemical potential, the transition temperature (except for a small hump), the speed of sound and the frequencies of shape oscillations, which all vary monotonically.

4˙8. *Finite temperatures*. – At finite temperature, the superfluid state has thermal excitations in the form of the quasiparticles introduced in Eq. 135. These quasiparticles modify the gap and number equations for the BCS state from which we derive an expression for the superfluid transition temperature.

4˙8.1. Gap equation at finite temperature. At finite temperature, the expectation value for the pairing field $C_k = \langle c_{k\uparrow} c_{-k\downarrow} \rangle$ becomes

$$(163) \qquad \langle c_{k\uparrow} c_{-k\downarrow} \rangle = -u_k v_k \left(1 - \left\langle \gamma^\dagger_{k\uparrow} \gamma_{k\uparrow} \right\rangle - \left\langle \gamma^\dagger_{k\downarrow} \gamma_{k\downarrow} \right\rangle \right)$$

As the quasi-particles are fermions, they obey the Fermi-Dirac distribution $\left\langle \gamma^\dagger_{k\uparrow} \gamma_{k\uparrow} \right\rangle = \frac{1}{1+e^{\beta E_k}}$. The equation for the gap $\Delta = \frac{V_0}{\Omega} \sum_k \langle c_{k\uparrow} c_{-k\downarrow} \rangle$ thus becomes (replacing V_0 as above by the scattering length a)

$$(164) \qquad -\frac{m}{4\pi\hbar^2 a} = \int \frac{d^3k}{(2\pi)^3} \left(\frac{1}{2E_k} \tanh\left(\frac{\beta E_k}{2} \right) - \frac{1}{2\epsilon_k} \right)$$

4˙8.2. Temperature of pair formation. We are interested in determining the temperature $T^* = 1/\beta^*$ at which the gap vanishes. In the BCS-limit, this procedure gives the critical temperature for the normal-to-superfluid transition. Setting $\Delta = 0$ in the gap equation, one needs to solve [41, 214, 188]

$$(165) \qquad -\frac{m}{4\pi\hbar^2 a} = \int \frac{d^3k}{(2\pi)^3} \left(\frac{1}{2\xi_k} \tanh\left(\frac{\beta^* \xi_k}{2} \right) - \frac{1}{2\epsilon_k} \right)$$

simultaneously with the constraint on the total number of atoms. Above the temperature T^*, we have a normal Fermi gas with a Fermi-Dirac distribution for the occupation of momentum states, so the number equation becomes

$$(166) \qquad n = 2 \int \frac{d^3k}{(2\pi)^3} \frac{1}{1 + e^{\beta^* \xi_k}}$$

In the BCS-limit, we expect $\mu \gg k_B T^*$ and thus find $\mu \approx E_F$. Inserted into the gap equation, this gives the critical temperature for BCS superfluidity

$$(167) \qquad T^*_{\mathrm{BCS}} = T_{C,\mathrm{BCS}} = \frac{e^\gamma}{\pi} \frac{8}{e^2} e^{-\pi/2k_F|a|} = \frac{e^\gamma}{\pi} \Delta_0$$
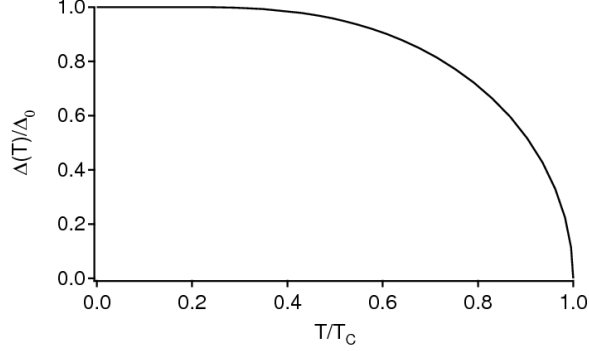
Fig. 28. – Temperature dependence of the gap in the BCS regime. $\Delta(T)$ is normalized by its value Δ_0 at zero temperature, and temperature is given in units of $T^* \approx T_C$.

with Euler's constant γ, and $e^\gamma \approx 1.78$. Here, we distinguish Δ_0, the value of the superfluid gap at zero temperature, from the temperature dependent gap $\Delta(T)$. From Eq. 164 one can show that

$$(168) \qquad \Delta(T) \approx \begin{cases} \Delta_0 - \sqrt{2\pi\Delta_0\, k_B T}\, e^{-\Delta_0/k_B T}, & \text{for } T \ll T_C \\ \sqrt{\frac{8\pi^2}{7\zeta(3)}}\, k_B T_C \sqrt{1 - \frac{T}{T_C}}, & \text{for } T_C - T \ll T_C \end{cases}$$

The full temperature dependence is shown in Fig. 28.

In the BEC-limit, the chemical potential $\mu = E_B/2 = -\hbar^2/2ma^2$ is again given by half the molecular binding energy as before, and the temperature T^* is found to be

$$(169) \qquad T^*_{\mathrm{BEC}} \approx \frac{1}{3} \frac{|E_b|}{W\left[\left(\frac{\pi}{6}\right)^{\frac{1}{3}} \frac{|E_b|}{2E_F}\right]}$$

where $W(x)$ is the Lambert W-function, solution to $x = We^W$ with expansion $W(x) \approx \ln(x) - \ln(\ln(x))$ (useful for $x \gtrsim 3$).

T^*_{BEC} is *not* the critical temperature for the superfluid transition but simply the temperature around which pairs start to form. The factor involving $W(x)$ has its origin in the entropy of the mixture of molecules and free fermions, which favors unbound fermions and lowers $k_B T^*$ below the binding energy E_b. There is no phase transition at T^*, but a smooth crossover.

4˙8.3. Critical temperature. Determining T_C, the temperature at which long-range order is established, requires an additional term in the number equation, namely the inclusion of non-condensed pairs [41, 214, 188, 203, 215]. The result is that in the deep BEC-regime, the critical temperature is simply given by the non-interacting value for the

BEC transition of a gas of molecules at density $n_M = n/2$ and mass $m_M = 2m$,

$$(170) \qquad T_{C,\mathrm{BEC}} = \frac{2\pi\hbar^2}{m_M}\left(\frac{n_M}{\zeta(\frac{3}{2})}\right)^{2/3} = \frac{\pi\hbar^2}{m}\left(\frac{n}{2\zeta(\frac{3}{2})}\right)^{2/3} = 0.22 E_F$$

This result holds for weakly interacting gases. For stronger interactions, there is a small *positive* correction $T_C/T_{C,\mathrm{BEC}} = 1 + 1.31 n_M^{1/3} a_M$, with $a_M = 0.60a$ [216, 217, 218, 219, 220]. On the BCS-side, the critical temperature should smoothly connect to the BCS result given above. This implies that there must thus be a local maximum of the critical temperature in the crossover [215]. The value of T_C at unitarity has been calculated analytically [41, 188, 203, 215], via renormalization-group methods [221] and via Monte-Carlo simulations [184, 222]. The result is $T_C = 0.15 - 0.16 T_F$ [215, 222]. Note that these values hold for the homogeneous case, with $k_B T_F = \hbar^2 (6\pi^2 n)^{2/3}/2m$. In the trapped case, they apply locally, but require knowledge of the local T_F and therefore the Fermi energy in the center of the trap. This requires knowledge of the central density n_U as a function of temperature and the global Fermi energy $E_F = \hbar\bar{\omega}(3N)^{1/3}$. Using, as a first approximation, the zero-temperature relation $n_U = \xi^{-3/4} n_F$ from Eq. 41, with n_F the density of a non-interacting Fermi gas of the same number of atoms, gives $k_B T_{C,\mathrm{Unitarity}} = 0.15\epsilon_F(\mathbf{0}) = 0.15\frac{1}{\sqrt{\xi}} E_F \approx 0.23 E_F$. Fig. 29 shows the behavior of T_C as a function of the interaction strength.

$4\dot{}8.4.$ "Preformed" pairs. In the region between T_C and T^*, we will already find bound pairs in the gas, which are not yet condensed. In the BCS-limit, where $T^* \to T_C$, condensation occurs at the same time as pairing, which, as we see now, is no longer true for stronger interactions. Deep on the molecular side, it is of course not surprising to find thermal molecules above T_C. However, the qualitative picture of thermal (i.e. non-condensed) pairs still holds in the entire crossover region from $-1 < 1/k_F a < 1$. These uncondensed pairs are sometimes called "preformed" (pairing occurs before condensation) and also occur in a part of the phase diagram of High-T_C superconductors, the Nernst regime of the pseudogap [44].

$4\dot{}9.$ *Long-range order and condensate fraction.* – In this and the following section, we discuss in detail the condensate and superfluid fractions. In dilute gas BECs, the difference between the two quantities is negligible, but their distinction is crucial in the BEC-BCS crossover and in the BCS limit.

Fritz London proposed in 1938 that superfluidity is a quantum mechanical phenomenon. It should thus be possible to encode the properties of the superfluid in a macroscopic wave function that depends only on one or a few coordinates. In the case of Bose gases, it is the 1-particle density matrix that describes superfluidity [223, 212],

$$(171) \qquad \rho_1(\mathbf{r}, \mathbf{r}') = \left\langle \Psi_B^\dagger(\mathbf{r}) \Psi_B(\mathbf{r}') \right\rangle$$

where $\Psi_B^\dagger(\mathbf{r})$ is the creation operator for a boson at point $\mathbf{r}$. The sum of all eigenvalues
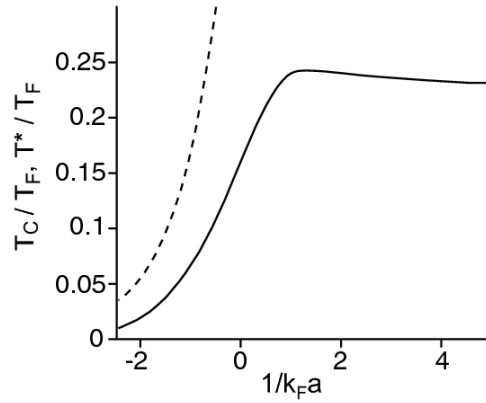
Fig. 29. – Superfluid transition temperature T_C and pair creation temperature T^* (dashed line) in the BEC-BCS crossover. In the BEC regime, T_C corresponds to the BEC transition temperature for a gas of molecules. In the BCS regime, the critical temperature depends exponentially on the interaction strength, drastically reducing T_C. T_C extracted from [215], T^* calculated from Eq. 166.

of this matrix is equal to the number of particles N. The criterion for Bose-Einstein condensation, as first introduced by Onsager and Penrose [223], is the existence of exactly one macroscopic eigenvalue, i.e. with a value of order N. Such a macroscopically occupied state implies long-range order, signalled by an off-diagonal ($\mathbf{r} \neq \mathbf{r}'$) matrix element that does not vanish for large distances $|\mathbf{r} - \mathbf{r}'|$.

$$(172) \qquad \lim_{|\mathbf{r}-\mathbf{r}'|\to\infty} \rho_1(\mathbf{r}, \mathbf{r}') = \psi_B(\mathbf{r})\psi_B^*(\mathbf{r}')$$

where $\psi_B(\mathbf{r})$ is the macroscopic wave function or order parameter describing the Bose superfluid ([18]). "Macroscopic" means that the number of condensed bosons $N_0 = \int \mathrm{d}^3 r \, |\psi_B(\mathbf{r})|^2$ is extensive, i.e. large compared to 1, or more precisely that the condensate fraction N_0/N is finite in the thermodynamic limit. $n_0(\mathbf{r}) \equiv |\psi_B(\mathbf{r})|^2$ is the density

---

([18]) For a discussion of the relation between condensation and superfluidity, see chapter **6**.

of the condensed gas. Thus, an absorption image of a weakly interacting Bose-Einstein condensate directly reveals the magnitude of the wave function. This has led to the direct visualization of coherence between two Bose condensates [224], spatial coherence within a condensate [225] and of vortex lattices [226, 227, 228, 229].

For *fermionic* gases, the 1-particle density matrix can *never* have a macroscopic matrix element, as the occupation number of a particular quantum state cannot exceed unity due to the Pauli principle. After our discussion of fermionic pairing, it does not come as a surprise that for fermionic superfluids, long-range order shows up in the 2-particle density matrix [212, 230]

$$(173) \qquad \rho_2(\mathbf{r}_1, \mathbf{r}_2, \mathbf{r}'_1, \mathbf{r}'_2) = \left\langle \Psi_\uparrow^\dagger(\mathbf{r}_1)\Psi_\downarrow^\dagger(\mathbf{r}_2)\Psi_\downarrow(\mathbf{r}'_2)\Psi_\uparrow(\mathbf{r}'_1) \right\rangle$$

where we added spin labels corresponding to the case of s-wave pairing. Analogous to the Bose case, we can check for the presence of a *pair condensate* by increasing the distance between the primed and the unprimed coordinates, that is between the two centers of mass $\mathbf{R} = (\mathbf{r}_1 + \mathbf{r}_2)/2$ and $\mathbf{R}' = (\mathbf{r}'_1 + \mathbf{r}'_2)/2$. If there is long-range order, one will find a macroscopic "off-diagonal" matrix element

$$(174) \qquad \lim_{|\mathbf{R}-\mathbf{R}'|\to\infty} \rho_2(\mathbf{r}_1, \mathbf{r}_2, \mathbf{r}'_1, \mathbf{r}'_2) = \psi(\mathbf{r}_1, \mathbf{r}_2)\psi^*(\mathbf{r}'_1, \mathbf{r}'_2)$$

The function $\psi(\mathbf{r}_1, \mathbf{r}_2) = \left\langle \Psi_\uparrow^\dagger(\mathbf{r}_1)\Psi_\downarrow^\dagger(\mathbf{r}_2) \right\rangle$ is a macroscopic quantity in BCS theory. It is equal to the Cooper pair wave function discussed above and given by the Fourier transform of the pairing field $-C_k^* = \left\langle c_{k\uparrow}^\dagger c_{-k\downarrow}^\dagger \right\rangle$. The density of condensed fermion pairs $n_0(\mathbf{R})$ is obtained from $|\psi(\mathbf{r}_1, \mathbf{r}_2)|^2$ by separating center of mass $\mathbf{R}$ and relative coordinates $\mathbf{r} = \mathbf{r}_2 - \mathbf{r}_1$ and integrating over $\mathbf{r}$:

$$(175) \qquad n_0(\mathbf{R}) = \int \mathrm{d}^3 r \, |\psi(\mathbf{R} - \mathbf{r}/2, \mathbf{R} + \mathbf{r}/2)|^2$$

More accurately, n_0 is the total density of pairs $n/2$, times the average occupancy of the paired state. With $-C_k^* = u_k v_k \tanh(\frac{\beta E_k}{2})$, we can calculate the condensate density in a uniform system [231, 194]:

$$(176)$$

$$n_0 = \frac{1}{\Omega} \sum_k u_k^2 v_k^2 \tanh^2\left(\frac{\beta E_k}{2}\right) \overset{T\to 0}{=} \frac{1}{\Omega} \sum_k u_k^2 v_k^2 = \frac{3\pi\sqrt{2}}{32} \, n \, \frac{\Delta}{E_F} \sqrt{\frac{\mu + \sqrt{\mu^2 + \Delta^2}}{E_F}}$$

The condensate fraction $2n_0/n$ is non-vanishing in the thermodynamic limit $\Omega \to \infty, n \to$ const, and therefore macroscopic. It is shown in Fig. 30 as a function of temperature in the BCS-regime, and in Fig. 46 of section **6**˙4.1, where it is compared to experimental results in the BEC-BCS crossover. In the BEC-limit, with the help of Eq. 139, n_0

becomes the density of molecules or half the total atomic density n, as expected,

$$(177) \qquad\qquad n_0 = n/2$$

corresponding to a condensate fraction of 100%. As interactions increase, the Bogoliubov theory of the interacting Bose gas predicts that the zero-momentum state occupation decreases and higher momentum states are populated. This quantum depletion is $\frac{8}{3}\sqrt{\frac{n_M a_M^3}{\pi}}$ for a molecular gas of density n_M and scattering length a_M. At $k_F a = 1$, this would reduce the condensate fraction to 91% (using $a_M = 0.6\, a$). The mean field ansatz for the BEC-BCS crossover cannot recover this beyond-mean field correction proportional to $\sqrt{na^3}$. Indeed, the only way the repulsion between two molecules is built into the mean field theory is via the Pauli exclusion principle for the constituent fermions. Rather, Eq. 176 predicts a depletion proportional to na^3, which underestimates the true quantum depletion. Monte-Carlo studies are consistent with the Bogoliubov correction [232]. On resonance, Eq. 176 predicts a condensate fraction $2n_0/n = 70\%$, whereas the Monte-Carlo value is 57(2)% [232]. In the BCS-regime, where $\mu \approx E_F$ and the gap is exponentially small, one finds from Eq. 176:

$$(178) \qquad\qquad n_0 = \frac{mk_F}{8\pi\hbar^2}\,\Delta = \frac{3\pi}{16}\,n\,\frac{\Delta}{E_F}$$

The condensate fraction thus decreases exponentially with the interaction strength, like the gap Δ. This strong depletion is entirely due to the Pauli principle, which can be seen from Eq. 176. Fully occupied ($u_k = 0$) and unoccupied ($v_k = 0$) momentum states do not contribute to the condensate fraction. The bulk contribution comes from states in only a narrow energy range of width $\sim \Delta$ around the Fermi surface, as they are in a superposition of being occupied (with amplitude v_k) or unoccupied (amplitude u_k). Their total number is $\sim N\Delta/E_F$ (see Eq. 178). The phase of this superposition state (the relative phase between the complex numbers u_k and v_k, the same for all $\mathbf{k}$) defines the macroscopic phase of the superfluid state. Indeed, introducing a global phase factor $e^{i\alpha}$ into the BCS state, $|\psi_{\mathrm{BCS}}\rangle = \prod_k (u_k + e^{i\alpha} v_k c_{k\uparrow}^\dagger c_{-k\downarrow}^\dagger)\,|0\rangle$ is equivalent to a rotation of the "coherent state" in Eq. 115 by an angle α, from $\exp\left(\sqrt{N_p}\, b^\dagger\right)|0\rangle$ to $\exp\left(\sqrt{N_p}\, e^{i\alpha} b^\dagger\right)|0\rangle$. This is in direct analogy with BEC and the optical laser.

4˙10. *Superfluid density.* – It is important to distinguish the density of condensed fermion pairs n_0, which is smaller than the total density even at zero temperature, from the superfluid density n_s. The superfluid density is the part of the system that does not respond to external rotation or shear motion. At zero temperature the entire system is superfluid and thus $n_s = n$. As discussed above, one encounters this difference between n_0 and n_s already in BECs [233]. Fig. 30 compares the two quantities for the BCS-regime.

The distinction between superfluid and normal density n_n provides the basis of the two-fluid hydrodynamic model of superfluids and superconductors [234, 235]. To obtain n_s, one can place the system in a long tube that is slowly set in motion with velocity
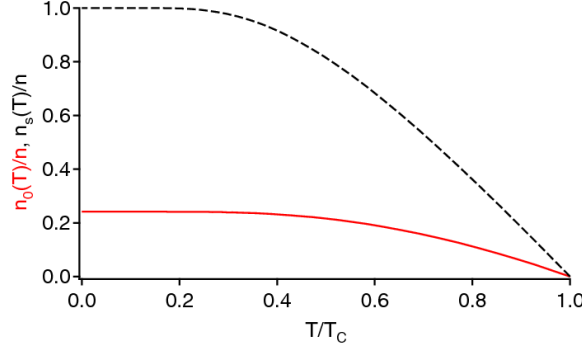
Fig. 30. – Condensate density n_0 (straight line) and superfluid density n_s (dashed line) versus temperature in the BCS-regime ($1/k_F a = -1$). The superfluid fraction is 100% at $T = 0$, while the condensate fraction saturates at 24%. Note that both densities vanish linearly with temperature (within mean-field theory) as they approach T_C.

v [236]. According to Landau's criterion (**4˙**7.4), as long as $v < v_c$, no new excitations from the superfluid are created, so the superfluid stays at rest. However, due to friction with the walls of the tube, the collection of already existing excitations will be dragged along by the tube. The total momentum density **P** of the system is thus only due to this normal gas of excitations, $\mathbf{P} = n_n m \mathbf{v}$, which defines the normal density n_n. The superfluid density is then $n_s = n - n_n$.

We have seen in section **4˙**7 that there are two types of excitations in a fermionic superfluid: Excitations of fermionic (quasi-)particles, related to pair breaking, and bosonic excitations of pairs of fermions. Both types will contribute to the normal density [212, 237, 238, 239]. Single-particle excitations are frozen out for temperatures well below the characteristic temperature T^* for pair formation. In a molecular BEC, $T_C \ll T^*$, and fermions are strongly bound. The only relevant thermal excitations are thus due to non-condensed pairs. For $k_B T \ll \mu_M$, the excitations are dominantly phonons. In the BCS-regime, $T_C = T^*$, and the normal density contains both single-fermion excitations from broken pairs as well as bosonic excitations of pairs of fermions, the Bogoliubov-Anderson sound mode (see **4˙**7.3). Near T_C, which is close to T^* in the BCS regime, single fermion excitations dominate. At low temperatures $k_B T \ll \Delta$, they are frozen out and the contribution from sound waves dominates. At intermediate temperatures, the two types of excitations are coupled, leading to damping of the sound waves [239].

The normal density is obtained from the total momentum of the gas of excitations, that moves with velocity **v** with respect to the stationary superfluid part. In the reference frame moving with the normal gas, the excitation energies ϵ of the superfluid are Doppler shifted to $\epsilon - \hbar \mathbf{k} \cdot \mathbf{v}$ [212]. The momentum is thus

$$(179) \qquad \mathbf{P}_{B,F} = \sum_k \hbar \mathbf{k} \, f_{B,F}(\epsilon - \hbar \mathbf{k} \cdot \mathbf{v})$$

where the subscripts B or F correspond to the bosonic and fermionic contribution, respectively, and $f_{B,F}(\epsilon)$ is the Bose-Einstein and Fermi-Dirac distribution, resp. For small velocities, this gives

$$(180) \qquad \mathbf{P}_{B,F} = \sum_k \hbar\mathbf{k}(\hbar\mathbf{k} \cdot \mathbf{v})\left(-\frac{\partial f_{B,F}}{\partial\epsilon}\right) = \frac{1}{3}\mathbf{v}\sum_k \hbar^2 k^2 \left(-\frac{\partial f_{B,F}}{\partial\epsilon}\right)$$

The last equation follows from spherical symmetry, obeyed by the energy levels and the gap Δ in an s-wave fermionic superfluid. It implies that $\mathbf{P}$ is in the direction of $\mathbf{v}$ and allows to replace $(\mathbf{k} \cdot \frac{\mathbf{v}}{v})^2$ by its angular average, $\frac{1}{3}k^2$. The final formula for the normal density is, with $\epsilon_k = \hbar^2 k^2/2m$ [212],

$$(181) \qquad n_n^{B,F} = \frac{2}{3}\frac{1}{\Omega}\sum_k \epsilon_k\left(-\frac{\partial f_{B,F}}{\partial\epsilon}\right)$$

Contribution from sound waves. Sound waves have $\epsilon = \hbar c_s k$ and thus

$$(182) \qquad n_n^B = -\frac{\hbar}{3mc_s}\int\frac{\mathrm{d}^3k}{(2\pi)^3}k^2\frac{\partial f_B}{\partial k} = \frac{2\pi^2}{45}\frac{k_B^4 T^4}{m\hbar^3 c_s^5} = \frac{\pi^4}{120}n\left(\frac{k_B T}{E_F}\right)^4\left(\frac{v_F}{c_s}\right)^5$$

In the crossover and on the BCS-side, $c_s \approx v_F$, and so $n_n^B/n \approx (k_B T/E_F)^4$, a small contribution that dominates only for $k_B T \ll \Delta$ (see below).

Contribution from fermionic quasi-particle excitations. Fermionic quasi-particle excitations have $\epsilon = E_k$. Spin up and spin down excitations both contribute, giving a normal density

$$(183) \qquad n_n^F = \frac{4}{3}\frac{1}{\Omega}\sum_k \epsilon_k\left(-\frac{\partial f_F}{\partial E_k}\right) = \frac{1}{3\Omega}\sum_k \beta\epsilon_k\frac{1}{\cosh^2\left(\frac{\beta E_k}{2}\right)}$$

Via partial integration, it is not hard to see that for $\Delta = 0$, $n_n^F = n$, that is, the entire system is normal and consists exclusively of thermally excited quasi-particles. This is because in mean-field BCS theory, $\Delta = 0$ implies that $T > T^*$, the temperature for pair formation. Below T^*, both quasi-particles and thermal pairs contribute to the normal gas. Below T_C, the superfluid density n_s becomes non-zero. In the BCS-regime, we find [240, 212]

$$(184) \qquad n_n^F = \quad n\sqrt{\frac{2\pi\Delta_0}{k_B T}}\,e^{-\Delta_0/k_B T} \qquad \text{for } T \ll T_C$$

$$(185) \qquad n_s = n\frac{7\zeta(3)}{4\pi^2 T_C^2}\Delta^2 = 2\,n\left(1 - \frac{T}{T_C}\right) \qquad \text{for } T \approx T_C$$

Close to T_C, the superfluid density is proportional to the square of the gap. This provides a natural normalization of the superfluid order parameter in the next section. The

exponential suppression of the quasi-particle contribution at low temperatures is characteristic for a gapped excitation spectrum. At temperatures $k_B T \ll \Delta$, bosonic sound waves dominate the normal component. In the BEC-regime, the role of the excitation gap is played by $|\mu|$, which is (half) the binding energy of molecules. Hence, already far above T_C, fermionic excitations are frozen out and exponentially suppressed like $e^{-|\mu|/k_B T}$. Bosonic excitations dominate at all temperatures $T < T_C$.

4'11. *Order parameter and Ginzburg-Landau equation.* – A Bose superfluid is described by $\psi_B(\mathbf{r})$, the macroscopic wave function or order parameter. For fermionic superfluids, $\psi(\mathbf{r}_1, \mathbf{r}_2)$ is the wave function for fermions bound in Cooper pairs in the condensate. Then the function

(186)
$$\psi_C(\mathbf{R}) \equiv \psi(\mathbf{R}, \mathbf{R})$$

describes the motion of the center of mass of these pairs and lends itself as the order parameter for a fermionic superfluid. In a uniform system, $\psi_C(\mathbf{R})$ is a constant proportional to the gap Δ:

(187)
$$\psi_C(\mathbf{R}) = \frac{1}{\Omega} \sum_k \left\langle c_{k\uparrow}^\dagger c_{-k\downarrow}^\dagger \right\rangle = -\frac{1}{V_0} \Delta$$

where we have used the gap equation ([19]). This can be extended to a non-uniform system in which the density and $\Delta(\mathbf{R})$ does not vary rapidly (local density approximation). One should point out that it is the presence of a non-zero order parameter, defined via the two-particle density matrix, that signals superfluidity, not the presence of a gap in the excitation spectrum. Gapless superfluidity might occur when the quasi-particle excitations are different for spin up and spin down fermions, one branch touching zero (for example $E_{k\downarrow} = 0$) close to a second-order phase transition to the normal state. Such breaking of time-reversal symmetry leading to gapless superconductivity can occur for example in thin superconducting films in a magnetic field, or in the presence of magnetic impurities [241, 242].

Close to T_C, the order parameter will be small, and after Ginzburg and Landau one can expand the free energy of the superfluid in terms of the small parameter $\psi_C(\mathbf{r})$. From here, one derives the famous Ginzburg-Landau equation for the order parameter [240, 212]

(188)
$$-\frac{\hbar^2 \nabla^2}{2m^*} \psi_C + a\, \psi_C + b\, |\psi_C|^2\, \psi_C = 0$$

The Ginzburg-Landau theory was developed for superconductors on purely phenomenological grounds in 1950, before the advent of BCS theory. m^* was introduced as the mass

---

([19]) In the BEC-regime, one needs to include thermal molecules in the number equation if Δ is to vanish at $T = T_C$ [41, 188].

of the "superelectrons" carrying the supercurrent. It is conventional to choose $m^* = 2m$, the mass of a fermion pair. However, this choice modifies the normalization of ψ_C from Eq. 187 to $|\psi_C|^2 = n_s/2$, one-half the superfluid density ([20]). This is consistent with Eq. 185, which shows that $n_s \propto \Delta^2$ close to T_C. Note that one could have equally well normalized $|\psi_C|^2 = n_0$ via the density of condensed fermion pairs, as this also vanishes like $n_0 \propto T - T_C \propto \Delta^2$ at T_C. This would, however, change the mass m^* into $2\,m\,n_0/n_s$. The parameter b has to be positive, otherwise one could gain energy by making $|\psi_C|$ arbitrarily large. In a uniform system, the squared magnitude of the order parameter, in the superfluid state, is $|\psi_C|^2 = -a/b$, which should start from zero at $T = T_C$ and then grow. Taylor expansion gives $a(T) = a'(T - T_C)/T_C$. The Ginzburg-Landau equation was later *derived* from BCS theory by Gorkov. With the choice $m^* = 2m$, his derivation gives [240] $a' = \frac{6(\pi T_C)^2}{7\zeta(3)E_F}$ and $b = a'/n$.

The Ginzburg-Landau equation has exactly the form of a non-linear Schrödinger equation for the center-of-mass wave function of a fermion pair. In the BEC-regime at $T = 0$, a rigorous microscopic theory, which does not require a small order parameter is the Gross-Pitaevskii equation describing the condensate of molecules. It is formally identical to Eq. 188 if we set $-a = \mu_M$, the chemical potential of molecules, and $b = 4\pi\hbar^2 a_M/m_M$, describing the interactions between molecules. In a uniform system and at $T = 0$, $-a = b\,n_M$, as $|\psi_C|^2 = n_M = n/2$ in the BEC-regime.

For a non-uniform system, Eq. 188 defines a natural length scale over which the order parameter varies, the Ginzburg-Landau coherence length

$$(189) \qquad \xi_{\text{GL}}(T) = \sqrt{\frac{\hbar^2}{4m\,|a|}} = \begin{cases} 0.74\,\xi_{\text{BCS}}\,\left(\frac{T_C}{T_C-T}\right)^{1/2} & \text{in BCS-regime} \\ \xi_{\text{BEC}}\,\left(\frac{T_C}{T_C-T}\right)^{1/2} & \text{in the BEC-regime} \end{cases}$$

$\xi_{\text{BEC}} = \sqrt{\frac{1}{8\pi a_M n_M}}$ is the healing length of the molecular condensate. ξ_{GL} becomes very large close to the critical temperature, and in particular it can be large compared to the BCS-coherence length $\xi_{\text{BCS}} = \hbar v_F/\pi\Delta_0$, defined above via the zero-temperature gap Δ_0. Spatial variations of the wave function ψ_C then occur at a length scale much larger than the size of a Cooper pair, and in this regime, the wave function can be described by a *local* equation, although the pairs are extended [243]. While the G.-L. equation was originally derived close to T_C, assuming a small order parameter, its validity can be extended to all temperatures under the only condition that $\Delta(\mathbf{r})$ varies slowly compared to $\xi_{\text{GL}}(0)$ [244]. This condition is less and less stringent as we cross-over into the BEC-regime of tightly bound molecules.

Note that very close to T_C, fluctuations of the order parameter are large and the G.-L.

([20]) The origin of this normalization is the free energy density F of a superflow with velocity $v_s = \hbar\nabla\phi/2m$, where ϕ is the phase of the wave function $\psi_C = |\psi_C|\,e^{i\phi}$. By definition of the superfluid density, $F = \frac{1}{2}mv_s^2\,n_s = \frac{1}{8}\hbar^2\,|\nabla\phi|^2\,/m$, but in terms of ψ_C we have $F = \frac{1}{2}\hbar^2\,|\psi_C|^2\,|\nabla\phi|^2\,/m^*$. From $m^* = 2m$ follows $|\psi_C|^2 = n_s/2$.

equations are no longer valid. The size of this critical region is given by $|T - T_C|/T_C \ll (T_C/E_F)^4$ in the BCS-regime, and $|T - T_C|/T_C \ll k_F a$ in the BEC-regime [188]. The correlation length then diverges as $(T_C - T)^{-\nu}$ and the superfluid density vanishes as [212] $(T_C - T)^{(2-\alpha)/3}$ with universal critical exponents α and ν, instead of the linear behavior $\propto T_C - T$ implied in the Ginzburg-Landau theory ($\alpha \approx 0$ and $\nu \approx 0.67$ for a complex scalar order parameter in 3D [245, 246]).

Detecting the order parameter. One appealing feature of dilute gas experiments is the ability to directly visualize the order parameter. In the BEC-limit, the entire gas is condensed. As with atomic BECs, density profiles of the molecular gas then directly measure the condensate density n_0. In particular, the contrast of interference fringes and of vortex cores approaches 100%. However, in the BCS regime, the condensate fraction decreases. Furthermore, pairs dissociate in ballistic expansion. This can be avoided by ramping towards the BEC-regime during expansion. As described in section **6**, it has been possible to observe condensates and vortices across the entire BEC-BCS crossover.

4˙12. *Crossing over from BEC to BCS.* – Throughout the BEC-BCS crossover, all quantities vary smoothly, many of them even monotonously with $1/k_F a$. Still, the question has often been raised in what region(s) of the crossover qualitative changes occur. When the initial observations of condensation of fermion pairs were announced [65, 55, 66, 67, 69, 70], the value $1/k_F a = 0$ was regarded as special, since this value separates the regimes where two atoms in isolation will or will not form a weakly bound pair. Observations at $1/k_F a > 0$ were classified as molecular condensates, and those at $1/k_F a < 0$ as fermionic condensates. However, it is clear that the absence or presence of an extremely weakly bound two-body state (with $a \gg 1/k_F$) does not affect the many-body system, since many-body pairing is dominant in this regime. In the following section, we summarize all qualitative criteria we are aware of, which define specific values of $1/k_F a$ where qualitative changes in physical properties occur. Of course, different criteria lead to different values. It appears that for the case of a broad Feshbach resonance, all important qualitative changes occur in the window $0.2 < 1/k_F a < 0.9$. We therefore suggest that one should refer to molecular BEC only in the regime $1/k_F a > 1$. Although BCS theory seems to be qualitatively correct already for $1/k_F a < 0$, we refer to the whole region $1/k_F|a| < 1$ as the crossover region, in accordance with most other authors. It seems most natural to use the word fermionic condensates for the regime with $1/k_F a < -1$ and apply it to superconductors, superfluid ^{3}He and the atomic Fermi gases. The big and unique accomplishment of the field of ultracold atoms has been the creation of the first crossover condensates, which connect two regimes that could be studied only separately before. In this crossover regime, bosonic and fermionic descriptions are merged or co-exist.

- *Excitation spectrum.* At $\mu = 0$, the character of single-particle excitations changes (see Fig. 25): For $\mu < 0$, the minimum excitation energy lies at $k = 0$, while for $\mu > 0$, the minimum occurs at non-zero momenta, around $k = k_F$ in the BCS-

regime. In the BCS mean-field solution, this point lies at $1/k_F a = 0.55$, a more refined theory gives $1/k_F a = 0.41$ [215].

- *Critical velocity.* In the BEC-limit, the critical velocity is due to excitations of sound waves, while in the BCS-regime, it is determined by pair breaking. Both types of excitations become more costly closer to resonance, and consequently there is a maximum in the critical velocity that occurs at $1/k_F a \approx 0.3$ (see Fig. 27).

- *Normal density.* Close to T_C and in the BEC-limit, n_n is dominated by bosonic excitations, thermal fermion pairs, while in the BCS-limit it is broken pairs that contribute mostly to the normal density. The point where the two contributions are equal lies at about $1/k_F a \approx 0.2$, and the crossover between the two occurs rapidly, between $1/k_F a \approx 0$ and 0.4 [238].

- *Balanced superfluidity.* The pairing gap Δ in the BCS-regime presents a natural barrier for excess atoms to enter the superfluid. A dramatic consequence of this is the observable phase separation in a trap between an equal superfluid mixture of spin up and spin down atoms and a normal imbalanced gas surrounding it [80]. In fact, on the BCS-side this is the consequence of a first order phase transition between the balanced superfluid and the normal gas [247]. Only if the chemical potential difference $\mu_\uparrow - \mu_\downarrow$ between the spin up and spin down species becomes larger than 2Δ (or $2\sqrt{\mu^2 + \Delta^2}$ if this occurs at $\mu < 0$), can unpaired atoms (quasi-particles) enter the superfluid. From that point on the situation can be described as an interacting Bose-Fermi mixture of bosonic molecules and single unpaired fermions. This is likely to occur around $\mu = 0$ [248], so again on the BEC-side of the resonance, around $1/k_F a = 0.41$.

- *Absence of unpaired minority fermions.* As we already introduced imbalanced Fermi systems, we can go to the extreme case of a single spin down atom emersed in a sea of spin up atoms. A natural question to ask is: Will the single spin down fermion still form a "monogamous" molecular pair with a spin up fermion (BEC limit), or will it rather interact with an entire collection of majority atoms ("polaron" or polygamous pairing)? This intriguing question has recently been studied via a diagrammatic Monte-Carlo calculation, and a critical interaction strength $1/k_F a = 0.90(2)$ separating the two regimes of "pairing" has been found [249].

- *Pair condensate in the presence of a Fermi sea.* On the BCS side and on resonance, a large population imbalance destroys superfluidity (Clogston-Chandrasekhar-limit, see section **7**˙3.2). It is a feature of the BEC limit that a small number of molecules can condense even in the presence of a large Fermi sea of one of the two spin components. This "BEC" property is probably lost around the point where the chemical potential $\mu_\uparrow + \mu_\downarrow$ becomes positive, as a very small molecular BEC will have $\mu \approx 0$. It is likely that a necessary and sufficient criterion for having a BEC is the existence of a "monogamous" molecular paired state, so again $1/k_F a \approx 0.9$.

118

- *Critical temperature.* On the BEC-side, the critical temperature is given by the value for a non-interacting gas of bosonic molecules, $T_{C,\mathrm{BEC}} = 0.22\,T_F$ (see section **4·**8.3). For increasing interactions, the critical temperature first *increases*, before it drops to $T_{C,\mathrm{Unitarity}} \approx 0.15\,T_F$ at unitarity and then to exponentially small values on the BCS-side of the resonance. There is thus a (low-contrast) maximum of the critical temperature in the crossover, which lies around $1/k_F a \approx 1.3$ [215].

- *Pair size.* Another crossover occurs in the pair size, which can be smaller or larger than the interparticle spacing. With the definition for the pair size given above (section **4·**6.3), we found $\xi_0 \approx 1/k_F$ on resonance, $1/3$ of the interparticle spacing. At $k_F a \approx -0.9$, $\xi_0 \approx n^{-1/3}$. Of course, different definitions of an average size can easily differ by factors of 2 or 3, and it is not clear whether the pair size should be compared to $n^{-1/3}$ or to $1/k_F$. However, it is clear that long-range Cooper pairs as found in superconductors - with many other particles fitting in between - are only encountered for $1/k_F a \ll -1$.

- *Narrow Feshbach resonance.* For a narrow Feshbach resonance (see section **5·**4.4), the crossover from closed channel dominated molecular BEC to open channel BCS-type superfluidity occurs at $1/k_F a \ll -1$.

- *Equation of state exponent (Fig. 15).* The exponent γ in the approximate equation of state $\mu(n) \sim n^\gamma$, as calculated in the BEC-BCS model, has a (low-contrast) minimum at $1/k_F a \approx -0.45$. γ changes from the bosonic value ($\gamma = 1$) on the BEC-side to the fermionic value ($\gamma = 2/3$) on the BCS-side. However, since universality demands $\gamma = 2/3$ already on resonance, the crossover region is located mainly between $1/k_F a = 1$ and $1/k_F a = 0$. Near the Feshbach resonance, but still on the BEC side, the equation of state is then already fermionic ($\gamma \approx 2/3$), which is a strong reason not to call this system a molecular BEC.

5. – Feshbach resonances

Feshbach resonances are crucial for the study of strongly interacting fermions. Typical scattering lengths in alkali atoms are on the order of the van der Waals range $r_0 \approx 50 - 100\,a_0$. Common interparticle spacings in ultradilute gases are $n^{-1/3} \sim 10\,000\,a_0$, corresponding to $k_F = (2\,500\,a_0)^{-1}$. For such small interaction strengths $k_F\,|a| \sim 0.03$, the critical temperature for achieving fermionic superfluidity is exponentially small, $T_C \approx 10^{-23}\,T_F$. Clearly, one requires a way to enhance the interatomic interactions, for example via scattering resonances.

Early on, ^{6}Li was considered as an exception and as a promising candidate to achieve fermionic superfluidity [13], as its triplet scattering length was found to be unusually large and negative, about $-2\,000\,a_0$ [12]. The reason is that the (triplet or electron-spin aligned) interatomic potential of ^{6}Li could, if it were just a bit deeper, support an additional bound state, so low-energy collisions are almost resonant. What first seemed to be special for ^{6}Li, namely a large negative scattering length, can now be created in many two-atom systems by tuning the scattering length near a *Feshbach resonance*. These resonances occur as a bound state in the interatomic potential is tuned into resonance with the energy of two colliding atoms. This tuning is possible via an applied magnetic field if the magnetic moment of the bound state differs from that of the two unbound atoms.

In this chapter, we provide a quantitative description of Feshbach resonances. Our goal is to provide a thorough discussion of the conditions on which the closed channel molecular state can be eliminated, so that the physics is reduced to potential scattering (so-called single channel scattering). This is the case of the so-called broad Feshbach resonance. We start first by summarizing the features of scattering resonances in a single channel, by using the attractive spherical well as an exactly solvable example, and then present a model for Feshbach resonances.

5˙1. *History and experimental summary*. – Herman Feshbach introduced a formalism to treat nuclear scattering in a unified way [250, 251]. In elastic collisions, for example, a free nucleon colliding with a target nucleus can undergo resonant scattering. This occurs whenever the initial scattering energy is equal to that of a "closed channel" bound state between the nucleon and nucleus in the absence of the incoming "scattering channel". A "closed channel" has a higher asymptotic energy than the "incoming" or initial scattering energy and inelastic decay into such a channel is energetically forbidden. The Feshbach formalism allowed to treat scattering entirely in the "open channel" by introducing an effective potential that described coupling into and out of the closed channel. In atomic physics, a related type of resonance is encountered for example in highly excited atoms and ions, where a discrete autoionized state is coupled to a continuum of scattering states. Various aspects of such resonances were studied by Fano [252].

Feshbach resonances at zero energy are realized by tuning an external magnetic field. This was predicted for hydrogen in 1976 [5] and for cold alkali atoms in 1993 [6]. In cold atom experiments, the initial emphasis was on modification of elastic and inelastic

atomic collisions [7, 8, 148], but it soon turned out that Feshbach resonances opened a new avenue towards ultracold molecules: Instead of cooling the molecules themselves, it became possible to create them cold by associating ultracold atoms. The first observation of a Feshbach resonance in ultracold atoms [7, 10] showed strong losses in the atomic signal that were attributed [253, 140, 254] to the formation of ultracold, highly vibrationally excited molecules. However, it was predicted that these molecules, formed out of two bosonic atoms, would undergo fast vibrational relaxation into more tightly bound molecular states. Still, in experiments on ^{85}Rb, the presence of the molecules, as short-lived as they were (lifetime $\sim 100\,\mu$s), could be detected via coherent beats between the free atomic and the bound molecular state [255]. Studies of the decay of *fermionic* gases close to a Feshbach resonance [56, 124, 18] held a peculiar surprise: The maximum atom loss was not centered on resonance, but was shifted towards regions where the Feshbach molecular state was already quite deeply bound. The gas close to resonance was *stable* [56, 60, 124, 18], in stark contrast to the bosonic case. This molecular state could be *reversibly* populated via a magnetic field sweep across resonance [61], at a conversion efficiency exceeding 90% [15, 141]. Most importantly, it was found to be long-lived [15, 17, 16, 18], with lifetimes between about 100 ms (for ^{40}K) and several 10 s (for ^{6}Li). This is to be compared to the molecular lifetimes on the order of only 5 ms observed in bosonic gases [62, 63, 64]. The remarkable stability of fermion dimers near Feshbach resonances is directly linked to the Pauli principle [200]: The characteristic size of dimers is a, the scattering length for atom-atom collisions. A relaxation into more deeply bound molecular states of size r_0 (roughly the van der Waals-range) requires at least three fermions to be within a distance r_0 from each other. As two of them necessarily have the same spin, the relative wave function has to be antisymmetric, i.e. it has a node when the relative distance $r = 0$ and varies proportional to kr for small values of r, where $k \sim 1/a$ is the characteristic momentum spread of the dimer. This suppresses relaxation processes by a certain power of $(kr_0) \sim (r_0/a)$. For dimer-dimer scattering, the power is 2.55 [200]. What is crucial for this suppression is the Pauli principle and the large ratio between initial and final size. For bosons, the reverse is true, i.e. the relaxation rate diverges with $a^{3.5\dots4}$ [256, 257, 258, 259, 260], although the overlap integral between initial and final state decreases. The ratio between good to bad collisions can be very high for fermion dimers near Feshbach resonances, since in contrast to inelastic collisions, elastic scattering is not suppressed.

For an extensive discussion of dimer stability, we refer the reader to the lecture notes of G. Shlyapnikov in these proceedings.

5˙2. *Scattering resonances*. – We summarize first some results for the attractive spherical well potential which are derived in many text books. Our model for Feshbach resonances will have a region in detuning around the resonance, where the interaction and the scattering look very similar to the case of the spherical well.

A three-dimensional spherical well potential of radius R and depth V has scattering states with energy $E > 0$ and also bound states with energy $E < 0$ when the depth is larger than a critical value V_c. We define $E = \hbar^2 k^2/m$ for $E > 0$ and wave vector k,

$|E| = \hbar^2 \kappa^2 / m$ for $E < 0$, $V \equiv \hbar^2 K^2 / m$ and $E_R = \hbar^2 / m R^2$. The critical well depth is $V_c = \frac{\pi^2}{4} E_R$. New bound states appear when $K_n R = (2n+1)\pi/2$ at $V_n = (2n+1)^2 V_c$.

In the ultracold regime $E \ll E_R$, or eqv. $kR \ll 1$, and for $E \ll V$, scattering states have the same radial wave function inside the well as bound states with $|E| \ll V$: $u(r < R) = A \sin(Kr)$. Outside the well, $u(r)$ for scattering states is of the form $u(r > R) = \sin(kr + \delta_s)$. Matching value and slope of $u(r > R)$ and $u(r < R)$ at $r = R$ fixes the phase shift δ_s via the condition: $k \cot(kR + \delta_s) = K \cot(KR)$. The scattering length is

$$(190) \qquad a = -\lim_{k \ll 1/R} \frac{\tan \delta_s}{k} = R \left(1 - \frac{\tan KR}{KR} \right)$$

By expanding $k \cot \delta_s = -1/a + \frac{1}{2} r_{\text{eff}} k^2 + \ldots$, we obtain the effective range $r_{\text{eff}} = R - 1/(K^2 a) - \frac{1}{3} R^3 / a^2$, which is small and on the order of R, unless the well is very shallow $K^2 R a \ll 1$, or a is smaller then R. We will see below that Feshbach resonances lead to *negative* values of r_{eff} that can be large.

The scattering length in Eq. 190 diverges whenever a new bound state enters the potential. This relationship applies to any potential scattering of finite range R: A diverging scattering length signifies that the phase shift δ_s due to the potential well is approaching $\pi/2$. At R, we then have a normalized slope $u'(r)/u(r) \approx k/\tan \delta_s = -1/a$ for the scattering wave function. For *positive a*, this can just as well be continued by a bound state wave function $e^{-\kappa r}$ with matching slope, which gives $\kappa = 1/a$. So apart from the scattering solution, we find a new bound state solution of Schrödinger's equation at negative energy

$$(191) \qquad E_B = -\hbar^2 / m a^2 \qquad \text{for } a > 0.$$

Away from resonances, the scattering length is close to the "background" scattering length R. Close to a resonance (at $V_n = \hbar^2 K_n^2 / m$), the scattering length diverges as

$$(192) \qquad a \approx \frac{1}{KR(K - K_n)} \approx \frac{2\hbar^2}{mR(V - V_n)}$$

and for $a > 0$ the bound state energy depends on V like

$$(193) \qquad E_B = -\frac{\hbar^2}{ma^2} = -\frac{1}{4} \frac{(V - V_n)^2}{E_R}$$

This general behavior for weakly bound states was found already in chapter **4**˙3.1: The binding energy depends quadratically on the "detuning", and the scattering length is inversely proportional to the "detuning". The beauty and power of Feshbach resonances is that this detuning is now controlled by an externally applied field.
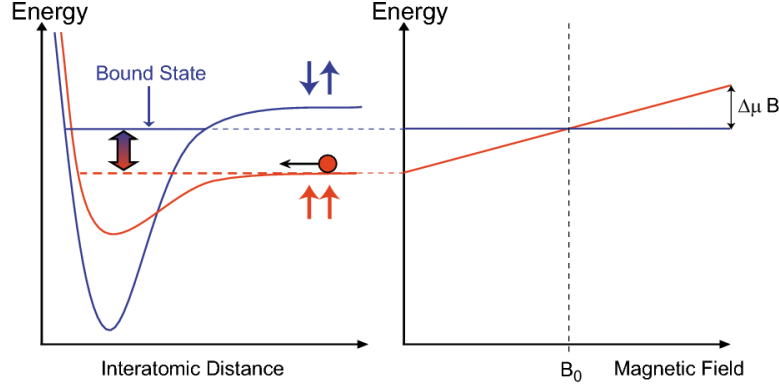
Fig. 31. – Origin of Feshbach resonances. Atoms entering for example in the triplet potential are coupled to a singlet bound molecular state. By tuning the external magnetic field, this bound state can be brought into resonance with the incoming state (at B_0 in the graph on the right).

5˙3. *Feshbach resonances.* – We now turn to realistic interaction potentials between alkali atoms. Here, the interaction actually depends on the internal structure of the two colliding atoms, namely on the relative spin orientation of their valence electrons, singlet or triplet. In Fig. 31 for example, the atoms enter in a triplet configuration. If there was no coupling between the singlet V_S and the triplet potential V_T, the atoms would simply scatter off each other in $V_T(r)$, acquiring some certain, fixed phase shift. However, the *hyperfine interaction* V_{hf} is not diagonal in the total electronic spin $\mathbf{S} = \mathbf{s}_1 + \mathbf{s}_2$ of the two atoms and thus provides a coupling between singlet and triplet potentials [261]:

$$
\begin{aligned}
V_{\text{hf}} &= a_{\text{hf}} \left(\mathbf{s}_1 \cdot \mathbf{i}_1 + \mathbf{s}_2 \cdot \mathbf{i}_2 \right) \\
&= \frac{a_{\text{hf}}}{2} \mathbf{S} \left(\mathbf{i}_1 + \mathbf{i}_2 \right) + \frac{a_{\text{hf}}}{2} \left(\mathbf{s}_1 - \mathbf{s}_2 \right) \left(\mathbf{i}_1 - \mathbf{i}_2 \right) \\
&= V_{\text{hf}}^+ + V_{\text{hf}}^-
\end{aligned}
$$

(194)

with the hyperfine constant a_{hf} and the nuclear spins $\mathbf{i}_{1,2}$ of the two atoms.

The coupling V_{hf}^- connects singlet and triplet states since the operator $\mathbf{s}_1 - \mathbf{s}_2$ is antisymmetric in 1 and 2, and therefore couples symmetric (triplet) electronic spin states to antisymmetric (singlet) states. It is thus fully off-diagonal in the singlet/triplet basis, implying that coupling matrix elements are on the order of unity. V_{hf}^- should thus have matrix elements on the order of a_{hf}.

The singlet potential is a "closed channel", meaning that singlet continuum states are not available as final scattering states by energy conservation. A Feshbach resonance occurs when the state that the atoms collide in (the "incoming" state) is resonant with a bound state in this singlet potential. The energy difference between the incoming and the Feshbach bound state can be tuned via an applied magnetic field, due to their different magnetic moments (see Fig. 31).
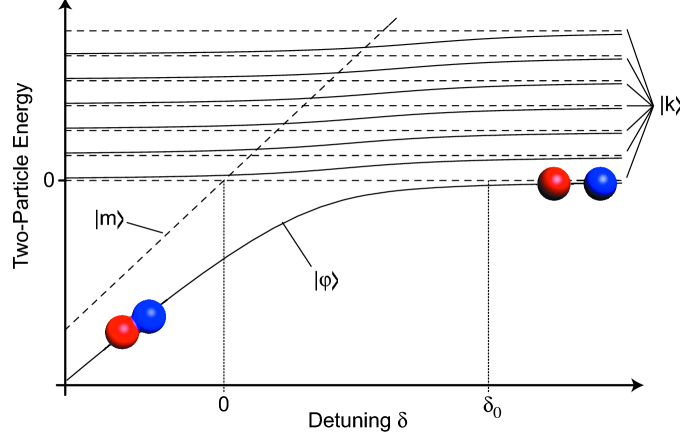
123

Fig. 32. – Simple model for a Feshbach resonance. The dashed lines show the uncoupled states: The closed channel molecular state $|m\rangle$ and the scattering states $|k\rangle$ of the continuum. The uncoupled resonance position lies at zero detuning, $\delta = 0$. The solid lines show the coupled states: The state $|\varphi\rangle$ connects the molecular state $|m\rangle$ at $\delta \ll 0$ to the lowest state of the continuum above resonance. At positive detuning, the molecular state is "dissolved" in the continuum, merely causing an upshift of all continuum states as φ becomes the new lowest continuum state. In this illustration, the continuum is discretized in equidistant energy levels. In the continuum limit (Fig. 33), the dressed molecular energy reaches zero at a finite, shifted resonance position δ_0.

5˙3.1. A model for Feshbach resonances. Good insight into the Feshbach resonance mechanism can be gained by considering two coupled spherical well potentials, one each for the open and closed channel [262]. Other models can be found in [142, 247]. Here, we will use an even simpler model of a Feshbach resonance, in which there is only one bound state of importance $|m\rangle$ in the closed channel, the others being too far detuned in energy (see Fig. 32). The continuum of plane waves of relative momentum $\mathbf{k}$ between the two particles in the incoming channel will be denoted as $|k\rangle$. In the absence of coupling, these are eigenstates of the free hamiltonian

$$H_0 |k\rangle = 2\epsilon_k |k\rangle \qquad \text{with } \epsilon_k = \frac{\hbar^2 k^2}{2m} > 0$$

(195)
$$H_0 |m\rangle = \delta |m\rangle \qquad \text{with } \delta \lessgtr 0$$

where δ, the bound state energy of the "bare" molecular state, is the parameter under experimental control. We consider interactions explicitly only between $|m\rangle$ and the $|k\rangle$'s. If necessary, scattering that occurs exclusively in the incoming channel can be accounted for by including a phase shift into the scattering wave functions $|k\rangle$ (see Eq. 213), i.e. using $\psi_k(r) \sim \sin(kr + \delta_{\text{bg}})/r$, where δ_{bg} and $a_{\text{bg}} = -\lim_{k \to 0} \tan \delta_{\text{bg}}/k$ are the (so-called background) phase shift and scattering length, resp., in the open channel. First, let us see how the molecular state is modified due to the coupling to the continuum $|k\rangle$. For

124

this, solve

$$H \left| \varphi \right> = E \left| \varphi \right>$$

(196)
$$\text{with } \left| \varphi \right> = \alpha \left| m \right> + \sum_k c_k \left| k \right>$$

for $E < 0$, where $H = H_0 + V$ and the only non-zero matrix elements of V are $\left< m \right| V \left| k \right> = g_k / \sqrt{\Omega}$ and their complex conjugates (we will take g_k to be real). Ω is the volume of the system and introduced in this definition for later convenience. We quickly find

$$\left(E - 2\epsilon_k \right) c_k = \frac{g_k}{\sqrt{\Omega}} \alpha$$

$$\left(E - \delta \right) \alpha = \frac{1}{\sqrt{\Omega}} \sum_k g_k c_k = \frac{1}{\Omega} \sum_k \frac{g_k^2 \alpha}{E - 2\epsilon_k}$$

(197)
$$\text{and thus} \quad E - \delta = \frac{1}{\Omega} \sum_k \frac{g_k^2}{E - 2\epsilon_k}$$

We only consider low-energy s-wave scattering, where the range of the potential r_0 is much smaller than the de Broglie wave lengths, $r_0 \ll 1/k$. The closed channel molecular state $\left| m \right>$ will have a size R on the order of r_0, that the de Broglie waves of colliding atoms cannot resolve. The couplings g_k will not vary much for such low-energy collisions with $k \ll 1/R$. One can thus take $g_k \approx g_0$ constant, up to a natural cut-off $E_R = \hbar^2/mR^2$, and $g_k = 0$ beyond. We then find:

(198)
$$|E| + \delta = \frac{g_0^2}{\Omega} \int_0^{E_R} d\epsilon \frac{\rho(\epsilon)}{2\epsilon + |E|}$$

The integral on the RHS is identical to that in the bound state equation in one-channel scattering, Eq. 102. There, the LHS was simply the inverse scattering strength $-1/V_0$. The two-channel problem introduces an energy-dependence in the strength of the potential, $V_0 \to g_0^2/(E - \delta)$. The integral gives

(199)
$$|E| + \delta = \frac{g_0^2 \rho(E_R)}{\Omega} \left\{ 1 - \sqrt{\frac{|E|}{2E_R}} \arctan \left(\sqrt{\frac{2E_R}{|E|}} \right) \right\}$$

$$\approx \begin{cases} \delta_0 - \sqrt{2E_0 |E|} & \text{for } |E| \ll E_R \\ \delta_0 \frac{2}{3} \frac{E_R}{|E|} & \text{for } |E| \gg E_R \end{cases}$$

$$\text{with} \quad \delta_0 \equiv \frac{g_0^2}{\Omega} \sum_k \frac{1}{2\epsilon_k} = \frac{4}{\pi} \sqrt{E_0 E_R}$$

$$\text{and} \quad E_0 \equiv \left(\frac{g_0^2}{2\pi} \left(\frac{m}{2\hbar^2} \right)^{3/2} \right)^2$$

125

E_0 is an energy scale associated with the coupling constant g_0. As illustrated in Fig. 32, for positive detuning $\delta > \delta_0$ the original molecular state is "dissolved" in the continuum. Due to the coupling of the molecular state with the continuum, the resonance position is shifted by δ_0. For $\delta - \delta_0 < 0$, we find a true bound state at

$$(200) \qquad E = \begin{cases} -E_0 + \delta - \delta_0 + \sqrt{(E_0 - \delta + \delta_0)^2 - (\delta - \delta_0)^2} & \text{for } |E| \ll E_R \\ \frac{\delta}{2} - \sqrt{\frac{\delta^2}{4} + \frac{2}{3}\delta_0 E_R}, & \text{for } |E| \gg E_R \end{cases}$$

The "dressed" bound state energy E is shown in Fig. 33. Far away from the resonance region, for $\delta \ll -(E_R^3 E_0)^{1/4}$, one finds $E \approx \delta$, thus recovering the original bound state. On the other hand, close to resonance, the energy $E \approx -\frac{1}{2}(\delta - \delta_0)^2/E_0 = -\frac{8}{\pi^2}E_R(\delta - \delta_0)^2/\delta_0^2$ depends quadratically on the detuning $\delta - \delta_0$, as expected.

Scattering amplitude. To find the scattering amplitude, we solve Schrödinger's equation for $E > 0$. A small imaginary part $i\eta$ with $\eta > 0$ is added to the energy to ensure that the solution will correspond to an outgoing wave. The goal is to see how the coupling to the molecular state affects scattering in the incoming channel. In an approach formally equivalent to the solution for bound states, Eq. 197, we find for the amplitudes c_k in the open channel:

$$(201) \qquad (E - 2\epsilon_k)\, c_k = \frac{g_k}{\sqrt{\Omega}}\, \alpha = \sum_q \frac{g_k}{\sqrt{\Omega}} \frac{1}{E - \delta + i\eta} \frac{g_q}{\sqrt{\Omega}}\, c_q \equiv \sum_q V_{\text{eff}}(k, q)\, c_q$$

By eliminating the closed-channel molecular amplitude α from the equations, the scattering problem is now entirely formulated in the open channel. The molecular state causes an effective interaction V_{eff} that corresponds to two atoms colliding and forming a molecule (matrix element $\frac{g_q}{\sqrt{\Omega}}$), spending some small amount of time (of order $\hbar/(E - \delta)$) in the molecular state (propagator $\frac{1}{E - \delta + i\eta}$) and exiting again as two unbound atoms (matrix element $\frac{g_k}{\sqrt{\Omega}}$).

The *s*-wave scattering amplitude can now be obtained using the general expression we found in chapter **4˙1**, equation 92. We only need to insert the effective potential $V_{\text{eff}}(k, q)$ in place of $V(\mathbf{k} - \mathbf{q})/\Omega$. The problem is simplified by setting as before all $g_k = g_0$ for $E < E_R$ and $g_k = 0$ for $E > E_R$. The replacement is

$$(202) \qquad V_0 \to V_{\text{eff}}\, \Omega = \frac{g_0^2}{E - \delta}$$

as we had found for the bound state problem, and Eq. 92 becomes

$$(203) \qquad \frac{1}{f_0(k)} \approx -\frac{4\pi\hbar^2}{mg_0^2}(E - \delta) + 4\pi \int \frac{d^3q}{(2\pi)^3} \frac{1}{k^2 - q^2 + i\eta}$$

The integral on the RHS is identical to what one encounters in one-channel scattering:

it generates the necessary $-ik$ (see Eqs. 84 and 95), it determines the resonance position by introducing a shift $-4\pi \int \frac{d^3q}{(2\pi)^3} \frac{1}{q^2} = -\frac{2}{\pi} \frac{\sqrt{2}}{R}$ and it contributes to the effective range r_{eff} with a term $\propto R$ (which we neglect in the following, as E_R is taken to be the largest energy scale in the problem). All the physics of the two-channel model is contained in the first term, which includes the molecular state energy δ and a term proportional to $E \propto k^2$ that will give another contribution to the effective range. Using $-4\pi \int \frac{d^3q}{(2\pi)^3} \frac{1}{q^2} = -\frac{4\pi\hbar^2\delta_0}{mg_0^2}$ and replacing g_0 in favor of E_0 via Eq. 200, we have

$$(204) \qquad \frac{1}{f_0(k)} \approx -\sqrt{\frac{m}{2\hbar^2 E_0}}(\delta_0 - \delta) - \frac{1}{2}\sqrt{\frac{2\hbar^2}{mE_0}}k^2 - ik$$

The scattering amplitude is now in the general form of Eq. 84, and we can read off the scattering length and the effective range of the model:

$$(205) \qquad a = \sqrt{\frac{2\hbar^2 E_0}{m}}\frac{1}{\delta_0 - \delta}$$

$$(206) \qquad r_{\text{eff}} = -\sqrt{\frac{2\hbar^2}{mE_0}}$$

The scattering length, shown in Fig. 33, diverges at the *shifted* resonance position $\delta = \delta_0$. Not surprisingly, we recover $E = -\hbar^2/ma^2$ for the bound state energy close to resonance for positive $a > 0$, as it should be (see Eq. 200).

In the experiment, the Feshbach resonance occurs for a certain magnetic field B_0. With the magnetic moment difference $\Delta\mu$ between the incoming state and the closed (uncoupled) molecular state, we have $\delta - \delta_0 = \Delta\mu(B - B_0)$ (taking $\Delta\mu$ to be constant). Including the background scattering length a_{bg} for collisions that occur entirely in the open channel, the scattering length can be written in its usual form

$$(207) \qquad a = a_{\text{bg}}\left(1 - \frac{\Delta B}{B - B_0}\right) \qquad \text{with } \Delta B = \sqrt{\frac{2\hbar^2 E_0}{m}}\frac{1}{\Delta\mu\, a_{\text{bg}}}$$

5˙4. *Broad versus narrow Feshbach resonances.* – Initially it was assumed that all Feshbach resonances represent a novel mechanism for fermionic pairing and superfluidity. Treatments of "resonance superfluidity" [170] and "composite Fermi-Bose superfluid" [263] explicitly introduced coupled atomic and molecular fields as an extension of the standard BEC-BCS crossover theory presented in chapter **4**. On the other hand, as discussed in the previous chapter, the closed channel molecular state can be formally eliminated from the description by introducing an effective potential acting on the atoms in the open channel. We will see in this section that sufficiently close to the Feshbach resonance, and for sufficiently small Fermi energies, the physics is indistinguishable from a single channel model such as the attractive spherical well (with $R \ll 1/k_F$) discussed in section **5˙2** or a (suitably regularized) contact interaction. It turns out that this sim-
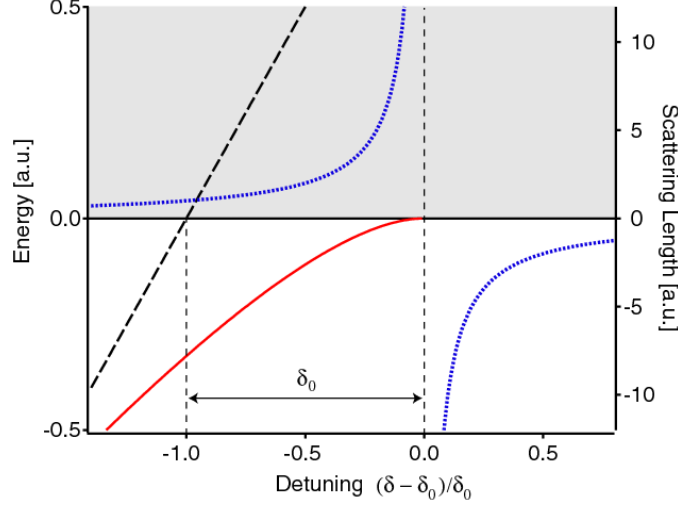
Fig. 33. – Bare, uncoupled molecular state (dashed line), coupled, bound molecular state (solid line) and scattering length (dotted line) close to a Feshbach resonance. The shaded area represents the continuum of scattering states, starting at the collision threshold at $E = 0$. Interaction between the molecular state and the continuum shifts the position of the resonance by δ_0 from the crossing of the uncoupled molecular state with threshold. Note the quadratic behavior of the bound state energy with detuning $(\delta - \delta_0)$ close to resonance.

ple description applies to the experimental studies in ^{6}Li and ^{40}K. In these cases, that involve so-called broad Feshbach resonances, the resonance simply provides a knob to turn $1/k_F a$ continuously from large positive values to negative values. The physics is independent of the nature of the molecular state. Therefore, these system are universal, i.e. they are ideal realizations of the "standard" BEC-BCS crossover physics described in chapter **4**, and not a new form of "Feshbach" or "resonance" superfluidity.

5˙4.1. Energy scales. To address the question on the range of parameters where the molecular state does play a role, we consider the energy scales in the problem. They are E_0, the energy scale associated with the coupling strength, the detuning from resonance $\delta - \delta_0$, as a function of which we want to study the system, and E_F, the Fermi energy. As we will show, the ratio E_F/E_0 of the Fermi energy to the coupling energy scale is the parameter that decides whether the physics around the resonance is universal ($E_0 \gg E_F$) or whether the closed molecular channel still plays a role ($E_0 \ll E_F$) [264, 265, 266, 247]. With Eq. 205 this can be equivalently expressed as $k_F r_{\text{eff}} \ll 1$, that is, universality requires the effective range of the potential to be much smaller than the interparticle distance. In principle, we have two more energy scales, the cutoff energy scale E_R and the shift δ_0. E_R is much larger than the Fermi energy, as we deal with dilute gases where the interatomic distance is large compared to the range of the potential. Then, the shift $\delta_0 \sim \sqrt{E_R E_0}$ is much larger than E_F if $E_0 \gg E_F$, and does not lead to an additional

criterion.

5˙4.2. Criterion for a broad resonance. The criterion $E_0 \gg E_F$ for a broad resonance is found in several different ways, each of which is insightful.

BEC-side. For a spherical well potential, the bound state energy is given by the universal relation $E_B = -\hbar^2/ma^2$ (as long as $|E_B| \ll E_R$). This signifies that the character of the molecular state is entirely described by the scattering length, a property of the scattering states in the open channel. However, for the two-channel Feshbach model discussed above, this relation holds only for $\delta_0 - \delta \ll E_0$ (see Eq. 200) or equivalently for $\hbar^2/ma^2 \ll E_0/2$. To observe the universal version of the BEC-BCS crossover presented in the last chapter, the bound state should obey the universal behavior already when $k_F a \approx 1$. This yields the condition $E_F \ll E_0$ for the "BEC"-side of the resonance.

A more quantitative way to see this is by calculating the contribution of the closed channel molecule to the "dressed" molecular state

$$(208) \qquad\qquad |\varphi\rangle = \alpha \, |m\rangle + \sum_k c_k \, |k\rangle$$

This can be calculated from the magnetic moment of $|\varphi\rangle$, relative to two free atoms: Bare molecules have a relative magnetic moment $\Delta\mu$, so $\mu_{|\varphi\rangle} = \alpha^2 \Delta\mu$. One finds with Eq. 207: $\mu_{|\varphi\rangle} = \frac{\partial E_B}{\partial B} = \sqrt{\frac{2|E_B|}{E_0}} \, \Delta\mu$. When the binding energy $|E_B|$ becomes comparable to the Fermi energy E_F near resonance, the closed channel contribution $\alpha^2 = \sqrt{\frac{2|E_B|}{E_0}}$ should already be negligible in order for the physics to be dominated by the open channel. Again, this gives the criterion $E_F \ll E_0$.

BCS-side. For $\delta > \delta_0$ the molecular bound state has disappeared, but the closed channel molecule still leaves its mark in the scattering cross section [247] ($E = \hbar^2 k^2/m$):

$$\sigma(E) = 4\pi |f(E)|^2 = 4\pi r_{\rm eff}^2 \frac{E_0^2}{(E - \delta + \delta_0)^2 + 2E_0 E}$$

$$(209) \qquad\qquad = 4\pi r_{\rm eff}^2 \frac{E_0^2}{(E - E_{\rm res})^2 + \Gamma^2/4}$$

$$\text{with } E_{\rm res} = \delta - \delta_0 - E_0$$

$$(210) \qquad\qquad \text{and } \Gamma^2 = 4E_0^2 \left(\frac{2(\delta - \delta_0)}{E_0} - 1 \right)$$

For $\delta - \delta_0 > E_0$ (equivalently $\hbar^2/ma^2 > E_0/2$), $E_{\rm res} > 0$ and a resonance appears in the scattering cross section at finite energies. This resonance is just the (shifted) bare molecular state that has acquired a finite lifetime $\hbar\Gamma^{-1}$ due to the coupling to the continuum. While the width Γ increases with detuning like $\sim \sqrt{\delta - \delta_0}$ for $E_{\rm res} \gg E_0$, the relative width $\Gamma/E_{\rm res} \sim 1/\sqrt{\delta - \delta_0}$ *decreases*, so that the relative position of the
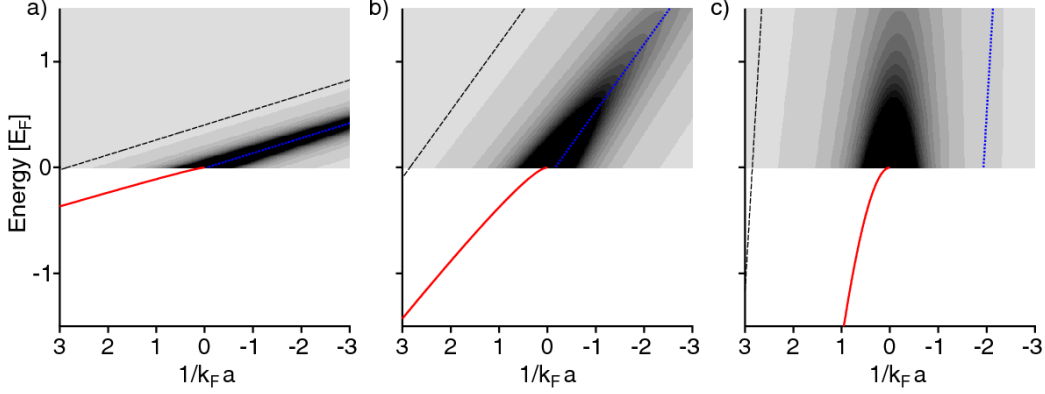
Fig. 34. – Broad versus narrow Feshbach resonances. Shown are the two-body bound state energy (straight line, in units of E_F), and scattering cross section contours (in gray shades) for various Feshbach coupling strengths E_0. The dashed line is the bare molecular state (here, $E_R = 20E_F$, thus $\delta = 0$ at $1/k_F a = \frac{2}{\pi}\sqrt{E_R/E_F} = 2.85$). The dotted line marks the position of finite-energy maxima of the cross section for $\hbar^2/ma^2 > E_0/2$ (see text). a) $E_0 = 0.005\,E_F$, b) $E_0 = 0.1\,E_F$, c) $E_0 = 15\,E_F$. In c), bound state and scattering cross section contours closely approach those for a contact potential. A similar figure can be found in [247].

molecular state resonance can in principle be measured more and more accurately in scattering experiments. For large values of δ, the expression Eq. 210 for Γ approaches the result of Fermi's Golden Rule, $\Gamma = 2\pi\, g_0^2\, \rho(\epsilon)/\Omega$, where $\epsilon = (\delta - \delta_0)/2$ is the energy of the fragments after molecular dissociation, and $\rho(\epsilon) \propto (\delta - \delta_0)^{1/2}$ is the density of final states. This relation was verified by observing the decay of molecules after a rapid ramp across the resonance [149]. Clearly, in this region, the molecular state has a life of its own.

The closed channel molecular state causes a finite-energy scattering resonance on the "BCS"-side starting at $\delta - \delta_0 = E_0$ that is non-universal. In single-channel scattering off a delta-potential or a spherical well potential, no such finite-energy resonances exist. We require for universal behavior that such resonances do not occur within the BEC-BCS crossover, i.e. within the strongly interacting regime, where $k_F|a| \gtrsim 1$, or equivalently $\delta - \delta_0 \lesssim E_F$. This leads again to the condition $E_0 \gg E_F$.

Fig. 34 summarizes these findings. The BEC-BCS crossover occurs for $-1 \lesssim 1/k_F a \lesssim 1$. If $E_0 \gg E_F$, the "dressed" molecular state is almost completely dissolved in the open channel continuum throughout the crossover and the details of the original molecular state $|m\rangle$ do not play a role (case of a "broad" Feshbach resonance). The binding energy is given by $E_B = -\hbar^2/ma^2$ on the BEC-side, and the scattering cross section has the universal form $\sigma(k) = 4\pi\frac{a^2}{1+k^2a^2}$. On the other hand, if E_0 is comparable to E_F, then the molecular state affects the many-body physics and it needs to be included in the description of the gas (case of a "narrow" Feshbach resonance) [267, 268, 247].

130

On resonance. A stringent criterion for universal behavior requires that all scattering properties for detunings $\delta - \delta_0 \leq E_F$ and for energies $E < E_F$ are identical to the case of a (regularized) delta-potential or a localized spherical well potential, where the scattering amplitude f is given by $1/f = -1/a - ik$, i.e. the contribution of the effective range, $\frac{1}{2}r_{\text{eff}}k^2$ to $1/f$ is negligible. For the total cross section, which is proportional to $|f|^2$ (Eq. 209), the effective range correction is negligible for $k \ll 1/r_{\text{eff}}$, or equivalently, $E_F \ll E_0$. However, the real part of f, which determines the mean field energy for a dilute gas, depends more strongly on the effective range: it is equal to $-1/ak^2$ for large a, but approaches a constant $r_{\text{eff}}/2$ if $r_{\text{eff}} \neq 0$. This does not spoil universality, though, as the mean field energy associated with such a small effective scattering length, $\propto \hbar^2 n r_{\text{eff}}/m$, has to be compared to the many-body interaction energy, $\beta E_F \propto \hbar^2 k_F^2/m \propto \hbar^2 n/m k_F$ (see chapter **4**), which dominates as long as $k_F \ll 1/r_{\text{eff}}$ or $E_0 > E_F$.

Magnetic moment. Finally, we want to come back to the schematic description of the Feshbach resonance in Fig. 32 that uses discrete states in a finite volume L^3. Each energy curve has two avoided crossings. For small coupling, the slope in between these crossings is still given by the magnetic moment of the molecule, i.e. in this region, population can be purely in the closed channel. This picture is lost when many states couple, i.e. the resonant coupling $g_k/L^{3/2}$ is larger than the level spacing, which is about $E_L = \hbar^2/mL^2$. In order to still maintain some character of the closed channel molecule, one must have $g_k < \hbar^2/mL^{1/2}$ or $E_0 < E_L$. However, any finite volume approximation has to choose L at least comparable to the interatomic spacing, or equivalently, the zero-point energy E_L has to be less than the Fermi energy. Therefore, for the case of a broad resonance with $E_0 > E_F$, the simple picture of two-level avoided crossings no longer applies, the molecular state gets "smeared" out and "distributed" over many open channel states.

5˙4.3. Coupling energy scale. We can relate the coupling energy scale E_0 to experimentally observable parameters. Using Eq. 207 and the definition for E_0, Eq. 200, one has

$$(211) \qquad E_0 = \frac{1}{2}\frac{(\Delta\mu\Delta B)^2}{\hbar^2/ma_{\text{bg}}^2}$$

The fraction of the dressed molecular wave function that is in the deeply bound state $|m\rangle$ is

$$(212) \qquad \alpha^2 = \sqrt{\frac{2E_B}{E_0}} = 2\sqrt{\frac{E_F}{E_0}}\frac{1}{k_F a}$$

For the resonance used in the experiments by D. Jin on ^{40}K, $E_0/k_B \approx 1\,\text{mK}$, which should be compared to a typical Fermi energy of $E_F/k_B = 1\,\mu\text{K}$. This resonance is thus broad [269]. Still, at $k_F a = 1$ the fraction of the wave function in the closed channel molecule is $\alpha^2 \approx 6\%$. This might possibly explain the shorter lifetime of the gas of molecules ^{40}K$_2$ close to resonance [18] as compared to the case in ^{6}Li$_2$ [270]. For the wide

Feshbach resonance in ^{6}Li, one has $E_0/k_B \approx 50\,\mathrm{K}$, an unusually broad resonance. The strongly interacting regime where $1/k_F|a| < 1$ is thus completely in the universal regime. The simple relation $E_B = -\hbar^2/ma^2$ holds to better than 3% already at a magnetic field of 600 G, 230 G away from resonance, while the strongly interacting regime is entered only above ≈ 750 G. Indeed, the closed channel contribution to the dressed molecular state has been measured in the group of R. Hulet [76] to be less than 1% at magnetic fields beyond 600 G and less than 10^{-3} throughout the entire strongly interacting regime beyond $k_F|a| \approx 1$.

5'4.4. *Narrow Feshbach resonance.* The Feshbach resonance in ^{6}Li at 543 G, in turn, has $E_0/k_B \approx 1\,\mu\mathrm{K}$ and is thus narrow. In the case of a narrow resonance, the many-body physics is qualitatively different from the BEC-BCS crossover picture since molecular states will be populated even above the resonance. However, we have just shown how the molecular states have "disappeared" or have become scattering resonances. So how does many-body physics modify these results of two-body physics?

For a narrow resonance and detunings $\delta - \delta_0 < 0$, all fermion pairs are still tightly bound in the closed channel molecular state, where they form a condensate. For $0 < \delta - \delta_0 < 2E_F$, the molecular condensate coexists with a BCS-type fermionic superfluid. Here, the molecular state (unstable in vacuum above threshold, represented by the resonances in the scattering cross section in Fig. 34) is stabilized by Pauli blocking, as the outgoing momentum states are occupied by fermions in the BCS-state. Equilibrium between fermions and molecules requires that the chemical potential of the fermions is $\mu = (\delta - \delta_0)/2$. This means that the molecular state "shaves off" all fermions above μ (they form molecules), and the Fermi sea is only filled up to this energy [271]. Only for $\delta - \delta_0 > 2E_F$ is the molecular state no longer occupied and we are left with a BCS-type superfluid. However, since the resonance is narrow, the interactions for $\delta - \delta_0 > 2E_F \gg E_0$ will be very small, $k_F\,|a| < \sqrt{\frac{E_0}{E_F}} \ll 1$, rendering the observation of such a state very difficult.

The transition from the narrow to the broad resonance requires a more complete two-channel description (see [247] and references therein), where even the two-body scattering physics is modified by the Fermi sea. One example is the transition from the narrow to the broad case right on resonance. In the two-body picture, no scattering resonances (and therefore identifiable molecular states) exist. This remains true for a small Fermi sea, with $E_F \ll E_0$, that cannot appreciably affect the open channel states. However, as the Fermi energy becomes comparable to the coupling E_0, more and more k-states are occupied and Pauli blocked, and the closed channel molecular state can no longer completely dissolve in the continuum states. For $E_F \gg E_0$, the closed channel molecular state is present in its "undressed" form, and one expects a condensate of these "protected" closed channel molecules to coexist with a Fermi sea. For an extensive discussion of one and two-channel descriptions, we refer the reader to the contribution of M. Holland to these lecture notes.

5'5. *Open channel resonance and the case of ^6Li.* – ^{6}Li stands out compared to all other fermionic atoms studied thus far by its enormously broad Feshbach resonance. It is
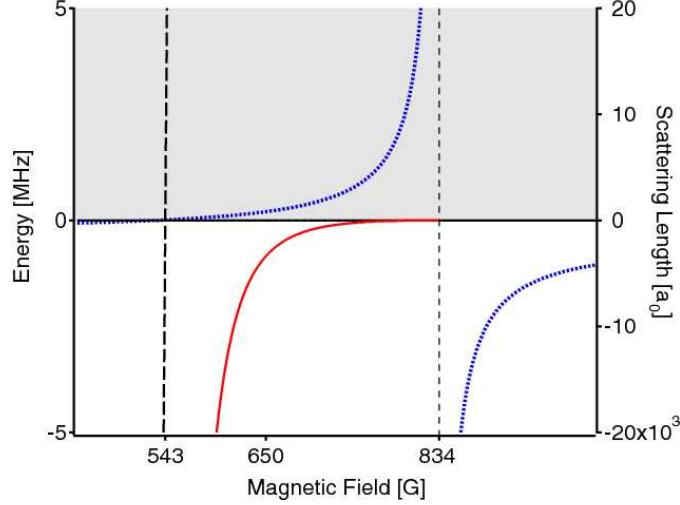
Fig. 35. – Feshbach resonances in ^{6}Li between the two lowest hyperfine states $|F, m\rangle = |1/2, 1/2\rangle$ and $|1/2, -1/2\rangle$. A wide Feshbach resonance occurs at 834.15 G. The resonance position is shifted by an unusually large amount of ~ 300 G from the crossing of the uncoupled molecular state at 543 G (thick dashed line). A second, narrow Feshbach resonance occurs right at 543 G, shifted by less than 200 mG. The solid line shows the energy of the bound molecular state, and the dotted line the scattering length.

this fact that has allowed direct evaporation of the gas at a fixed magnetic field directly into a molecular condensate, an experiment almost as straightforward in principle as Bose-Einstein condensation of bosonic atoms in a magnetic trap. Lithium is the fermion of choice at Duke, Rice, Innsbruck, ENS and MIT, and also in a growing number of new experimental groups.

Fig. 35 shows the s-wave scattering length for collisions between the two lowest hyperfine states of ^{6}Li, $|F, m\rangle = |1/2, 1/2\rangle$ and $|1/2, -1/2\rangle$. The prominent feature is the broad Feshbach resonance centered around $B_0 = 834.15$ G. The resonance is approximately described by Eq. 207 with $a_{\mathrm{bg}} = -1\,405\,a_0$, $\Delta B = 300$ G [135]. These values are very untypical when compared with scattering lengths and Feshbach resonance widths in other alkali atoms. Background scattering lengths are typically on the order of $\pm 100\,a_0$ or less, roughly the range of the van der Waals-potential. Widths of other observed Feshbach resonances are two, rather three orders of magnitude smaller than ΔB. Clearly, the broad Feshbach resonance in ^{6}Li is a special case.

The unusually large background scattering length of ^{6}Li that approaches $-2\,100\,a_0$ at high fields, signals a resonance phenomenon even away from the wide Feshbach resonance. Indeed, if the triplet potential of ^{6}Li were just about $\hbar^2/ma_{\mathrm{bg}}^2 \approx h \cdot 300$ kHz deeper, it would support a new bound state. This "missing" potential depth should be compared to *typical* spacings between the highest lying bound states of the van der Waals potential, several tens of GHz. The resulting very large background scattering length modifies the
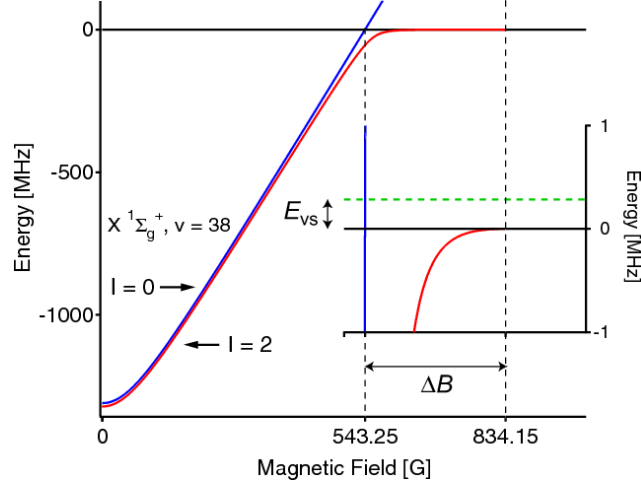
133

Fig. 36. – Bound state energies for ^{6}Li$_2$ in a magnetic field. The most weakly bound state of the singlet potential, $X^1\Sigma_g^+, v = 38$, splits into two hyperfine components with total nuclear spin $I = 0$ and $I = 2$. The state with $I = 0$ is almost not coupled to the triplet scattering continuum, causing the narrow resonance at 543.2 G. In turn, the state $I = 2$ is very strongly coupled and leads to the broad resonance at 834 G, a shift of $\Delta B \approx 300$ G. The strong coupling is caused by the large background scattering length a_{bg} in the triplet potential. The dashed line in the inset shows the associated energy of the "virtual", almost bound state $E_{\text{vs}} \approx h \cdot 300$ kHz, very close to threshold ($E = 0$).

free continuum states $|k\rangle$ in a simple but important way: It increases the probability for the two colliding atoms to be close to each other. This leads to a much better wave function overlap between the free continuum states and the closed channel bound state — in the language of molecular spectroscopy, one has a much larger Franck-Condon factor.

In the following, we want to show this quantitatively by directly calculating the coupling strength $g_k = \langle m|V|k\rangle$ as a function of the background scattering length. The states $|k\rangle$ are eigenstates of the Hamiltonian H_0, which includes the scattering potential in the open channel. Outside that potential, the wave function $\psi_k(\mathbf{r}) = \langle \mathbf{r}|k\rangle$ becomes

$$(213) \qquad \psi_k(\mathbf{r}) = \frac{1}{\sqrt{\Omega}} \frac{\sin(kr + \delta_{\text{bg}})}{kr}$$

For a background scattering length much larger than the range of the potential $a_{\text{bg}} \gg r_0$, we can neglect the short-range behavior of ψ at $r \lesssim r_0$. The chosen normalization ensures the closure relation $\sum_k c_k \langle k'|k\rangle = c'_k$ to hold. The closed channel molecular state will be taken to be of the form

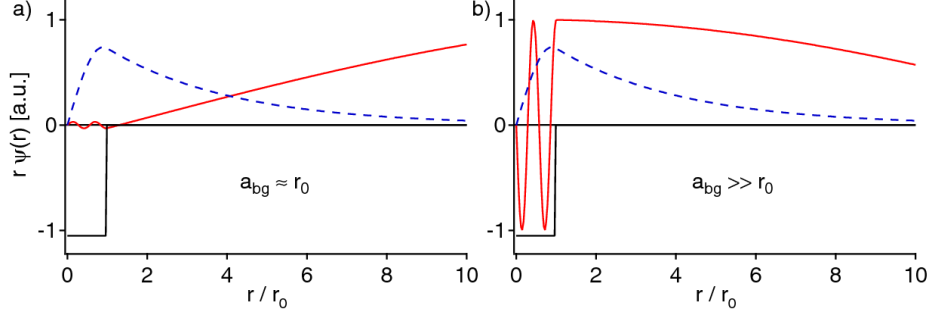$$(214) \qquad \psi_m(\mathbf{r}) = \frac{1}{\sqrt{2\pi R}} \frac{e^{-r/R}}{r}$$

134

Fig. 37. – Influence of the background scattering length on the Feshbach coupling. Shown is a spherical well example, with a well of radius r_0. Solid line: Open channel radial wave function $r\psi(r)$. Dashed line: Molecular state in the closed channel, with an assumed smaller well depth. a) "typical" background scattering length, $a_{\mathrm{bg}} \approx r_0$, b) large scattering length, $a_{\mathrm{bg}} \gg r_0$. The probability to overlap with the bound state is resonantly enhanced.

This also neglects the short-range behavior of $\psi_m(\mathbf{r})$ for $r \lesssim r_0$, permissible if the size of the molecule is much larger than the interatomic potential, $R \gg r_0$.

Fig. 37 shows the situation for two different background scattering lengths. For $k \ll 1/R$ we have $r\psi_k(\mathbf{r}) \approx \frac{1}{\sqrt{\Omega}}(r - a_{\mathrm{bg}})$. For $a_{\mathrm{bg}} \lesssim R$, the probability for two colliding particles to be within a range R of each other is simply $\sim R^3/\Omega$, as it would be for non-interacting particles. However, for $a_{\mathrm{bg}} \gtrsim R$, the probability increases to $\sim a_{\mathrm{bg}}^2 R/\Omega$. The coupling to the closed channel molecular state should be enhanced by the same factor, so we expect $|\langle m|V|k\rangle|^2 \propto a_{\mathrm{bg}}^2$. A simple calculation gives

$$
\langle m|V|k\rangle = V_{\mathrm{hf}} \int \mathrm{d}^3 r\, \psi_m^*(\mathbf{r})\psi_k(\mathbf{r}) \tag{215}
$$

$$
= \frac{V_{\mathrm{hf}}}{k} \sqrt{\frac{8\pi R}{\Omega}} \frac{\sin\delta_{\mathrm{bg}} + kR\cos\delta_{\mathrm{bg}}}{1 + k^2 R^2} \tag{216}
$$

where V_{hf} is the amplitude of the hyperfine interaction V_{hf}^- between the open and closed channel. In the s-wave limit of large de Broglie wavelengths, we can approximate $\tan\delta_{\mathrm{bg}} \approx -k\, a_{\mathrm{bg}}$. We then get

$$
g_k^2 = \Omega\,|\langle m|V|k\rangle|^2 = 8\pi\,|V_{\mathrm{hf}}|^2\, R^3\, \frac{(1 - a_{\mathrm{bg}}/R)^2}{\left(1 + k^2 a_{\mathrm{bg}}^2\right)\left(1 + k^2 R^2\right)^2} \tag{217}
$$

g_k^2 is just proportional to the background scattering cross section $\sigma_{\mathrm{bg}} = 4\pi a_{\mathrm{bg}}^2/(1+k^2 a_{\mathrm{bg}}^2)$, including its k-dependence and the unitarity limit:

$$
g_k^2 = 2\,|V_{\mathrm{hf}}|^2\, R\, \sigma_{\mathrm{bg}} \frac{(1 - R/a_{\mathrm{bg}})^2}{(1 + k^2 R^2)^2} \tag{218}
$$

135

In section **5** 4.2 we have seen how g_k^2 determines the lifetime of a molecular state placed in the continuum at energy E. In our model, this lifetime becomes, by Fermi's Golden Rule,

$$(219) \qquad \Gamma(E) = \frac{2\pi}{\hbar} \sum_k |\langle m|V|k\rangle|^2 \, \delta(2\epsilon_k - E) = \frac{\pi}{\hbar} \frac{1}{\Omega} \, \rho\,(E/2) \; g_{k(E/2)}^2$$

$$(220) \qquad = \frac{4}{\hbar} |V_{\mathrm{hf}}|^2 \, \left(1 - \frac{a_{\mathrm{bg}}}{R}\right)^2 \frac{\sqrt{E}\sqrt{E_R}\,E_{\mathrm{bg}}}{(E_{\mathrm{bg}} + E)\,(E_R + E)^2}$$

where $E_{\mathrm{bg}} = \hbar^2/ma_{\mathrm{bg}}^2$. The latter is the *exact* same expression that one obtains for a bound-free radio-frequency transition that dissociates (or associates) a molecule into (from) two free atoms [206] (valid in the threshold regime $a_{\mathrm{bg}}, R \gg r_0$). One merely has to replace the hyperfine coupling by the Rabi coupling $\frac{1}{2}\hbar\Omega_R$. The dependence on $\sqrt{E}$ is the usual Wigner threshold law. This reiterates the analogy between Feshbach resonances and photo or RF association.

The k-dependent coupling g_k^2 rolls off over a characteristic range $1/R$, as expected. So the natural cut-off energy is $E_R = \hbar^2/mR^2$, as before. For $k \ll 1/R$, we obtain

$$(221) \qquad g_0^2 = 2\,|V_{\mathrm{hf}}|^2\, R\,\sigma_{\mathrm{bg}}\,(1 - R/a_{\mathrm{bg}})^2$$

with the limiting cases

$$(222) \qquad g_0^2 = \quad 8\pi\,|V_{\mathrm{hf}}|^2\,R^3 \qquad \text{for } a_{\mathrm{bg}} \ll R$$

$$(223) \qquad g_0^2 = 8\pi\,|V_{\mathrm{hf}}|^2\,R\,a_{\mathrm{bg}}^2 \qquad \text{for } a_{\mathrm{bg}} \gg R$$

The resonant limit $a_{\mathrm{bg}} \gg R$ is valid if $ka_{\mathrm{bg}} \ll 1$. In the strongly interacting regime where $ka_{\mathrm{bg}} \gg 1$, the Feshbach coupling is unitarity limited to $g_0^2 = 8\pi\,|V_{\mathrm{hf}}|^2\,R/k^2$.

We thus arrive at the conclusion that a large background scattering length resonantly enhances the coupling to the closed channel molecular state. This is simply because of the increased probability for two particles colliding in the open channel to be near each other.

Since g_0^2 determines the effective range of the Feshbach scattering amplitude, Eq. 205, we can say that the background scattering length tunes the effective range. In fact, for $a_{\mathrm{bg}} \gg R$, we find

$$(224) \qquad r_{\mathrm{eff}} = -\frac{\hbar^2}{ma_{\mathrm{bg}}^2}\frac{E_R}{|V_{\mathrm{hf}}|^2}R$$

The larger the background scattering length, the smaller the effective range. The criterion for a broad Feshbach resonance, $E_0 \gg E_F$, now reads

$$(225) \qquad E_F \ll \frac{2\,|V_{\mathrm{hf}}|^4}{E_R}\frac{m^2 a_{\mathrm{bg}}^4}{\hbar^4}$$

136

Knowing that ^{40}K does not have an unusually long background scattering length, this relation implies that for reasonably strong couplings V_{hf} (a sizeable fraction of the hyperfine splitting), but only "standard" background scattering lengths, molecular sizes R and for typical Fermi energies, Feshbach resonances are broad.

We can now easily calculate the energy shift δ_0 due to this enhanced Feshbach coupling. This directly gives the magnetic field shift $B_0 - B^* = \delta_0/\Delta\mu$ between the Feshbach resonance position at B_0, where the dressed bound state energy vanishes, and the magnetic field B^* where the uncoupled molecular state would cross threshold. In ^{6}Li, $B_0 = 834\,\mathrm{G}$, whereas $B^* = 543\,\mathrm{G}$ (in fact, an almost uncoupled, second closed channel molecular state causes a narrow resonance at B^*, see Fig. 36). With the definition in Eq. 200, and again in the limit $1/k \gg a_{\mathrm{bg}} \gg R$,

$$(226) \qquad \delta_0 = \frac{4}{\pi}\sqrt{E_0 E_R} = \frac{1}{\sqrt{2}\pi^2}\frac{m\,g_0^2}{\hbar^2 R} = \frac{4\sqrt{2}}{\pi}\left|V_{\mathrm{hf}}\right|^2 \frac{m a_{\mathrm{bg}}^2}{\hbar^2}$$

With the known magnetic field shift in ^{6}Li, using $a_{\mathrm{bg}} \approx 2100\,a_0$ and $\Delta\mu = 2\mu_B = 2.8\,\mathrm{MHz/G}$, we can now obtain an estimate of the hyperfine coupling strength, $V_{\mathrm{hf}} \approx h \cdot 10\,\mathrm{MHz}$. This is indeed a "typical" coupling strength: The hyperfine constant for ^{6}Li is $a_{\mathrm{hf}} \approx h \cdot 150\,\mathrm{MHz}$, setting an upper bound on the matrix element V_{hf} which is less than a_{hf} due to Clebsch-Gordan coefficients. Of course, our model neglects short range physics that may affect g_0^2.

Some authors [272, 273] arrive at the same conclusion of Eq. 226 by introducing a "virtual state" at the energy $E_{\mathrm{vs}} \sim \hbar^2/m a_{\mathrm{bg}}^2$ above threshold and replacing the interaction of the molecular state with the scattering continuum by an effective interaction between molecular and virtual state only. In this language, second-order perturbation theory predicts an energy shift of $\delta_0 \approx \left|V_{\mathrm{hf}}\right|^2/E_{\mathrm{vs}} = \left|V_{\mathrm{hf}}\right|^2 m a_{\mathrm{bg}}^2/\hbar^2$, exactly as we have obtained above. We point out that there is no finite energy scattering resonance associated with this "imaginary" state. Rather, it signifies that if the potential were deeper by $\sim E_{\mathrm{vs}}$, it would support a new bound state just below threshold.

To summarize: the history of interactions in Fermi gases has gone full circle. At first, ^{6}Li was thought to be a great candidate for fermionic superfluidity because of its large and negative background scattering length. Then it was realized that scattering lengths can be tuned at will close to a Feshbach resonance – so essentially any fermionic atom that could be laser cooled became a good candidate (as Feshbach resonances have so far been found for any atom, whenever experimentalists started to search for them). But in the end, it is still ^{6}Li that is the most robust choice, and this indeed *because* of its large scattering length – since this is what enhances the Feshbach coupling and makes the resonance abnormally – fantastically – large.

System	BEC	Superfluid
3D	$\sqrt{}$	$\sqrt{}$
Ideal gas	$\sqrt{}$	$\emptyset$
2D, $T \neq 0$	$\emptyset$	$\sqrt{}$
2D, $T = 0$	$\sqrt{}$	$\sqrt{}$
1D, $T = 0$	$\emptyset$	$\sqrt{}$

TABLE VIII. – *Condensation versus superfluidity. Condensation and superfluidity are two different, but related phenomena. The ideal gas is Bose condensed, but not superfluid. In lower dimensions, fluctuations can destroy the condensate, but still allow for superfluidity.*

6. – Condensation and superfluidity across the BEC-BCS crossover

In this section, we present experimental results on condensation and superfluid flow across the BEC-BCS crossover. We will start with some general remarks on different signatures for superfluidity, give some background on vortices and describe the experimental methods to observe condensation and vortex lattices in gases of fermionic atoms together with the results achieved.

6˙1. *Bose-Einstein condensation and superfluidity.* – Two phenomena occurring at low temperature have received special attention: Bose-Einstein condensation and superfluidity. An interesting question is how the two are related. K. Huang has pointed out [274] that Bose-Einstein condensation is not necessary for superfluidity, but also not sufficient. This is illustrated by the examples in table VIII.

The ideal Bose gas can undergo Bose-Einstein condensation, but it does not show superfluid behavior since its critical velocity is zero. Superfluidity requires interactions. The opposite case (superfluidity without BEC) occurs in lower dimensions. In 1D at $T = 0$ [275, 276] and in 2D at finite temperature, superfluidity occurs [277], but the condensate is destroyed by phase fluctuations [278, 279, 280]. In 2D at zero temperature, there is both a condensate and superfluidity [281].

In 3D, condensation and superfluidity occur together. An interesting case that has been widely discussed are bosons in a random potential. For weak disorder and weak interactions, there is an unusual regime where the superfluid fraction is smaller than the condensate fraction [282, 283]. It appears that some part of the condensate is pinned by the disorder and does not contribute to the superfluid flow. However, the extrapolation to strong disorder and the conclusion that the system can be Bose condensed without being superfluid [282, 274] is not correct [284, 285]. The condensate and superfluid fraction disappear together when the disorder is sufficiently strong [284, 285].

A very comprehensive discussion on the relation between superfluidity and BEC is presented in the Appendix of Ref. [286]. When condensation is generalized to quasi-condensation in lower dimensions the two phenomena become equivalent. It is shown that superfluidity plus finite compressibility are sufficient conditions for either condensation or quasi-condensation. The reverse is also true, i.e. condensation or quasi-condensation are necessary for superfluidity. Here, superfluidity is defined by the rigidity of the system

against changes in the phase of the boundary condition and condensation by the presence of a macroscopic eigenvalue of the density matrix, which, for translationally invariant systems, implies off-diagonal long range order. Quasi-condensates are local condensates without long range order.

This discussion on bosons applies directly to a gas of bosonic molecules created at a Feshbach resonance. For a Fermi gas, the examples for lower dimensions apply as well [278] (for a discussion of superconductivity in 2D films and arrays, see [242]). The example of the non-interacting Bose gas, however, does not carry over: A non-interacting Fermi gas does not form a pair condensate. The effect of disorder on a BCS superfluid is complex. The pair condensate survives in the presence of local impurities (weak disorder), with the order parameter and T_C unchanged [287], while condensate fraction and superfluid density are reduced [288].

These examples lead to the conclusion that experimentalists need to study both condensation and superfluidity!

6˙2. *Signatures for superfluidity in quantum gases*. – What constitutes an observation of superfluidity? Even theoretically, superfluidity is defined in several different ways. The most frequent definition employs the concept of rigidity against phase-twisting [289, 290]. In some definitions, even a non-interacting BEC qualifies as a superfluid [291].

From the experimentalists' point of view, superfluidity consists of a host of phenomena, including phase coherence, transport without dissipation, an excitation spectrum which results in a non-zero value of Landau's critical velocity (usually a phonon spectrum), the Meissner effect, the existence of quantized vortices, and a reduction of the moment of inertia. After the discovery of Bose-Einstein condensation in 1995, it still took until 1999 before researchers agreed that superfluidity was established, through the observation of vortices [292, 226] and a critical velocity in a stirred condensate [293, 294]. The general consensus was that the experimental verification of superfluidity required the observation of some aspect of superfluid flow that would not be possible in a classical system. Therefore, neither the hydrodynamic expansion of a condensate was regarded as evidence (since collisionally dense classical clouds would behave in the same way), nor the observation of phonon-like excitations, nor the interference of condensates, which established phase coherence only for a stationary cloud. The observation of a critical velocity [293, 294] provided evidence for superfluid flow, although the contrast between the behavior in the superfluid and normal regime did not even come close to the drop in resistivity or viscosity that was observed when superconductors or superfluids were discovered. Long-lived flow in the form of vortices has been regarded as a smoking gun for superfluids. However, vortices can be long lived even in classical liquids [295]. What sets the superfluid apart is the quantization of vortices and the fact that the ground state with angular momentum is necessarily a state with vortices. The emergence of vortex arrays and vortex lattices [226, 227, 228, 229] after driving surface excitations [296] dramatically demonstrated both properties. Although there is no rigorous derivation showing that ordered lattices of uniformly charged vortices prove superfluidity, we are not aware of any system or observation that could provide a counter example.

The reduction of the moment of inertia is another distinguishing feature of superfluid flow. It can be observed through the so-called scissors mode, a collective excitation created by a sudden rotation [297, 298, 26], or by observing the expansion of a rotating superfluid [299, 300, 301]. Both methods have been regarded as a way to *directly* observe superfluidity. However, studies with normal Fermi gases have impressively demonstrated that both features, originally regarded as a unique signature of superfluids, occur already for normal gases deep in the hydrodynamic regime where dissipation is extremely small [302, 303].

It appears that superfluid and low-viscosity collisional hydrodynamics can only be distinguished if there is sufficient time for the small but finite viscosity in the normal phase to create vorticity, a velocity field with $\nabla \times \mathbf{v} \neq 0$ whereas the superfluid will always continue to be irrotational (unless quantized vortices are nucleated). For instance, if the flow field has equilibrated with a slowly rotating container, then collective excitations will reveal the difference between a superfluid and a normal fluid [304].

The last example shows how the physics of strong interactions can "obscure" the seemingly dramatic transition to a superfluid state. The normal state of a Fermi gas around the Feshbach resonance is already almost "super" due to its very low viscosity. Many experiments uncovered the unique properties of this strongly interacting gas, and eventually its transition into the superfluid state. The observation of anisotropic expansion [60] was initially believed to provide evidence for superfluidity. However, such an expansion was also observed in a normal strongly interacting Fermi gas [60, 124, 131] and was predicted to occur even at $T = 0$ since Pauli blocking is no longer effective during expansion [305].

Can the damping of modes distinguish between superfluid and normal flow? In a simple picture, damping in collisional hydrodynamics increases with lower temperature, because Pauli blocking lowers the collision rate and increases the mean free path. In contrast, damping of superfluid hydrodynamics decreases with lower temperature, because the normal density, which provides friction, decreases. The observation of such a decrease of the damping rate of collective excitations was regarded as evidence for superfluidity [73]. Later, however, it was found that a similar positive slope of damping vs. temperature occurs for a normal strongly interacting Fermi gas [91].

The observation of a "paring gap" in RF spectroscopy was regarded as strong evidence for superfluidity [75, 306], mainly based on the theoretical interpretation of the experimental data. However, experiments with population imbalanced Fermi gases showed that RF spectra of normal and superfluid clouds are identical, and that RF spectroscopy cannot distinguish between the two phases, at least not at the current level of resolution [77]. The reason is the presence of strong pair correlations in the normal phase and possibly also strong interactions in the final state used for spectroscopy, which were not included in the models used to interpret the data.

When collective excitations were studied as a function of the scattering length, intriguing sudden peaks in the damping rate were observed [74, 307]. The conjecture is that this may reflect a resonance of the collective mode with the pairing energy Δ, and damping would occur due to pair breaking. This phenomenon remains to be systemat-

ically studied. The observation of pair correlations across the BEC-BCS crossover was consistent with predictions of a theory for the superfluid state [76], but it seems that similar pair correlations also exist in the normal state [308]. Finally, a kink was observed when the specific heat [72] or the entropy [183] were determined as a function of the temperature or the energy of the cloud. Due to the signal-to-noise ratio, these kinks could be distilled only by separately fitting the low- and high-temperature regions.

The discussion above has summarized many aspects of superfluid systems, some of which are shared with strongly interacting normal gases. In the following sections we will focus on the two phenomena that do not occur in a normal gas: condensation and the formation of quantized vortices in rotating superfluids.
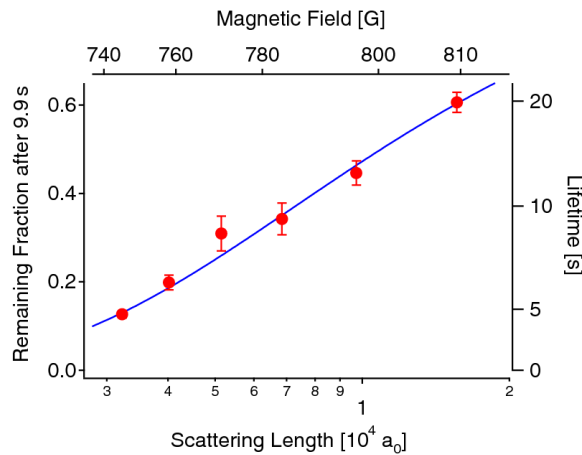

Fig. 38. – Lifetime of molecules in partially condensed clouds. The cloud with initially about 1×10^6 molecules was held for 9.9 s (initial density about $5 \times 10^{12}\,\mathrm{cm}^{-3}$, slightly varying with the interaction strength). Shown is the remaining fraction as a function of scattering length. The lifetime $1/\Gamma$ is calculated under the simplifying assumption of a pure exponential decay $e^{-\Gamma t}$. The line is a fit with a power law for $\Gamma = ca^{-p}$, giving $p = -0.9$. The clouds were partially condensed (up to 80% condensate fraction at the largest scattering length), and all measurements were done in the strongly interacting regime where $a > 1/k_F$, so the expression for the relaxation rate differs from the prediction for weakly interacting, thermal molecules ($\Gamma = c\,a^{-2.55}$) [200].

6˙3. *Pair condensation below the Feshbach resonance.* – The successful creation of ultracold molecules out of ultracold atoms via Feshbach resonances in gases of fermions [61, 15, 17, 16] and bosons [255, 62, 63, 64] brought the goal of Bose-Einstein condensation of molecules into close reach. Indeed, molecular samples in cesium close to [62] and in sodium clearly within [63] the regime of quantum degeneracy were generated. However, their lifetime was too short to observe an equilibrium Bose-Einstein condensate. Molecules formed of fermions turned out to have a much longer lifetime due to greater stability against inelastic decay (see chapter **2** and section **5˙1**). Within a few months,

this favorable property allowed the successful Bose-Einstein condensation of molecules, or more precisely of strongly interacting fermion pairs [65, 55, 66, 67, 71, 76].
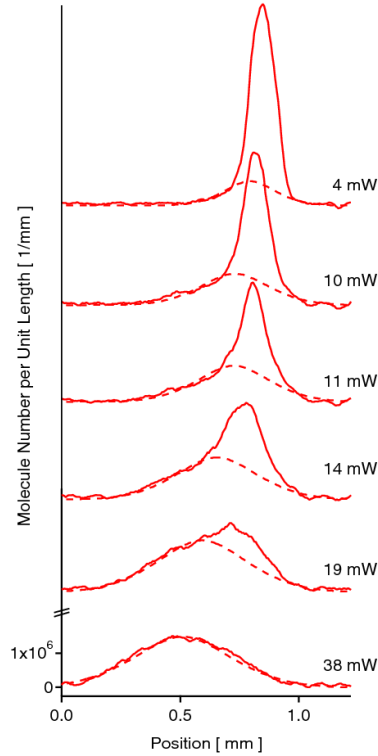

Fig. 39. – Bimodal density distribution emerging in a cloud of molecules. Shown are radially integrated profiles of absorption images such as those in Fig. 40, as a function of final laser power. The dashed lines are fits to the thermal clouds.

In the case of ^{6}Li, the long lifetime of molecules [15] (see Fig. 38) enables us to evaporate the Fermi mixture at a fixed magnetic field, just like cooling a cloud of bosonic atoms towards BEC. As the mixture is cooled by ramping down the trapping laser power, molecules form as the temperature becomes comparable to the binding energy. Accordingly, the atomic signal observed in zero-field imaging vanishes: We can see this in Fig. 10 for fields below resonance, where essentially no atomic signal is measured. Below a certain temperature, one observes the striking onset of a bimodal density distribution, the hallmark of Bose-Einstein condensation (see Figs. 40 and 39). The emergence of the bimodality was actually accentuated by an anharmonic trapping potential where a shallow minimum of the potential was offset with respect to the deeper potential which held the thermal cloud. Fig. 40 shows the gallery of molecular Bose-Einstein condensates observed at JILA [65], MIT [66], Innsbruck [67], at the ENS [71] and at Rice [76].
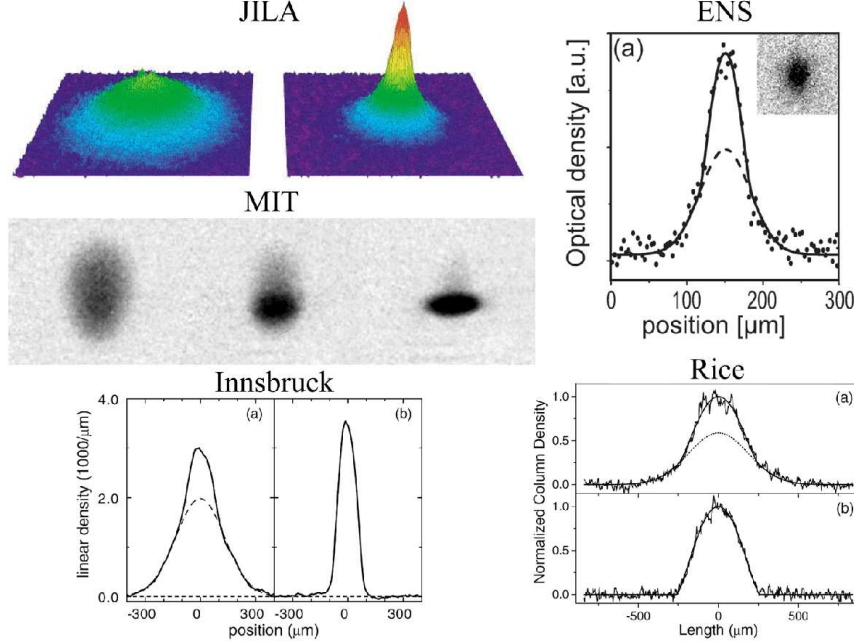
142

Fig. 40. – Observation of Bose-Einstein condensation of molecules. The gallery shows bimodal density distributions observed after expansion and molecule dissociation at JILA [65], after expansion, dissociation and zero-field imaging at MIT [66] and at the ENS [71], and in-situ profiles from Innsbruck [67] and Rice [76].

In contrast to weakly interacting Bose gases, the condensate peak is not much narrower than the thermal cloud, indicating a large mean-field energy of the BEC, comparable to k_B times the condensation temperature. As we move closer to the Feshbach resonance, the size of the condensate grows to be almost that of a degenerate Fermi gas (see Figure 41). The average distance $n_M^{-1/3}$ between molecules becomes comparable to the molecular size in free space, given approximately by the scattering length. Thus we have entered the strongly interacting regime of the BEC-BCS crossover where two-body pairing is modified by Pauli pressure.

6˙4. *Pair condensation above the Feshbach resonance*. – When the Feshbach resonance is approached, the bimodality of the cloud becomes almost undetectable. There is no strong spatial signature of the phase transition, even at a much better signal-to-noise ratio than in the initial observations (see Fig. 18 in section **3**˙3.2). We have observed weak signatures in these spatial profiles (see section **6**˙5.1 below). A second difficulty with fermion pair condensates on the BCS-side is the instability of the pairs during expansion. When the gas becomes more dilute the pair binding energy can decrease below (k_B times) the local temperature, causing pairs to break during time of flight. See
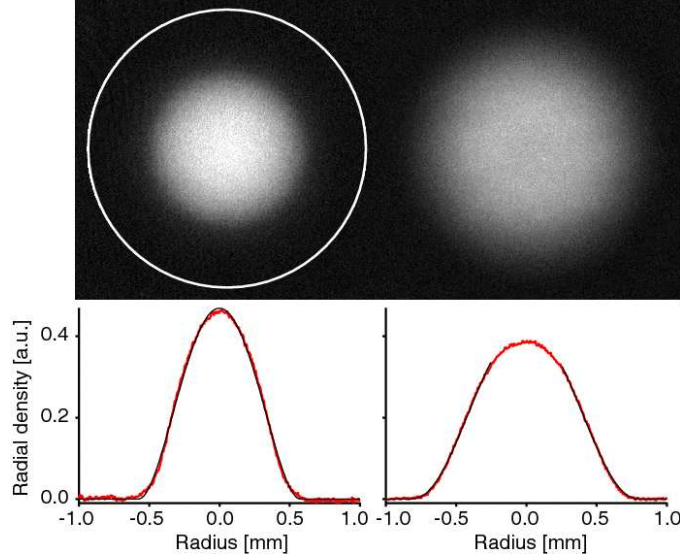
Fig. 41. – Comparison between a molecular BEC (a) and a degenerate Fermi sea (b). The condensate containing $N_m = 6 \times 10^6$ molecules is in the strongly interacting regime at a magnetic field of 780 G ($1/k_F a = 0.6$). Its expanded size is almost as large (factor ~ 0.7) as an expanded non-interacting Fermi gas containing N_m atoms, indicated by the white circle. Image and profile b) show an essentially spin-polarized Fermi sea (minority component of $< 2\%$ not shown) containing $N = 8 \times 10^6$ atoms at the same field. The images were taken after 12 ms expansion with the probe light aligned with the long axis of the cigar-shaped clouds.

section **6**˙6.8 below for a study of this effect using vortices.

To extend the study of pair condensation from below to above the Feshbach resonance, a new detection method was needed. Such a method was introduced by the JILA group [69] and later adapted to ^{6}Li by our group [70]. The rapid ramp technique is discussed in detail in section **2**˙4.5 and also in the contribution of D. Jin to these proceedings. The concept of this technique is to prevent the fragile fermion pairs from dissociating by sweeping the magnetic field towards the BEC-side of the resonance, thereby transforming them into stable molecules (see Fig. 12). This is done in the moment the trap is switched off for expansion. If each fermion pair is transferred into a tightly bound molecule, the momentum information of the original pair is preserved. Time-of-flight analysis of the resulting molecules should thus allow one to infer the momentum distribution of pairs in the gas above resonance. The momentum distribution might be broadened by the residual mean-field interaction of molecules after the ramp. However, these interactions are greatly reduced by sweeping sufficiently far away from the Feshbach resonance into the weakly interacting regime where $k_F a \ll 1$.

This technique enabled us to demonstrate fermion pair condensation in the entire BEC-BCS crossover. Sample images and profiles of the resulting molecular clouds are

144

shown in Fig. 42. The drastically reduced interaction results in a clear separation of the condensate from the "thermal" or uncondensed part of the cloud ([21]).
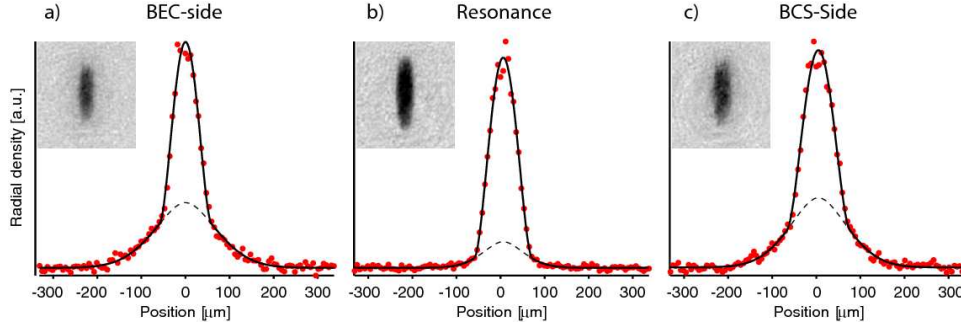

Fig. 42. – Fermion pair condensates. Axial density of the atomic cloud after switching off the optical trap, a rapid ramp to zero field (in $< 100\,\mu s$), further expansion (for 10 ms), and dissociation of the resulting molecules by ramping back across resonance. The initial field B_0, the number of fermion pairs N, the condensate fraction and the interaction parameter $1/k_F a$ where a) 745 G, 700 000, 47%, 1.2; b) 835 G, 1.4×10^6, 81%, 0.0 (resonance); c) 912 G, 1×10^6, 49%, -0.5.

The condensate fraction was determined by fitting a bimodal distribution to the profiles like those in Fig. 42, a parabola for the central dense part and a gaussian for the thermal background (see chapter **3**). Remarkably large condensate fractions were found throughout the entire BEC-BCS crossover, with a peak of 80% at $B \approx 820\,\mathrm{G}$, close to the resonance, but still on its BEC-side (see Fig. 43).

The high condensate fraction is a hint that the pairs in the strongly interacting regime on the BCS-side of the resonance are still smaller than the interparticle spacing, not larger, as one would expect for conventional Cooper pairs. An intuitive assumption is that during the magnetic field sweep an atom preferably forms a molecule with its nearest neighbor ([22]). In the case of localized pairs, molecules are then formed from the original "Cooper partners". In the case of delocalized Cooper pairs, molecules might rather form

---

([21]) At zero field, the scattering length between molecules should be on the order of the singlet scattering length of lithium atoms, which is about 40 a_0. The exact value is not known. In fact, the residual mean-field interaction at zero field is so low that the condensate practically does not expand if the rapid ramp is performed immediately after switching off the trap. For this reason, it is sometimes beneficial to let the cloud expand by some amount *before* the rapid ramp is performed. This converts some of the interaction energy in the cloud into kinetic energy, which allows one to "choose" the final expanded size of the molecular condensate.

([22]) This should happen as long as the relative momentum is not larger than the inverse distance, i.e. the neighbor populates the same phase space cell. This is the case in the regime of quantum degeneracy, and it is experimentally confirmed by the almost 100% conversion from atoms into molecules (see **2**˙4.2).
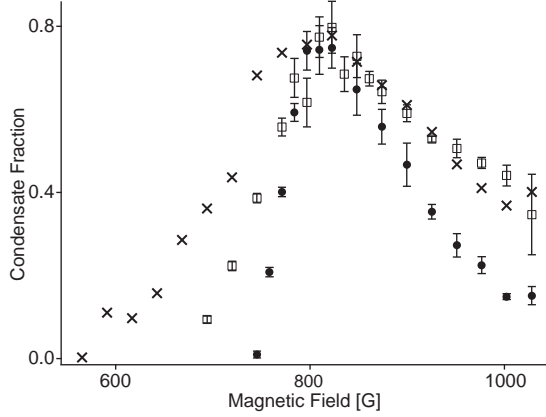
Fig. 43. – Condensate fraction in the BEC-BCS crossover as a function of the magnetic field before the rapid ramp. The symbols correspond to different hold times, 2 ms (crosses), 100 ms (squares) and 10 s (circles). From [70].

out of uncorrelated atoms, resulting in a thermal cloud after the ramp.

In accord with this argument, BEC-BCS crossover theory predicts that the pair size ξ will be smaller than the interparticle spacing $n^{-1/3}$ up to $k_F a \approx -1$ (see section 4˙6.3). So far no experiment on Fermi gases has shown condensation or superfluidity in a regime where $k_F|a|$ $(a < 0)$ is significantly less than 1 and hence where pairing is truly long-range. Observing superfluidity for $k_F a < -1$ would require exponentially lower temperatures of $T/T_F < 0.28\, e^{-\pi/2k_F|a|} \ll 0.06$ and, furthermore, the sweep technique may no longer allow the observation of pair condensation.

A simple theoretical model (see below) agrees with the high condensate fraction, but the latter is in stark contrast to the maximum fraction of about 14% found in experiments with ^{40}K [69] (see Fig. 44). The reason for this discrepancy might be related to the shorter lifetime of the Fermi mixture in ^{40}K close to resonance, on the order of 100 ms [18]. In addition, technical issues particular to ^{40}K may play a role including strong losses during the probing procedure.

In our experiments, the condensates were found to be very long-lived. For a hold time of 10 s, the condensate fraction on resonance was observed to be still close to its initial value. In fact, these lifetimes can compare very favorably to those found for atomic Bose-Einstein condensates. On the BEC-side, the condensate decayed more rapidly due to the increasing rate of vibrational relaxation of the molecules away from resonance. The decay of the condensate fraction on the BCS-side can be caused by heating and atom loss due to inelastic collisions or a larger sensitivity to fluctuations of the trapping fields.

6˙4.1. Comparison with theory. Figs. 44 and 45 show "phase diagrams" for the condensate fraction as a function of temperature and interaction strength. Several theoretical
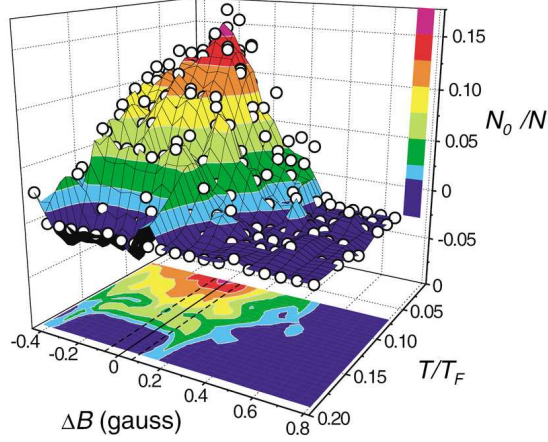
146

Fig. 44. – Condensate fraction in the BEC-BCS crossover obtained by the JILA group using ^{40}K, as a function of degeneracy T/T_F and magnetic field (interaction strength) around the Feshbach resonance. From [69].

studies [152, 309, 310] have confirmed the general behavior of the "critical temperature" of the observed condensation phenomenon in ^{40}K and in ^{6}Li.

In section **4**, we discussed the BEC-BCS crossover theory which predicts a condensate fraction (see Eq. 176) of

$$(227) \qquad n_0 \;=\; \frac{N_0}{\Omega} \;=\; \frac{1}{\Omega}\sum_k u_k^2 v_k^2 \;=\; \frac{m^{3/2}}{8\pi\hbar^3}\Delta^{3/2}\sqrt{\frac{\mu}{\Delta}+\sqrt{1+\frac{\mu^2}{\Delta^2}}}$$

Fig. 46 compares the variational BCS prediction to our results. The very close agreement must be considered fortuitous since the simple crossover theory is only qualitatively correct near resonance. Furthermore, it is not clear how accurately the observed molecular condensate fraction after the ramp reflects the pair condensate fraction before the ramp.

The strongest confirmation that the bimodal density distributions observed after the ramp are an indicator of a phase transition comes from the direct detection of condensation in population imbalanced clouds (see section **6**˙5.2). In the next section we summarize experimental evidence that the condensate fraction cannot change strongly during the sweep time. On the other hand, some evidence has been reported [311], that the conversion efficiency into molecules is higher for condensates. This effect increases the condensate fraction during the sweep, but the effect is small [311]. As discussed in section **2**˙4.5, the system's dynamics during the sweep poses a difficult challenge to theory, due to the presence of several timescales for coherent and incoherent evolution.
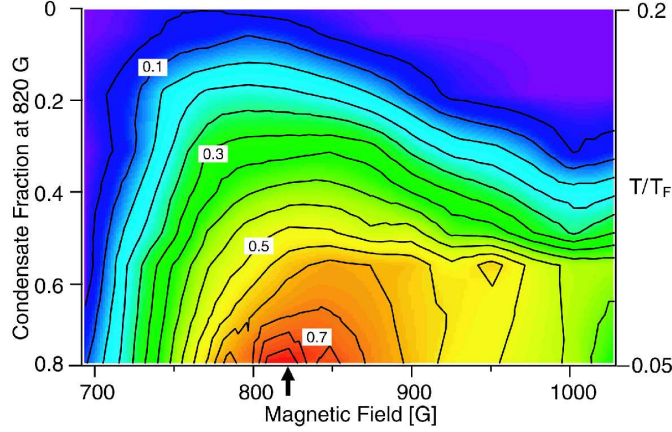
147

Fig. 45. – Condensate fraction as a function of magnetic field and temperature in the MIT experiments on ^{6}Li. Condensates are obtained in the entire BEC-BCS crossover. The highest condensate fraction and highest onset temperature are obtained on the BEC-side close to resonance. As a model-independent measure of temperature, the condensate fraction at 822 G (see arrow) is used as the vertical axis. The Feshbach resonance lies close to this point, at 834 G. From [70].

6˙4.2. *Formation Dynamics*. The underlying assumption for the rapid sweep technique is that the momentum distribution of pairs is not changing during the sweep time. Evidence for this was obtained both in the JILA and MIT experiments, where it was shown that the condensate fraction did not change when the sweep rate was varied or when the density was changed. However, since in both experiments the sweep time through the strongly interacting regime was comparable to the inverse Fermi energy, dynamics during the sweep could not be fully ruled out. We addressed this issue by directly measuring the relaxation time of the strongly interacting Fermi system. This was done by modulating the magnetic field (and therefore the scattering length) and observing the growth or decay of the condensate. In the experiment, we used a periodic modulation of the magnetic field and measured the phase shift of the induced condensate modulation (see Fig. 47).

The observed relaxation time of 500 μs was much longer than the time to sweep through the strongly interacting regime (10 μs). Therefore, it should not be possible for the condensate fraction to change noticeably during the sweep. Still, a possible loophole is some exotic mechanism for such a change that is not captured by the simple relaxation models assumed in the experimental tests.

In conclusion, the rapid ramp to the BEC-side has proven to be a very valuable tool for the detection of condensation in the BEC-BCS crossover. Moreover, the ramp provides us with a way to preserve the topology of the pair wave function on the BCS-side. This allows the observation of vortex lattices in the entire BEC-BCS crossover, as will be
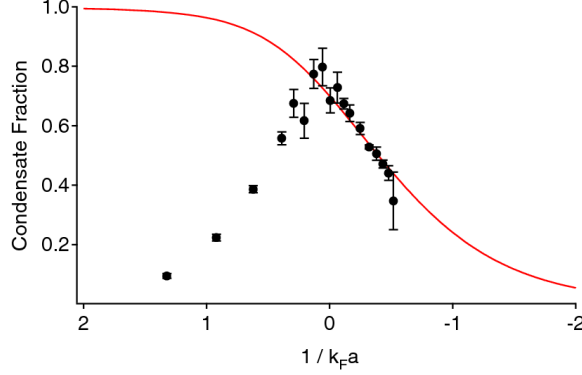
148

Fig. 46. – Condensate fraction as a function of the interaction strength in the BEC-BCS crossover. The circles show the 100 ms data of Fig. 43. The interaction strength is calculated using the known scattering length as a function of magnetic field and the experimental value $1/k_F = 2\,000\,a_0$. The curve shows the variational BCS prediction for the condensate fraction. On the BEC-side, heating due to vibrational relaxation leads to fast decay on the condensate. Figure adapted from [231] using Eq. 176.

discussed in section **6**˙6. In the following, we will show that condensates can be detected without any ramp, by direct absorption imaging.

6˙5. *Direct observation of condensation in the density profiles*. – The hallmark of Bose-Einstein condensation in atomic Bose gases was the sudden appearance of a dense central core in the midst of a large thermal cloud [1, 2]. This direct signature in the
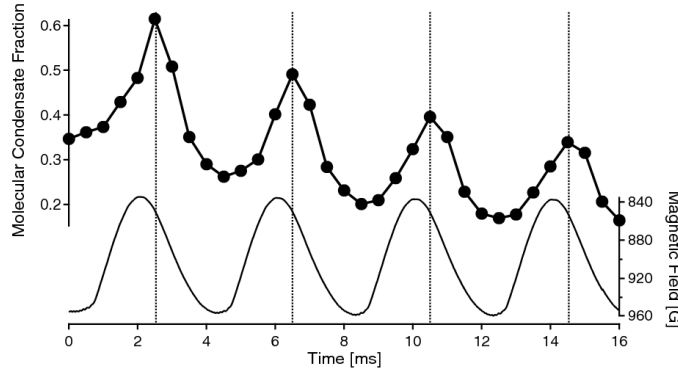

Fig. 47. – Relaxation time of fermionic pair condensates. Shown is the delayed response of the condensate fraction to a 250 Hz magnetic field modulation on the BCS side of the Feshbach resonance. From [311].
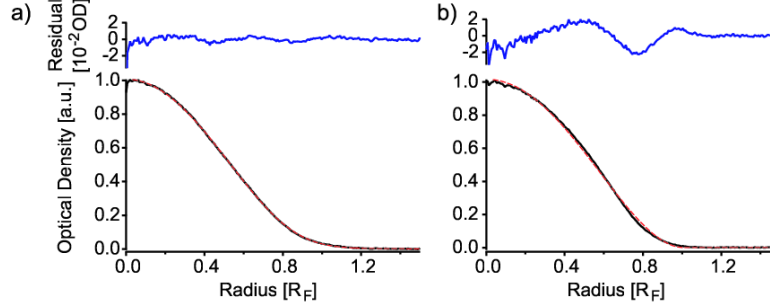
149

Fig. 48. – Density profiles of an equal Fermi mixture on resonance. The temperature in a) was $T/T_F \approx 0.15$, whereas in b) it was $T/T_F \approx 0.09$. Temperatures were determined from the thermal molecular cloud after the rapid ramp, and might not be quantitatively accurate. Both gas clouds contained a condensate after the rapid ramp to the BEC-side. The condensate fraction was: a) 7%, b) 60%.

density distribution derives from a clear separation of energy scales in weakly interacting gases. The condensate's repulsive mean-field $\mu \propto na$ is much smaller than the critical temperature (times k_B) at which condensation occurs, $T_C \propto n^{2/3}$: The gas parameter na^3 is much less than 1 (about 4×10^{-6} for ^{23}Na condensates). In a harmonic trap, the different energy scales directly translate into the different sizes of a thermal cloud, $R_{\text{th}} \propto \sqrt{T}$, and of a condensate $R_C \propto \sqrt{\mu}$. This is the situation we encounter with weakly interacting molecular clouds in Fermi mixtures on the "BEC"-side of the Feshbach resonance. However, as the interactions between molecules are increased by moving closer to the Feshbach resonance, the size of the molecular condensate grows and the bimodal feature close to T_C becomes almost invisible. In strongly interacting Fermi gases, the separation of energy scales is no longer given. On resonance, the size of the condensate is governed by $\mu \approx 0.5E_F$, while $k_B T_C \approx 0.15E_F \ll E_F$, so that the normal cloud's size is dominated not by temperature, but by the Fermi energy. The question arises whether the condensate still leaves a trace in the cloud as the gas undergoes the phase transition.

6˙5.1. Anomalous density profiles at unitarity. [23]   We have indeed found a faint signature of condensation in density profiles of the unitary gas on resonance after expansion. To a very good approximation, the trapping potential was cylindrically symmetric (see section **2˙2.2**). This allowed us to obtain low-noise profiles via azimuthal averaging.

Sample profiles are shown in Fig. 48. To observe a *deviation* from the shape of a non-interacting Fermi cloud, an unconstrained finite-temperature fit is performed on the profiles. The relevant information is now contained in the residuals of such a fitting procedure.

The fit residuals deviate at most by 2% from the non-interacting Fermi shape. This

___

[23] The results of this section have not been published elsewhere.

explains why this effect has not been observed in earlier experiments. Despite of the rather small deviation, the non-interacting fit is affected by the "kinks". This draws into question whether the "effective temperature" typically obtained from such fits to the whole profile, is a well-defined quantity. For a well controlled determination of an effective temperature, only the profile's wings should be fit, where the gas is normal.
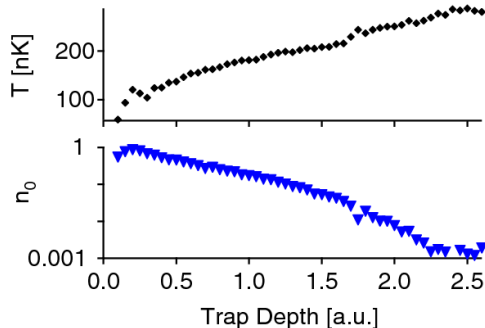

Fig. 49. – Condensate fraction n_0 and temperature as a function of evaporation depth on resonance. The condensate starts to form around a trap depth of $U \sim 2.2$ corresponding to 4.2 μK. The temperature was determined from the thermal wings of expanding molecular clouds after the rapid ramp. The Fermi temperature decreased slowly from 1.5 μK for $U = 2.6$ to 1.4 μK at $U = 0.4$, and dropped quickly due to atom spilling below $U = 0.2$. All measurements were done after recompression into a deeper trap with $U = 2.0$.

A convenient way to graph fit residuals as a function of temperature is by means of a "density" plot of gray shades, with white and black corresponding to positive or negative deviations of the measured profile from the fit. This is shown in Fig. 50. Also included in this figure is the information on the density profiles and their curvature. While the profiles themselves do not appear to change with temperature (trap depth) on the scale of the plot, we observe an intriguing structure appearing in the residuals at an evaporation depth of about $U = 2 \mu$K. The curvature of the density profiles shows a similar qualitative behavior.

To indicate that the observed feature indeed stems from the superfluid, we also include a density plot of the profiles obtained with the rapid ramp method from section **6**˙4 above. This allows to clearly separate the condensate and thermal cloud in expansion. The condensate fraction is included in Fig. 49, and shows that the condensate appears around a trap depth of 4.2 μK. We observe that a small condensate does not leave a strong signature in the gas cloud, unlike the case of weakly interacting Bose gases. Only when the condensate has grown to an appreciable size (about 20% in our data) does it significantly deform the density profiles.

At the lowest temperatures and high condensate fractions, the quality of Fermi fits improves again, indicating that now a large fraction of the gas is in the superfluid state. The size of the cloud is then $R_{\text{TF}} = 0.83 \, R_F$, which gives $\xi(0) \approx 0.47$, in accord with
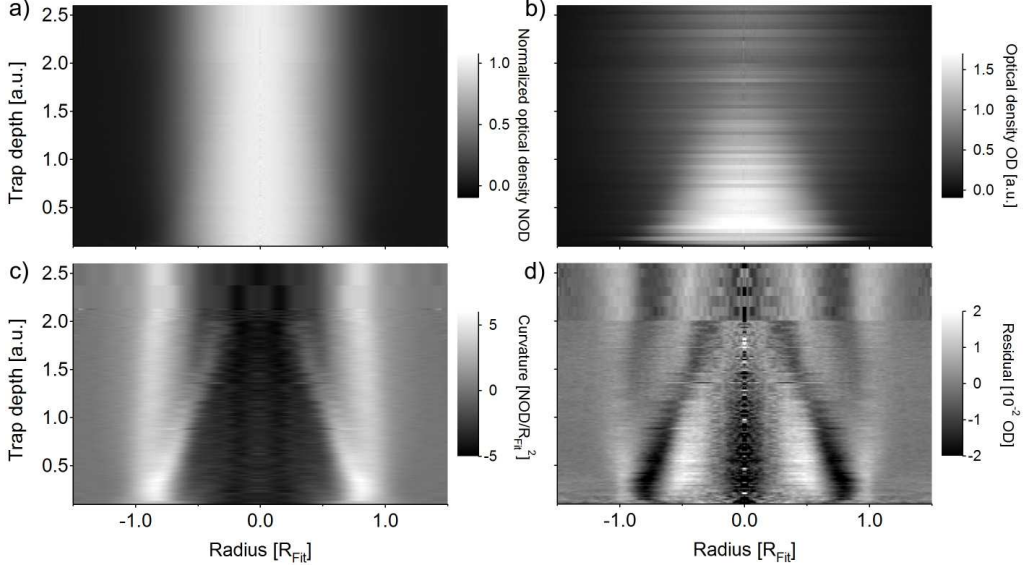
Fig. 50. – Density profiles, their curvature and their fit-residuals on resonance. a) Density profiles on resonance as a function of trap depth. There is no sign of a phase transition at this resolution. b) After the rapid ramp to the BEC-side and expansion, a condensate is clearly visible below a certain trap depth. c) The curvature of the density profiles on resonance in a) carries a signature of the condensate. No field ramp is required. d) The fit residuals for a finite temperature Thomas-Fermi fit. Also here, the condensate's imprint in the density profile is clearly visible. To obtain the curvature, the noisy central region of $\pm 0.1 R_F$ in each profile was replaced by a fit.

other experiments and theory (see section **3**˙1.2 above).

To conclude, the density profiles in resonantly interacting Fermi gases are modified in the presence of a superfluid core. Such features have been predicted by several authors [170, 168, 45, 171], but had previously been too small to be observable. In the next section, we will demonstrate how an imbalance in the spin up versus spin down population in the gas greatly enhances the visibility of the condensate and leads to a striking signature of condensation.

6˙5.2. *Direct observation of the onset of condensation in Fermi mixtures with unequal spin populations.* We have seen that a balanced mixture of spin up and spin down fermions at unitarity does not show a strong signature of condensation. The reason is that on resonance, due to the symmetry in atom numbers, only one energy scale is available, the Fermi energy. In stark contrast, breaking the symmetry in atom numbers and working with Fermi mixtures with unequal spin populations produces a direct and striking signature of the superfluid phase transition in the spatial density profiles both in expansion [312] and in trap [80]. A similar situation has been encountered in
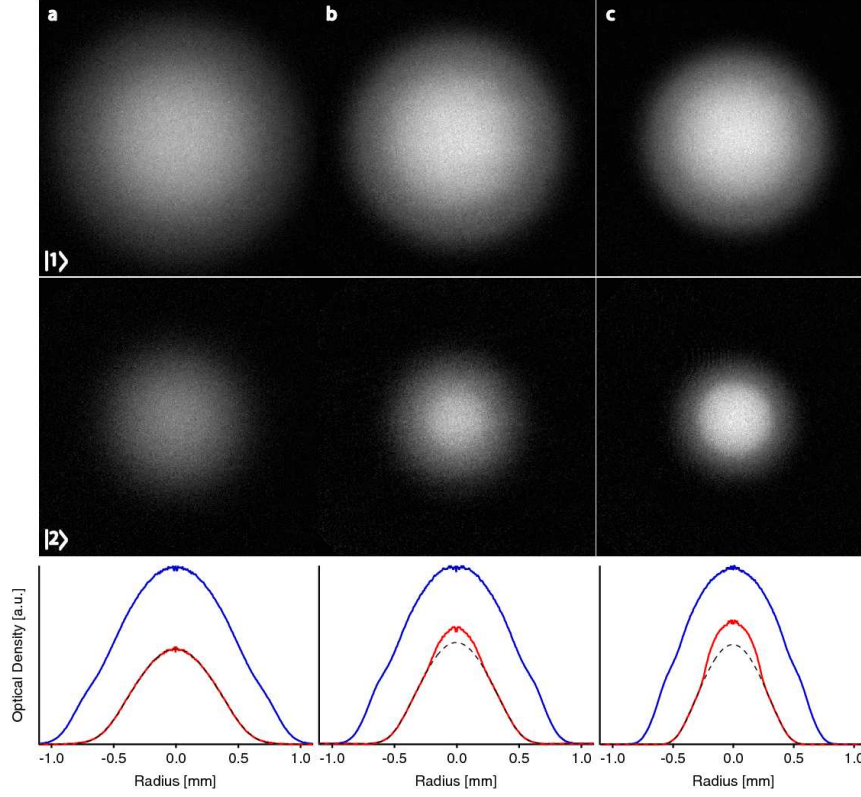
Fig. 51. – Direct observation of condensation in imbalanced clouds on resonance. The upper row shows majority clouds, the lower row minority clouds, for an imbalance of $\delta = 60\%$. The dashed line is a fit to the wings of the minority cloud to a Thomas-Fermi profile, clearly missing the central feature. Temperature was varied by lowering the trapping power. To within 20%, temperatures can be obtained from the ballistically expanding wings of the majority cloud. We have $T/T_F = 0.14$ (a), 0.09 (b) and 0.06 (c). Here, $k_B T_F$ is the Fermi temperature of an equal mixture containing the same total atom number. The figure shows data from [312].

Bose-Einstein condensation, where breaking the symmetry of a spherical trap resulted in dramatic anisotropic expansion of the condensate, now a hallmark of the BEC phase transition.

Part of the reason for the direct signature is the new hierarchy of energy scales. The normal majority and minority cloud sizes are governed by the respective Fermi energies (rather, chemical potentials) $\mu_\uparrow$ and $\mu_\downarrow$, while the cloud size of fermion *pairs* is governed by the average chemical potential, $(\mu_\uparrow + \mu_\downarrow)/2$. The deeper reason for the sudden change of the spatial profile at the phase transition is that fermionic superfluids (around resonance and in the BCS-regime) do not tolerate unpaired fermions, at least at zero temperature. The superfluid gap presents an energy barrier for these "singles" to
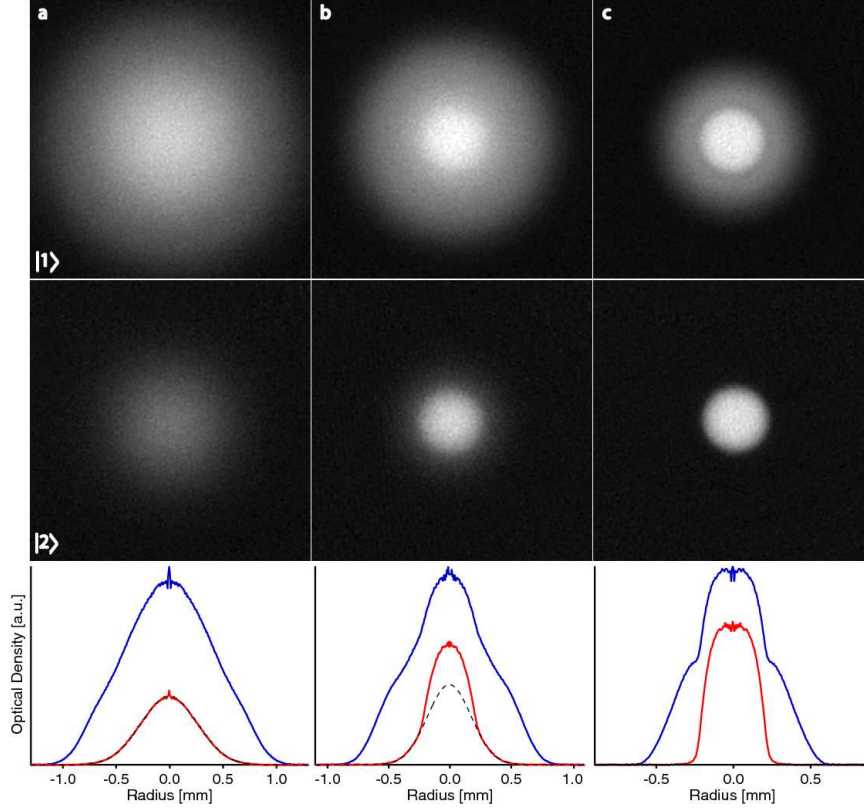
153

Fig. 52. – Condensation in a strongly interacting, imbalanced Fermi mixture on the BEC-side, at $B = 780$ G or $1/k_F a \approx 0.5$. In this regime one may start to describe the imbalanced gas as a strongly interacting atom-molecule mixture. Unlike on resonance, essentially all minority atoms are part of condensed fermion pairs. Temperatures were $T/T_F = 0.2$ (a), $T/T_F = 0.12$ (b) and $T/T_F \leq 0.05$ (c). The figure shows data from [312].

enter the superfluid. This leads to a superfluid central region of equal spin populations surrounded by the polarized normal phase. The two regimes are separated by a first order phase transition, at which the density imbalance jumps. The presence of such a sudden change in the density distribution allowed the first direct observation of the phase transition, without the need for sweeps to the BEC side of the Feshbach resonance [312].

We present here, side by side, the density profiles of an imbalanced Fermi mixture at unitarity (Fig. 51) and on the BEC-side of the Feshbach resonance (Fig. 52). In the BEC-regime, the sharp phase boundary between a balanced superfluid and the normal region no longer occurs. It is replaced by an expulsion of the normal cloud of unpaired atoms from the molecular condensate, which can be understood from a mean-field picture. The imbalanced gas has turned into a Bose-Fermi mixture of molecules and unpaired

fermions. We know from section **4**˙7 that molecules repel unpaired fermions with a "Bose-Fermi" scattering length $a_{\mathrm{BF}} = 1.18\,a$ [205]. As a result, unpaired fermions experience a "Mexican-hat" potential $V(\mathbf{r}) + \frac{4\pi\hbar^2}{a_{\mathrm{BF}}}m_{\mathrm{BF}}n_M(\mathbf{r})$ in the presence of molecules at density n_M.

The physics of imbalanced fermionic superfluids is discussed in section **7**˙3.2. The detailed analysis of the spatial density profiles for population imbalanced Fermi clouds is still an area of current research, and will not be covered in these lecture notes.

The sudden change in the density profile of imbalanced mixtures – as a function of temperature at fixed imbalance, or as a function of imbalance at fixed temperature – occurred simultaneously with the appearance of a condensate peak after a rapid ramp to the BEC side [312, 80]. This provides strong confirmation that condensates observed via the rapid ramp technique truly mark a phase transition. In the following section, we will present the demonstration that these condensates are indeed superfluid — the observation of vortex lattices.

6˙6. *Observation of vortex lattices*. – The most dramatic demonstration of superfluidity in Bose-Einstein condensates is the observation of vortex lattices in rotating systems (see section **6**˙6.1). It was a natural goal to repeat such experiments for ultracold Fermi gases and to demonstrate superfluidity due to fermionic pairing. In this section, based on the Ph.D. thesis of one of the authors, we include details on the experimental techniques and results that were not included in the original publication [68].

Before we discuss the experimental realization, we will summarize some basic properties of vortices. In particular, we will show how a macroscopic wave function can accommodate vortices, and emphasize that it is not the existence of vortices, but rather the quantization of circulation, that is unique to superfluids and superconductors.

6˙6.1. Some basic aspects of vortices. Superfluids are described by a macroscopic wave function $\psi(\mathbf{r})$ which is zero in the normal state and non-zero in the superfluid state, so it qualifies as the order parameter of the superfluid phase transition (see section **4**˙11). As a wave function, it is a complex quantity with a magnitude and phase ϕ

$$(228) \qquad\qquad \psi(\mathbf{r}) = |\psi(\mathbf{r})|\, e^{i\phi(\mathbf{r})}$$

The velocity of the superfluid is the gradient of its phase,

$$(229) \qquad\qquad \mathbf{v} = \frac{\hbar}{m^*}\nabla\phi$$

where m^* is the mass of the bosonic entities forming the superfluid. In the case of fermionic superfluids, we have $m^* = 2m$, where m is the fermion mass. Integrating Eq. 229 around a closed loop inside the superfluid, we immediately arrive at the Onsager-Feynman quantization condition [313, 314, 315],

$$(230) \qquad\qquad \oint \mathbf{v}\cdot d\mathbf{l} = n\frac{h}{m^*}$$

with integer n. If the superfluid wave function has no nodal lines and the loop fully lies in a simply connected region of space, we must have $n = 0$. However, Eq. 230 can be fulfilled with $n \neq 0$ if the wave function contains a *vortex*, that is, a flow field that depends on the vortex core distance r like $v \sim 1/r$. At the location of the vortex, the wave function vanishes, it has a nodal line. This is the way a superfluid can carry angular momentum. In case of cylindrical symmetry (with the vortex core at the center), the angular momentum per boson or fermion pair is quantized in units of $\hbar$. Note that vortices are a property of the superfluid in the ground state at given angular momentum. This is in marked contrast to *classical* vortices, which exist only in metastable or non-equilibrium situations. Vortex patterns will ultimately decay into rigid body rotation whenever the viscosity is non-zero.

Vortices of equal charge repel each other. This immediately follows from kinetic energy considerations. Two vortices on top of each other double the velocities and quadruple the energy. Two vortices far separated have only twice the energy of a single vortex. As a result, vortices with charge $|n| > 1$ will quickly decay into singly charged vortices [316]. If many vortices are created, they minimize the total kinetic energy of the cloud by arranging themselves into a regular hexagonal lattice, called Abrikosov lattice [317].

How can quantized vortices nucleate? Vortices cannot suddenly appear within the condensate, as the angular momentum contained within a closed loop inside the condensate cannot abruptly jump. Rather, the nodal lines have to enter the condensate from a *surface*, where the condensate's wave function is zero. This surface can also be the surface of a stirrer, if it fully expels the condensate.

One pathway to generate vortices is to excite *surface* modes. They are generated by moving a boundary condition (stirrer or container walls) faster than the local critical velocity v_c for such excitations [318]. Which surface excitations are efficiently created depends on the shape of the stirrer [319, 320], or, in the case of a rotating container, the roughness of the container walls. Accordingly, the necessary critical angular velocity Ω_c to nucleate vortices will depend on the stirrer's shape. Note that Ω_c can be much higher than the *thermodynamic* critical angular velocity Ω_{th}. The latter is the angular velocity at which, in the rotating frame, the ground state of the condensate contains a single vortex. But simply rotating the condensate at Ω_{th} will not lead to this ground state, because a vortex has to form on the surface where its energy is higher than in the center presenting an energy barrier. Driving a surface excitation provides the necessary coupling mechanism to "pump" angular momentum into the condensate, which can subsequently relax into a state containing vortices.

6˙6.2. Realization of vortices in superconductors and superfluids. The Lorentz force on charged particles due to a magnetic field is equivalent to the Coriolis force on neutral particles due to rotation. Therefore, a magnetic field does to a superconductor what rotation does to a neutral superfluid. Weak magnetic fields are completely expelled by a superconductor (the Meissner effect), analogous to a slow rotation with angular velocity less than Ω_{th} for which the neutral superfluid does not acquire angular momentum. For higher magnetic fields, quantized magnetic flux lines, vortices, penetrate the supercon-
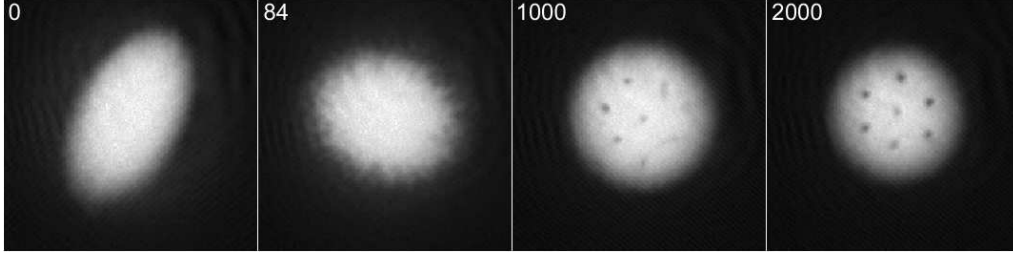
Fig. 53. – Fate of a quadrupole oscillation in a rotating atomic Bose-Einstein condensate. The images show a sodium condensate in the magnetic trap after stirring slightly above the quadrupole resonance (at 52 Hz, trapping frequencies $\nu_\perp = 73$ Hz and $\nu_z = 18$ Hz) and equilibrating for a certain time t (time given in ms). First, the condensate rotates in the form of a perfect quadrupolar collective excitation. After about 100 ms, density depletions looking like vortex cores start to appear at the edges of the condensate. Between 500 ms and 1 s, some of these penetrate into the condensate as vortex lines, which arrange themselves into an ordered lattice after about 1-2 s.

ductor.

Quantized circulation in superfluid ^{4}He was observed by Vinen in 1958 [321] by measuring the frequency of a thin wire's circular motion placed at the center of the rotating superfluid. Quantized magnetic flux was measured by Deaver and Fairbanks [322] and Doll and Näbauer in 1961 [323] by moving a thin superconducting cylinder of tin toward and away from a conducting coil and measuring the electromotive force induced in the coil as a function of applied field. Entire Abrikosov lattices of magnetic flux lines were observed by using ferromagnetic particles that were trapped at the lines' end-points (Träuble and Essmann [324], Sarma [325], independently in 1967). The direct observation of vortex lattices in superfluid ^{4}He was achieved in 1979 by Yarmchuk, Gordon and Packard [326] by imaging ions trapped in the core of the vortex lines. In gaseous Bose-Einstein condensates, single vortices were created by a phase imprinting technique [292], and vortex lattices were created by exposing the condensate to a rotating potential [226, 227, 228, 229]. Using the method of the vibrating wire, the presence of quantized circulation was confirmed for the fermionic superfluid ^{3}He in 1990 by Davis, Close, Zieve and Packard [327]. The MIT work described here represents the first direct imaging of vortices in a fermionic superfluid. It is worth adding that glitches in the frequency of pulsars, fast rotating neutron stars, have been attributed to the spontaneous decay of vortex lines leaving the neutron pair superfluid [328, 329].

6˙6.3. Experimental concept. For weakly interacting Bose gases in magnetic traps, the techniques for setting the cloud in rotation are well established [296, 226, 227, 330, 228]. In [330, 228], the initially axially symmetric magnetic potential is deformed into an ellipse in the radial plane, which is then set in rotation. In [226, 296], an asymmetric optical dipole potential is superimposed with a cylindrically symmetric magnetic trap, again

resulting in an elliptically deformed potential. In these cases, the role of the "rotating container walls" needed to nucleate vortices is played by the smooth elliptical deformation. This potential can excite only a specific surface excitation of the condensate, a rotating quadrupole mode. This collective excitation carries angular momentum $m = \pm 2$ (the axial component of angular momentum) and can only be excited around a resonant angular frequency [24] $\Omega_Q = \omega_\perp/\sqrt{2}$, where $\omega_\perp$ is the radial trapping frequency [25]. The excited quadrupole mode will eventually decay (via a dynamical instability) into vortices [332] (see Fig. 53).

In the MIT experiments [296, 227, 333], two (or more) small, focused laser beams were symmetrically rotated around the cloud. Vortices could be created efficiently over a large range of stirring frequencies [227, 320]. The small beams presented a sharp obstacle to the superfluid, most likely creating vortices *locally* at their surface [320], corresponding to high angular momentum excitations with low critical angular velocities. This is the strategy followed in our experiment on rotating Fermi gases.

A major technical challenge was to create a trapping potential which had a high degree of cylindrical symmetry. In Bose gases, this was provided by a magnetic trap, a TOP trap in [226, 229] that can be accurately adjusted for a very symmetric potential, or a Ioffe-Pritchard trap in [227] that has a high degree of cylindrical symmetry built-in. For fermions, one had to engineer an optical trap with a very round laser beam for optical trapping and carefully align it parallel to the symmetry axis of the magnetic saddle point potential, formed by the magnetic Feshbach fields and gravity. In this "sweet spot", gravity is balanced by magnetic field gradients, and the only remaining force acting on the atoms is from the laser beam (see section **2**˙2.2).

Experimentally, the trapping potential was designed using a sodium BEC as a test object. This had the advantage that the experimental parameters for the creation of vortex lattices were well-known. After this had been accomplished, the next challenge was to identify the window in parameter space that would allow to observe vortices in a Fermi gas. It was not evident whether such a window existed at all, where heating during the stirring would not destroy the superfluid, and where the decay rate of vortices would be slow enough to allow their crystallization and observation.

6˙6.4. *Experimental setup.* The experimental setup is presented in Fig. 54. It was tested and optimized using sodium Bose-Einstein condensates. Figure 55 shows how we determined the parameters for stirring and equilibration using a sodium BEC in a magnetic trap. The next step was to repeat these experiments in an optical trap, initially without high magnetic field, optimizing the shape of the optical trap. Then magnetic fields were added. This required a careful alignment of the optical trap to the magnetic saddle point. We estimate the residual ellipticity of the transverse potential to be less

[24] While a collective excitation carrying angular momentum m has an energy $\hbar\omega_\perp\sqrt{m}$, it is m-fold symmetric and is thus excited at a frequency $\Omega = \omega_\perp/\sqrt{m}$, see [331].
[25] In the presence of an elliptic deformation, one needs to replace $\omega_\perp$ by $\sqrt{(\omega_x^2 + \omega_y^2)/2}$, where $\omega_{x,y}$ are the trapping frequencies in the direction of the long and short axis of the ellipse.
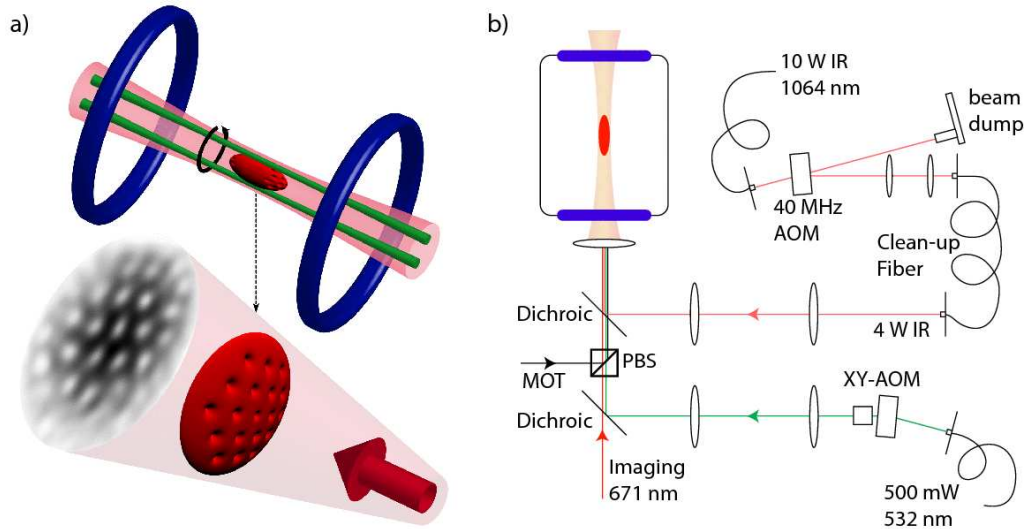
Fig. 54. – Experimental setup for the observation of vortices in a Fermi gas. a) Sketch of the geometry. The atomic cloud (in red) is trapped in a weakly focused optical dipole trap (pink). The coils (blue) provide the high magnetic offset field to access the Feshbach resonance as well as the axial confinement (additional curvature coils not shown). Two blue-detuned laser beams (green) rotate symmetrically around the cloud. An absorption image of the expanded cloud shows the vortices. b) Optical setup for the vortex experiment. The laser beam forming the dipole trap is spatially filtered using a high-power optical fiber. Care is taken not to deteriorate the quality of the gaussian beam's roundness when passing through several lenses after the fiber exit. The stirring beam (green) passes through two crossed AOMs that deflect it in the transverse (XY) plane. These beams are overlapped with the imaging light by dichroic mirrors. The light for the magneto-optical trap (MOT) is overlapped on a polarizing beam splitter cube (PBS).

than 2% (^{26}). Magnetic fields were left on during the expansion. For lithium this was crucial: molecules at the initial densities are only stable against collisions at magnetic fields close to the Feshbach resonance. During the expansion at high magnetic field, the cloud could tilt, revealing small misalignments between the optical trap and the saddle point. Even more importantly, additional steps were necessary to ensure vortex visibility after expansion into the saddle point potential, as discussed below.

Finally, large vortex lattices containing about 120 vortices were created in sodium Bose-Einstein condensates both in magnetic and optical traps with similar lifetimes (see Fig. 56), and we were ready to proceed with lithium. This required two changes to

---

(^{26}) Of course, this cannot compare with the almost perfect roundness of a (magnetic) TOP trap, with residual ellipticity of less than 0.1% [330].
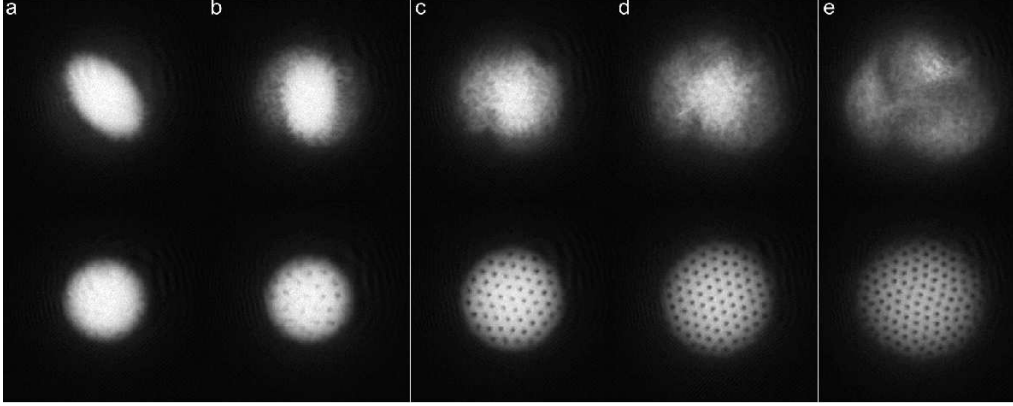
Fig. 55. – Vortex nucleation for violent stirring in an atomic BEC. The upper row shows expansion images of sodium condensates after 500 ms of stirring at the quadrupole frequency, for different laser powers of the stirring beam. The lower row shows the resulting BEC after 300 ms of equilibration time. This suggests that the condensate has to be severely excited to generate many vortices. From left to right, the laser power was increased for each subsequent image by a factor of two. The cloud was held in a magnetic trap.

the trap geometry: (1) lithium is lighter, and keeping the saddle point of the combined magnetic and gravitational potential in place requires reducing the field curvature. (2) The higher chemical potential of lithium required a larger beam waist to obtain the correct trap depth for evaporative cooling (see equation 6 in section **2**˙2.2).

Expansion of vortex lattices. In the trap, the vortex size is on the order of the healing length (for an atomic or a molecular BEC) or of the inverse Fermi wavevector (for a strongly interacting Fermi gas), about 200 nm. This small size is prohibitive for in-situ detection using optical techniques. Fortunately, angular momentum conservation allows vortices to survive the expansion of the condensate, which we can thus use as a "magnifying glass". However, only in simple geometries is the expansion a faithful magnification. Complications arise due to the expansion into a saddle potential.

Hydrodynamic expansion into a saddle point potential has been discussed in chapter **3**. How does the vortex core size change during expansion? There are two regimes one can simply understand, the initial hydrodynamic expansion and the ballistic expansion at long times of flight. In the first part of the expansion, the mean-field $\mu \propto na$ changes so slowly that the condensate wave function can still react to the change in density: Adjustments on the healing length scale ξ - about the size of a vortex in equilibrium - can occur at a rate $\hbar/m\xi^2 = \mu/\hbar$. As long as the rate of change of μ - essentially the rate of change of the radial Thomas-Fermi radius R_r - is smaller than $\mu/\hbar$, the vortex core can still adjust in size to the local mean-field. It thus grows as $\xi \propto 1/\sqrt{n(t)a} \propto R_r(t)\sqrt{\frac{R_a(t)}{a}}$ where $R_a(t)$ is the axial Thomas-Fermi radius after expansion time t. If R_a does not vary
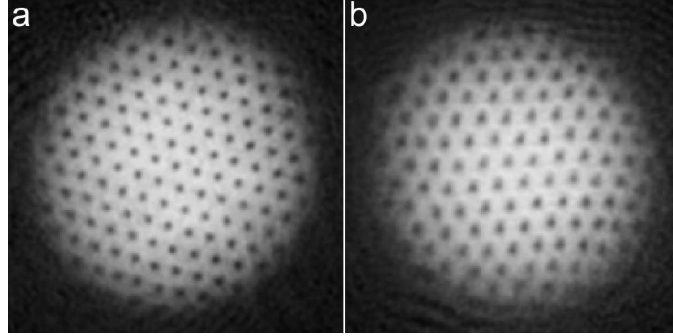
Fig. 56. – Vortex lattice in a Bose-Einstein condensate of sodium atoms in the magnetic trap (left) and the optical trap (right image). The optical trap (highest number obtained $\sim$ 120 vortices) can favorably compare with the magnetic trap (highest number in our experiment $\sim$ 150 vortices).

appreciably, $\xi/R_r(t)$ will remain *constant* during the expansion, the vortex core grows just as the size of the condensate, and the magnification is faithful.

Once the rate of change of $\mu(t)$ becomes comparable to $\mu(t)/\hbar$, the condensate can no longer adiabatically adapt to the lowering density. The characteristic expansion rate being ω_r, this occurs when $\mu(t) \approx \hbar\omega_r$. For much longer expansion times, we are in the limit of ballistic expansion. Here, each particle escapes outward with the given velocity (in free space) or, in the case of the saddle potential, with a radial acceleration proportional to its distance from the origin. This simply rescales the radial dimension, and thus stretches the vortex core and the cloud size by the same factor. Again the magnification is faithful.

However, in our experiment we are not in the quasi-2D regime where $R_a \gg R_r$. The saddle potential "squishes" the cloud in the axial dimension, as the decreasing mean-field no longer stabilizes the condensate's axial size. According to the above estimate, the vortex cores will *shrink* in comparison to the cloud size by a factor $\propto \sqrt{R_a(t)}$. We can see the effect on a sodium condensate in our optical trap in Fig. 57, where the axial curvature was left on for longer and longer times during expansion.

To work around this problem, the magnetic field curvature was quickly reduced after releasing the cloud from the trap, by ramping down the current in the curvature coils (in about 1 ms). As this increases the overall offset field (the curvature bias field is aligned opposite to the Feshbach bias), the current in the Feshbach coils is decreased accordingly, so as to leave the offset field B_0 - and the interaction parameter of the Fermi mixture - constant. The radial expansion is sped up even further in comparison to the axial evolution by actively "squishing" the cloud about 3 ms before release. This is done by simply ramping up the power in the optical trapping beam by a factor of 4. Not only does this increase the radial trapping frequency, but it also excites a "breathing" mode in the condensate. The result is that the condensate expands almost twice as fast radially
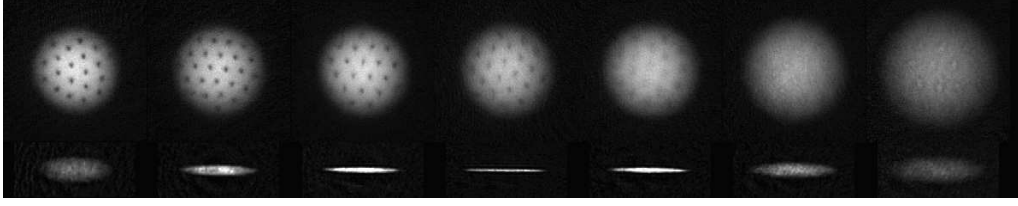
161

Fig. 57. – Decrease of vortex visibility for a sodium condensate expanding from the optical trap into a magnetic saddle potential. Top and bottom row show axially and radially integrated optical densities, respectively. The saddle potential is confining in the axial and anti-confining in the radial direction. As the condensate expands radially, it collapses in the axial dimension, a direct consequence of hydrodynamic flow. The vortex cores shrink and collapse onto themselves, thereby filling in completely and forming ring-like structures (see text for details). For the images, the magnetic field curvature ($\nu_z = 26$ Hz) was switched off after, from left to right, 0, 2, 3, 4, 5, 7 and 10 ms. The total time of flight was constant at 35 ms.

as without these steps.

6˙6.5. *Observation of vortex lattices.* The search for vortices in Fermi gases started on the BEC side of the Feshbach resonance. We hoped that far on the molecular side, in the regime where $k_F a$ is small, the situation would be fully analogous to the case of atomic condensates. However, too far away from resonance, the molecules (which are in the highest vibrational state of the interatomic potential!) can undergo rapid vibrational relaxation via three-body collisions, leading to heating and trap loss. The lifetime of the gas needs to be longer than the vortex nucleation and equilibration time (typically 1 s). If the entire preparation of vortex lattices is to happen at the same magnetic field, this limits the smallest values of $k_F a$ one can study ($k_F a \gtrsim 2$ in our experiment).

On the other hand, closer to resonance, the vortex cores become smaller. The core size in the BEC regime is given by the healing length $\xi \propto \frac{1}{k_F} \frac{1}{\sqrt{k_F a}}$ and decreases for increasing $k_F a$, eventually saturating in the unitarity regime at a value on the order of $1/k_F$. Furthermore, closer to resonance, quantum depletion becomes important: The condensate density n_0 is no longer equal to the total density, and the vortex core loses contrast.

Fortunately, it turned out that a window existed, and at a field of 766 G ($1/k_F a = 1.3$), we were successful: After stirring the cloud for 800 ms and letting the cloud equilibrate in 400 ms, we observed a vortex lattice in the density profile (Fig. 58). This established superfluidity for fermion pairs.

Starting from here, different methods were developed to improve the vortex contrast. Not surprisingly it turned out that reducing the interaction strength had the largest impact. In the moment the vortex lattice is released from the trap, the magnetic field is lowered to fields around 700 G ($1/k_F a \approx 3$ initially, further increasing during expansion). If the condensate still has time to react to this change in scattering length, the vortex size $\xi \propto R_r(t)/\sqrt{a}$ will increase relative to the condensate's radius (the expression for ξ
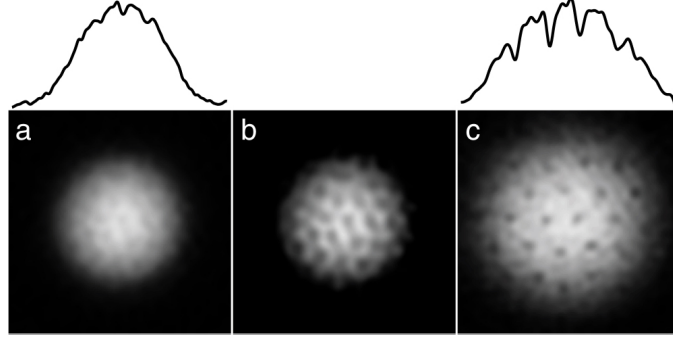
Fig. 58. – Vortex lattice in a ^{6}Li$_2$ molecular condensate. In a), stirring, equilibration and imaging of the vortex lattice all took place at a fixed field of 766 G ($1/k_F a = 1.3$). Image a) shows the very first clear signature we observed. The vortex core depletion is barely 10%. b) A Fourier filter applied to a) clearly shows the Abrikosov vortex lattice. c) The improved scheme of "squishing and release" (see text), as well as a sudden reduction of the interaction strength led to an improved vortex contrast. From [68].

is valid in the BEC-limit, and assumes radial expansion, see previous section). On the other hand, we found that the ramp should not move too far into the weakly interacting regime: The condensate would simply not expand anymore as practically all the repulsive mean-field has been taken out of the cloud. We also explored delaying the ramp until some expansion has taken place. However, if the delay was too long, the condensate had reduced its density to the point where it was not able to adjust quickly enough to the new interaction strength and increase its vortex size. For this, the "reaction rate" of the condensate wave function, $\mu/\hbar$ at the final field should be faster than the rate of change of μ, that is, the rate of change of $R_r(t)$.

This technique of observing vortices worked on both sides of the Feshbach resonance. Stirring, equilibration and initial expansion could be performed at magnetic fields between 740 G ($1/k_F a = 2$) and 860 G ($1/k_F a = -0.35$), before switching to the BEC-side during expansion for imaging. The observation of ordered vortex lattices above the Feshbach resonance at 834 G, on the BCS-side of the resonance, establishes superfluidity and phase coherence of fermionic gases at interaction strengths where there is no two-body bound state available for pairing.

The sweep down to 735 G solved another potential difficulty in detecting vortices on the BCS side. The condensate fraction is reduced by quantum depletion on the BEC-side, and on the BCS side it is only $\sim \Delta/E_F$ (see **4**.9). In a simplified picture, it is only this "coherent" part of the atomic density which vanishes at the vortex core, reducing the contrast (for more elaborate treatments, see [334, 213, 335]). By sweeping to the weakly interacting BEC regime, the low contrast vortices on the BCS-side are transformed into BEC-type vortices with high contrast.

Since a ramp is involved in the detection of vortex lattices, the relevant time scales
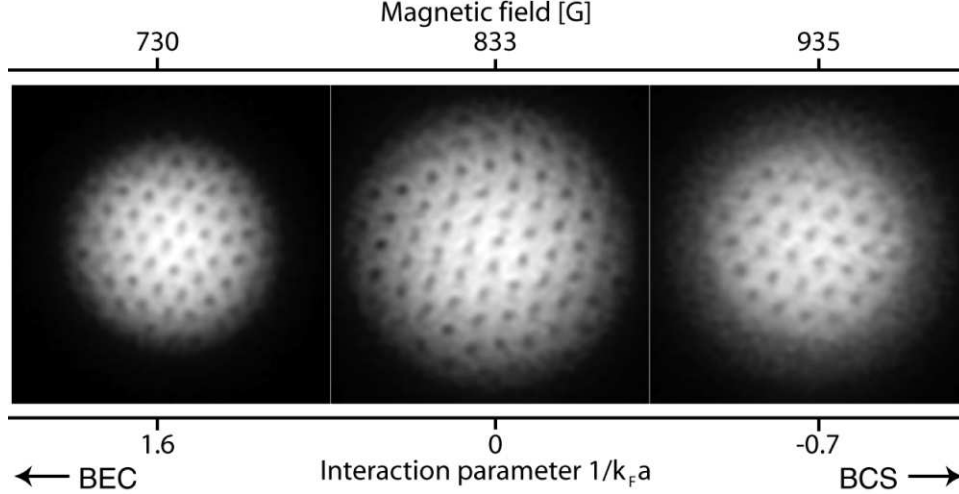
Fig. 59. – Observation of vortices in a strongly interacting Fermi gas, below, at and above the Feshbach resonance. This establishes superfluidity and phase coherence in fermionic gases. After a vortex lattice was created at 812 G, the field was ramped in 100 ms to 792G (BEC-side), 833G (resonance) and 853G (BCS-side), where the cloud was held for 50 ms. After 2ms of ballistic expansion, the magnetic field was ramped to 735G for imaging (see text for details). The field of view of each image is 880 μm x 880 μm. More recent version of Fig. 3 in [68].

need to be analyzed, as in the case of the observation of condensation via rapid ramps. The conclusion is that vortex lattices cannot form during the 10 ms of expansion at the imaging field, on the BEC-side of the resonance. We observed that the vortex lattice needs many hundreds of milliseconds to form in the stirred cloud. This is the same time scale found for the lattice formation in atomic BECs [332, 333]. This time scale was found to be independent of temperature [333] and seems to represent an intrinsic time scale of superfluid hydrodynamics, dependent only on the trapping frequencies. It is also in agreement with a theoretical study of vortex formation in strongly interacting Fermi gases [336]. When a thermal cloud is slowly cooled through the transition temperature [330], the condensate first forms without a vortex. As the condensate grows, vortices are nucleated at the surface and then enter the condensate [318]. When a thermal cloud is suddenly cooled, a condensate with phase fluctuations will form [337, 338] which can arrange themselves into a vortex tangle. In either case, one would expect a crystallization time of at least several hundred milliseconds before a regular vortex lattice would emerge. Also, it takes several axial trapping periods for the vortex tangle to stretch out. Even if these time scales were not known, it is not possible to establish a regular vortex lattice with long-range order in a gas that expands at the speed of sound of the trapped gas. Opposing edges of the expanding cloud simply cannot "communicate" fast enough with each other.
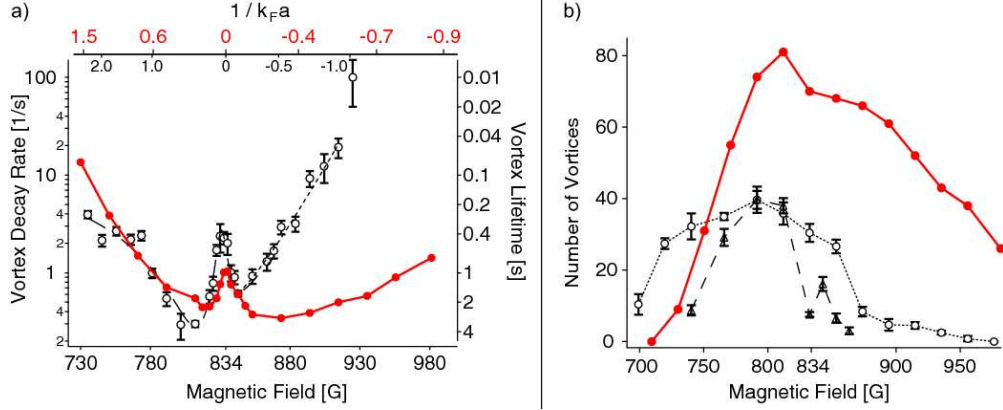
164

Fig. 60. – 1/e-Lifetime (a) and number (b) of vortices in the BEC-BCS crossover. Vortices are long-lived across the entire BEC-BCS crossover. A narrow dip in the lifetime on resonance is presumably due to pair breaking (see text). Open symbols are data from April 2005 [68]. Optimization of the system using a deeper trap resulted in improved characteristics on the BCS-side, shown by the full symbols (data from June 2005). In b), the triangles give the number obtained by stirring and equilibrating both at the given field. Stirring at 812 G and subsequently ramping to the final field for equilibration resulted in the data shown as circles. Figure adapted from [68], incorporating more recent results.

The regularity of the lattice proves that all vortices have the same vorticity. From their number, the size of the cloud and the quantum of circulation $h/2m$ for each vortex, we can estimate the rotational frequency of the lattice. For an optimized stirring procedure, we find that it is close to the stirring frequency.

6˙6.6.   Vortex number and lifetime. The number of vortices that could directly be created on the BCS-side was rather low in the first experiments, as the stirring seems to have had an adverse effect on the stability of the pairs. This corresponds to the expectation that the gas is more robust on the BEC-side, where the lowest excitations are sound waves, while on the BCS-side it is pair breaking. To optimize the vortex number on the BCS-side, first a large vortex lattice was produced close to resonance, at 812 G, before ramping the magnetic field beyond the Feshbach resonance. In this way, large numbers of vortices could be obtained in the entire BEC-BCS crossover (see Fig. 59).

By monitoring the number of vortices after a variable delay time, the vortex lifetime was determined (Fig. 60a). The vortex lifetime around the Feshbach resonance is on the same order of what was found for atomic BECs. This displays the high degree of metastability of vortices in superfluids. One picture for vortex decay assumes that thermal excitations (or the normal component) provide friction between some residual trap anisotropies and the rotating superfluid [339, 340]. The difference in lifetimes observed in two different data sets (Fig. 60a) can be explained by changes in the trap geometry,
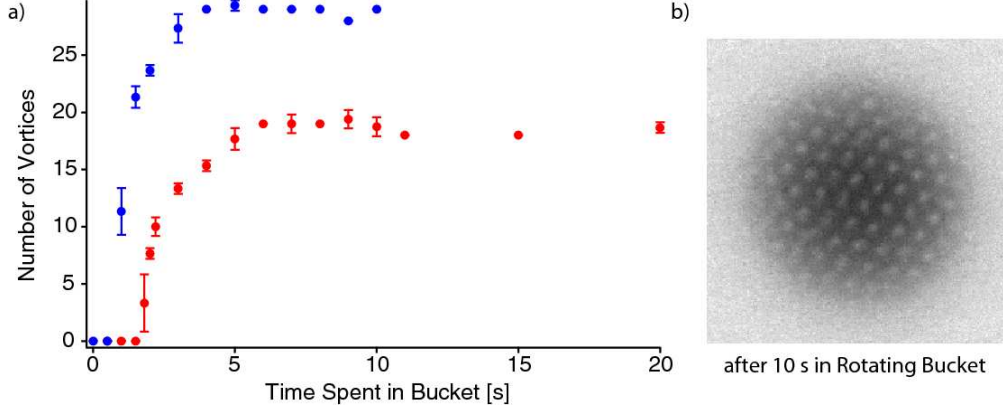
Fig. 61. – Rotating bucket for superfluid Fermi gases. a) Vortex number vs time spent in the rotating trap. After am equilibration time, the number of vortices stays constant. The final vortex number depends on the power of the green stirring beam, indicating slippage due to residual friction with the "container walls". The lower and upper curve correspond to lower and higher green beam power. b) Absorption image of an optimized vortex lattice, containing about 75 vortices, after 10 s hold time in the rotating bucket. The magnetic field for all data was 812 G, corresponding to $1/k_F a \approx 0.2$.

different atom number and temperature. A deeper trap can hold large Fermi clouds on the BCS-side better, leading to a longer lifetime in this regime.

There is a peculiar dip in the lifetime on resonance, which may be caused by the coupling of external motion to internal degrees of freedom. One possibility is a resonance between the pair binding energy and the rotation frequency. This requires pairs with a very small binding energy, which should exist only in the far outside wings of the cloud. For example, the (two-body) molecular binding energy at 830 G, 4 G away from resonance, is only $k_B \times 3$ nK or $h \times 60$ Hz. This is on the order of $\hbar \times$ the rotation frequency Ω of the vortex lattice. If the molecules rotate around the trap, trap anisotropies may excite them resonantly and cause dissociation. On the BCS-side, any possible resonance may be suppressed by density dependent broadening. Of course, the fraction of pairs at such low binding energies is very small, and they can contribute to damping in a major way only if surface effects are important.

6˙6.7. A rotating bucket. [27]

All the experiments described so far first set the cloud in rotation using the stirring beam and then let the gas equilibrate in the stationary trap into a vortex lattice. In the stationary trap, the vortex lattice is of course only metastable (lasting as long as the angular momentum L_z is conserved), whereas in a trap rotating at a constant angular

---

[27] The results of this section have not been published elsewhere.

frequency Ω, the vortex lattice would be the true ground state. Mathematically speaking, both situations are described by the Hamiltonian $H - \Omega L_z$, where the second term is, in the latter case, the usual transformation to a frame rotating at frequency Ω, whereas in the first case, the Lagrangian multiplier Ω enforces the conservation of L_z.

In some previous experiments with BECs the rotating anisotropy needed to be switched off before an ordered vortex lattice could form [227], possibly because the rotating laser beam was not moving smoothly enough to allow equilibration into a vortex lattice. In our setup, it has become possible to observe vortex lattices in the presence of a rotating bucket and even increase the lifetime of the vortex lattice by maintaining the rotating drive.

The experiment was performed at 812 G in a trap with radial trapping frequency $\nu_R = 90$ Hz. The two stirring laser beams (power in each beam ≈ 100 μW, waist w $= 16\,\mu$m) created only a weak potential of about 20 nK each on the cloud (mean-field $\mu \approx 400$ nK). They were rotated around the cloud at a frequency of 70 Hz. For imaging, the atoms were released from the combined trap, the confining optical potential plus the repulsive stirring beam. We found that it was possible to stabilize a vortex lattice containing 19 vortices for 20 s (see Fig. 61), limited only by the computer memory controlling the experiment.

The final vortex number depended on the laser power of the stirrer. Increasing the power in the stirring laser by 60% increased the equilibrium vortex number to 29. This suggests that the equilibrium vortex lattice, at least at the weaker laser power, had not reached the angular velocity of the stirrer. It appears that the drive was necessary to compensate for friction with some residual trap anisotropy. At later stages of the experiment, we were able to stabilize 75 vortices for 10 s in a deeper trap with $\nu_r = 120$ Hz.

These experiments are analogous to the pioneering "rotating bucket" experiments on ^{4}He [326], where it was possible to maintain a rotating superfluid containing four vortices for eleven hours, only limited by the eventual exhaustion of the refrigerator helium supply.

6˙6.8. Superfluid expansion of a rotating gas. What will happen when a fermionic superfluid expands? First, it should follow the hydrodynamic equations for a superfluid flow [342]. However, ultimately, pairing is a many-body effect, and when the cloud becomes very dilute, at finite temperature, the pairs will eventually break and superfluidity will be quenched. This is different from the situation for a BEC and at unitarity. Since phase space density is preserved during expansion, T/T_F or T/T_C is, here, constant and the gas remains superfluid (^{28})

By using rotating Fermi gases, vortices serve now as a convenient marker for the superfluid phase. When the superfluid is quenched, the vortices will disappear [341]. We allow the Fermi gas to expand on the BCS-side for a certain time t_{BCS}, then ramp

---

(^{28}) For interacting condensates, there is a small variation of critical phase space density as function of particle density, and therefore the gas can cross the phase transition during adiabatic expansion [343].
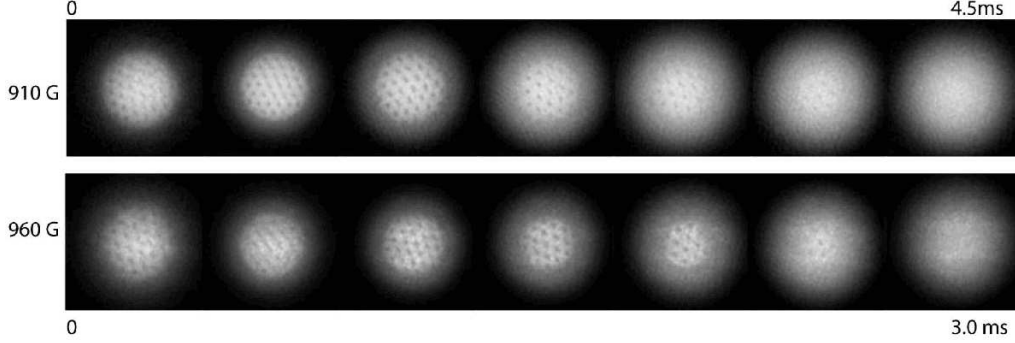
Fig. 62. – Superfluid expansion of a strongly interacting rotating Fermi gas. Shown are absorption images for different expansion times on the BCS-side of the Feshbach resonance at 910 G (0,1,2,3,3.5,4, and 4.5 ms) and at 960 G (0, 0.5, 1, 1.5, 2, 2.5, and 3 ms), before ramping to the BEC-side for further expansion and imaging. The total time-of-flight was constant. The vortices served as markers for the superfluid parts of the cloud. Superfluidity survived during expansion for several ms, and was gradually lost from the low-density edges of the cloud towards its center. The field of view of each image is 1.2 mm × 1.2 mm. From [341].

down to the BEC-side for further expansion and imaging. Vortices can be observed only when the gas is still a superfluid at the moment of the magnetic field sweep. The total expansion time is kept constant.

It is found that superfluid flow initially persists during the expansion. Then, vortices start to disappear first at the edges of the cloud, then, for longer BCS-expansion $t_{\rm BCS}$, further inwards until the last vortex disappears at the cloud's center (see Fig. 62). The time $t_{\rm BCS}$ for which the last vortex disappears, increases the closer we are to resonance, that is, the larger the interaction strength and the stronger the fermion pairs are bound. Vortices and therefore superfluid flow in free expansion were observed up to expansion times, for example, of 2.5 ms at 960 G and of 5 ms at 910 G.

By varying the magnetic field and thus the scattering length, we find that the last vortex always disappears at about the same value of the interaction parameter $k_F a \approx -0.8$ (see Fig. 63). The simplest explanation for this observation is that we cross the phase transition line during expansion. While T/T_F is an adiabatic constant for the expansion, T/T_C is not, as T_C/T_F depends exponentially on the density. As the density decreases, the critical temperature in the outer regions of the cloud eventually drops below T, superfluidity is lost starting from the edges inwards.

We can estimate the critical interaction strength for this breakdown to occur. At our lowest temperatures, $T/T_F = 0.05$. The formula for T_C due to Gorkov and Melik-Barkhudarov [199] gives $T_C = \frac{e^\gamma}{\pi} \left(\frac{2}{e}\right)^{7/3} T_F \, e^{-\pi/2k_F|a|} = 0.28 \, T_F \, e^{-\pi/2k_F|a|}$. This formula
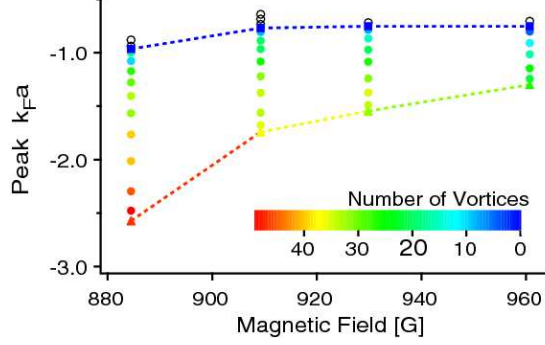
Fig. 63. – (Color online) Central interaction strength $k_F a$ during superfluid expansion. Starting at a central $k_F a$ in the optical trap, vortices survive up to an interaction strength $k_F a \approx -0.8$, almost independent of the magnetic field (scattering length a). Filled circles correspond to partially superfluid, open circles to normal clouds. The observed number of vortices is color coded. From [341].

should be valid in the BCS-regime where $k_F|a| \lesssim 1$. The equation

$$(231) \qquad 1 = \frac{T}{T_C} = \frac{T}{T_F}\frac{T_F}{T_C} \approx 0.05\,\frac{T_F}{T_C} = 0.18\,e^{\pi/2k_F|a|}$$

gives a critical interaction strength $k_F\,|a| = 0.9$, close to the observed value. For a discussion of other mechanisms which can explain the observed disappearance of vortices, we refer to the original publication [341]. On resonance we have $1/k_F a = 0$ during the whole expansion, and the gas should remain superfluid. Indeed, in the experiment we do not see evidence for a sudden quenching of vortices, but rather a gradual loss in contrast. Vortices could be discerned at total densities as low as $1.2 \times 10^{11}\,\mathrm{cm}^{-3}$, thus providing evidence for fermionic pairing and superfluidity at average interatomic distances of $2\ \mu\mathrm{m}$.

169

7. – BEC-BCS crossover: Energetics, excitations, and new systems

In the previous chapter, we focused on two key observations in the BEC-BCS crossover, pair condensation and vortices, that provide direct access to the phenomena of coherence, a macroscopic wave function, and superfluid flow. A host of other studies have been performed in this regime, which we summarize here. We divide these experiments into three different categories: characterization of the equilibrium state by energy, entropy and momentum distribution, dynamic measurements addressing collective excitations, sound and the critical velocity for superfluidity, and thirdly new systems, where the original two-component fermion system has been modified, either by an optical lattice, or by imbalanced populations. Both of these modifications add another "dimension" to the system, which is the lattice depth and the imbalance.

7˙1. *Characterization of the equilibrium state.* –

7˙1.1. Energy measurements. The total energy of the cloud determines how large the cloud is in the harmonic oscillator potential, or how fast it expands after switching off the trap ([29]). On resonance, the virial theorem provides a simple relationship between cloud size and total energy. Using the universality hypothesis that the only relevant energy scale is the Fermi energy, it follows that the potential energy is half the total energy, as for a non-interacting gas [176]. In a homogenous system (and locally for a trapped system), the energy content of an interacting Fermi gas is parameterized as $E = (1 + \beta)E_F$ where βE_F is the contribution of interactions. For unitarity limited interactions, β is an important universal parameter characterizing the ground state of strongly interacting fermions.

The total energy of an interacting Fermi gas at or close to resonance was derived from measurements of the cloud size either in trap or after expansion [60, 344, 67, 72, 79, 345]. In an interesting variant, the Paris group applied a rapid switching of the magnetic field to zero, which was faster than the trap period [124]. In this case, the interaction energy could be removed before it had been converted to kinetic energy. By comparing expansion with immediate or delayed magnetic field switching, the interaction energy could be directly measured. This work showed a surprising behavior of the interaction energy in a wide region of magnetic fields below the Feshbach resonance. This behavior was later explained by the formation of molecules and was probably the first hint that these molecules would be stable.

Current experiments (including a measurement of the speed of sound [84]) give $\beta \approx 0.58$, different experiments agree to within 10%, and most importantly agree with theoretical predictions (via analytical methods [346, 347, 348, 349, 203, 215, 350], Monte-Carlo calculations [351, 352, 353] and renormalization group methods [221]). A table summarizing all experimental and theoretical determinations of β can be found in the

---

(^{29}) The binding energy of molecules must be subtracted, as this internal energy cannot be converted into external, mechanical energy.

contribution of C. Salomon to these proceedings. The fact that the same value of β was found for ^{6}Li and ^{40}K is an impressive confirmation of universality [350] and is a powerful demonstration for the use of ultracold atoms as a model system for many-body physics.

It is possible to obtain the entropy of the cloud from size or energy measurements. For this, the magnetic field is adiabatically swept to transform the system into a weakly interacting Fermi gas. The observed size or energy in this regime gives the entropy, since their relation is accurately known for an ideal Fermi gas. This allows the determination of entropy vs. energy for the strongly interacting gas [183] (see Fig. 64). The results of this study agreed well with the predictions from Monte Carlo simulations that vary smoothly across the phase transition. By using a split power law fit, a value for a critical energy E_c had been obtained. However, since the fit did not address the behavior in the critical region, it is not clear how accurately the split power law fit can determine the transition point.

When energy measurements were combined with empirical thermometry and theoretical corrections, the dependence of the heat capacity of the Fermi gas on temperature could be deduced [72].
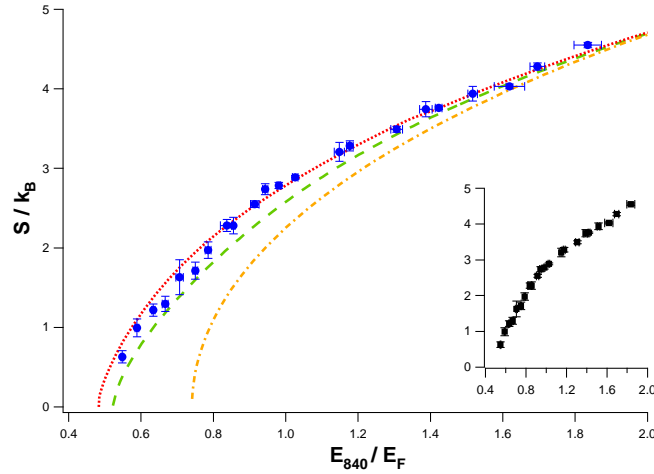
Fig. 64. – Measured entropy per particle of a strongly interacting Fermi gas at 840 G versus its total energy per particle (blue dots). Various theoretical predictions are compared. Reprinted from [183].

Further discussion of energy measurements can be found in the contributions of C. Salomon and S. Stringari to these lecture notes.

7˙1.2. *Momentum distribution.* The momentum distribution of the atoms in the cloud can be determined by releasing them from the trap and simultaneously switching the scattering length to zero. Such studies have been performed in both ^{40}K [354] and ^{6}Li (see C. Salomon's contribution to these proceedings).

Far on the BCS side, one finds the momentum distribution of an ideal Fermi gas in a harmonic trap. On the BEC side, the momentum distribution approaches the squared magnitude of the molecular wave function's Fourier transform. The crossover region smoothly interpolates between these two limits. The modification of the momentum distribution due to the superfluid phase transition is too small to be discernable in these measurements [355]. Momentum distributions are discussed in the contributions of D. Jin and C. Salomon to these proceedings.

7'1.3. *Molecular character.* Near a Feshbach resonance, the closed channel molecular state responsible for the resonance is mixed with the continuum of scattering states in the open channel. In the case of ^{6}Li, those two channels have singlet and triplet character, respectively. Close to the Feshbach resonance, the loosely bound molecular state becomes completely dominated or "dressed" by the open channel. This was confirmed by applying a molecular probe to a cold Fermi gas, thereby exciting atom pairs to an electronically excited, singlet molecular state at a rate that was proportional to their closed channel character Z [76].

The wave function describing the dressed molecule or fermion pair can be written [76]

$$(232) \qquad |\psi_p\rangle = \sqrt{Z}\,|\psi_{v=38}(S=0)\rangle + \sqrt{1-Z}\,|\phi_a(S=1)\rangle$$

where $|\psi_{v=38}(S=0)\rangle$ denotes the closed channel, singlet molecular state, and $|\phi_a(S=1)\rangle$ the open channel, triplet contribution, with relative probability amplitude $\sqrt{Z}$ and $\sqrt{1-Z}$, respectively. In the singlet channel, only the $v = 38$ vibrational state is relevant due to its near-resonant energy.

By monitoring trap loss during the excitation, Z could be determined (see Fig. 65) and it was verified that the Feshbach resonance in ^{6}Li is indeed broad, that is, the closed channel contribution to the pair wave function is negligible throughout the crossover region.

In the two-channel BEC-BCS crossover description, Z is proportional to Δ^2 [76], and one might hope that by measuring Z one actually measures the magnitude of the macroscopic order parameter. However, a spectroscopic determination of the singlet character is a *local* probe, sensitive only to $g^2(\mathbf{0})$, the two-particle correlation function at zero distance. As such, it can measure local pair correlations, but not global phase coherence or condensation of pairs. In fact, the BEC-BCS crossover allows for pair correlations above T_C, that can be seen in RF spectra (see section **7**'2.4). A closed channel character of these pairs has indeed been identified even in the normal phase, on both sides of the Feshbach resonance [308].

7'2. *Studies of excitations.* – To explore a new form of matter, one should probe its response to perturbations. In this section we summarize experimental studies on excitations of Fermi gases in the BEC-BCS crossover region. These studies include sound waves (resonant standing waves and sound propagation), observation of the critical velocity for superfluid flow, and single particle excitations probed via RF spectroscopy.
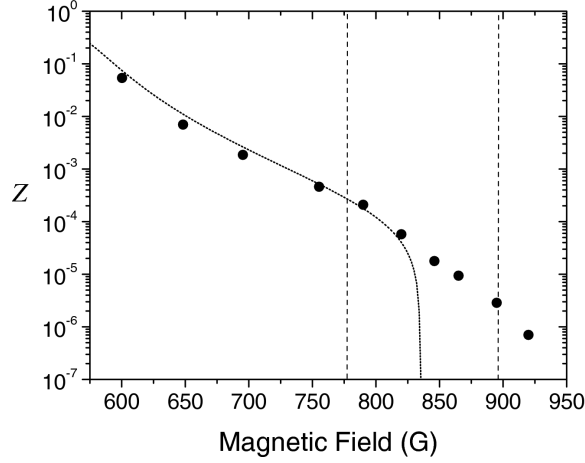
Fig. 65. – Closed channel character Z of lithium atom pairs versus magnetic field. The dotted line shows the closed channel character of the bound molecular state below the Feshbach resonance. Reprinted from [76].

7˙2.1. Collective excitations. By a sudden or periodic modulation of the trapping potential, eigenmodes of the trapped cloud can be excited. The eigenfrequencies can be sensitive to the equation of state, $\mu(n)$, and thus characterize the interactions in the system. Collective excitations were among the first properties studied in the case of atomic BECs. They provided stringent tests of the Gross-Pitaevskii-equation governing those condensates [356, 357, 358, 173, 359], and posed challenges to finite-temperature theories.

In the case of fermions, collective excitations were studied already for weakly interacting gases in the "pre-Feshbach era" [360]. After the realization of fermion pair condensation, extensive studies were carried out at Duke and Innsbruck. These are discussed in detail in the contribution of R. Grimm to this volume.

Chapter **3** discusses the equations of motion for strongly interacting gases, including collisional and superfluid hydrodynamics. To obtain the response to a small perturbation of the confining (harmonic) potential, one can directly use Eq. 51 in the case of classical hydrodynamics, or Eq. 55 for superfluid hydrodynamics, and linearize the equations for small oscillatory changes of the cloud radius. For instance, a "breathing" mode of a cigar-shaped cloud can be excited by suddenly squeezing the cigar in both radial directions. By only squeezing one radial dimension, one excites a "standing quadrupole" mode. Depending on the symmetry of the excited mode, different eigenfrequencies are found that depend more or less strongly (or do not depend at all) on the equation of state. The latter is parameterized by the exponent γ in $\mu(n) \propto n^\gamma$. Both the Duke [73] and Innsbruck [74] group have confirmed the value of $\gamma = 2/3$ at the Feshbach resonance, which is the same as for a weakly interacting Fermi gas. A precision study of collective oscillations on the

173

BEC side of crossover has verified the famous Lee-Yang-Huang correction to the equation of state of a strongly interacting Bose gas [211].

We refer the reader to section **6**˙2 for a discussion of further experimental studies of collective excitations. They characterized the strongly interacting and superfluid regimes as a function of scattering length and temperature and revealed an intriguing (and not yet fully understood) picture of hydrodynamic behavior and smooth or sudden transitions to collisionless dynamics.

7˙2.2. Speed of sound. Density perturbations propagate at the speed of sound. In section **4**˙7.3 we discussed that the Bogoliubov sound mode on the BEC side smoothly evolves into the Bogoliubov-Anderson mode on the BCS side.

A laser beam focused into the center of the cloud can create a localized density perturbation, which then propagates along a cigar-shaped atom cloud [361]. Using this technique, the Duke group has recently measured the speed of sound in a Fermi gas across the BEC-BCS crossover and found very good agreement with Monte-Carlo predictions [84] (see Fig. 66).
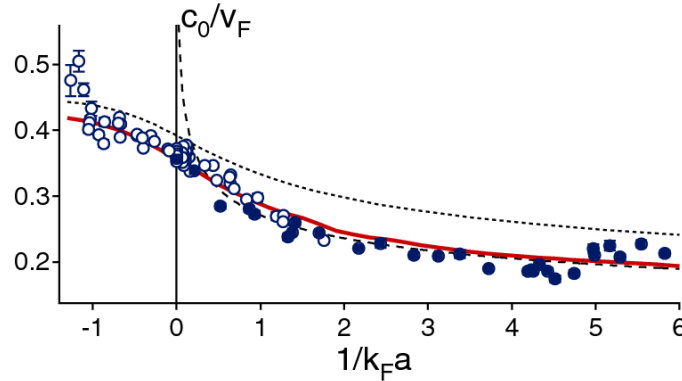

Fig. 66. – Sound velocity normalized by the Fermi velocity v_F versus the interaction parameter, $1/k_F a$. Black dotted curve: mean-field theory based on the Leggett ground state (see **4**˙7.4). Gray (red) solid curve: quantum Monte Carlo calculation [362]. Black dashed curve: Thomas-Fermi theory for a molecular BEC. Reprinted from [84].

7˙2.3. Critical velocity. Superfluid flow breaks down above a critical velocity. This critical velocity is a threshold velocity for creating excitations. For density fluctuations, it is the speed of sound, discussed in the previous paragraph, and this provides the critical velocity on the BEC side. It monotonously increases towards resonance. On the BCS side, as discussed in section **4**˙7.4, pair breaking becomes the dominant mechanism. The pairing energy is largest near resonance, resulting in a maximum of the critical velocity around resonance.

This has been recently observed at MIT [85]. By recording the onset of dissipation in

a Fermi cloud exposed to a weak one-dimensional lattice moving at a variable velocity, critical velocities were obtained. When the magnetic field was varied, they showed a peak near resonance. In these experiments the lattice was created by two focused laser beams crossing at an angle of about 90 degrees exposing only the central part of the cloud to the moving lattice (Fig. 67). When the whole cloud was excited by the moving lattice, much lower critical velocities were found, most likely due the breakdown of superfluidity in the low density spatial wings of the cloud. Using larger depths of the moving lattice, smaller values of the critical velocity were found. This shows that the lattice is not only a way to probe the Fermi gas, it is also a way to create new systems with interesting properties (see section **7**˙3).
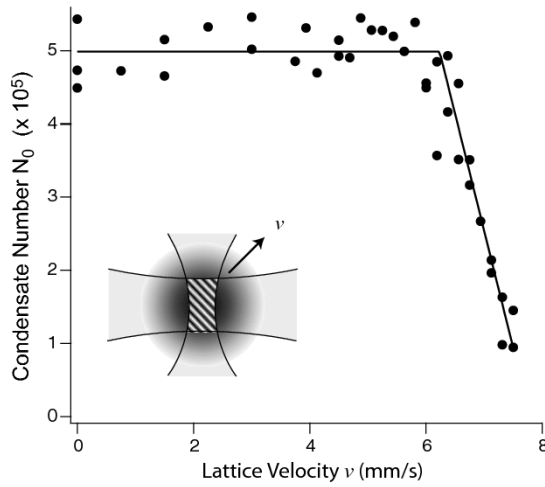

Fig. 67. – Onset of dissipation for superfluid fermions in a moving optical lattice. (Inset) Schematic of the experiment in which two intersecting laser beams produced a moving optical lattice at the center of an optically trapped cloud (trapping beams not shown). Number of fermion pairs which remained in the condensate after being subjected to an optical lattice of depth 0.2 E_F for 500 ms, at a magnetic field of 822 G ($1/k_F a = 0.15$). An abrupt onset of dissipation occurred above a critical velocity. Reprinted from [85].

7˙2.4. *RF spectroscopy.* Single-particle excitations can reveal the nature of pairing. On the BEC side, the excitation of a single atom requires breaking a molecular bond, thus providing information about the binding energy. On the BCS side, single particle excitations reveal the superfluid energy gap and give access to the microscopic physics underlying these Fermi mixtures.

In condensed matter samples, the presence of an excitation gap is clearly seen in tunnelling experiments between a superconductor and a normal metal, divided by a thin insulating barrier. The tunnel effect allows individual electrons to pass through the barrier. For this to occur, electrons must first be excited from the pair condensate,

which costs an energy Δ. For applied voltages smaller than Δ/e, no tunnelling occurs. Abstracting from the tunnelling example, what is required to measure an excitation spectrum is the coupling (= tunnelling) between the initial many-body state of interest and a well-characterized reference state (= metal). In atomic Fermi gases, this situation can be established to some degree using RF spectroscopy. Starting with a Fermi mixture of atoms in, say, the hyperfine states $|1\rangle$ and $|2\rangle$, an RF pulse couples atoms from state $|2\rangle$ into an empty state $|3\rangle$. If state $|3\rangle$ is non-interacting with states $|1\rangle$ and $|2\rangle$, it serves as a reference state. This situation is illustrated in Fig. 68. It is important to note that, because the final state is empty, the RF pulse can excite the entire Fermi sea, and not just atoms at the Fermi surface as in tunnelling experiments.
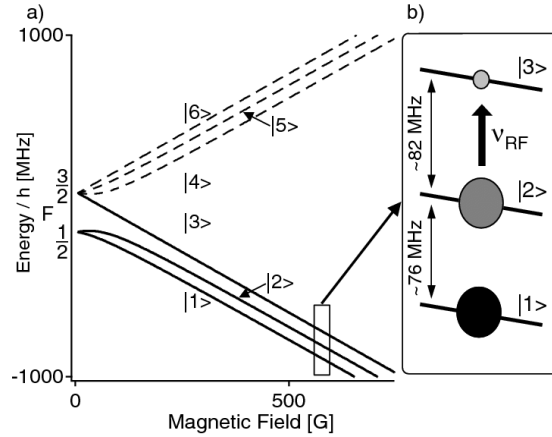

Fig. 68. – RF spectroscopy using a three-level system in ^{6}Li. a) Hyperfine structure of lithium. b) Close-up on the three lowest hyperfine states involved in RF spectroscopy. Typically, the Fermi mixture is prepared in state $|1\rangle$ and $|2\rangle$, and the RF pulse drives the transition to the initially empty state $|3\rangle$. Figure adapted from [127].

In chapter **2** we presented RF spectroscopy as an experimental tool, summarized the basics of RF spectroscopy in a two-level system (where no line shifts due to interactions can be observed), and discussed simple (weak interactions, mean field shift) and exact (sum rule for average shift) limits for the case of three levels. In section **4**˙7.2, we calculated the spectrum for an RF excitation of spin up ($|2\rangle$) atoms out of the BCS state and into the empty state $|3\rangle$.

In this section, we want to summarize how this "RF tool" has been applied to strongly interacting Fermi systems. The full interpretation of these results is still an open question.

RF spectroscopy of normal Fermi gases. For an isolated atom, the resonant frequency ω_{23} for this transition is known to an extreme accuracy. In the presence of a surrounding cloud of interacting atoms, however, the transition can be shifted and broadened. The shifts can originate from the atom experiencing the "mean-field" of the surrounding gas.

Pairing between fermions can lead to additional frequency shifts, as the RF field has to provide the necessary energy to first "break" the pair before the excited atom can be transferred into the final state (this picture implies that final state interactions are negligible). Broadening can be inhomogeneous, for example due to averaging over a range of densities in a trapped sample, or intrinsic (homogeneous), reflecting the local correlations (and thus pairing) between atoms.

When a $|2\rangle$ atom is transferred into state $|3\rangle$ in the presence of a cloud of $|1\rangle$ atoms, its "mean-field" interaction energy changes: The final state interacts differently with $|1\rangle$ than the initial state. This leads to a clock shift in the RF spectrum (see chapter **2**). The first experiments on RF spectroscopy in Fermi gases observed such "mean-field" interaction shifts close to a Feshbach resonance [131, 127] (see Fig. 69) and demonstrated the tunability of interactions around such resonances. Furthermore, it was found that near the Feshbach resonance, the mean-field shifts did not diverge [127], contrary to the simple picture that shifts should be proportional to the difference in scattering lengths. In fact, in the case of ^{6}Li, mean-field shifts were found to be practically absent close to the Feshbach resonances. In this experiment, both the initial and the final state were strongly interacting with state $|1\rangle$ and it was supposed that the two, unitarity limited energy shifts cancel out in the transition. This interpretation was recently confirmed in [132], where it was found that average clock shifts depend on the *inverse* of scattering lengths and thus become small near Feshbach resonances.

RF spectroscopy was used to detect and to study Feshbach molecules. Potassium molecules formed via a sweep across the Feshbach resonance were detected by RF spectroscopy [61]. The molecular line was shifted with respect to the atomic resonance by the molecular binding energy. Bound-bound and bound-free transitions in ^{6}Li were used to precisely determine the position of the Feshbach resonance and other scattering properties [135, 206].

RF spectroscopy of superfluid Fermi gases. After the arrival of fermion pair condensates, the Innsbruck group traced the evolution of the molecular spectrum all the way across resonance [75] (see also the article by R. Grimm in these proceedings). Although two-body physics no longer supports a bound state beyond the resonance, the spectra were still shifted and broad, providing evidence for a pairing gap in the strongly interacting Fermi mixture. As expected for fermionic pairing, the observed feature scaled with the Fermi energy, whereas an "atomic" peak, observed at higher temperature, was narrow and showed only a small shift from the resonance position for isolated atoms. Theoretical modelling suggested that the gas was in the superfluid regime at the lowest temperatures, where the "atomic" peak had fully disappeared [363]. However, the interpretation of the spectra relied on a theory that neglected interactions in the final state, between states $|3\rangle$ and $|1\rangle$ (such spectra were calculated in section **4**.7.2). Recent theoretical work [132, 133, 207] and also experimental studies by the MIT group [99] have demonstrated the importance of such final state interactions.

Furthermore, using fermion mixtures with population imbalance it was shown that
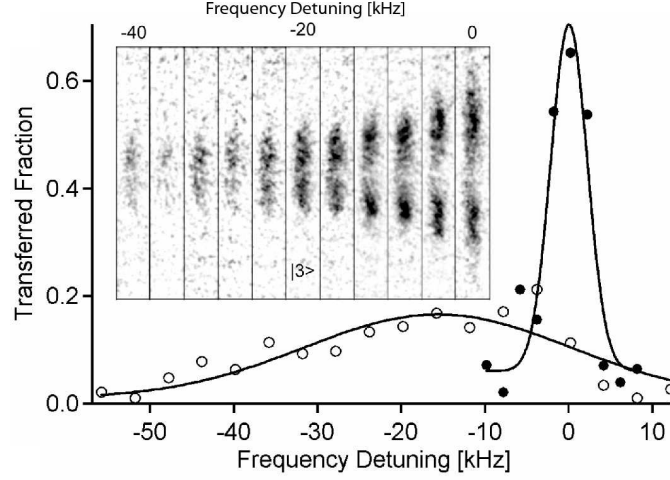
Fig. 69. – Mean field clock shift in an interacting Fermi mixture. RF spectroscopy is performed on the transition from $|2\rangle \rightarrow |3\rangle$ in the presence (open circles) and absence (filled circles) of atoms in state $|1\rangle$. The broadening reflects the inhomogeneous density distribution in the trap, as can be verified via absorption images of atoms in the final state shortly after the RF pulse. Atoms in the low-density wings have smaller shifts than at the center at high density. Figure adapted from [127].

RF spectra of the $|2\rangle \rightarrow |3\rangle$ transition do not change as the gas undergoes the superfluid to normal transition [77] (see Fig. 70). The gas can be normal without any "atomic peak" in the RF spectrum, in contrast to earlier interpretations of such "pure" pairing spectra. The conclusion is that RF spectra probe correlations and pairing only locally and, at the current level of sensitivity, cannot distinguish between a normal and a superfluid phase.

One important technical advance is the introduction of spatially resolved RF "tomography" [134] that allows the reconstruction of local spectra free of inhomogeneous broadening (see also section 2˙5.2). For the resonantly interacting superfluid, this method was used to demonstrate a true frequency gap and a sharp onset of the spectrum at a frequency shift corresponding to about 40% of the Fermi energy.

Final state interactions are currently a major limitation in the interpretation of RF spectra. In lithium, for the resonant superfluid in states $|1\rangle$ and $|2\rangle$ the final state interaction between states $|1\rangle$ and $|3\rangle$ has a large scattering length of $a_{13} = -3300a_0$. Recent results show that Fermi mixture initially in states $|1\rangle$ and $|3\rangle$ provide clearer spectra, presumably because the final state $|2\rangle$ is less strongly interacting with either state $|1\rangle$ or $|3\rangle$ ($a_{23} = 1100a_0$ and $a_{12} = 1400a_0$ at the $|1\rangle$-$|3\rangle$ resonance at $B = 690$ G) [99].

7˙3. New systems with BEC-BCS crossover. – The field of physics stays vibrant by creating new systems to find new phenomena. Two major extensions of the BEC-BCS
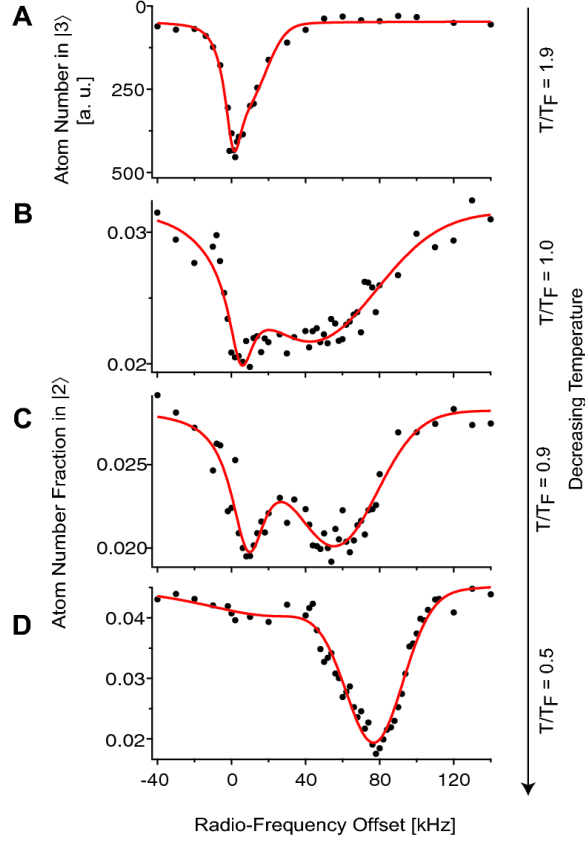
Fig. 70. – Radio-frequency spectroscopy of the minority component in a strongly interacting mixture of fermionic atoms at an imbalance of 0.9, clearly above the Chandrasekhar-Clogston limit of superfluidity (see section 7˙3.2). As the temperature is lowered, the spectrum shows the transition from an "atomic peak" (A, with some asymmetry and broadening) to an almost pure "pairing" peak (D). Figure adapted from Ref. [77].

crossover in an equal mixture of two fermionic states are the addition of optical lattices and population imbalanced Fermi mixtures.

7˙3.1. Optical lattices. Early studies of ^{40}K in an optical lattice were carried out at Zürich [102]. The band structure and Fermi surfaces for non-interacting fermions and interacting fermion mixtures were observed and a normal conductor and band insulator were realized. For a discussion of these experiments, see the contribution of T. Esslinger to these proceedings.

Loading a superfluid fermion mixture into a weak optical lattice should not destroy superfluidity. The only effect of the lattice is to replace the bare mass by an effective mass. Evidence for superfluid behavior was recently observed at MIT [83]. When the

fermionic cloud was released from the lattice, and a rapid magnetic field sweep converted atom pairs into molecules, the characteristic lattice interference pattern was observed, the signature of long-range coherence providing indirect evidence for superfluidity (Fig. 71). Delayed rapid switching of the magnetic field out of the strongly interacting region was necessary to prevent collisions during ballistic expansion, which would have destroyed the interference pattern.

For deeper lattice depths, the interference pattern disappeared. This is analogous to the superfluid-to-Mott-insulator transition in bosons, but now in the regime of strong interactions, which will need a multi-band picture for its full description [364].
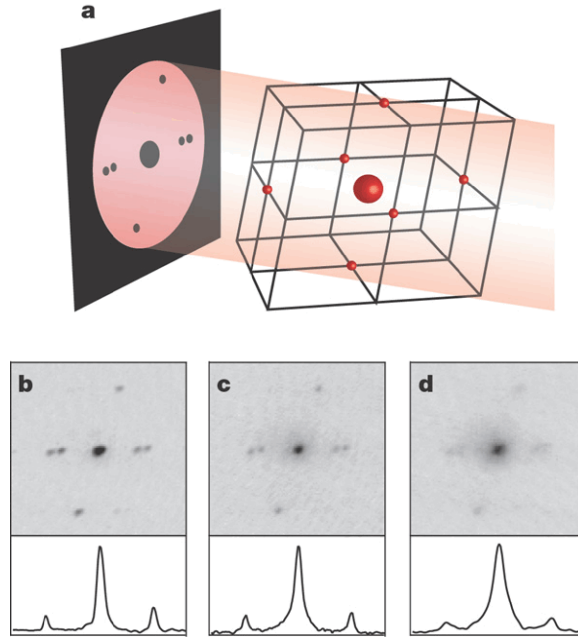
Fig. 71. – Observation of high-contrast interference of fermion pairs released from an optical lattice below and above the Feshbach resonance. a, The orientation of the reciprocal lattice, also with respect to the imaging light. bd, Interference peaks are observed for magnetic fields of 822 G (b), 867 G (c) and 917 G (d). The lattice depth for all images is 5 recoil energies. The field of view is 1 mm. Density profiles through the vertical interference peaks are shown for each image. Figure reprinted from [83].

7˙3.2. *Population imbalanced Fermi mixtures.* The subject of superfluidity with population imbalanced Fermi gases is almost as old as BCS theory itself. Over the last three years, with its realization in ultracold gases, it became a new frontier with major theoretical and experimental activities, and would deserve a review article on its own. Here we can only summarize some basic aspects of this rich system. For an extensive discussion of imbalanced gases see the contribution of F. Chévy to these lectures notes.

180

Often, breaking a symmetry provides additional insight into a system, even into its symmetric configuration. Breaking the equality of the two spin populations has given us new and very direct ways to observe the superfluid phase transition, without need for magnetic field sweeps [312, 80] (see Figs. 51 and 52 in section **6**˙5.2, and Fig. 13 in section **2**˙5). In addition, it opened a way to measure the absolute temperature for a strongly interacting system, using the non-interacting wings of the majority component as a thermometer (see section **3**˙3.1). Scientifically, imbalance is another way (besides temperature, and scattering length) to probe how stable the superfluid is. In addition, in an imbalanced gas, there is no longer a smooth crossover between the BEC- and the BCS-regimes. Instead, a first-order transition takes place: If the attractive interactions become too weak, the superfluid state becomes normal. This is in contrast to the population balanced case, where superfluidity occurs for arbitrarily small interactions. The stronger the imbalance, the smaller is the window of superfluidity.

Or phrased differently, on the BCS side (and also on the BEC side close to the resonance) there is a critical imbalance, beyond which superfluidity breaks down. This quantum phase transition (^{30}) is called the Chandrasekhar-Clogston limit, which we will derive in the next paragraph.

Imbalance introduces a much richer phase diagram. The quantum phase transition at zero temperature continues as a first order phase transition at finite temperature up to tricritical point, where it becomes second order [365]. At high imbalance, the system is normal even at zero temperature, and one can study a highly correlated normal phase without the complications of thermal excitations [77]. Imbalance also offers new opportunities to investigate pairing. Using RF spectroscopy, our group is currently studying differences in the RF spectrum of the majority and minority component. One question, which we address, is whether the majority atoms show a bimodal spectrum reflecting a paired and unpaired component. This will occur in a molecular picture far on the BEC side, but one may expect that on the BCS side the distinction between unpaired and paired atoms is blurred or vanishes.

Chandrasekhar-Clogston limit. The Chandrasekhar-Clogston limit follows from a simple model. A two component Fermi gas can either be in a normal state with two different Fermi energies for the two components, or in a superfluid state that requires balanced populations. The superfluid is stabilized by the condensation energy density δE_s, which we will later set equal to the BCS result $\frac{1}{2}\rho_F\Delta^2$ where Δ is the superfluid gap, and $\rho_F \equiv \rho(E_F)/\Omega$ is the density of states (per spin state and per volume) at the Fermi energy. A balanced superfluid region can only be created by expelling majority atoms which requires extra kinetic energy. It is the interplay between superfluid stabilization energy and kinetic energy which determines the phase boundary.

We consider $N_\uparrow$ and $N_\downarrow$ fermions in a box of volume Ω. Since the imbalance can only

(^{30}) The name "quantum" is deserved as it occurs at zero temperature. Sometimes, the term "quantum phase transition" is reserved for second order phase transitions.

be accommodated in the normal phase, we assign a volume fraction η to it, and the rest of the volume is superfluid. The superfluid and (average) normal densities, n_s and n_n, may be different, and are constrained by the constant total number of atoms

(233) $$N = N_\uparrow + N_\downarrow = 2n_s(1 - \eta)\,\Omega + 2n_n\,\eta\,\Omega.$$

The energy density of the superfluid gas is

(234) $$E_s = 2\frac{3}{5}E_F[n_s]\,n_s - \delta E_s$$

where $E_F[n] \propto n^{2/3}$ is the Fermi energy of a Fermi gas at density n. For the normal phase we have

(235) $$E_n = \frac{3}{5}\left\{E_F\left[n_n + \frac{\Delta n}{\eta}\right]\left(n_n + \frac{\Delta n}{\eta}\right) + E_F\left[n_n - \frac{\Delta n}{\eta}\right]\left(n_n - \frac{\Delta n}{\eta}\right)\right\}$$

(236) $$\approx 2\frac{3}{5}E_F[n_n]\,n_n + \frac{1}{\rho_F}\left(\frac{\Delta n}{\eta}\right)^2$$

where we have assumed that the density difference $\Delta n = (N_\uparrow - N_\downarrow)/2\Omega$ is much smaller than the total average density per spin state $n = (N_\uparrow + N_\downarrow)/2\Omega$.

The total energy is minimized as a function of η and $n_s - n_n$. For $\eta = 1$ the whole system becomes normal. The calculation is simplified if we introduce a Lagrangian multiplier μ to account for the constraint on the total number of atoms, and then minimize the total free energy $E_{tot} - \mu N$ with respect to η, n_s and n_n.

$$E_{tot} - \mu N = \left(2\frac{3}{5}E_F[n_s]n_s - \delta E_s\right)\Omega\,(1 - \eta)$$

$$+ \left(2\frac{3}{5}E_F[n_n]n_n + \frac{1}{\rho_F}\left(\frac{\Delta n}{\eta}\right)^2\right)\Omega\,\eta$$

(237) $$- \mu\,2\Omega\,((1 - \eta)n_s + \eta\,n_n)$$

Using $\frac{3}{5}E_F[n_s]n_s - \frac{3}{5}E_F[n_n]n_n = E_F[n_{av}](n_s - n_m)$ where n_{av} is between n_n and n_s, and setting the η derivative to zero, we obtain

(238) $$\eta^2 = \frac{(\Delta n)^2}{\rho_F\left\{\delta E_s + 2\,(\mu - E_F[n_{av}])\,(n_s - n_n)\right\}}$$

Setting the other two derivatives (with respect to n_s and n_n) of Eq. 237 to zero provides expressions for the density difference and the chemical potential. They show that both $\mu - E_F[n_{av}]$ and $n_s - n_n$ scale linearly with δE_s, i.e. that the second term in the denominator of Eq. 238 is second order in δE_s and negligible for weak interactions
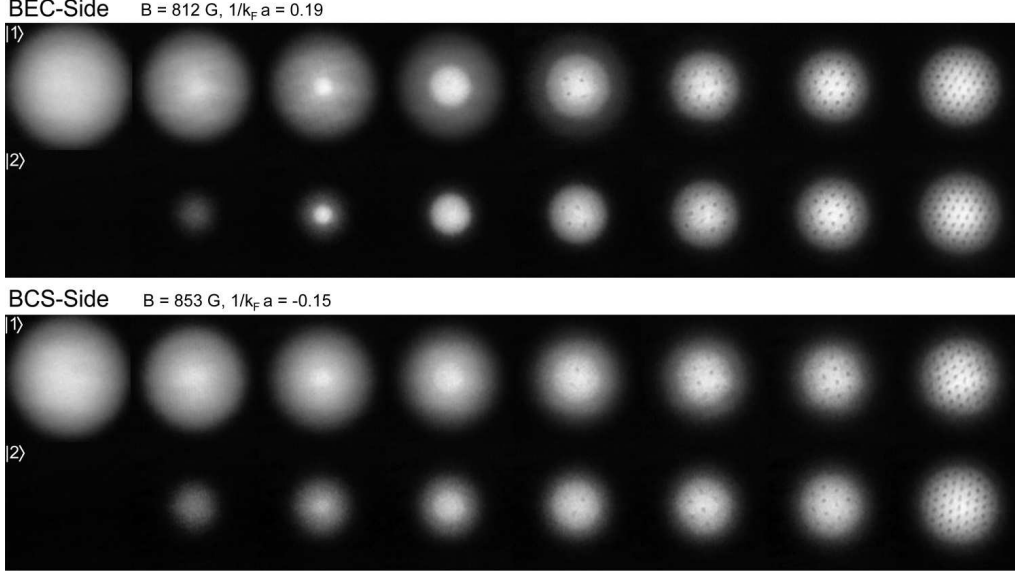
Fig. 72. – Observation of vortices in a strongly interacting Fermi gas with imbalanced spin populations. For the 812 G data, the population imbalance $(N_\uparrow - N_\downarrow)/(N_\uparrow + N_\downarrow)$ was (from left to right) 100, 90, 80, 62, 28, 18, 10 and 0%. For the 853 G data, the mismatch was 100, 74, 58, 48, 32, 16, 7 and 0%. From [78].

(BCS limit). Substituting $\frac{1}{2}\rho_F\Delta^2$ for δE_s, one obtains for the normal volume fraction

$$\eta = \frac{\sqrt{2}\Delta n}{\rho_F \Delta} \tag{239}$$

This becomes one for $\Delta n = \rho_F \Delta/\sqrt{2}$, which is the Chandrasekhar-Clogston limit for the superfluid to normal quantum phase transition.

In case of superconductors, the number imbalance can be created by a magnetic field B (assuming that the Meissner effect is suppressed, e.g. in heavy fermion or layered superconductors [94]) $\Delta n = \rho_F \mu_B B$ which leads to the Chandrasekhar-Clogston limit in its original form $\mu_B B_c = \Delta/\sqrt{2}$ where B_c is the critical magnetic field [366, 367]. Using Eq. 167, one obtains $B_c = 18500\,\text{G}\,\frac{T_C}{\text{K}}$, much larger than the thermodynamic critical field of a conventional superconductor, which is $B_c = \sqrt{\mu_0 \rho_F}\Delta \approx 50\,\text{G}\,\frac{T_C}{\text{K}}$. This shows that conventional superconductors will be quenched by orbital effects of the magnetic field (Meissner effect and flux quanta), and not by spin effects (Chandrasekhar-Clogston limit).

Experimental observations. The proof for the occurrence of superfluidity in imbalanced gases was obtained, as in the balanced case, by the observation of superfluid flow in
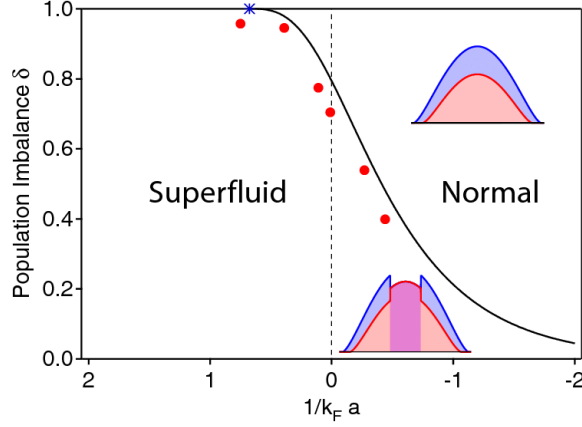
Fig. 73. – Critical population imbalance $\delta = (N_\uparrow - N_\downarrow)/(N_\uparrow + N_\downarrow)$ between the two spin states for which the superfluid-to-normal transition is observed. The profiles indicate the distribution of the gas in the harmonic trap. Data from [78].

the form of vortices (Fig. 72). Since vortices can be difficult to create and observe near the phase boundaries, the superfluid phase diagram has been mapped out by using pair condensation as an indicator for superfluidity. The phase diagram (Fig. 73) shows that on the BEC side, the Chandrasekhar-Clogston limit approaches 100%. So even if there are only a few minority atoms in a majority Fermi sea, they can form bosonic molecules and Bose-Einstein condense. The observed deviation from 100% is probably due to finite temperature. On resonance, the critical population imbalance converged towards $\approx 70\%$ when the temperature was varied [78].

First hints for phase separation between the normal and superfluid phase were seen in refs. [78, 79]. Using tomographic techniques, a sharp separation between a superfluid core and a partially polarized normal phase was found [80]. Finally, the phase diagram of a spin-polarized Fermi gas at unitarity was obtained, by mapping out the superfluid phase versus temperature and density imbalance [82]. Using tomographic techniques, spatial discontinuities in the spin polarization were revealed, the signature of a first-order phase transition that disappears at a tricritical point (Fig. 74). These results are in excellent agreement with recent theoretical predictions [368, 369]. The Chandrasekhar-Clogston limit was not observed in the work at Rice, from which it was concluded that the critical imbalance on resonance was close to 100%. The discrepancy to the MIT results is probably related to the lower atom number and higher aspect ratio used in these experiments [79, 81].

The phase diagram in Fig. 74 highlights how far experimental studies on degenerate Fermi gases have progressed since their first observation in 1999. It is a rich diagram including first and second order phase transitions, phase separation and a tricritical point. It is expressed using only local quantities (density, spin polarization, local Fermi
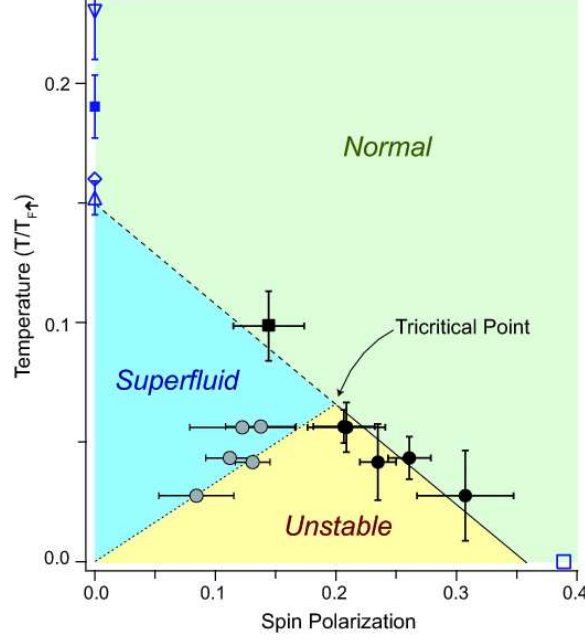
Fig. 74. – Phase diagram for a homogeneous spin-polarized Fermi gas with resonant interactions, as a function of spin polarization and temperature. Below the tricritical point phase boundaries have been observed, characteristic for a first order phase transition. The polarization jumps from the value in the superfluid (shown by the gray solid circles) to the higher value in the normal phase (black solid circles). Above the tricritical point, no abrupt change in spin polarization was observed, and the phase transition in the center of the cloud was determined from the onset of pair condensation (black square). The blue open symbols show theoretical predictions for the critical temperature of a homogeneous equal mixture (see Ref. [82] for a full discussion).

temperature) and therefore applies directly to the homogeneous case. Experimentally, it required 3D spatial resolution using tomographic techniques. Finally, it is worth pointing out that the position of the tricritical point could not be predicted and has even been controversial until it had been experimentally determined.

8. – Conclusion

In this review paper, we have given a comprehensive description of the concepts, methods and results involved in the exploration of the BEC-BCS crossover with ultracold fermionic atoms. Of course, many of the techniques and concepts apply to other important areas where experiments with ultracold fermions are conducted.

One area is atom optics and precision measurements. The important feature of fermions is the suppression of interactions in a one-component gas due to Pauli blocking. The Florence group studied transport behavior of fermions in an optical lattice and observed collisionally induced transport [370], and conducting and insulating behavior of ideal Fermi gases [371]. The realization of atom interferometry and observation of Bloch oscillation in a Fermi gas [372] demonstrated the potential of fermions for precision measurements unaffected by atomic collisions [373].

Another area is the study of mixtures of fermions with other species. Bose-Fermi mixtures have been used to study how the addition of fermionic atoms affects the bosonic superfluid-to-Mott-insulator transition [374, 375]. Also intriguing is the study of boson-mediated interactions between fermions [376, 377]. Interspecies Feshbach resonances between fermionic and bosonic atoms have already been identified [147, 101], and heteronuclear molecules observed [103, 378]. Mixtures between two fermionic species (e.g. ^{6}Li and ^{40}K) may allow the study of pairing and superfluidity where the pairs are made from atoms with different masses [105, 379].

p-wave interactions provide a different way of pairing atoms, and ultimately may connect the study of superfluidity in ^{3}He (which is based on p-wave pairing) with ultracold atoms. p-wave Feshbach resonances have already been observed by various groups [145, 144, 146, 380], and p-wave molecules have been produced [86].

And finally, a whole new area is the study of fermions with repulsive interactions in optical lattices. At low temperature and half filling, the system should be antiferromagnetic [381, 382], and at lower filling, it may show d-wave superfluidity [381] and help to elucidate the nature of pairing in high-temperature superconductors. For a discussion of these effects, we refer to the contribution of A. Georges to these lecture notes.

With many new systems on the drawing board or already in preparation, and with a flurry of theoretical papers predicting new aspects of superfluidity and other novel phenomena, it seems certain that we have exciting years ahead of us.

REFERENCES

[1] ANDERSON, M. H., ENSHER, J. R., MATTHEWS, M. R., WIEMAN, C. E., AND CORNELL, E. A., Observation of Bose-Einstein condensation in a dilute atomic vapor, *Science,* **269** (1995) 198–201.

[2] DAVIS, K. B., MEWES, M.-O., ANDREWS, M. R., VAN DRUTEN, N. J., DURFEE, D. S., KURN, D. M., AND KETTERLE, W., Bose-Einstein condensation in a gas of sodium atoms, *Phys. Rev. Lett.,* **75** (1995) 3969–3973.

[3] GREINER, M., MANDEL, O., ESSLINGER, T., HÄNSCH, T. W., AND BLOCH, I., Quantum phase transition from a superfluid to a mott insulator in a gas of ultracold atoms, *Nature,* **415** (2002) 39–44.

[4] BLOCH, I., Ultracold quantum gases in optical lattices, *Nature Physics,* **1** (2005) 23.

[5] STWALLEY, W. C., Stability of spin-aligned hydrogen at low temperatures and high magnetic fields: New field-dependent scattering resonances and predissociations, *Phys. Rev. Lett.,* **37** (1976) 1628.

[6] TIESINGA, E., VERHAAR, B. J., AND STOOF, H. T. C., Threshold and resonance phenomena in ultracold ground-state collisions, *Phys. Rev. A,* **47** (1993) 4114–4122.

[7] INOUYE, S., ANDREWS, M. R., STENGER, J., MIESNER, H.-J., STAMPER-KURN, D. M., AND KETTERLE, W., Observation of Feshbach resonances in a Bose-Einstein condensate, *Nature,* **392** (1998) 151–154.

[8] COURTEILLE, P., FREELAND, R. S., HEINZEN, D. J., VAN ABEELEN, F. A., AND VERHAAR, B. J., Observation of a Feshbach resonance in cold atom scattering, *Phys. Rev. Lett.,* **81** (1998) 69–72.

[9] KETTERLE, W., DURFEE, D. S., AND STAMPER-KURN, D. M., Making, probing and understanding Bose-Einstein condensates, in *Bose-Einstein condensation in atomic gases, Proceedings of the International School of Physics Enrico Fermi, Course CXL, Varenna, 7-17 July 1998*, edited by M. Inguscio, S. Stringari, and C. Wieman, (IOS Press, Amsterdam) 1999, pp. 67–176.

[10] STENGER, J., INOUYE, S., ANDREWS, M. R., MIESNER, H.-J., STAMPER-KURN, D. M., AND KETTERLE, W., Strongly enhanced inelastic collisions in a Bose-Einstein condensate near Feshbach resonances, *Phys. Rev. Lett.,* **82** (1999) 2422–2425.

[11] CORNISH, S. L., CLAUSSEN, N. R., ROBERTS, J. L., CORNELL, E. A., AND WIEMAN, C. E., Stable ^{85}Rb Bose-Einstein condensates with widely tunable interactions, *Phys. Rev. Lett.,* **85** (2000) 1795–1798.

[12] ABRAHAM, E. R. I., MCALEXANDER, W. I., GERTON, J. M., HULET, R. G., CÔTÉ, R., AND DALGARNO, A., Triplet s-wave resonance in ^{6}Li collisions and scattering lengths of ^{6}Li and ^{7}Li, *Phys. Rev. A,* **55** (1997) R3299.

[13] STOOF, H. T. C., HOUBIERS, M., SACKETT, C. A., AND HULET, R. G., Superfluidity of spin-polarized ^{6}Li, *Phys. Rev. Lett.,* **76** (1996) 10.

[14] HOUBIERS, M., STOOF, H. T. C., MCALEXANDER, W. I., AND HULET, R. G., Elastic and inelastic collisions of ^{6}Li atoms in magnetic and optical traps, *Phys. Rev. A,* **57** (1998) R1497.

[15] CUBIZOLLES, J., BOURDEL, T., KOKKELMANS, S. J. J. M. F., SHLYAPNIKOV, G. V., AND SALOMON, C., Production of long-lived ultracold Li_2 molecules from a Fermi gas, *Phys. Rev. Lett.,* **91** (2003) 240401.

[16] STRECKER, K. E., PARTRIDGE, G. B., AND HULET, R. G., Conversion of an atomic Fermi gas to a long-lived molecular Bose gas, *Phys. Rev. Lett.,* **91** (2003) 080406.

[17] JOCHIM, S., BARTENSTEIN, M., ALTMEYER, A., HENDL, G., CHIN, C., HECKER-DENSCHLAG, J., AND GRIMM, R., Pure gas of optically trapped molecules created from fermionic atoms, *Phys. Rev. Lett.,* **91** (2003) 240402.

[18] REGAL, C. A., GREINER, M., AND JIN, D. S., Lifetime of molecule-atom mixtures near a Feshbach resonance in ^{40}K, *Phys. Rev. Lett.,* **92** (2004) 083201.

[19] PETROV, D. S., Three-body problem in Fermi gases with short-range interparticle interaction, *Phys. Rev. A,* **67** (2003) 010703.

[20] STOOF, H. T. C., AND HOUBIERS, M., Condensed matter physics with trapped atomic Fermi gases, in *Bose-Einstein condensation in atomic gases, Proceedings of the International School of Physics Enrico Fermi, Course CXL, Varenna, 7-17 July 1998,* edited by M. Inguscio, S. Stringari, and C. Wieman, (IOS Press, Amsterdam) 1999, pp. 537–553.

[21] HOUBIERS, M., FERWERDA, R., STOOF, H. T. C., McALEXANDER, W. I., SACKETT, C. A., AND HULET, R. G., Superfluid state of atomic ^{6}Li in a magnetic trap, *Phys. Rev. A,* **56** (1997) 4864.

[22] ZHANG, W., SACKETT, C. A., AND HULET, R. G., Optical detection of a Bardeen-Cooper-Schrieffer phase transition in a trapped gas of fermionic atoms, *Phys. Rev. A,* **60** (1999) 504.

[23] WEIG, F., AND ZWERGER, W., Optical detection of a BCS transition of lithium–6 in harmonic traps, *Europhys. Lett.,* **49** (2000) 282.

[24] TÖRMÄ, P., AND ZOLLER, P., Laser probing of atomic Cooper pairs, *Phys. Rev. Lett.,* **85** (2000) 487.

[25] BARANOV, M. A., AND PETROV, D. S., Low-energy collective excitations in a superfluid trapped Fermi gas, *Phys. Rev. A,* **62** (2000) 041601(R).

[26] MINGUZZI, A., AND TOSI, M. P., Scissors mode in a superfluid Fermi gas, *Phys. Rev. A,* **63** (2001) 023609.

[27] CHIOFALO, M. L., KOKKELMANS, S. J. J. M. F., MILSTEIN, J. N., AND HOLLAND, M. J., Signatures of resonance superfluidity in a quantum Fermi gas, *Phys. Rev. Lett.,* **88** (2002) 090402.

[28] ONNES, K., Investigations into the properties of substances at low temperatures, which have led, amongst other things, to the preparation of liquid helium, nobel lecture, december 13, 1913, in *Nobel Lectures, Physics 1901-1921,* (Elsevier Publishing Company, Amsterdam) 1967.

[29] SCHAFROTH, M. R., Remarks on the Meissner effect, *Phys. Rev.,* **111** (1958) 72.

[30] REYNOLDS, C. A., SERIN, B., WRIGHT, W. H., AND NESBITT, L. B., Superconductivity of isotopes of mercury, *Phys. Rev.,* **78** (1950) 487.

[31] MAXWELL, E., Isotope effect in the superconductivity of mercury, *Phys. Rev.,* **78** (1950) 477.

[32] FRÖHLICH, H., Theory of the superconducting state. I. the ground state at the absolute zero of temperature, *Phys. Rev.,* **79** (1950) 845.

[33] COOPER, L. N., Bound electron pairs in a degenerate Fermi gas, *Phys. Rev.,* **104** (1956) 1189–1190.

[34] BARDEEN, J., COOPER, L. N., AND SCHRIEFFER, J. R., Theory of superconductivity, *Phys. Rev.,* **108** (1957) 1175.

[35] LONDON, F., *Superfluids, Vol. II,* (Dover, New York) 1964.

[36] SCHRIEFFER, J. R., *Theory of Superconductivity,* (Westview Press, Boulder, Colorado) 1999.

[37] POPOV, V. N., Theory of a Bose gas produced by bound states of Fermi particles, *Zh. Eksp. Teor. Fiz.,* **50** (1966) 1550, [Sov. Phys. JETP 23, 1034 (1968)].

[38] KELDYSH, L. V., AND KOZLOV, A. N., Collective properties of excitons in semiconductors, *Zh. Eksp. Teor. Fiz.,* **54** (1968) 978, [Sov. Phys. JETP 27, 521 (1968)].

[39] EAGLES, D. M., Possible pairing without superconductivity at low carrier concentrations in bulk and thin-film superconducting semiconductors, *Phys. Rev.,* **186** (1969) 456.

[40] LEGGETT, A. J., Diatomic molecules and Cooper pairs, in *Modern Trends in the Theory of Condensed Matter. Proceedings of the XVIth Karpacz Winter School of Theoretical Physics, Karpacz, Poland,* (Springer-Verlag, Berlin) 1980, pp. 13–27.

[41] NOZIÈRES, P., AND SCHMITT-RINK, S., Bose condensation in an attractive fermion gas: from weak to strong coupling superconductivity, *J. Low Temp. Phys.,* **59** (1985) 195–211.

[42] GINZBURG, V. L., High-temperature superconductivity (history and general review), *Soviet Physics Uspekhi,* **34** (1991) 283–288.

[43] BEDNORZ, J. G., AND MÜLLER, K. A., Possible high-T_c superconductivity in the Ba-La-Cu-O system, *Z. Phys. B,* **64** (1986) 189.

[44] LEE, P. A., NAGAOSA, N., AND WEN, X.-G., Doping a Mott insulator: Physics of high-temperature superconductivity, *Rev. Mod. Phys.,* **78** (2006) 17.

[45] HO, T.-L., Universal thermodynamics of degenerate quantum gases in the unitarity limit, *Phys. Rev. Lett.,* **92** (2004) 090402.

[46] MYATT, C. J., BURT, E. A., GHRIST, R. W., CORNELL, E. A., AND WIEMAN, C. E., Production of two overlapping Bose-Einstein condensates by sympathetic cooling, *Phys. Rev. Lett.,* **78** (1997) 586–589.

[47] BLOCH, I., GREINER, M., MANDEL, O., HÄNSCH, T. W., AND ESSLINGER, T., Sympathetic cooling of ^{85}Rb and ^{87}Rb, *Phys. Rev. A,* **64** (2001) 021402–4.

[48] STAMPER-KURN, D. M., ANDREWS, M. R., CHIKKATUR, A. P., INOUYE, S., MIESNER, H.-J., STENGER, J., AND KETTERLE, W., Optical confinement of a Bose-Einstein condensate, *Phys. Rev. Lett.,* **80** (1998) 2027–2030.

[49] DEMARCO, B., AND JIN, D. S., Onset of Fermi degeneracy in a trapped atomic gas, *Science,* **285** (1999) 1703–1706.

[50] ROATI, G., RIBOLI, F., MODUGNO, G., AND INGUSCIO, M., Fermi-Bose quantum degenerate ^{40}K - ^{87}Rb mixture with attractive interaction, *Phys. Rev. Lett.,* **89** (2002) 150403.

[51] TRUSCOTT, A. G., STRECKER, K. E., MCALEXANDER, W. I., PARTRIDGE, G. B., AND HULET, R. G., Observation of Fermi pressure in a gas of trapped atoms, *Science,* **291** (2001) 2570–2572.

[52] SCHRECK, F., KHAYKOVICH, L., CORWIN, K. L., FERRARI, G., BOURDEL, T., CUBIZOLLES, J., AND SALOMON, C., Quasipure Bose-Einstein condensate immersed in a Fermi sea, *Phys. Rev. Lett.,* **87** (2001) 080403.

[53] GRANADE, S. R., GEHM, M. E., O'HARA, K. M., AND THOMAS, J. E., All-optical production of a degenerate Fermi gas, *Phys. Rev. Lett.,* **88** (2002) 120405.

[54] HADZIBABIC, Z., STAN, C. A., DIECKMANN, K., GUPTA, S., ZWIERLEIN, M. W., GÖRLITZ, A., AND KETTERLE, W., Two species mixture of quantum degenerate Bose and Fermi gases, *Phys. Rev. Lett.,* **88** (2002) 160401.

[55] JOCHIM, S., BARTENSTEIN, M., ALTMEYER, A., HENDL, G., RIEDL, S., CHIN, C., HECKER-DENSCHLAG, J., AND GRIMM, R., Bose-Einstein condensation of molecules, *Science,* **302** (2003) 2101.

[56] DIECKMANN, K., STAN, C. A., GUPTA, S., HADZIBABIC, Z., SCHUNCK, C., AND KETTERLE, W., Decay of an ultracold fermionic lithium gas near a Feshbach resonance, *Phys. Rev. Lett.,* **89** (2002) 203201.

[57] LOFTUS, T., REGAL, C. A., TICKNOR, C., BOHN, J. L., AND JIN, D. S., Resonant control of elastic collisions in an optically trapped Fermi gas of atoms, *Phys. Rev. Lett.,* **88** (2002) 173201.

[58] O'Hara, K. M., Hemmer, S. L., Granade, S. R., Gehm, M. E., Thomas, J. E., V.Venturi, Tiesinga, E., and Williams, C. J., Measurement of the zero crossing in a Feshbach resonance of fermionic ^{6}Li, *Phys. Rev. A,* **66** (2002) 041401(R).

[59] Jochim, S., Bartenstein, M., Hendl, G., Hecker-Denschlag, J., Grimm, R., Mosk, A., and Weidemüller, M., Magnetic field control of elastic scattering in a cold gas of fermionic lithium atoms, *Phys. Rev. Lett.,* **89** (2002) 273202.

[60] O'Hara, K. M., Hemmer, S. L., Gehm, M. E., Granade, S. R., and Thomas, J. E., Observation of a strongly interacting degenerate Fermi gas of atoms, *Science,* **298** (2002) 2179.

[61] Regal, C. A., Ticknor, C., Bohn, J. L., and Jin, D. S., Creation of ultracold molecules from a Fermi gas of atoms, *Nature,* **424** (2003) 47.

[62] Herbig, J., Kraemer, T., Mark, M., Weber, T., Chin, C., Nägerl, H.-C., and Grimm, R., Preparation of a pure molecular quantum gas, *Science,* **301** (2003) 1510.

[63] Xu, K., Mukaiyama, T., Abo-Shaeer, J. R., Chin, J. K., Miller, D. E., and Ketterle, W., Formation of quantum-degenerate sodium molecules, *Phys. Rev. Lett.,* **91** (2003) 210402.

[64] Dürr, S., Volz, T., Marte, A., and Rempe, G., Observation of molecules produced from a Bose-Einstein condensate, *Phys. Rev. Lett.,* **92** (2004) 020406.

[65] Greiner, M., Regal, C. A., and Jin, D. S., Emergence of a molecular Bose-Einstein condensate from a Fermi gas, *Nature,* **426** (2003) 537.

[66] Zwierlein, M. W., Stan, C. A., Schunck, C. H., Raupach, S. M. F., Gupta, S., Hadzibabic, Z., and Ketterle, W., Observation of Bose-Einstein condensation of molecules, *Phys. Rev. Lett.,* **91** (2003) 250401.

[67] Bartenstein, M., Altmeyer, A., Riedl, S., Jochim, S., Chin, C., Hecker-Denschlag, J., and Grimm, R., Crossover from a molecular Bose-Einstein condensate to a degenerate Fermi gas, *Phys. Rev. Lett.,* **92** (2004) 120401.

[68] Zwierlein, M. W., Abo-Shaeer, J. R., Schirotzek, A., Schunck, C. H., and Ketterle, W., Vortices and superfluidity in a strongly interacting Fermi gas, *Nature,* **435** (2005) 1047–1051.

[69] Regal, C. A., Greiner, M., and Jin, D. S., Observation of resonance condensation of fermionic atom pairs, *Phys. Rev. Lett.,* **92** (2004) 040403.

[70] Zwierlein, M. W., Stan, C. A., Schunck, C. H., Raupach, S. M. F., Kerman, A. J., and Ketterle, W., Condensation of pairs of fermionic atoms near a Feshbach resonance, *Phys. Rev. Lett.,* **92** (2004) 120403.

[71] Bourdel, T., Khaykovich, L., Cubizolles, J., Zhang, J., Chevy, F., Teichmann, M., Tarruell, L., Kokkelmans, S. J. J. M. F., and Salomon, C., Experimental study of the BEC-BCS crossover region in lithium-6, *Phys. Rev. Lett.,* **93** (2004) 050401.

[72] Kinast, J., Turlapov, A., Thomas, J. E., Chen, Q., Stajic, J., and Levin, K., Heat capacity of a strongly-interacting Fermi gas, *Science,* **307** (2005) 1296–1299.

[73] Kinast, J., Hemmer, S. L., Gehm, M. E., Turlapov, A., and Thomas, J. E., Evidence for superfluidity in a resonantly interacting Fermi gas, *Phys. Rev. Lett.,* **92** (2004) 150402.

[74] Bartenstein, M., Altmeyer, A., Riedl, S., Jochim, S., Chin, C., Hecker-Denschlag, J., and Grimm, R., Collective excitations of a degenerate gas at the BEC-BCS crossover, *Phys. Rev. Lett.,* **92** (2004) 203201.

[75] Chin, C., Bartenstein, M., Altmeyer, A., Riedl, S., Jochim, S., Hecker-Denschlag, J., and Grimm, R., Observation of the pairing gap in a strongly interacting Fermi gas, *Science,* **305** (2004) 1128.

[76] Partridge, G. B., Strecker, K. E., Kamar, R. I., Jack, M. W., and Hulet, R. G., Molecular probe of pairing in the BEC-BCS crossover, *Phys. Rev. Lett.,* **95** (2005) 020404.

[77] Schunck, C. H., Shin, Y., Schirotzek, A., Zwierlein, M. W., and Ketterle, W., Pairing without superfluidity: The ground state of an imbalanced Fermi mixture, *Science,* **316** (2007) 867.

[78] Zwierlein, M. W., Schirotzek, A., Schunck, C. H., and Ketterle, W., Fermionic superfluidity with imbalanced spin populations, *Science,* **311** (2006) 492–496.

[79] Partridge, G. B., Li, W., Kamar, R. I., Liao, Y., and Hulet, R. G., Pairing and phase separation in a polarized Fermi gas, *Science,* **311** (2006) 503.

[80] Shin, Y., Zwierlein, M. W., Schunck, C. H., Schirotzek, A., and Ketterle, W., Observation of phase separation in a strongly interacting imbalanced Fermi gas, *Phys. Rev. Lett.,* **97** (2006) 030401.

[81] Partridge, G. B., Li, W., Liao, Y., Hulet, R. G., Haque, M., and Stoof, H. T. C., Deformation of a trapped Fermi gas with unequal spin populations, *Phys. Rev. Lett.,* **97** (2006) 190407.

[82] Shin, Y., Schunck, C. H., Schirotzek, A., and Ketterle, W., Phase diagram of a two-component Fermi gas with resonant interactions, Nature, in print; preprint arXiv:0709.3027.

[83] Chin, J. K., Miller, D. E., Liu, Y., Stan, C., Setiawan, W., Sanner, C., Xu, K., and Ketterle, W., Evidence for superfluidity of ultracold fermions in an optical lattice, *Nature,* **443** (2006) 961–964.

[84] Joseph, J., Clancy, B., Luo, L., Kinast, J., Turlapov, A., and Thomas, J. E., Measurement of sound velocity in a Fermi gas near a Feshbach resonance, *Phys. Rev. Lett.,* **98** (2007) 170401.

[85] Miller, D. E., Chin, J. K., Stan, C. A., Liu, Y., Setiawan, W., Sanner, C., and Ketterle, W., Critical velocity for superfluid flow across the BEC-BCS crossover, *Phys. Rev. Lett.,* **99** (2007) 070402.

[86] Gaebler, J. P., Stewart, J. T., Bohn, J. L., and Jin, D. S., p-wave Feshbach molecules, *Phys. Rev. Lett.,* **98** (2007) 200403.

[87] Rom, T., Best, T., v. Oosten, D., Schneider, U., Fölling, S., Paredes, B., and Bloch, I., Free fermion antibunching in a degenerate atomic Fermi gas released from an optical lattice, *Nature,* **444** (2006) 733–736.

[88] Tuoriniemi, J., Juntunen-Nurmilaukas, K., Uusvuori, J., Pentti, E., Salmela, A., and Sebedash, A., Superconductivity in lithium below 0.4 millikelvin at ambient pressure, *Nature,* **447** (2007) 187–189.

[89] Schäfer, T., What atomic liquids can teach us about quark liquids, preprint hep-ph/0703141.

[90] Back, B. B., *et al.*, The PHOBOS perspective on discoveries at RHIC, *Nuclear Physics A,* **757** (2005) 28–101.

[91] Kinast, J., Turlapov, A., and Thomas, J. E., Damping of a unitary Fermi gas, *Phys. Rev. Lett.,* **94** (2005) 170404.

[92] Kovtun, P. K., Son, D. T., and Starinets, A. O., Viscosity in strongly interacting quantum field theories from black hole physics, *Phys. Rev. Lett.,* **94** (2005) 111601.

[93] Schäfer, T., Ratio of shear viscosity to entropy density for trapped fermions in the unitarity limit, *Phys. Rev. A,* **76** (2007) 063618–5.

[94] Casalbuoni, R., and Nardulli, G., Inhomogeneous superconductivity in condensed matter and QCD, *Rev. Mod. Phys.,* **76** (2004) 263, and references therein.

[95] Alford, M., Color-superconducting quark matter, *Annual Review of Nuclear and Particle Science,* **51** (2001) 131–160.

[96] Bowers, J. A., and Rajagopal, K., Crystallography of color superconductivity, *Phys. Rev. D,* **66** (2002) 065002.

[97] MCNAMARA, J. M., JELTES, T., TYCHKOV, A. S., HOGERVORST, W., AND VASSEN, W., Degenerate Bose-Fermi mixture of metastable atoms, *Phys. Rev. Lett.,* **97** (2006) 080404.

[98] FUKUHARA, T., TAKASU, Y., KUMAKURA, M., AND TAKAHASHI, Y., Degenerate Fermi gases of Ytterbium, *Phys. Rev. Lett.,* **98** (2007) 030401.

[99] SCHUNCK, C. H., SCHIROTZEK, A., SHIN, Y.-I., AND KETTERLE, W., (to be published).

[100] HADZIBABIC, Z., GUPTA, S., STAN, C. A., SCHUNCK, C. H., ZWIERLEIN, M. W., DIECKMANN, K., AND KETTERLE, W., Fifty-fold improvement in the number of quantum degenerate fermionic atoms, *Phys. Rev. Lett.,* **91** (2003) 160401.

[101] INOUYE, S., GOLDWIN, J., OLSEN, M. L., TICKNOR, C., BOHN, J. L., AND JIN, D. S., Observation of heteronuclear Feshbach resonances in a mixture of bosons and fermions, *Phys. Rev. Lett.,* **93** (2004) 183201.

[102] KÖHL, M., MORITZ, H., STÖFERLE, T., GÜNTER, K., AND ESSLINGER, T., Fermionic atoms in a three dimensional optical lattice: Observing Fermi surfaces, dynamics, and interactions, *Phys. Rev. Lett.,* **94** (2005) 080403.

[103] OSPELKAUS, C., OSPELKAUS, S., HUMBERT, L., ERNST, P., SENGSTOCK, K., AND BONGS, K., Ultracold heteronuclear molecules in a 3D optical lattice, *Phys. Rev. Lett.,* **97** (2006) 120402.

[104] SILBER, C., GÜNTHER, S., MARZOK, C., DEH, B., COURTEILLE, P. W., AND ZIMMERMANN, C., Quantum-degenerate mixture of fermionic lithium and bosonic rubidium gases, *Phys. Rev. Lett.,* **95** (2005) 170408.

[105] TAGLIEBER, M., VOIGT, A.-C., AOKI, T., HÄNSCH, T. W., AND DIECKMANN, K., Quantum degenerate two-species Fermi-Fermi mixture coexisting with a Bose-Einstein condensate, *Phys. Rev. Lett.,* **100** (2008) 010401.

[106] STAN, C. A., AND KETTERLE, W., Multiple species atom source for laser-cooling experiments, *Rev. Sci. Instr.,* **76** (2005) 063113.

[107] BARRETT, M. D., SAUER, J. A., AND CHAPMAN, M. S., All-optical formation of an atomic Bose-Einstein condensate, *Phys. Rev. Lett.,* **87** (2001) 010404–4.

[108] WEBER, T., HERBIG, J., MARK, M., NÄGERL, H.-C., AND GRIMM, R., Bose-Einstein condensation of cesium, *Science,* **299** (2003) 232–235.

[109] DUMKE, R., JOHANNING, M., GOMEZ, E., WEINSTEIN, J. D., JONES, K. M., AND LETT, P. D., All-optical generation and photoassociative probing of sodium Bose-Einstein condensates, *New Journal of Physics,* **8** (2006) 64.

[110] TAKASU, Y., MAKI, K., KOMORI, K., TAKANO, T., HONDA, K., KUMAKURA, M., YABUZAKI, T., AND TAKAHASHI, Y., Spin-singlet Bose-Einstein condensation of two-electron atoms, *Phys. Rev. Lett.,* **91** (2003) 040404.

[111] HOLLAND, M. J., DEMARCO, B., AND JIN, D. S., Evaporative cooling of a two-component degenerate Fermi gas, *Phys. Rev. A,* **61** (2000) 053610.

[112] GEIST, W., AND KENNEDY, T. A. B., Evaporative cooling of mixed atomic fermions, *Phys. Rev. A,* **65** (2002) 063617.

[113] TIMMERMANS, E., Degenerate fermion gas heating by hole creation, *Phys. Rev. Lett.,* **87** (2001) 240403–4.

[114] CARR, L. D., BOURDEL, T., AND CASTIN, Y., Limits of sympathetic cooling of fermions by zero-temperature bosons due to particle losses, *Phys. Rev. A,* **69** (2004) 033603–14.

[115] IDZIASZEK, Z., SANTOS, L., AND LEWENSTEIN, M., Sympathetic cooling of trapped fermions by bosons in the presence of particle losses, *Europhys. Lett.,* **70** (2005) 572–578.

[116] WOUTERS, M., TEMPERE, J., AND DEVREESE, J. T., Three-fluid description of the sympathetic cooling of a boson-fermion mixture, *Phys. Rev. A,* **66** (2002) 043414.

[117] ONOFRIO, R., AND PRESILLA, C., Reaching Fermi degeneracy in two-species optical dipole traps, *Phys. Rev. Lett.,* **89** (2002) 100401.

[118] Timmermans, E., and Côté, R., Superfluidity in sympathetic cooling with atomic Bose-Einstein condensates, *Phys. Rev. Lett.,* **80** (1998) 3419–3423.

[119] Mølmer, K., Bose condensates and Fermi gases at zero temperature, *Phys. Rev. Lett.,* **80** (1998) 1804.

[120] Modugno, G., Roati, G., Riboli, F., Ferlaino, F., Brecha, R. J., and Inguscio, M., Collapse of a degenerate Fermi gas, *Science,* **297** (2002) 2240.

[121] Ospelkaus, C., Ospelkaus, S., Sengstock, K., and Bongs, K., Interaction-driven dynamics of ^{40}K / ^{87}Rb Fermi-Bose gas mixtures in the large particle number limit, *Phys. Rev. Lett.,* **96** (2006) 020401.

[122] Grimm, R., Weidemüller, M., and Ovchinnikov, Y. B., Optical dipole traps for neutral atoms, *Adv. At. Mol. Phys.,* **42** (2000) 95–170.

[123] Takekoshi, T., and Knize, R. J., CO_2 laser trap for cesium atoms, *Optics Lett.,* **21** (1995) 77.

[124] Bourdel, T., Cubizolles, J., Khaykovich, L., Magalhães, K. M. F., Kokkelmans, S. J. J. M. F., Shlyapnikov, G. V., and Salomon, C., Measurement of the interaction energy near a Feshbach resonance in a ^{6}Li Fermi gas, *Phys. Rev. Lett.,* **91** (2003) 020402.

[125] Mosk, A., Jochim, S., Moritz, H., Elsässer, T., Weidemüller, M., and Grimm, R., Resonator-enhanced optical dipole trap for fermionic lithium atoms, *Optics Lett.,* **26** (2001) 1837–1839.

[126] Sortais, Y., Bize, S., Nicolas, C., Clairon, A., Salomon, C., and Williams, C., Cold collision frequency shifts in a ^{87}Rb atomic fountain, *Phys. Rev. Lett.,* **85** (2000) 3117.

[127] Gupta, S., Hadzibabic, Z., Zwierlein, M. W., Stan, C. A., Dieckmann, K., Schunck, C. H., v. Kempen, E. G. M., Verhaar, B. J., and Ketterle, W., RF spectroscopy of ultracold fermions, *Science,* **300** (2003) 1723–1726.

[128] Zwierlein, M. W., Hadzibabic, Z., Gupta, S., and Ketterle, W., Spectroscopic insensitivity to cold collisions in a two-state mixture of fermions, *Phys. Rev. Lett.,* **91** (2003) 250404.

[129] Oktel, M. Ö., and Levitov, L. S., Optical excitations in a nonideal Bose gas, *Phys. Rev. Lett.,* **83** (1999) 6.

[130] Oktel, M. Ö., Killian, T. C., Kleppner, D., and Levitov, L. S., Sum rule for the optical spectrum of a trapped gas, *Phys. Rev. A,* **65** (2002) 033617.

[131] Regal, C. A., and Jin, D. S., Measurement of positive and negative scattering lengths in a Fermi gas of atoms, *Phys. Rev. Lett.,* **90** (2003) 230404.

[132] Baym, G., Pethick, C. J., Yu, Z., and Zwierlein, M. W., Coherence and clock shifts in ultracold Fermi gases with resonant interactions, *Phys. Rev. Lett.,* **99** (2007) 190407.

[133] Punk, M., and Zwerger, W., Theory of rf-spectroscopy of strongly interacting fermions, *Phys. Rev. Lett.,* **99** (2007) 170404.

[134] Shin, Y., Schunck, C. H., Schirotzek, A., and Ketterle, W., Tomographic RF spectroscopy of a trapped Fermi gas at unitarity, *Phys. Rev. Lett.,* **99** (2007) 090403.

[135] Bartenstein, M., Altmeyer, A., Riedl, S., Geursen, R., Jochim, S., Chin, C., Hecker-Denschlag, J., Grimm, R., Simoni, A., Tiesinga, E., Williams, C. J., and Julienne, P. S., Precise determination of ^{6}Li cold collision parameters by radio-frequency spectroscopy on weakly bound molecules, *Phys. Rev. Lett.,* **94** (2004) 103201.

[136] Jones, K. M., Tiesinga, E., Lett, P. D., and Julienne, P. S., Ultracold photoassociation spectroscopy: Long-range molecules and atomic scattering, *Rev. Mod. Phys.,* **78** (2006) 483–53.

[137] Hutson, J. M., and Soldán, P., Molecule formation in ultracold atomic gases, *International Reviews in Physical Chemistry,* **25** (2006) 497 – 526.

[138] LeRoy, R. J., and Bernstein, R. B., Dissociation energy and long-range potential of diatomic molecules from vibrational spacings of higher levels, *The Journal of Chemical Physics,* **52** (1969) 3869.

[139] Gao, B., Zero-energy bound or quasibound states and their implications for diatomic systems with an asymptotic van der Waals interaction, *Phys. Rev. A,* **62** (2000) 050702(R).

[140] Mies, F. H., Tiesinga, E., and Julienne, P. S., Manipulation of Feshbach resonances in ultracold atomic collisions using time-dependent magnetic fields, *Phys. Rev. A,* **61** (2000) 022721.

[141] Hodby, E., Thompson, S. T., Regal, C. A., Greiner, M., Wilson, A. C., Jin, D. S., Cornell, E. A., and Wieman, C. E., Production efficiency of ultracold Feshbach molecules in bosonic and fermionic systems, *Phys. Rev. Lett.,* **94** (2005) 120402.

[142] Köhler, T., Góral, K., and Julienne, P. S., Production of cold molecules via magnetically tunable Feshbach resonances, *Rev. Mod. Phys.,* **78** (2006) 1311.

[143] Thompson, S. T., Hodby, E., and Wieman, C. E., Ultracold molecule production via a resonant oscillating magnetic field, *Phys. Rev. Lett.,* **95** (2005) 190404.

[144] Schunck, C. H., Zwierlein, M. W., Stan, C. A., Raupach, S. M. F., Ketterle, W., Simoni, A., Tiesinga, E., Williams, C. J., and Julienne, P. S., Feshbach resonances in fermionic lithium-6, *Phys. Rev. A,* **71** (2004) 045601.

[145] Regal, C. A., Ticknor, C., Bohn, J. L., and Jin, D. S., Tuning p-wave interactions in an ultracold Fermi gas of atoms, *Phys. Rev. Lett.,* **90** (2003) 053201.

[146] Zhang, J., Kempen, E. G. M. V., Bourdel, T., Khaykovich, L., Cubizolles, J., Chevy, F., Teichmann, M., Tarruell, L., Kokkelmans, S. J. J. M. F., and Salomon, C., P-wave Feshbach resonances of ultra-cold ^{6}Li, *Phys. Rev. A,* **70** (2004) 030702.

[147] Stan, C. A., Zwierlein, M. W., Schunck, C. H., Raupach, S. M. F., and Ketterle, W., Observation of Feshbach resonances between two different atomic species, *Phys. Rev. Lett.,* **93** (2004) 143001.

[148] Roberts, J. L., Claussen, N. R., Jr., J. B., Greene, C. H., Cornell, E. A., and Wieman, C. E., Resonant magnetic field control of elastic scattering in cold ^{87}Rb, *Phys. Rev. Lett.,* **81** (1998) 5109.

[149] Mukaiyama, T., Abo-Shaeer, J. R., Xu, K., Chin, J. K., and Ketterle, W., Dissociation and decay of ultracold sodium molecules, *Phys. Rev. Lett.,* **92** (2004) 180402.

[150] Dürr, S., Volz, T., and Rempe, G., Dissociation of ultracold molecules with Feshbach resonances, *Phys. Rev. A,* **70** (2004) 031601.

[151] Chwedenczuk, J., Góral, K., Köhler, T., and Julienne, P. S., Molecular production in two component atomic Fermi gases, *Phys. Rev. Lett.,* **93** (2004) 260403.

[152] Diener, R. B., and Ho, T.-L., Projecting fermion pair condensates into molecular condensates, Preprint cond-mat/0404517.

[153] Perali, A., Pieri, P., and Strinati, G. C., Extracting the condensate density from projection experiments with Fermi gases, *Phys. Rev. Lett.,* **95** (2005) 010407.

[154] Altman, E., and Vishwanath, A., Dynamic projection on Feshbach molecules: A probe of pairing and phase fluctuations, *Phys. Rev. Lett.,* **95** (2005) 110404.

[155] Yuzbashyan, E. A., Altshuler, B. L., Kuznetsov, V. B., and Enolskii, V. Z., Nonequilibrium Cooper pairing in the nonadiabatic regime, *Phys. Rev. B,* **72** (2005) 220503.

[156] Gehm, M. E., Hemmer, S. L., O'Hara, K. M., and Thomas, J. E., Unitarity-limited elastic collision rate in a harmonically trapped Fermi gas, *Phys. Rev. A,* **68** (2003) 011603(R).

[157] BARANKOV, R. A., AND LEVITOV, L. S., Atom-molecule coexistence and collective dynamics near a Feshbach resonance of cold fermions, *Phys. Rev. Lett.,* **93** (2004) 130403.

[158] BARANKOV, R. A., LEVITOV, L. S., AND SPIVAK, B. Z., Collective Rabi oscillations and solitons in a time-dependent BCS pairing problem, *Phys. Rev. Lett.,* **93** (2004) 160401.

[159] STENGER, J., INOUYE, S., STAMPER-KURN, D. M., MIESNER, H.-J., CHIKKATUR, A. P., AND KETTERLE, W., Spin domains in ground-state Bose-Einstein condensates, *Nature,* **396** (1998) 345–348.

[160] CHANG, M.-S., HAMLEY, C. D., BARRETT, M. D., SAUER, J. A., FORTIER, K. M., ZHANG, W., YOU, L., AND CHAPMAN, M. S., Observation of spinor dynamics in optically trapped ^{87}Rb Bose-Einstein condensates, *Phys. Rev. Lett.,* **92** (2004) 140403.

[161] SCHMALJOHANN, H., ERHARD, M., KRONJAGER, J., KOTTKE, M., V. STAA, S., CACCIAPUOTI, L., ARLT, J. J., BONGS, K., AND SENGSTOCK, K., Dynamics of F=2 spinor Bose-Einstein condensates, *Phys. Rev. Lett.,* **92** (2004) 040402.

[162] HIGBIE, J. M., SADLER, L. E., INOUYE, S., CHIKKATUR, A. P., LESLIE, S. R., MOORE, K. L., SAVALLI, V., AND STAMPER-KURN, D. M., Direct nondestructive imaging of magnetization in a spin-1 Bose-Einstein gas, *Phys. Rev. Lett.,* **95** (2005) 050401.

[163] DRIBINSKI, V., OSSADTCHI, A., MANDELSHTAM, V., AND REISLER, H., Reconstruction of Abel-transformable images: The basis-set expansion Abel transform method, *Rev. Sci. Inst.,* **73** (2002) 2634.

[164] OZERI, R., STEINHAUER, J., KATZ, N., AND DAVIDSON, N., Direct observation of the phonon energy in a Bose-Einstein condensate by tomographic imaging, *Phys. Rev. Lett.,* **88** (2002) 220401.

[165] BUGGLE, C., LEONARD, J., VON KLITZING, W., AND WALRAVEN, J. T. M., Interferometric determination of the s and d-wave scattering amplitudes in Rb, *Phys. Rev. Lett.,* **93** (2004) 173202–4.

[166] THOMAS, N. R., KJAERGAARD, N., JULIENNE, P. S., AND WILSON, A. C., Imaging of s and d partial-wave interference in quantum scattering of identical bosonic atoms, *Phys. Rev. Lett.,* **93** (2004) 173201–4.

[167] HUANG, K., *Statistical Mechanics*, (Wiley, New York) 1987.

[168] PERALI, A., PIERI, P., PISANI, L., AND STRINATI, G. C., BCS-BEC crossover at finite temperature for superfluid trapped Fermi atoms, *Phys. Rev. Lett.,* **92** (2004) 220404.

[169] PETHICK, C. J., AND SMITH, H., *Bose-Einstein Condensation in Dilute Gases*, (Cambridge University Press, Cambridge) 2002.

[170] HOLLAND, M., KOKKELMANS, S. J. J. M. F., CHIOFALO, M. L., AND WALSER, R., Resonance superfluidity in a quantum degenerate Fermi gas, *Phys. Rev. Lett.,* **87** (2001) 120406.

[171] STAJIC, J., CHEN, Q., AND LEVIN, K., Density profiles of strongly interacting trapped Fermi gases, *Phys. Rev. Lett.,* **94** (2005) 060401.

[172] GREINER, M., REGAL, C. A., STEWART, J. T., AND JIN, D. S., Probing pair-correlated fermionic atoms through correlations in atom shot noise, *Phys. Rev. Lett.,* **94** (2005) 110401.

[173] STAMPER-KURN, D. M., MIESNER, H.-J., INOUYE, S., ANDREWS, M. R., AND KETTERLE, W., Collisionless and hydrodynamic excitations of a Bose-Einstein condensate, *Phys. Rev. Lett.,* **81** (1998) 500–503.

[174] SHVARCHUCK, I., BUGGLE, C., PETROV, D. S., KEMMANN, M., VON KLITZING, W., SHLYAPNIKOV, G. V., AND WALRAVEN, J. T. M., Hydrodynamic behavior in expanding thermal clouds of ^{87}Rb, *Phys. Rev. A,* **68** (2003) 063603.

[175] KAGAN, Y., SURKOV, E. L., AND SHLYAPNIKOV, G. V., Evolution of a Bose gas in anisotropic time-dependent traps, *Phys. Rev. A,* **55** (1997) R18.

[176] Thomas, J. E., Kinast, J., and Turlapov, A., Virial theorem and universality in a unitary Fermi gas, *Phys. Rev. Lett.,* **95** (2005) 120402.

[177] Guéry-Odelin, D., Zambelli, F., Dalibard, J., and Stringari, S., Collective oscillations of a classical gas confined in harmonic traps, *Phys. Rev. A,* **60** (1999) 4851.

[178] Pedri, P., Guéry-Odelin, D., and Stringari, S., Dynamics of a classical gas including dissipative and mean-field effects, *Phys. Rev. A,* **68** (2003) 043608.

[179] Menotti, C., Pedri, P., and Stringari, S., Expansion of an interacting Fermi gas, *Phys. Rev. Lett.,* **89** (2002) 250402.

[180] Castin, Y., and Dum, R., Bose-Einstein condensation in time dependent traps, *Phys. Rev. Lett.,* **77** (1996) 5315–5319.

[181] Hu, H., Minguzzi, A., Liu, X.-J., and Tosi, M. P., Collective modes and ballistic expansion of a Fermi gas in the BCS-BEC crossover, *Phys. Rev. Lett.,* **93** (2004) 190403.

[182] Castin, Y., Exact scaling transform for a unitary quantum gas in a time dependent harmonic potential, *Comptes Rendus Physique,* **5** (2004) 407–410.

[183] Luo, L., Clancy, B., Joseph, J., Kinast, J., and Thomas, J. E., Measurement of the entropy and critical temperature of a strongly interacting Fermi gas, *Phys. Rev. Lett.,* **98** (2007) 080402.

[184] Bulgac, A., Drut, J. E., and Magierski, P., Spin 1/2 fermions in the unitary regime at finite temperature, *Phys. Rev. Lett.,* **96** (2006) 090404.

[185] Naraschewski, M., and Stamper-Kurn, D. M., Analytical description of a trapped semi-ideal Bose gas at finite temperature, *Phys. Rev. A,* **58** (1998) 2423.

[186] Landau, L. D., and Lifshitz, E. M., *Quantum Mechanics: Non-Relativistic Theory*, (Pergamon Press, New York) 1987.

[187] Flambaum, V. V., Gribakin, G. F., and Harabati, C., Analytical calculation of cold-atom scattering, *Phys. Rev. A,* **59** (1999) 1998.

[188] Sá de Melo, C. A. R., Randeria, M., and Engelbrecht, J. R., Crossover from BCS to Bose superconductivity: Transition temperature and time-dependent Ginzburg-Landau theory, *Phys. Rev. Lett.,* **71** (1993) 3202.

[189] Haussmann, R., *Self-consistent Quantum Field Theory and Bosonization for Strongly Correlated Electron Systems*, (Springer Verlag, Berlin) 1999.

[190] Brayshaw, D. D., Off-shell t matrix for the boundary-condition model, *Phys. Rev. C,* **3** (1971) 35–45.

[191] Kohn, W., and Luttinger, J. M., New mechanism for superconductivity, *Phys. Rev. Lett.,* **15** (1965) 524.

[192] Baranov, M. A., and Petrov, D. S., Critical temperature and Ginzburg-Landau equation for a trapped Fermi gas, *Phys. Rev. A,* **58** (1998) R801.

[193] Randeria, M., Duan, J.-M., and Shieh, L.-Y., Bound states, Cooper pairing, and Bose condensation in two dimensions, *Phys. Rev. Lett.,* **62** (1989) 981.

[194] Ortiz, G., and Dukelsky, J., BCS-to-BEC crossover from the exact BCS solution, *Phys. Rev. A,* **72** (2005) 043611.

[195] Marini, M., Pistolesi, F., and Strinati, G. C., Evolution from BCS superconductivity to Bose condensation: analytic results for the crossover in three dimensions, *Eur. Phys. J. B,* **1** (1998) 151–159.

[196] Bogoliubov, N. N., On a new method in the theory of superconductivity, *Nuovo Cimento,* **7** (1958) 794.

[197] Valatin, J., Comments on the theory of superconductivity, *Nuovo Cimento,* **7** (1958) 843.

[198] Dukelsky, J., Pittel, S., and Sierra, G., Colloquium: Exactly solvable Richardson-Gaudin models for many-body quantum systems, *Rev. Mod. Phys.,* **76** (2004) 643.

[199] GOR'KOV, L. P., AND MELIK-BARKHUDAROV, T. K., Contribution to the theory of superfluidity in an imperfect Fermi gas, *Zh. Eskp. Theor. Fiz.,* **40** (1961) 1452, [Sov. Phys. JETP 34, 61 (1961)].

[200] PETROV, D. S., SALOMON, C., AND SHLYAPNIKOV, G. V., Weakly bound dimers of fermionic atoms, *Phys. Rev. Lett.,* **93** (2004) 090404.

[201] PIERI, P., AND STRINATI, G. C., Strong-coupling limit in the evolution from BCS superconductivity to Bose-Einstein condensation, *Phys. Rev. B,* **61** (2000) 15370.

[202] HOLLAND, M., MENOTTI, C., AND VIVERIT, L., The role of boson-fermion correlations in the resonance theory of superfluids, preprint cond-mat/0404234.

[203] HU, H., LIU, X.-J., AND DRUMMOND, P. D., Equation of state of a superfluid Fermi gas in the BCS-BEC crossover, *Europhys. Lett.,* **74** (2006) 574–580.

[204] PISTOLESI, F., AND STRINATI, G. C., Evolution from BCS superconductivity to Bose condensation: Role of the parameter $k_F\xi$, *Phys. Rev. B,* **49** (1994) 6356.

[205] SKORNIAKOV, G. V., AND TER-MARTIROSIAN, K. A., Three-body problem for short-range forces, I, scattering of low-energy neutrons by deuterons, *Zh. Eksp. Teor. Fiz.,* **31** (1956) 775, [JETP Letters 4, 648 (1957)].

[206] CHIN, C., AND JULIENNE, P. S., Radio-frequency transitions on weakly bound ultracold molecules, *Phys. Rev. A,* **71** (2005) 012713.

[207] PERALI, A., PIERI, P., AND STRINATI, G. C., Competition between final-state and pairing-gap effects in the radio-frequency spectra of ultracold Fermi atoms, *Phys. Rev. Lett.,* **100** (2008) 010402.

[208] OHASHI, Y., AND GRIFFIN, A., Superfluidity and collective modes in a uniform gas of Fermi atoms with a Feshbach resonance, *Phys. Rev. A,* **67** (2003) 063612–24.

[209] COMBESCOT, R., KAGAN, M. Y., AND STRINGARI, S., Collective mode of homogeneous superfluid Fermi gases in the BEC-BCS crossover, *Phys. Rev. A,* **74** (2006) 042717–14.

[210] GIORGINI, S., PITAEVSKII, L. P., AND STRINGARI, S., Theory of ultracold Fermi gases, preprint arXiv:0706.3360.

[211] ALTMEYER, A., RIEDL, S., KOHSTALL, C., WRIGHT, M. J., GEURSEN, R., BARTENSTEIN, M., CHIN, C., HECKER-DENSCHLAG, J., AND GRIMM, R., Precision measurements of collective oscillations in the BEC-BCS crossover, *Phys. Rev. Lett.,* **98** (2007) 040401.

[212] LIFSHITZ, E. M., AND PITAEVSKII, L. P., *Statistical Physics, Part 2,* (Elsevier, Amsterdam) 1980.

[213] SENSARMA, R., RANDERIA, M., AND HO, T.-L., Vortices in superfluid Fermi gases through the BEC to BCS crossover, *Phys. Rev. Lett.,* **96** (2006) 090403.

[214] DRECHSLER, M., AND ZWERGER, W., Crossover from BCS-superconductivity to Bose-condensation, *Annalen der Physik,* **1** (1992) 15–23.

[215] HAUSSMANN, R., RANTNER, W., CERRITO, S., AND ZWERGER, W., Thermodynamics of the BCS-BEC crossover, *Phys. Rev. A,* **75** (2007) 023610.

[216] BAYM, G., BLAIZOT, J.-P., HOLZMANN, M., LALOË, F., AND VAUTHERIN, D., The transition temperature of the dilute interacting Bose gas, *Phys. Rev. Lett.,* **83** (1999) 1703.

[217] BAYM, G., BLAIZOT, J.-P., AND ZINN-JUSTIN, J., The transition temperature of the dilute interacting Bose gas for N internal states, *Europhys. Lett.,* **49** (2000) 150–155.

[218] BAYM, G., BLAIZOT, J.-P., HOLZMANN, M., LALOË, F., AND VAUTHERIN, D., Bose-Einstein transition in a dilute interacting gas, *Eur. Phys. J. B,* **24** (2001) 107–124.

[219] ARNOLD, P., AND MOORE, G., BEC transition temperature of a dilute homogeneous imperfect Bose gas, *Phys. Rev. Lett.,* **87** (2001) 120401.

[220] KASHURNIKOV, V. A., PROKOF'EV, N. V., AND SVISTUNOV, B. V., Critical temperature shift in weakly interacting Bose gas, *Phys. Rev. Lett.,* **87** (2001) 120402.

[221] Nishida, Y., and Son, D. T., Epsilon expansion for a Fermi gas at infinite scattering length, *Phys. Rev. Lett.,* **97** (2006) 050403.

[222] Burovski, E., Prokof'ev, N., Svistunov, B., and Troyer, M., Critical temperature and thermodynamics of attractive fermions at unitarity, *Phys. Rev. Lett.,* **96** (2006) 160402.

[223] Penrose, O., and Onsager, L., Bose-Einstein condensation and liquid helium, *Phys. Rev.,* **104** (1956) 576.

[224] Andrews, M. R., Townsend, C. G., Miesner, H.-J., Durfee, D. S., Kurn, D. M., and Ketterle, W., Observation of interference between two Bose-Einstein condensates, *Science,* **275** (1997) 637–641.

[225] Bloch, I., Hänsch, T. W., and Esslinger, T., Measurement of the spatial coherence of a trapped Bose gas at the phase transition, *Nature,* **403** (2000) 166–170.

[226] Madison, K. W., Chevy, F., Wohlleben, W., and Dalibard, J., Vortex formation in a stirred Bose-Einstein condensate, *Phys. Rev. Lett.,* **84** (2000) 806–809.

[227] Abo-Shaeer, J. R., Raman, C., Vogels, J. M., and Ketterle, W., Observation of vortex lattices in Bose-Einstein condensates, *Science,* **292** (2001) 476–479.

[228] Hodby, E., Hechenblaikner, G., Hopkins, S. A., Maragò, O. M., and Foot, C. J., Vortex nucleation in Bose-Einstein condensates in an oblate, purely magnetic potential, *Phys. Rev. Lett.,* **88** (2002) 010405–4.

[229] Engels, P., Coddington, I., Haljan, P. C., and Cornell, E. A., Nonequilibrium effects of anisotropic compression applied to vortex lattices in Bose-Einstein condensates, *Phys. Rev. Lett.,* **89** (2002) 100403.

[230] Campbell, C. E., Bose-Einstein condensation, pairing and ODLRO: a view from coordinate space, in *Condensed Matter Theories*, vol. 12, (Nova Science, New York) 1997, p. 131.

[231] Salasnich, L., Manini, N., and Parola, A., Condensate fraction of a Fermi gas in the BCS-BEC crossover, *Phys. Rev. A,* **72** (2005) 023621.

[232] Astrakharchik, G. E., Boronat, J., Casulleras, J., and Giorgini, S., Momentum distribution and condensate fraction of a fermion gas in the BCS-BEC crossover, *Phys. Rev. Lett.,* **95** (2005) 230405.

[233] Giorgini, S., Pitaevskii, L. P., and Stringari, S., Scaling and thermodynamics of a trapped Bose-condensed gas, *Phys. Rev. Lett.,* **78** (1997) 3987–3990.

[234] Tisza, L., Transport phenomena in helium II, *Nature,* **141** (1938) 913.

[235] Landau, L., Theory of the superfluidity of helium II, *Phys. Rev.,* **60** (1941) 356.

[236] Leggett, A. J., A theoretical description of the new phases of liquid ^{3}He, *Rev. Mod. Phys.,* **47** (1975) 331.

[237] Engelbrecht, J. R., Randeria, M., and Sá de Melo, C. A. R., BCS to Bose crossover: Broken-symmetry state, *Phys. Rev. B,* **55** (1997) 15153.

[238] Andrenacci, N., Pieri, P., and Strinati, G. C., Evolution from BCS superconductivity to Bose-Einstein condensation: Current correlation function in the broken-symmetry phase, *Phys. Rev. B,* **68** (2003) 144507.

[239] Taylor, E., Griffin, A., Fukushima, N., and Ohashi, Y., Pairing fluctuations and the superfluid density through the BCS-BEC crossover, *Phys. Rev. A,* **74** (2006) 063626–15.

[240] Abrikosov, A. A., Gor'kov, L. P., and Dzyaloshinski, I. E., *Methods of Quantum Field Theory in Statistical Physics*, (Dover Publications, New York) 1975.

[241] Abrikosov, A. A., and Gor'kov, L. P., Contribution to the theory of superconducting alloys with paramagnetic impurities, *Zh. Eksp. Teor. Fiz.,* **39** (1960) 1781, [Sov. Phys. JETP 12, 1243 (1961)].

[242] Tinkham, M., *Introduction to Superconductivity*, (Dover, Mineola, New York) 2004.

[243] Stintzing, S., and Zwerger, W., Ginzburg-Landau theory of superconductors with short coherence length, *Phys. Rev. B,* **56** (1997) 9004.

[244] Werthamer, N. R., Theory of a local superconductor in a magnetic field, *Phys. Rev.,* **132** (1963) 663.

[245] Josephson, B. D., Relation between the superfluid density and order parameter for superfluid He near Tc, *Phys. Lett.,* **21** (1966) 608–609.

[246] Kleinert, H., Critical exponents from seven-loop strong-coupling ϕ^4 theory in three dimensions, *Phys. Rev. D,* **60** (1999) 085001.

[247] Sheehy, D. E., and Radzihovsky, L., BEC-BCS crossover, phase transitions and phase separation in polarized resonantly-paired superfluids, *Annals of Physics,* **322** (2007) 1790.

[248] Son, D. T., and Stephanov, M. A., Phase diagram of cold polarized Fermi gas, *Phys. Rev. A,* **74** (2006) 013614.

[249] Prokof'ev, N., and Svistunov, B., Fermi-Polaron: Diagrammatic Monte Carlo for divergent sign-alternating series, preprint arxiv.org:0707.4259.

[250] Feshbach, H., A unified theory of nuclear reactions, *Annals of Physics,* **5** (1958) 357–390.

[251] Feshbach, H., A unified theory of nuclear reactions II, *Annals of Physics,* **19** (1962) 287–313.

[252] Fano, U., Effects of configuration interaction on intensities and phase shifts, *Phys. Rev.,* **124** (1961) 1866.

[253] van Abeelen, F. A., and Verhaar, B. J., Time-dependent Feshbach resonance scattering and anomalous decay of a Na Bose-Einstein condensate, *Phys. Rev. Lett.,* **83** (1999) 1550–1553.

[254] Yurovsky, V. A., Ben-Reuven, A., Julienne, P. S., and Williams, C. J., Atom loss from Bose-Einstein condensates due to Feshbach resonance, *Phys. Rev. A,* **60** (1999) R765–R768.

[255] Donley, E. A., Claussen, N. R., Thompson, S. T., and Wieman, C. E., Atom-molecule coherence in a BoseEinstein condensate, *Nature,* **417** (2002) 529.

[256] Fedichev, P. O., Reynolds, M. W., and Shlyapnikov, G. V., Three-body recombination of ultracold atoms to a weakly bound s level, *Phys. Rev. Lett.,* **77** (1996) 2921–2924.

[257] Nielsen, E., and Macek, J. H., Low-energy recombination of identical bosons by three-body collisions, *Phys. Rev. Lett.,* **83** (1999) 1566.

[258] Esry, B. D., Greene, C. H., and Burke, J. P., Recombination of three atoms in the ultracold limit, *Phys. Rev. Lett.,* **83** (1999) 1751.

[259] Bedaque, P. F., Braaten, E., and Hammer, H.-W., Three-body recombination in Bose gases with large scattering length, *Phys. Rev. Lett.,* **85** (2000) 908.

[260] Petrov, D. S., Three-boson problem near a narrow Feshbach resonance, *Phys. Rev. Lett.,* **93** (2004) 143201.

[261] Moerdijk, A. J., Verhaar, B. J., and Axelsson, A., Resonances in ultra-cold collisions of ^{6}Li, ^{7}Li and ^{23}Na, *Phys. Rev. A,* **51** (1995) 4852–4861.

[262] Duine, R. A., and Stoof, H. T. C., Atom-molecule coherence in Bose gases, *Phys. Rep.,* **396** (2004) 115–195.

[263] Timmermans, E., Furuya, K., Milonni, P. W., and Kerman, A. K., Prospect of creating a composite Fermi Bose superfluid, *Phys. Lett. A,* **285** (2001) 228.

[264] Combescot, R., Feshbach resonance in dense ultracold Fermi gases, *Phys. Rev. Lett.,* **91** (2003) 120401.

[265] Bruun, G. M., and Pethick, C. J., Effective theory of Feshbach resonances and many-body properties of Fermi gases, *Phys. Rev. Lett.,* **92** (2004) 140404.

[266] BRUUN, G. M., Universality of a two-component Fermi gas with a resonant interaction, *Phys. Rev. A,* **70** (2004) 053602.

[267] DE PALO, S., CHIOFALO, M. L., HOLLAND, M. J., AND KOKKELMANS, S. J. J. M. F., Resonance effects on the crossover of bosonic to fermionic superfluidity, *Phys. Lett. A,* **327** (2004) 490–499.

[268] SIMONUCCI, S., PIERI, P., AND STRINATI, G. C., Broad versus narrow Fano-Feshbach resonances in the BCS-BEC crossover with trapped Fermi atom, *Europhys. Lett.,* **69** (2005) 713.

[269] SZYMANSKA, M. H., GÓRAL, K., KÖHLER, T., AND BURNETT, K., Conventional character of the BCS-BEC crossover in ultracold gases of ^{40}K, *Phys. Rev. A,* **72** (2005) 013610.

[270] BOURDEL, T., *Gaz de Fermi en interaction forte : Du condensat de molécules aux paires de Cooper*, PhD thesis, Laboratoire Kastler Brossel, Ecole Normale Supérieure, 24 rue Lhomond, 75231 Paris 05, France, 2004.

[271] FALCO, G. M., AND STOOF, H. T. C., Crossover temperature of Bose-Einstein condensation in an atomic Fermi gas, *Phys. Rev. Lett.,* **92** (2004) 130401.

[272] MARCELIS, B., V. KEMPEN, E. G. M., VERHAAR, B. J., AND KOKKELMANS, S. J. J. M. F., Feshbach resonances with large background scattering length: Interplay with open-channel resonances, *Phys. Rev. A,* **70** (2004) 012701.

[273] V. KEMPEN, E. G. M., MARCELIS, B., AND KOKKELMANS, S. J. J. M. F., Formation of fermionic molecules via interisotope Feshbach resonances, *Phys. Rev. A,* **70** (2004) 050701(R).

[274] HUANG, K., Bose-Einstein condensation and superfluidity, in *Bose-Einstein Condensation*, edited by A. Griffin, D. Snoke, and S. Stringari, (Cambridge University Press, Cambridge) 1995, pp. 31–50.

[275] LIEB, E. H., AND LINIGER, W., Exact analysis of an interacting Bose gas. I. The general solution and the ground state, *Phys. Rev.,* **130** (1963) 1605.

[276] LIEB, E. H., Exact analysis of an interacting Bose gas. II. The excitation spectrum, *Phys. Rev.,* **130** (1963) 1616.

[277] BISHOP, D. J., AND REPPY, J. D., Study of the superfluid transition in two-dimensional ^{4}He films, *Phys. Rev. Lett.,* **40** (1978) 1727.

[278] HOHENBERG, P. C., Existence of long-range order in one and two dimensions, *Phys. Rev.,* **158** (1967) 383.

[279] BEREZINSKII, V. L., Destruction of long-range order in one-dimensional and two-dimensional systems possessing a continuous symmetry group. II. Quantum systems., *Sov. Phys. JETP,* **34** (1972) 610.

[280] KOSTERLITZ, J. M., AND THOULESS, D. J., Ordering, metastability and phase transitions in two-dimensional systems, *Journal of Physics C: Solid State Physics,* **6** (1973) 1181.

[281] SCHICK, M., Two-dimensional system of hard-core bosons, *Phys. Rev. A,* **3** (1971) 1067.

[282] HUANG, K., AND MENG, H.-F., Hard-sphere Bose gas in random external potentials, *Phys. Rev. Lett.,* **69** (1992) 644.

[283] GIORGINI, S., PITAEVSKII, L., AND STRINGARI, S., Effects of disorder in a dilute Bose gas, *Phys. Rev. B,* **49** (1994) 12938.

[284] ASTRAKHARCHIK, G. E., BORONAT, J., CASULLERAS, J., AND GIORGINI, S., Superfluidity versus Bose-Einstein condensation in a Bose gas with disorder, *Phys. Rev. A,* **66** (2002) 023603.

[285] YUKALOV, V. I., YUKALOVA, E. P., KRUTITSKY, K. V., AND GRAHAM, R., Bose-Einstein-condensed gases in arbitrarily strong random potentials, *Phys. Rev. A,* **76** (2007) 053623–11.

[286] BLOCH, I., DALIBARD, J., AND ZWERGER, W., Many-body physics with ultracold gases, Rev. Mod. Phys., to be published, preprint arXiv:0704.3011.

[287] ANDERSON, P. W., Theory of dirty superconductors, *Journal of Physics and Chemistry of Solids,* **11** (1959) 26–30.

[288] ORSO, G., BCS-BEC crossover in a random external potential, *Phys. Rev. Lett.,* **99** (2007) 250402.

[289] LEGGETT, A. J., Topics in the theory of helium, *Physica Fennica,* **8** (1973) 125–170.

[290] FISHER, M. E., BARBER, M. N., AND JASNOW, D., Helicity modulus, superfluidity, and scaling in isotropic systems, *Phys. Rev. A,* **8** (1973) 1111.

[291] LIEB, E. H., SEIRINGER, R., AND YNGVASON, J., Superfluidity in dilute trapped Bose gases, *Phys. Rev. B,* **66** (2002) 134529.

[292] MATTHEWS, M. R., ANDERSON, B. P., HALJAN, P. C., HALL, D. S., WIEMAN, C. E., AND CORNELL, E. A., Vortices in a Bose-Einstein condensate, *Phys. Rev. Lett.,* **83** (1999) 2498–2501.

[293] RAMAN, C., KÖHL, M., ONOFRIO, R., DURFEE, D. S., KUKLEWICZ, C. E., HADZIBABIC, Z., AND KETTERLE, W., Evidence for a critical velocity in a Bose-Einstein condensed gas, *Phys. Rev. Lett.,* **83** (1999) 2502–2505.

[294] ONOFRIO, R., RAMAN, C., VOGELS, J. M., ABO-SHAEER, J. R., CHIKKATUR, A. P., AND KETTERLE, W., Observation of superfluid flow in a Bose-Einstein condensed gas, *Phys. Rev. Lett.,* **85** (2000) 2228–2231.

[295] SCHECTER, D. A., DUBIN, D. H. E., FINE, K. S., AND DRISCOLL, C. F., Vortex crystals from 2D Euler flow: Experiment and simulation, *Phys. Fluids,* **11** (1999) 905.

[296] ONOFRIO, R., DURFEE, D. S., RAMAN, C., KÖHL, M., KUKLEWICZ, C. E., AND KETTERLE, W., Surface excitations in a Bose-Einstein condensate, *Phys. Rev. Lett.,* **84** (2000) 810–813.

[297] GUÉRY-ODELIN, D., AND STRINGARI, S., Scissors mode and superfluidity of a trapped Bose-Einstein condensed gas, *Phys. Rev. Lett.,* **83** (1999) 4452–4455.

[298] MARAGÒ, O. M., HOPKINS, S. A., ARLT, J., HODBY, E., HECHENBLAIKNER, G., AND FOOT, C. J., Observation of the scissors mode and evidence for superfluidity of a trapped Bose-Einstein condensed gas, *Phys. Rev. Lett.,* **84** (2000) 2056–2059.

[299] EDWARDS, M., CLARK, C. W., PEDRI, P., PITAEVSKII, L., AND STRINGARI, S., Consequence of superfluidity on the expansion of a rotating Bose-Einstein condensate, *Phys. Rev. Lett.,* **88** (2002) 070405.

[300] HECHENBLAIKNER, G., HODBY, E., HOPKINS, S. A., MARAGÒ, O. M., AND FOOT, C. J., Direct observation of irrotational flow and evidence of superfluidity in a rotating Bose-Einstein condensate, *Phys. Rev. Lett.,* **88** (2002) 070406.

[301] MODUGNO, M., MODUGNO, G., ROATI, G., FORT, C., AND INGUSCIO, M., Scissors mode of an expanding Bose-Einstein condensate, *Phys. Rev. A,* **67** (2003) 023608.

[302] CLANCY, B., LUO, L., AND THOMAS, J. E., Observation of nearly perfect irrotational flow in normal and superfluid strongly interacting Fermi gases, *Phys. Rev. Lett.,* **99** (2007) 140401.

[303] WRIGHT, M. J., RIEDL, S., ALTMEYER, A., KOHSTALL, C., GUAJARDO, E. R. S., HECKER-DENSCHLAG, J., AND GRIMM, R., Finite-temperature collective dynamics of a Fermi gas in the BEC-BCS crossover, *Phys. Rev. Lett.,* **99** (2007) 150403.

[304] COZZINI, M., AND STRINGARI, S., Fermi gases in slowly rotating traps: Superfluid versus collisional hydrodynamics, *Phys. Rev. Lett.,* **91** (2002) 070401.

[305] GUPTA, S., HADZIBABIC, Z., ANGLIN, J. R., AND KETTERLE, W., Collisions in zero temperature Fermi gases, *Phys. Rev. Lett.,* **92** (2004) 100401.

[306] KINNUNEN, J., RODRIGUEZ, M., AND TÖRMÄ, P., Signatures of superfluidity for Feshbach-resonant Fermi gases, *Phys. Rev. Lett.,* **92** (2004) 230403–4.

[307] KINAST, J., TURLAPOV, A., AND THOMAS, J. E., Breakdown of hydrodynamics in the radial breathing mode of a strongly-interacting Fermi gas, *Phys. Rev. A,* **70** (2004) 051401.

[308] GREINER, M., REGAL, C. A., TICKNOR, C., BOHN, J. L., AND JIN, D. S., Detection of spatial correlations in an ultracold gas of fermions, *Phys. Rev. Lett.,* **92** (2004) 150405.

[309] AVDEENKOV, A. V., AND BOHN, J. L., Pair wave functions in atomic Fermi condensates, *Phys. Rev. A,* **71** (2005) 023609.

[310] CHEN, Q., REGAL, C. A., GREINER, M., JIN, D. S., AND LEVIN, K., Understanding the superfluid phase diagram in trapped Fermi gases, *Phys. Rev. A,* **73** (2006) 041601.

[311] ZWIERLEIN, M. W., SCHUNCK, C. H., STAN, C. A., RAUPACH, S. M. F., AND KETTERLE, W., Formation dynamics of a fermion pair condensate, *Phys. Rev. Lett.,* **94** (2005) 180401.

[312] ZWIERLEIN, M. W., SCHUNCK, C. H., SCHIROTZEK, A., AND KETTERLE, W., Direct observation of the superfluid phase transition in ultracold Fermi gases, *Nature,* **442** (2006) 54–58.

[313] ONSAGER, L., (discussion on a paper by C.J. Gorter), *Nuovo Cimento Suppl.,* **6** (1949) 249–50.

[314] FEYNMAN, R. P., Atomic theory of liquid helium near absolute zero, *Phys. Rev.,* **91** (1953) 1301.

[315] FEYNMAN, R. P., Atomic theory of the two-fluid model of liquid helium, *Phys. Rev.,* **94** (1954) 262.

[316] SHIN, Y., SABA, M., VENGALATTORE, M., PASQUINI, T. A., SANNER, C., LEANHARDT, A. E., PRENTISS, M., PRITCHARD, D. E., AND KETTERLE, W., Dynamical instability of a doubly quantized vortex in a Bose-Einstein condensate, *Phys. Rev. Lett.,* **93** (2004) 160406.

[317] ABRIKOSOV, A. A., On the magnetic properties of superconductors of the second group, *Zh. Eksp. Teor. Fiz.,* **32** (1957) 1442, [Sov. Phys. JETP 5, 1174 (1957)].

[318] ANGLIN, J. R., Local vortex generation and the surface mode spectrum of large Bose-Einstein condensates, *Phys. Rev. Lett.,* **87** (2001) 240401–4.

[319] DALFOVO, F., AND STRINGARI, S., Shape deformations and angular-momentum transfer in trapped Bose-Einstein condensates, *Phys. Rev. A,* **63** (2001) 011601–4.

[320] RAMAN, C., ABO-SHAEER, J. R., VOGELS, J. M., XU, K., AND KETTERLE, W., Vortex nucleation in a stirred Bose-Einstein condensate, *Phys. Rev. Lett.,* **87** (2001) 210402.

[321] VINEN, W. F., Detection of single quanta of circulation in rotating helium II, *Nature,* **181** (1958) 1524.

[322] DEAVER, B. S., AND FAIRBANK, W. M., Experimental evidence for quantized flux in superconducting cylinders, *Phys. Rev. Lett.,* **7** (1961) 43.

[323] DOLL, R., AND NÄBAUER, M., Experimental proof of magnetic flux quantization in a superconducting ring, *Phys. Rev. Lett.,* **7** (1961) 51.

[324] TRÄUBLE, H., AND ESSMANN, U., The direct observation of individual flux lines in type II superconductors, *Phys. Lett.,* **24A** (1967) 526.

[325] SARMA, N. V., Direct evidence for the laminar and flux line models of mixed state in type II superconductors, *Phys. Lett. A,* **25** (1967) 315.

[326] YARMCHUK, E. J., GORDON, M. J. V., AND PACKARD, R. E., Observation of stationary vortex arrays in rotating superfluid helium, *Phys. Rev. Lett.,* **43** (1979) 214.

[327] DAVIS, J. C., CLOSE, J. D., ZIEVE, R., AND PACKARD, R. E., Observation of quantized circulation in superfluid ^{3}He-B, *Phys. Rev. Lett.,* **66** (1991) 329.

[328] ALPAR, M., AND PINES, D., in *The Lives of the Neutron Star: Conference Proceedings*, edited by M. Alpar and J. Paradijs, (Kluwer Academic, Dordrecht) 1995.

[329] DONNELLY, R. J., *Quantized vortices in Helium II*, (Cambridge University Press, Cambridge) 1991.

[330] HALJAN, P. C., CODDINGTON, I., ENGELS, P., AND CORNELL, E. A., Driving Bose-Einstein-condensate vorticity with a rotating normal cloud, *Phys. Rev. Lett.,* **87** (2001) 210403–4.

[331] STRINGARI, S., Collective excitations of a trapped Bose-condensed gas, *Phys. Rev. Lett.,* **77** (1996) 2360–2363.

[332] MADISON, K. W., CHEVY, F., BRETIN, V., AND DALIBARD, J., Stationary states of a rotating Bose-Einstein condensate: Routes to vortex nucleation, *Phys. Rev. Lett.,* **86** (2001) 4443–4446.

[333] ABO-SHAEER, J. R., RAMAN, C., AND KETTERLE, W., Formation and decay of vortex lattices in Bose-Einstein condensates at finite temperatures, *Phys. Rev. Lett.,* **88** (2002) 070409.

[334] BULGAC, A., AND YU, Y., The vortex state in a strongly coupled dilute atomic fermionic superfluid, *Phys. Rev. Lett.,* **91** (2003) 190404.

[335] CHIEN, C.-C., HE, Y., CHEN, Q., AND LEVIN, K., Ground-state description of a single vortex in an atomic Fermi gas: From BCS to Bose–Einstein condensation, *Phys. Rev. A,* **73** (2006) 041603.

[336] TONINI, G., WERNER, F., AND CASTIN, Y., Formation of a vortex lattice in a rotating BCS Fermi gas, *Eur. Phys. J. D,* **39** (2006) 283.

[337] ANGLIN, J. R., AND ZUREK, W. H., Vortices in the wake of rapid Bose-Einstein condensation, *Phys. Rev. Lett.,* **83** (1999) 1707.

[338] SHVARCHUCK, I., BUGGLE, C., PETROV, D. S., DIECKMANN, K., ZIELONKOWSKI, M., KEMMANN, M., TIECKE, T. G., V. KLITZING, W., SHLYAPNIKOV, G. V., AND WALRAVEN, J. T. M., Bose-Einstein condensation into nonequilibrium states studied by condensate focusing, *Phys. Rev. Lett.,* **89** (2002) 270404.

[339] ZHURAVLEV, O. N., MURYSHEV, A. E., AND FEDICHEV, P. O., Dissipative dynamics of vortex arrays in anisotropic traps, *Phys. Rev. A,* **64** (2001) 053601.

[340] FEDICHEV, P. O., AND MURYSHEV, A. E., Equilibrium properties and dissipative dynamics of vortex arrays in trapped Bose-condensed gases, *Phys. Rev. A,* **65** (2002) 061601.

[341] SCHUNCK, C. H., ZWIERLEIN, M. W., SCHIROTZEK, A., AND KETTERLE, W., Superfluid expansion of a rotating Fermi gas, *Phys. Rev. Lett.,* **98** (2007) 050404.

[342] ANTEZZA, M., COZZINI, M., AND STRINGARI, S., Breathing modes of a fast rotating Fermi gas, *Phys. Rev. A,* **75** (2007) 053609.

[343] HOUBIERS, M., STOOF, H. T. C., AND CORNELL, E. A., Critical temperature of a trapped Bose gas: Mean-field theory and fluctuations, *Phys. Rev. A,* **56** (1997) 2041.

[344] GEHM, M. E., HEMMER, S. L., GRANADE, S. R., O'HARA, K. M., AND THOMAS, J. E., Mechanical stability of a strongly interacting Fermi gas of atoms, *Phys. Rev. A,* **68** (2003) 011401.

[345] STEWART, J. T., GAEBLER, J. P., REGAL, C. A., AND JIN, D. S., Potential energy of a ^{40}K Fermi gas in the BCS-BEC crossover, *Phys. Rev. Lett.,* **97** (2006) 220406.

[346] BAKER, G. A., Neutron matter model, *Phys. Rev. C,* **60** (1999) 054311.

[347] STEELE, J. V., Effective field theory power counting at finite density, preprint nucl-th/0010066.

[348] HEISELBERG, H., Fermi systems with long scattering lengths, *Phys. Rev. A,* **63** (2001) 043606.

[349] PERALI, A., PIERI, P., AND STRINATI, G. C., Quantitative comparison between theoretical predictions and experimental results for the BCS-BEC crossover, *Phys. Rev. Lett.,* **93** (2004) 100404.

[350] HU, H., DRUMMOND, P. D., AND LIU, X.-J., Universal thermodynamics of strongly interacting Fermi gases, *Nature Physics,* **3** (2007) 469–472.

[351] CARLSON, J., CHANG, S.-Y., PANDHARIPANDE, V. R., AND SCHMIDT, K. E., Superfluid Fermi gases with large scattering length, *Phys. Rev. Lett.,* **91** (2003) 050401.

[352] ASTRAKHARCHIK, G. E., BORONAT, J., CASULLERAS, J., AND GIORGINI, S., Equation of state of a Fermi gas in the BEC-BCS crossover: A Quantum Monte-Carlo study, *Phys. Rev. Lett.,* **93** (2004) 200404.

[353] CARLSON, J., AND REDDY, S., Asymmetric two-component fermion systems in strong coupling, *Phys. Rev. Lett.,* **95** (2005) 060401.

[354] REGAL, C. A., GREINER, M., GIORGINI, S., HOLLAND, M., AND JIN, D. S., Momentum distribution of a Fermi gas of atoms in the BCS-BEC crossover, *Phys. Rev. Lett.,* **95** (2005) 250404.

[355] CHEN, Q., REGAL, C. A., JIN, D. S., AND LEVIN, K., Finite-temperature momentum distribution of a trapped Fermi gas, *Phys. Rev. A,* **74** (2006) 011601.

[356] JIN, D. S., ENSHER, J. R., MATTHEWS, M. R., WIEMAN, C. E., AND CORNELL, E. A., Collective excitations of a Bose-Einstein condensate in a dilute gas, *Phys. Rev. Lett.,* **77** (1996) 420.

[357] MEWES, M.-O., ANDREWS, M. R., VAN DRUTEN, N. J., KURN, D. M., DURFEE, D. S., TOWNSEND, C. G., AND KETTERLE, W., Collective excitations of a Bose-Einstein condensate in a magnetic trap, *Phys. Rev. Lett.,* **77** (1996) 988–991.

[358] JIN, D. S., MATTHEWS, M. R., ENSHER, J. R., WIEMAN, C. E., AND CORNELL, E. A., Temperature-dependent damping and frequency shifts in collective excitations of a dilute Bose-Einstein condensate, *Phys. Rev. Lett.,* **78** (1997) 764.

[359] DALFOVO, F., GIORGINI, S., PITAEVSKII, L. P., AND STRINGARI, S., Theory of Bose–Einstein condensation in trapped gases, *Rev. Mod. Phys.,* **71** (1999) 463–512.

[360] GENSEMER, S. D., AND JIN, D. S., Transition from collisionless to hydrodynamic behavior in an ultracold Fermi gas, *Phys. Rev. Lett.,* **87** (2001) 173201.

[361] ANDREWS, M. R., KURN, D. M., MIESNER, H.-J., DURFEE, D. S., TOWNSEND, C. G., INOUYE, S., AND KETTERLE, W., Propagation of sound in a Bose-Einstein condensate, *Phys. Rev. Lett.,* **79** (1997) 553–556.

[362] ASTRAKHARCHIK, G., quoted for private communication in J. Joseph et al., *Phys. Rev. Lett.* **98** (2007), 170401.

[363] KINNUNEN, J., RODRIGUEZ, M., AND TORMA, P., Pairing gap and in-gap excitations in trapped fermionic superfluids, *Science,* **305** (2004) 1131–1133.

[364] DUAN, L.-M., Effective Hamiltonian for fermions in an optical lattice across a Feshbach resonance, *Phys. Rev. Lett.,* **95** (2005) 243202.

[365] PARISH, M. M., MARCHETTI, F. M., LAMACRAFT, A., AND SIMONS, B. D., Finite-temperature phase diagram of a polarized Fermi condensate, *Nature Physics,* **3** (2007) 124–128.

[366] CHANDRASEKHAR, B. S., A note on the maximum critical field of high-field superconductors, *Appl. Phys. Lett.,* **1** (1962) 7.

[367] CLOGSTON, A. M., Upper limit for the critical field in hard superconductors, *Phys. Rev. Lett.,* **9** (1962) 266.

[368] LOBO, C., RECATI, A., GIORGINI, S., AND STRINGARI, S., Normal state of a polarized Fermi gas at unitarity, *Phys. Rev. Lett.,* **97** (2006) 200403–4.

[369] GUBBELS, K. B., AND STOOF, H. T. C., Renormalization group theory for the imbalanced Fermi gas, preprint arXiv:0711.2963.

[370] OTT, H., D. MIRANDES, E., FERLAINO, F., ROATI, G., MODUGNO, G., AND INGUSCIO, M., Collisionally induced transport in periodic potentials, *Phys. Rev. Lett.,* **92** (2004) 160601.

[371] PEZZE, L., PITAEVSKII, L., SMERZI, A., STRINGARI, S., MODUGNO, G., D. MIRANDES, E., FERLAINO, F., OTT, H., ROATI, G., AND INGUSCIO, M., Insulating behavior of a trapped ideal Fermi gas, *Phys. Rev. Lett.,* **93** (2004) 120401.

[372] ROATI, G., D. MIRANDES, E., FERLAINO, F., OTT, H., MODUGNO, G., AND INGUSCIO, M., Atom interferometry with trapped Fermi gases, *Phys. Rev. Lett.,* **92** (2004) 230402.

[373] CARUSOTTO, I., PITAEVSKII, L., STRINGARI, S., MODUGNO, G., AND INGUSCIO, M., Sensitive measurement of forces at the micron scale using Bloch oscillations of ultracold atoms, *Phys. Rev. Lett.,* **95** (2005) 093202.

[374] OSPELKAUS, S., OSPELKAUS, C., WILLE, O., SUCCO, M., ERNST, P., SENGSTOCK, K., AND BONGS, K., Localization of bosonic atoms by fermionic impurities in a three-dimensional optical lattice, *Phys. Rev. Lett.,* **96** (2006) 180403.

[375] GÜNTER, K., STÖFERLE, T., MORITZ, H., KÖHL, M., AND ESSLINGER, T., Bose-Fermi mixtures in a three-dimensional optical lattice, *Phys. Rev. Lett.,* **96** (2006) 180402.

[376] HEISELBERG, H., PETHICK, C. J., SMITH, H., AND VIVERIT, L., Influence of induced interactions on the superfluid transition in dilute Fermi gases, *Phys. Rev. Lett.,* **85** (2000) 2418.

[377] BIJLSMA, M. J., HERINGA, B. A., AND STOOF, H. T. C., Phonon exchange in dilute Fermi-Bose mixtures: Tailoring the Fermi-Fermi interaction, *Phys. Rev. A,* **61** (2000) 053601.

[378] ZIRBEL, J. J., NI, K.-K., OSPELKAUS, S., D'INCAO, J. P., WIEMAN, C. E., YE, J., AND JIN, D. S., Collisional stability of fermionic Feshbach molecules, preprint arxiv:0710.2479.

[379] WILLE, E., SPIEGELHALDER, F. M., KERNER, G., NAIK, D., TRENKWALDER, A., HENDL, G., SCHRECK, F., GRIMM, R., TIECKE, T. G., WALRAVEN, J. T. M., KOKKELMANS, S. J. J. M. F., TIESINGA, E., AND JULIENNE, P. S., Exploring an ultracold Fermi-Fermi mixture: Interspecies Feshbach resonances and scattering properties of ^{6}Li and ^{40}K, preprint arXiv:0711.2916.

[380] GÜNTER, K., STÖFERLE, T., MORITZ, H., KÖHL, M., AND ESSLINGER, T., p-wave interactions in low-dimensional fermionic gases, *Phys. Rev. Lett.,* **95** (2005) 230401.

[381] HOFSTETTER, W., CIRAC, J. I., ZOLLER, P., DEMLER, E., AND LUKIN, M. D., High-temperature superfluidity of fermionic atoms in optical lattices, *Phys. Rev. Lett.,* **89** (2002) 220407.

[382] WERNER, F., PARCOLLET, O., GEORGES, A., AND HASSAN, S. R., Interaction-induced adiabatic cooling and antiferromagnetism of cold fermions in optical lattices, *Phys. Rev. Lett.,* **95** (2005) 056401–4.